INVESTIGATION OF CONDITIONS IN CLOSELY SPACED PARALLEL EXPLODING ALUMINUM WIRES USING POINT PROJECTION X-RAY ABSORPTION SPECTROSCOPY

A Dissertation

Presented to the Faculty of the Graduate School

of Cornell University

in Partial Fulfillment of the Requirements for the Degree of

Doctor of Philosophy

by

Patrick F Knapp

August 2011

INVESTIGATION OF CONDITIONS IN CLOSELY SPACED PARALLEL EXPLODING ALUMINUM WIRES USING POINT PROJECTION X-RAY ABSORPTION SPECTROSCOPY

Patrick F Knapp, Ph.D.

Cornell University 2011

This dissertation presents the results of experiments using point-projection absorption spectroscopy to measure conditions with $20\mu m$ spatial and sub-ns temporal resolution in closely spaced parallel and single exploding Al wires. Experiments were conducted on both the $0.5MA$ XP and $1MA$ COBRA generators at Cornell University. The intense continuum radiation pulse from micron scale Mo wire X-pinches was used to backlight the exploding wire plasmas. A spherically bent quartz crystal spectrometer was used to disperse the x-rays which, in conjunction with the small source size, provides very high spectral resolution ($\lambda/\Delta\lambda \sim 5000$) and is ideal for studying the detailed $1s-2p$ and $1s-3p$ absorption spectra in the plasmas generated by Al wire array z-pinches.

Absorption features of ionization stages from Mg-like to He-like Al have been identified in spectral structures surrounding the cold K-edge at 7.95Å ($1560eV$). This work represents the first time many of the $1s-3p$ features have been observed and identified. Changes in the spectral structure near the K-edge are correlated with the spatial structure of the dense residual wire core. The transition from cold dense core material to the tenuous coronal plasma is observed directly via the spatially resolved change in absorption near the wire core.

In the COBRA experiments a step wedge was used to calibrate the expo-

sure level on the film, which enabled us to determine the absolute transmission through the plasma within ±17%. A genetic algorithm was developed to fit synthetic spectra calculated using the collisional-radiative code SCRAM to the experimental spectra. This approach allowed the inferred plasma conditions to vary along the line of sight of the diagnostic. The distributions of density and temperature determined by the genetic algorithm are not unique, but were constrained to satisfy several criteria that ensure they are physically reasonable. In the two-wire experiments the temperature reaches $29 \pm 7eV$ in the plasma accumulating at the center line between the two wires. At the edge of the wire cores, where the density remains high ($\gtrsim 0.027 g/cc$), the temperature is less than $10eV$.

BIOGRAPHICAL SKETCH

Patrick Francis Knapp was born in South Bend, IN on May 28, 1982 to Pat and Maggie Knapp. He has one sister, Melanie Hooper and is married to his wonderful wife, Kathryn Knapp. On January 12, 2011 his wife gave birth to their son, Patrick Wallace. He is blessed with a large extended family including his two grandparents, Pat and Joanne Knapp, a niece and nephew, two brothers-in-law and an array of aunts, uncles and cousins.

Patrick moved to Las Cruces, NM when he was one and then again to Gaithersburg, MD when he was four, where he spent the remainder of his life until college. He graduated from Thomas S. Wootton High School in Rockville, MD in the year 2000. At Wootton he gained an immense interest in science and engineering, primarily through the teachings of Perry Bascom, his physics teacher for two years. He completed a B.S. in electrical and computer engineering from Syracuse University in 2004, after which he took a job at the Naval Research Laboratory (NRL) in the optical sciences division. It was there while working under Frank Bucholtz, Matt Rogge and Vince Urick that he realized he wanted a career in scientific research, though not in optical sciences. It was during this time that Patrick began looking for a new field. He happened upon various articles on fusion and plasma physics. The combination of the pursuit of near limitless energy coupled with the ability to work on large, dangerous machines was too much of an enticement for him. While he was sad to leave his new mentors, after two years at the NRL he decided he needed to leave to pursue his PhD at Cornell University

From his first day in the Laboratory of Plasma Studies he knew he was home. A few months after his arrival, his wife to be joined him in Ithaca where she began work as an insurance agent. They married in November of 2006. During

his study at Cornell under the direction of Professor David Hammer, Patrick pursued many areas of basic and applied science including classical mechanics, electrodynamics, quantum mechanics, plasma physics, astrophysics and radiation science. His interest in the dynamics of high energy density plasmas has only grown since starting his study. His work has afforded him the opportunity to meet many new friends, travel all over the country and learn about a wide array of new and exciting fields. Currently, he plans to begin work as an experimental high energy density scientist at Sandia National Laboratories in Albuquerque, NM.

This document is dedicated to my wife and son for whom I work so hard.

ACKNOWLEDGMENTS

This dissertation would not have been possible without the help, guidance, support and love of countless people. I am deeply indebted to every one of them.

I would like to thank my thesis advisor and committee chair, David Hammer. His guidance throughout my years in the Laboratory of Plasma Studies has been invaluable and has certainly improved my ability to do quality science. He helped me choose classes that would be both worthwhile and stimulating as well as research projects that would be exciting and educational. Every project I have started at LPS has helped increase my technical knowledge, my ability to engage with the community and my eagerness to learn more. I am always left with more questions than answers, which I think is an essential ingredient for good science.

I would also like to thank Dr.'s Ryan McBride and Jon Douglass for mentoring me in my first years in lab. I would not have know which end of a vacuum pump was which if it weren't for them. They taught me how to string arrays, analyze data, design experiments and find coffee at conferences. Additionally, I need to thank Jon for giving David Hammer the extra push needed to take me on as a student. None of this would have been possible if not for him.

Everything I know about experimental plasma physics that I didn't learn from Jon and Ryan, I learned from Sergei Pikuz and Tania Shelkovenko. They gave me the skills and confidence to dive head first into x-ray spectroscopy, opening a whole new world of experimental opportunities for me. Sergei's seemingly never ending knowledge of optics and his remarkable ability to build nearly anything out of lead tape have saved many experiments for me. Tania's ability to navigate the world of x-ray film and identify x-ray spectra by sight have guided me through the design and implementation of more experiments

than I can count. Without their knowledge of x-ray spectroscopy and x-pinches and their genuine excitement about absorption spectroscopy and my work in general I never would have been able to complete this work.

Professor Charles Seyler has helped provide me with valuable insight into the theoretical and computational side of plasma physics research. Through his course in advanced plasma physics, his seminar on computational methods and many discussions my basic understanding of the world of plasmas has grown immensely. He always stressed the need to obtain intuition about equations through simplified examples and parameter estimates. These skills have come in handy quite often while interpreting my data. Additionally, the simulation software written in conjunction with his former student, Dr. Matt Martin, has been incredibly useful in the study of plasma physics at LPS. Running the software has helped me learn much about the underlying physics of MHD, and, more importantly, where and how the approximations break down. These skills will undoubtedly prove useful for years to come.

Professor Bruce Kusse's courses in mathematical physics were some of the most challenging and fruitful courses I had the pleasure of taking at Cornell. Coming from an engineering background, I lacked many of the mathematical tools needed for research in applied physics. His courses brought these skills into focus for me and helped bring me the confidence I needed to research effectively. He has also been an effective leader of day to day lab operations. He is always checking on COBRA to ensure it is operating properly and helping to coordinate research between the students. He has a wealth of practical experimental advice and is always kind enough to share it with the students.

Though Professor Pierre Gourdain is a relatively new addition to LPS, he has certainly made an impact. He is a highly skilled researcher in both experi-

mental and theoretical plasma physics, an all too uncommon combination. My discussions with him have always been enlightening as well as entertaining. His passion and enthusiasm are unmatched at LPS and I will certainly miss working with him.

This thesis would not have been possible without the help of Dr. Stephanie Hansen of Sandia National Labs. Early on, her suggestions and preliminary analysis helped guide the research and shape it into its final form. She graciously donated her time and effort to calculate the opacities that were used to interpret the data and was always available to provide helpful references and share the tricks of the trade she has picked up along the way. I will always be grateful for her efforts.

As anyone who has worked in LPS knows, nothing of consequence gets done without the expert assistance of Todd Blanchard and Harry Wilhelm. In his time at LPS Harry has acquired an array of skills that few people on this planet possess. His assistance in carrying out experiments is invaluable, from building arrays, designing hardware and running the machine. And he is always available to cheer you up with a funny story or esoteric fact. Todd is truly an expert machinist. I could always count on him to take a vague description of something complicated and bulky and turn it into a sleek, functional and compact instrument. He takes pride in his work, as he should. Day in and day out, these two men have been in lab working and playing hard. They have truly made LPS a wonderful place to work.

Growing up I was never in need of encouragement to pursue my interests. My parents were always right behind me in anything I did, be it skateboarding, playing the guitar or my interest in science and engineering. Though neither of them was ever interested in the sciences, they never hesitated to drive me to

the library or help me work on my science fair project, and they always knew how to find the right people to talk to when my questions went beyond their knowledge. More importantly, they always believed in me and never hesitated to let me know. I will always be grateful for their enduring love and support.

I believe I owe much of my curiosity to my grandfathers. My paternal grandfather is an auto mechanic to this day. His ability to work with his hands and fix something so complex and daunting as a *car* was always inspiring. My maternal grandfather was in the army corps of engineers during World War II and worked as a civil engineer. He was an eternal tinkerer, never content to let something simply be broken. He knew how to fix seemingly anything, and understood how it all worked. I always aspired to attain the skill and knowledge these two men possessed.

Last but certainly not least I would like to thank my wife, Kathryn. She has always supported me. I took her away from her family to a small town in upstate New York that she had never been to, and she didn't think twice. I will soon be taking her even farther away, to Albuquerque New Mexico. When I was unsatisfied with my work at the Naval Research Laboratory she encouraged me to apply to graduate school to pursue my Ph.D. Through all the uncertainty and difficulty of this process she has been beside me to convince me that I can do this and remind me that I am my harshest critic. I can't thank her enough. In January of this year she gave birth to our son, Patrick Wallace. Her strength and grace throughout the entire process have been inspiring and have helped drive me to complete this work.

TABLE OF CONTENTS

LIST OF TABLES

LIST OF FIGURES

CHAPTER 1

INTRODUCTION

1.1 High Energy Density Physics (HEDP)

High energy density physics can be defined as the study of systems having pressures exceeding one million atmospheres ($1 Mbar$) or, alternatively, an internal energy exceeding $10^{12} erg/cm^3$, ($10^{11} J/m^3$). Under these conditions electrons are stripped from atoms, radiation can constitute a significant portion of the energy budget and solids can become compressible, allowing extreme densities to be reached. Figure 1.1 shows a phase space diagram depicting the conditions under which high energy density (HED) matter exists. Typical examples of systems in which these conditions can exist include the solar interior, cores of gas giant planets, inertial confinement fusion experiments, nuclear explosions, and accretion disks around, and jets emanating from, compact astrophysical objects. Though virtually nonexistent on earth, naturally occurring HED systems are widely varying and ubiquitous throughout the cosmos. On earth, we are forced to create and study these conditions in the laboratory using highly specialized equipment.

Historically, the primary focus for studying matter under these extreme conditions has been nuclear fusion and nuclear weapons research. Today, applications have extended to include the study of astrophysically relevant laboratory systems, radiation science, atomic physics, material properties and equations of state (EOS). Apart from the basic science of these broad areas, practical applications include the eventual realization of nuclear fusion as a viable energy source, the effects of radiation on materials and electronics, the effects of extreme con-

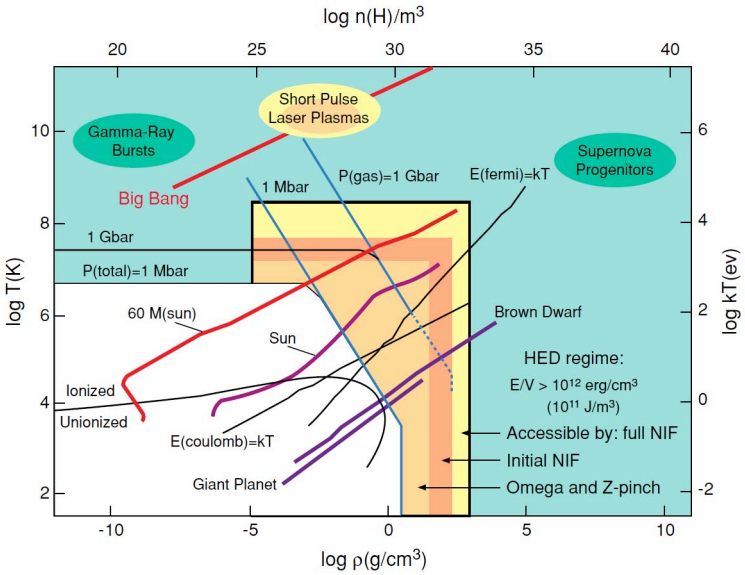

Figure 1.1: Phase space diagram indicating where high energy density matter exists. The entire colored portion of the plot is considered HED. The regions of phase space within reach of existing scientific facilities, such as the Z-machine and Omega, are noted[50].

ditions on materials, creating smaller, more powerful particle accelerators, and the development of advanced light and particle sources for science and engineering applications.

Creating these conditions in the laboratory is challenging and has become common only in the last 25 years. Large laser facilities are the most popular means of creating HED matter, and at the time of this writing the largest laser facility in the world, the NIF at Lawerence Livermore National Laboratory, is beginning its campaign to achieve ignition of a fusion fuel capsule for the first time. Lasers of sufficient intensities are able to directly ionize matter, drive strong shocks into solids, generate relativistic electrons and create high-flux x-ray sources. The advantages of using lasers to create HED matter are the ability to focus large energy fluxes into very small volumes and a high degree of control over timing, aiming and pulse shape.

An alternate approach to creating HED matter is to use pulsed power facilities to heat and compress matter using large, fast rising current pulses. The world's largest and most powerful pulsed power machine, the Z-machine at Sandia National Laboratories, generates up to 26 million amperes of current with a pulse rise time as short as $100ns$. This intense current pulse can be used for a variety of applications. By using the current to implode an array of hundreds of exploding wire plasmas in a cylindrical configuration, known as a wire array z-pinch, the Z-machine can generate extremely intense soft x-ray fluxes, up to $2MJ$ of x-ray energy in $5ns$ or less. These x-ray sources can be used to test the effects of x-rays on materials, to heat and photoionize matter and to compress a fusion fuel capsule for fusion energy research. Recently, research has begun on the Z-machine studying the viability of using the magnetic field produced by the current to directly compress and heat fuel for fusion, an approach known as Magnetized Liner Inertial Fusion (MagLIF)[71]. Additionally, magnetic compression of matter is used to study the Equation of State of various materials in previously unreachable regions of phase space. The advantages of using pulsed power over lasers to study HEDP are the ability to create and study comparatively large volumes of matter, the addition of high magnetic fields and low cost of the driver energy.

1.2 The Z-Pinch and Magnetic Forces

The key to generating extreme states of matter on pulsed power machines is the magnetic pinch effect. This effect arises from the Lorentz force, the force imposed upon charged particles interacting with electric and magnetic fields.

In the case of a single particle this force can be expressed in SI units as

$$\mathbf{F}_l = \mathrm{q}(\mathbf{E} + \mathbf{v} \times \mathbf{B}) \tag{1.1}$$

where q is the charge of the particle, $\mathbf{v}$ is the velocity of the particle and $\mathbf{E}$ and $\mathbf{B}$ are the electric and magnetic fields at the position of the particle.

In a plasma there will be many charged particles, potentially with varying charge, mass and number densities. The electric and magnetic fields generated by these particles will have to be taken into account along with the externally imposed $\mathbf{E}$ and $\mathbf{B}$, all of which must obey Maxwell's equations to self consistently solve the system of equations that determine the dynamics of such a collection of charged particles. Maxwell's equations are

$$\nabla \cdot \mathbf{E} = \frac{\rho}{\epsilon_o} \tag{1.2}$$

$$\nabla \cdot \mathbf{B} = 0 \tag{1.3}$$

$$\nabla \times \mathbf{E} = -\frac{\partial \mathbf{B}}{\partial t} \tag{1.4}$$

$$\nabla \times \mathbf{B} = \mu_o \mathbf{J} + \mu_o \epsilon_o \frac{\partial \mathbf{E}}{\partial t} \tag{1.5}$$

In addition there will be other forces at work on the plasma as a whole. These forces can be incorporated using a fluid description of the plasma, which is generally adequate to describe the dynamics, and is certainly adequate to understand the magnetic pinch effect. We can use a so-called *two-fluid* description where separate quantities, $Q_{i,e}$, are defined for the ion (i) and electron (e) fluids. In this description $Q_{i,e}$ can be any quantity describing the fluid such as the particle density $n_{i,e}$, fluid velocity, $\mathbf{u}_{i,e}$ or the pressure $p_{i,e}$ exerted by the particular fluid (assumed to be isotropic here). The equations of motion for the two species can then be written as

$$m_i n_i \dot{\mathbf{u}}_i = \mathrm{q}_i \mathrm{n}_i (\mathbf{E} + \mathbf{u}_i \times \mathbf{B}) - \nabla \mathrm{p}_i \tag{1.6}$$

$$m_e n_e \dot{\mathbf{u}}_e = \mathrm{q}_e \mathrm{n}_e(\mathbf{E} + \mathbf{u}_e \times \mathbf{B}) - \nabla \mathrm{p}_e \tag{1.7}$$

where $\nabla p_{i,e}$ is the force exerted by the thermal pressure of each fluid and $\dot{\mathbf{u}}$ denotes the convective, or Lagrangian, derivative.

In the simple example of two fluids we can consider each ion to be Z times ionized and therefore $q_i = -Zq_e$. Then, by invoking quasi-neutrality, the number density of electrons is simply related to the number density of ions by $n_e = Zn_i$. Substituting these two expressions into the equations of motion, eliminating q_i and n_i in favor of q_e and n_e, and summing the ion and electron equations we obtain a combined equation of motion

$$n_e\left(\frac{1}{Z} m_i \dot{\mathbf{u}}_i + m_e \dot{\mathbf{u}}_e\right) = q_e n_e(\mathbf{u}_e - \mathbf{u}_i) \times \mathbf{B} - \nabla \mathrm{p} \tag{1.8}$$

where $p = p_i + p_e$. It is easy to see by the way the equation of motion has been written above that the first term on the right involves the current density $\mathbf{J}$ which by definition is $\mathbf{J} = q_e n_e(\mathbf{u}_e - \mathbf{u}_i)$. For our purely illustrative purposes we can consider a system in static equilibrium whereby $\frac{dX}{dt} = 0$ for any quantity X. Therefore the equation of motion simplifies to become $0 = \mathbf{J} \times \mathbf{B} - \nabla \mathrm{p}$, or, rearranging terms

$$\nabla p = \mathbf{J} \times \mathbf{B} \tag{1.9}$$

This equation simply states that in a current carrying plasma in equilibrium the force exerted by the thermal pressure of the plasma must be balanced by the force of the current density interacting with the magnetic field. In an idealized example we take the plasma to be an infinitely long cylinder with radius a of uniform temperature and density coaxial with the z-axis, with current density flowing in an infinitely thin layer on the edge of the cylinder in the positive z-direction. There is no externally imposed magnetic field. Therefore the plasma

pressure vanishes at $r = a$ and the only field in the problem is that generated by the current, which is in the θ-direction only. Using ampere's law and neglecting displacement current (i.e. steady state) we obtain $\nabla \times \mathbf{B} = \mu_o \mathbf{J}$. In this situation the thermal pressure gradient exists only at the edge of the cylinder and exerts a force outward. The $\mathbf{J} \times \mathbf{B}$ force is directed inward and balances the pressure gradient exactly. Substituting for $\mathbf{J}$ in eqn. (1.9) and using a vector identity we derive

$$\nabla p = \frac{1}{\mu_o}(\nabla \times \mathbf{B}) \times \mathbf{B} \tag{1.10}$$

$$= \frac{1}{2\mu_o}(2(\mathbf{B} \cdot \nabla)\mathbf{B} - \nabla(\mathbf{B} \cdot \mathbf{B})) \tag{1.11}$$

In this example the magnetic field exists only in the θ-direction and varies only in the r-direction, therefore $\mathbf{B} = B\hat{\theta}$ and $\mathbf{B} \cdot \mathbf{B} = B^2$. Using a vector identity in the NRL plasma formulary[30] we find $(\mathbf{B} \cdot \nabla)\mathbf{B} = -(B^2/\mu_o r)\hat{r}$. Substituting into eqn. (1.11) we find

$$\nabla p = -\frac{B^2}{\mu_o r}\hat{r} - \nabla\left(\frac{B^2}{2\mu_o}\right) \tag{1.12}$$

Since the problem has variation only in the r-direction we can set $\nabla \to \partial/\partial r$. If we multiply both sides of eqn. (1.12) by r^2 and integrate from 0 to a, keeping in mind the plasma, and therefore the pressure, is uniform for $r < a$ and the current only exists at $r = a$, we find (with $p(a) = 0$ defining the boundary of the plasma)

$$\int_o^a \frac{\partial p}{\partial r} r^2 dr = -\int_o^a \frac{B^2}{\mu_o} r dr - \int_o^a \frac{\partial B^2}{\partial r}\frac{r^2}{2\mu_o} dr \tag{1.13}$$

$$\left(pr^2\right)\Big|_0^a - \int_o^a 2pr dr = -\int_o^a \frac{B^2}{\mu_o} r dr - \left(\frac{B^2 r^2}{2\mu_o}\Big|_o^a - \int_o^a \frac{B^2}{\mu_o} r dr\right) \tag{1.14}$$

$$\cancelto{0}{p(a)a^2} - \int_o^a p 2r dr = -\frac{B^2(a)a^2}{2\mu_o} \tag{1.15}$$

$$-p\int_o^a 2r dr = -\frac{B^2(a)a^2}{2\mu_o} \tag{1.16}$$

$$-pa^2 = -\frac{B^2(a)a^2}{2\mu_o} \tag{1.17}$$

$$p = \frac{B^2(a)}{2\mu_o} \equiv p_{mag}(a) \tag{1.18}$$

Where in the last line we have defined the *magnetic pressure* which we can see must balance the plasma pressure in this example. This exercise shows that via the $\mathbf{J} \times \mathbf{B}$ force a magnetic field can exert pressure on a conducting medium.

This magnetic pressure is the essence of confinement by magnetic fields. In addition, if the plasma is not in equilibrium the plasma can be compressed not simply confined. At the high densities and temperatures present in wire array z-pinches, this involves many non-ideal physical processes, such as radiation and ionization losses, resistive dissipation and instabilities. All of these effects and others combine to enable the production of high energy density matter that exhibit the rich physical phenomena we study in the laboratory.

1.3 Pulsed Power & the COrnell Beam Research Accelerator (COBRA)

Pulsed power is a technique by which a pulse of electromagnetic energy is repeatedly compressed in time, increasing its power with each compression. For example, the COBRA[23] generator at Cornell University stores $100kJ$ in two capacitor banks over approximately one and a half minutes, corresponding to an average power of about $1kW$. After a series of three compression stages, this energy is discharged into the load in approximately $100ns$, resulting in a power of $1TW$, a power gain of $\sim 10^9$. In COBRA this compression is accomplished by successively storing the energy in a capacitor and a transmission line and then

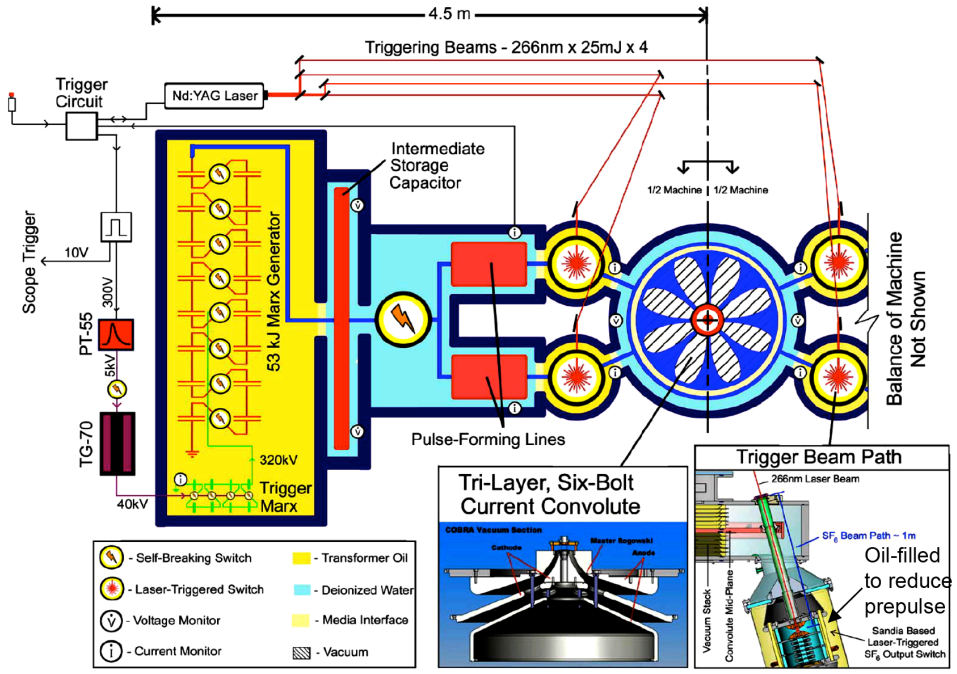

Figure 1.2: Schematic of the architecture of COBRA reproduced from ref. [17]

switching it, via low inductance gas filled switches, into a new transmission line or capacitor with a smaller characteristic time constant. The many criteria and constraints that were involved in choosing the particular architecture of COBRA are beyond the scope of this document. However, it is helpful to understand the basic operation of the machine and its limitations in order to better understand the constraints on and performance of the various loads studied at Cornell.

After its initial mission as a $3MeV$, $250kA$ light ion beam driver, COBRA was redesigned to drive $\sim 1MA$ current pulses into low-inductance wire array loads for the purpose of studying x-ray generation and HED plasmas. The redesign was based upon three main performance goals: the ability to drive $1MA$ peak current into a wire array, a minimum $100ns$ zero-to-peak rise-time and the ability to vary the pulse shape[23]. The architecture of COBRA is shown schematically in fig. 1.2. As mentioned above, the machine stores $100kJ$ in two capacitor

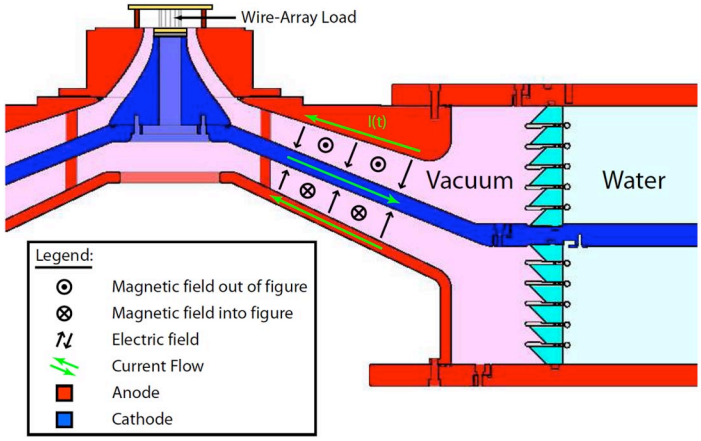

Figure 1.3: A diagram of the vacuum convolute region of COBRA. The green arrows indicate the direction of current flow, reproduced from ref. [48].

banks, known as Marx generators, each of which are discharged into an intermediate storage capacitor (ISC) via low inductance gas-filled spark gap switches. All of the gas switches on COBRA are filled with sulfur hexa-fluoride (SF_6), chosen for its high electronegativity and predictable properties in high voltage switches. It takes approximately $800ns$ for a Marx generator to fully charge each ISC, at which point they each discharge into two parallel pulse forming lines via two self-breaking, i.e. untriggered, spark gap switches. The use of four pulse forming lines in parallel was chosen to decrease the total power feed inductance, allowing shorter current rise times in the load.

The pulse forming lines are charged by the ISCs in about $200ns$, at which time the four output switches close, either by self-breaking or by laser triggering, discharging the energy into the vacuum convolute, a diagram of which is shown in fig. 1.3. The laser triggering is used to vary the closing times of the four switches to provide the pulse shaping capability. Minimum current rise time is achieved when all four switches close at the same time, i.e. within $\pm 10ns$. The vacuum convolute is a triaxial radial transmission line with constant

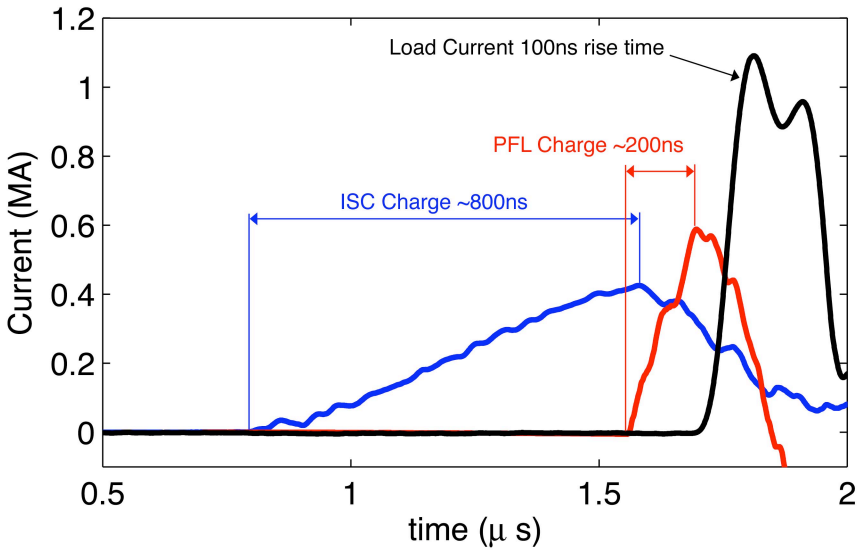

Figure 1.4: Traces from COBRA shot 2034 showing the pulse compression through successive stages. The charging waveform of the ISC is shown in blue with the charge time indicated. The charging waveform of one of the PFL's is shown in red. FInally, the $100ns$ zero-to-peak rise time current pulse is shown.

impedance per unit radius. The triaxial transmission line is converted to a coaxial feed near the base of the load. Figure 1.4 shows the sequence of charging and discharging the various stages just described, culminating in the final $1MA$ output pulse. A more detailed description of the operation of COBRA is provided in reference [23]. The output impedance of the machine is approximately 0.25Ω with an inductance of about $19nH$. In practice a peak current of $1.2MA$ with a rise time of $95ns$ is routinely achieved. Loads with intrinsic inductance comparable to or greater than the feed inductance can limit these values somewhat. However the machine performs with little change to the current waveform except when there is considerable dissipation.

A second, smaller pulsed power generator is in use at the Laboratory of Plasma studies. This machine, called XP[34], was designed to study x-pinches as an x-ray source for radiography and lithography. An x-pinch is an array of

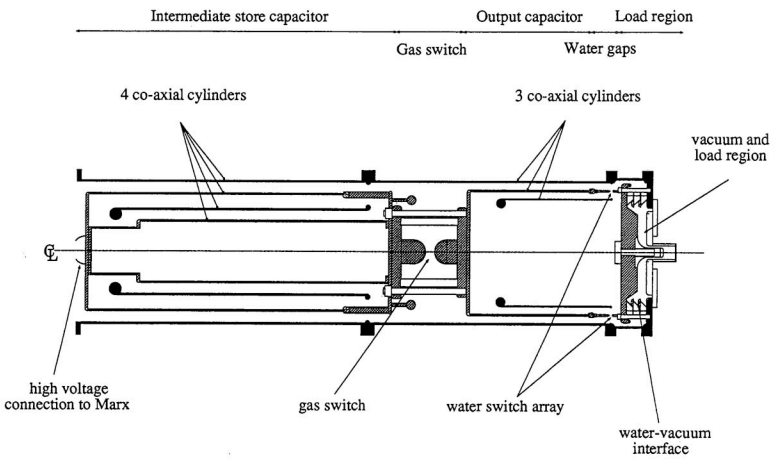

Figure 1.5: Schematic of the architecture of the XP pulser reproduced from ref. [34]

two or more wires which cross at a single point. They have been shown to produce very short x-ray bursts with micron scale spot sizes[69]. As they play an important role in this thesis, the details of the x-pinch will be discussed further in sec. 4.1. XP, whose architecture is shown in Fig. 1.5, operates in a similar manner to COBRA with a few important differences. It is capable of driving 500kA peak current into a low inductance load with a rise-time of 50 ns. A single Marx bank discharges into an intermediate storage capacitor which in turn discharges through a single gas switch into two parallel transmission lines. The output stage is an array of water-gap switches which breakdown and sharpen the pulse further before it reaches the load. The features of XP are detailed further in ref. [34]

The short rise-time makes XP ideal for studying x pinches, the behavior of which have been shown to be sensitive to the rate of rise of current. X-pinches have been used extensively to study the structure of exploding wires and wire array z-pinches[16, 64, 61, 66]. In addition to their diagnostic importance, x-

pinches present an interesting opportunity for studying dense, hot and transient plasma processes due to the extreme parameters reached leading up to and during the x-ray burst.

1.4 Research Motivation and Applications

Pulsed power driven HED plasmas present interesting and challenging prospects for studying the physics of matter under extreme conditions, including strongly radiating plasmas generated from intermediate and high atomic number (Z) materials. One of the unique challenges of wire-array z-pinch physics is the simultaneous existence of important phenomena on disparate scales. For instance, the residual wire core and surrounding coronal plasma can be seen as a single system. However, the core is micron scale, near solid density and only a few eV in temperature while the coronal plasma is millimeter scale, $\sim 10^{18} cm^{-3}$ particle density or lower and $10's$ of eV. It is very challenging to understand these two objects using the same theoretical tools or even the same diagnostics. However they interact strongly and understanding their mutual evolution is crucial to understanding the overall behavior of the wire array z-pinch.

This document focuses on the use of x-ray absorption spectroscopy to understand the density and temperature of the coronal plasma in a model system. Based upon the experimental results reported here, we anticipate that the same method will be applied to wire array z-pinches and more generally to ohmically driven metal plasmas. In the following chapters we will discuss the evolution of wire array z-pinches in general and a few particular unresolved issues re-

garding the wire core and coronal plasma system. We will give a background on the use of absorption spectroscopy to diagnose plasmas including the important physics behind absorption of photons by ions in a plasma. We will discuss in detail the design and characterization of the instrument used in this research and the data obtained with it. Finally we will discuss the data analysis, results obtained and conclusions.

CHAPTER 2

THE WIRE ARRAY Z-PINCH

2.1 A Brief Description of Z-pinch Processes

As mentioned in section 1.1 the wire array z-pinch is a well developed x-ray source capable of producing megajoules of x-ray energy in a $5ns$ FWHM pulse when powered by $\gtrsim 20MA$ of current on the Z machine[74, 14]. The high efficiency of these x-ray sources prompted a desire to study the physics at work on a smaller scale than that available on the Z-machine. This has been one of the primary purposes for running COBRA since its completion.

A wire array Z-pinch is an array of fine metallic wires, typically at least four, strung between the anode and cathode of a pulsed power generator capable of supplying a minimum of $100kA$ of current in a few hundred nanoseconds or less. The wires rapidly vaporize and ablate plasma which is driven to the current centroid under the action of the $\mathbf{J} \times \mathbf{B}$ force, as discussed in sec. 1.2. In a cylindrically symmetric configuration, such as that shown in fig. 2.1, this is the axis of the cylinder. At the axis, the plasmas from the wires merge, creating a single current-carrying column. Once most of the initial mass of the wires has reached the axis the current can compress the column further causing a short, intense burst of x-ray radiation to be released. In the remainder of this section we will discuss in more detail each of the processes leading up to and including the eventual x-ray pulse.

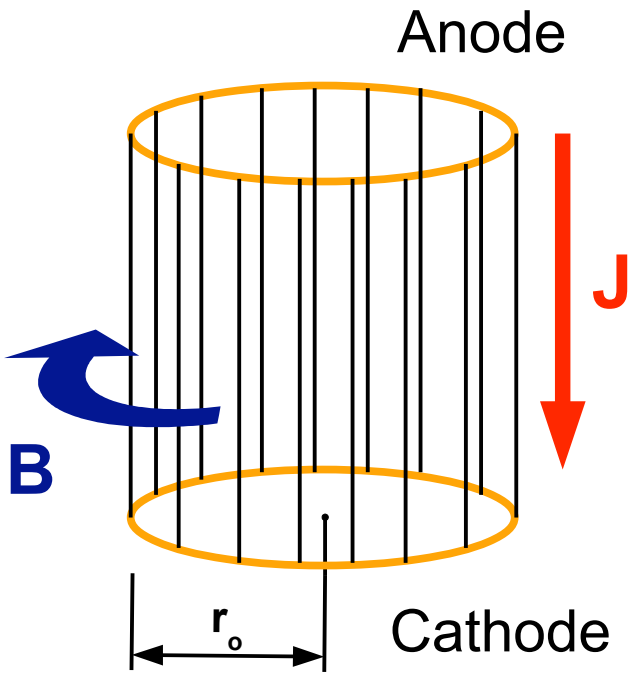

Figure 2.1: A schematic depiction of a cylindrical array of 16 wires with initial radius r_o. The current, **J**, flows from the anode to cathode producing an azimuthal magnetic field, **B**.

2.2 The Four Phases

Studies of the physics of wire array z-pinches have found it logical to divide the evolution of these objects into four distinct phases: initiation, ablation, implosion and stagnation. This evolution is shown graphically in fig. 2.2 using a visible light streak camera image. The initiation phase cannot be seen because the visible light emission levels are too low. However, the basic dynamics of the other three phases and their relative time scales are clearly visible. Each of these

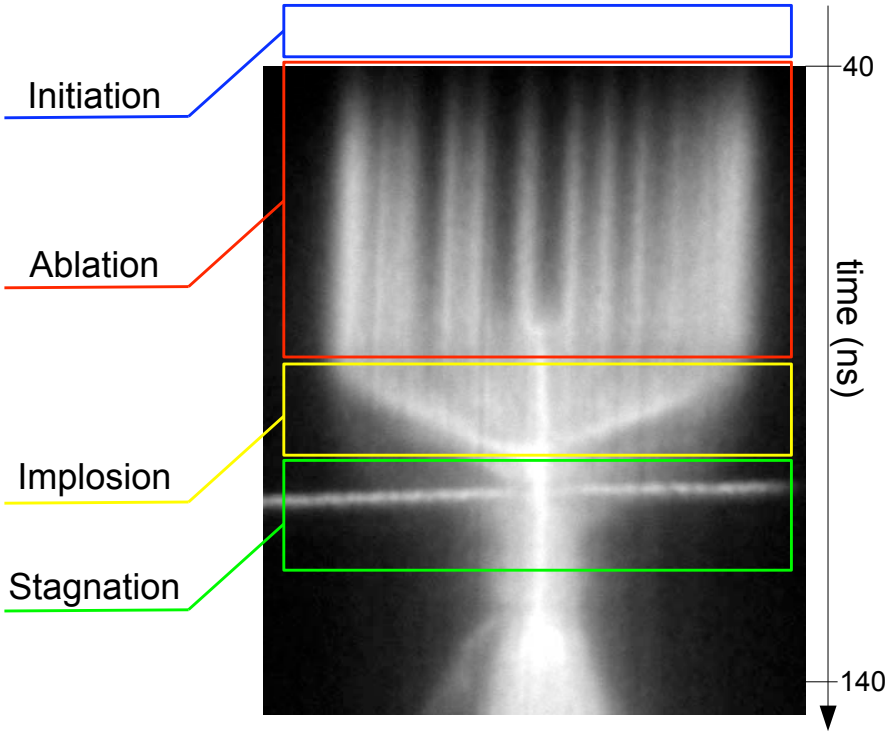

Figure 2.2: A radial visible streak image obtained on COBRA. The relative timing and durations of each of the four phases of the wire array z-pinch are shown. Initiation (blue) occurs before the beginning of the streak.

phases is characterized by having qualitatively different dynamics and dominating physical processes. The basic processes and defining characteristics of each phase are outlined below.

2.2.1 Initiation

Initiation is the earliest phase in the evolution of a wire array z-pinch. It is characterized by the formation of plasma around the wires, also known as *breakdown*.

As current begins to flow through the wires they begin to heat, which increases the resistivity of the metal. This process snowballs as the current increases, causing the voltage across the wires to rise quickly.

The wires begin to melt and vaporize, boiling off some amount of wire material including low-Z impurities within, and adsorbed gases at the surface of the wire. This vapor forms a sheath around the wires, which by this time, have a large electric field embedded in them. Eventually the field strength becomes high enough that the vapor and surface of the wires cannot sustain it and a few electrons are stripped away from the atoms. These electrons are accelerated by the electric field and collide with other atoms, in turn dislodging more electrons. This process, known as avalanche break-down, cascades very quickly until the entire surface of the wire is surrounded by ionized vapor. This ionized medium is much more conductive than the hot wire material left behind. This causes the current to switch from the bulk wire material to the surrounding plasma. Typically this process takes $5-30ns$ from the start of current rise to plasma formation depending on wire material and diameter.

Initiation is an extremely complicated process involving multi-phase matter and plasma physics processes. Currently, no model can capture all of the relevant physics, and due to the speed at which it happens, it is very difficult to study in detail experimentally.

2.2.2 Ablation

The ablation phase typically lasts considerably longer than initiation. After plasma forms around the wires a new dynamical system is setup, as depicted in

figure 2.3. This system is composed of a dense, cold wire core surrounded by a hot, tenuous coronal plasma. The wire core is a multi phase or foam-like object consisting of liquid metal with vapor bubbles throughout[55]. As a result it is highly resistive and carries little or no current, leaving it nearly force free and stationary for the entirety of the ablation phase. The coronal plasma is comparatively low density, much hotter and highly conductive. The vast majority of the current is carried by this plasma sheath around the wires. Early on, this plasma is symmetric about the wire center and is unstable to azimuthally symmetric perturbations due to the competition between thermal and magnetic pressures, the so-called MHD $m = 0$ instability. Short wavelength instabilities grow on the wire as it expands into the vacuum[36].

Since the corona is much hotter than the core, energy is transported from the corona inward to the residual dense wire core. It has been suggested that the primary means of energy coupling is by radiation transport from the coronal plasma into the core[76], heating the outer layer of the core and ablating material from it into the coronal plasma, where it can carry current and continue to heat. The plasma is confined and builds up around each of the wires until the current becomes sufficiently large that the magnetic field encircling the entire array, known as the "global field", is larger than that encircling the individual wires, known as the "local" field, within the coronal plasma. At this point the $\mathbf{J} \times \mathbf{B}$ force drives the coronal plasma towards the center of the array in steady, confined streams that can carry current and magnetic field along with the plasma.

These streams converge on the axis where they form a column of plasma known as the *precursor*[8]. The wire cores continue to ablate and replenish the coronal plasma, which in turn continues to supply plasma into the streams that

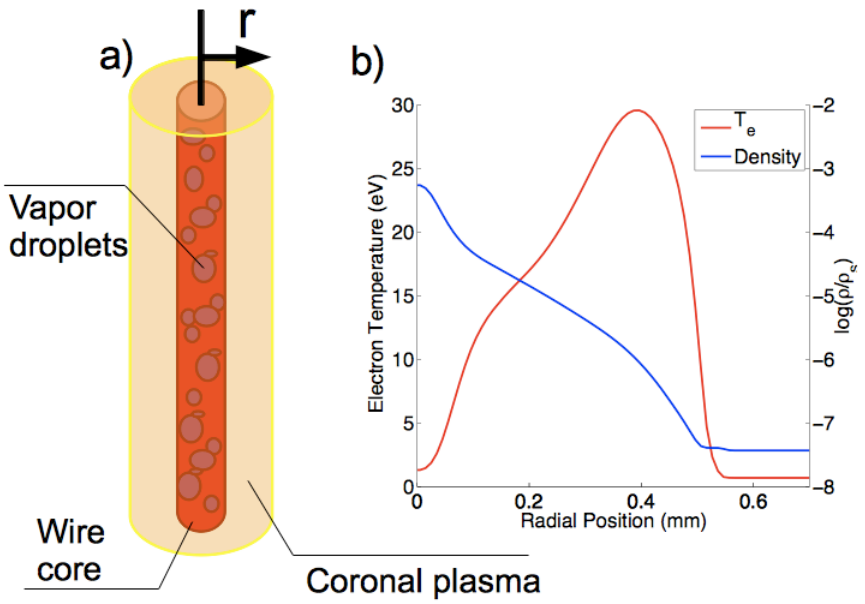

Figure 2.3: (a) The structure of the core-corona system resulting after initiation. (b) Sample radial density and temperature profiles showing the low temperature, high density core and low density, high temperature corona.

feed the precursor. This sets up a quasi-steady state system that lasts as long as the wire cores can continue to supply plasma to the streams while remaining poor electrical conductors.

2.2.3 Implosion

Once the wire cores have ablated enough of their mass that the residual wire core becomes hot enough to carry significant current density, the implosion

phase begins. At the onset of this phase the wire cores begin to show breaks where mass has been completely ablated in an axially nonuniform manner. At these points the remaining core material and much of the coronal plasma abruptly begin to implode and converge on the axis. Since the majority of the current is acting on all this plasma it is accelerated to higher speed than the streaming plasma that preceded it. As a result it sweeps up mass in front of it, carrying it to the axis like a snow plow.

This process is magnetically driven and, as a result, is susceptible to the Magneto Rayleigh-Taylor (MRT) instability, which causes large perturbations in the imploding front to form[65]. These perturbations are seeded by the shorter wavelength instabilities which grow during the ablation phase. The MRT instability causes the imploding front to broaden and leave a significant fraction of the original wire array mass behind, a process that is believed to have a significant impact on the peak power and width of the x-ray pulse[65].

2.2.4 Stagnation

Stagnation begins when the snow plow converges on the array axis. All of the mass from the array piles up over a period of time that depends on the implosion velocity and the final amplitude of the MRT instability and the kinetic energy of the plasma thermalizes, causing a significant heating of the resulting plasma column. Energy is further deposited into the column as the generator current causes it to compress. This rapid heating and compression causes the column to radiate a short, intense x-ray burst. However, since the MRT instability produces a broad implosion front, the mass does not all collide on the axis simultaneously. This causes the duration of the x-ray pulse to be broadened and

the peak power to be reduced.

2.3 Current Research

Though the picture just described of how the wire array z-pinch works is generally accepted there remain many details which are under active debate. The remainder of this document focuses on the use of x-ray absorption spectroscopy to study the state of the coronal plasma and wire core during the ablation phase in very simple exploding wire configurations. This phase is important because it sees many changes happen in the z-pinch. For instance, during this time the magnetic field architecture changes from one where field encircles each of the wires to one where it encircles the array and field around individual wire plasmas is open[46]. This change allows plasma to leave the wires and stream towards the axis. However, the details of how this change occurs are dependent upon the conditions of the plasma. Likewise, the transport of energy from the coronal plasma to the wire core is poorly understood. Understanding the spatial profile of temperature and density in this region could shed much needed light on this subject.

CHAPTER 3

ABSORPTION SPECTROSCOPY

3.1 An Introduction

Absorption spectroscopy is a broad ranging diagnostic technique which has found use in fields as diverse as chemistry, solid state physics, materials science and plasma physics. At its most basic level absorption spectroscopy is the measurement of the absorption of electromagnetic radiation (photons) through a sample as a function of wavelength. The photon source can be optical, radio frequency, gamma or, as in the case of the work presented here, x-ray radiation. The wavelength dependent absorption can be used to determine what elements or compounds make up the sample [35], what phase the sample is in [35], what the electronic or molecular structure looks like[35, 42] or what its charge state, density and temperature are[1, 57, 3, 11]. Absorption spectroscopy can also be used to identify transition wavelengths with high precision as in the present embodiment. This information can be resolved spatially, temporally, both or neither, depending on the characteristics of the source and the sample.

This technique has seen a great deal of use in HEDP[1, 3, 2, 20, 33, 44, 52, 57, 75] and more recently in the study of warm dense matter (WDM)[42, 41]. Generally in HEDP, x-rays are needed to probe the sample due to the high temperatures and densities involved. In these cases, the most effective means of diagnosing the plasma is through "satellite absorption spectroscopy", by which the charge state distribution of the plasma can be measured and from that a density and temperature inferred. We will discuss below exactly what satellite absorption means and how the charge states can be determined.

3.2 Atomic Absorption of Radiation

The absorption of radiation can be understood classically via the simple harmonic oscillator. In this case the oscillator is an electron which moves in response to a fluctuating electric field. Following the method of Griem [24], the equation of motion for the oscillator (assuming no damping) can be written

$$\ddot{\mathbf{x}} + \omega_o^2 \mathbf{x} = \frac{e}{m} \mathbf{E}_\omega cos(\omega t + \delta_\omega) \tag{3.1}$$

where $\mathbf{x}$ is the coordinate of the electron, ω_o is the characteristic frequency of the oscillator, e and m are the electron charge and mass respectively, $\mathbf{E}_\omega$ and δ_ω are the vector amplitude and phase of the ω Fourier component of the electric field.

The solution to this equation is

$$x(t) = \frac{e}{m} \mathbf{E}_\omega \frac{cos(\omega t + \delta_\omega) - cos(\omega_o t + \delta_\omega)}{\omega_o^2 - \omega^2} + x_o sin(\omega_o t + \phi) \tag{3.2}$$

The energy absorbed by the oscillator per unit time comes from the work done by the electric field on the oscillator and can be written as

$$P_a = e\dot{x} \cdot \mathbf{E}_\omega cos(\omega t + \delta_\omega) \tag{3.3}$$

If we assume that the phases of the various Fourier components of the field are random, as is usually justifiable unless laser radiation is considered, and we take the time average over many cycles of the electric field and then integrate over all frequencies, we find the total absorbed power to be

$$\langle P_a \rangle = \frac{\pi e^2}{4m} E_{\omega_o}^2 \tag{3.4}$$

It is convenient to express E_{ω_o} in terms of the spectral energy flux (i.e. the Poynting vector per unit frequency)

$$\langle S(\omega_o)\rangle = \langle |E_{\omega_o} \times H_{\omega_o}|\rangle = \frac{1}{2} c\epsilon_o E^2_{\omega_o} \tag{3.5}$$

$\langle P_a \rangle$ can finally be written as

$$\langle P_a \rangle = \frac{\pi e^2}{2\epsilon_o mc} \langle S(\omega_o)\rangle \tag{3.6}$$

The important consequences to take from this exercise are that absorption of electromagnetic radiation by an electron is a resonant process, i.e. occurs only at ω_o, and the power absorbed is dependent only on the intensity of the incident radiation field. The prefactor in eqn. 3.6 is an absorption cross section which determines the fraction of incident intensity absorbed by the oscillator. This cross section is defined as a frequency integrated quantity and is

$$\int \sigma_\omega d\omega = \frac{\pi e^2}{2\epsilon_o mc} \tag{3.7}$$

In the more complicated system of an electron bound to an atom or ion this cross section will be a multi-peaked function of frequency with peaks corresponding to the discrete transition energies between bound states. This is because the bound electron can occupy a large number of discrete states with definite energy and each transition can be thought of as a harmonic oscillator obeying the derivation outlined above.

An atomic or ionic system is intrinsically quantum mechanical and a proper description is beyond the scope of this document. However, a few of the important results from quantum mechanics are simple to understand qualitatively. Following Griem[24], we can write the transition probability per unit time for absorption from state n to state m as

$$W_{mn} = \frac{4\pi^2 e^2}{3\epsilon_o \hbar^2 c} g_m \sum_i |\langle n|x_i|m\rangle|^2_{av} I_\omega \tag{3.8}$$

where I_ω is the intensity of photons and $|\langle n|x_i|m\rangle|^2_{av}$ is the matrix element for a dipole transition between states n and m averaged over the substates designated by m and g_m is the statistical weight of state m. The sum is over directions of the electron coordinate vector **x**. In analogy to eqn. 3.6 we can write the power absorbed during this transition by multiplying eqn. 3.8 by the photon energy $\hbar\omega$

$$P_{mn} = \frac{4\pi^2 e^2 \omega}{3\epsilon_o \hbar c} g_m \sum_i |\langle n|x_i|m\rangle|^2_{av} I_\omega \tag{3.9}$$

We can see that the prefactor to the flux is analagous to the absorption cross section derived from eqn. 3.6. We can also define an *oscillator strength*, f_{mn} through this equation that strengthens the analogy between equations 3.6 and 3.9.

$$f_{mn} = \frac{2m\omega}{3\hbar} g_m \sum_i |\langle n|x_i|m\rangle|^2_{av} \tag{3.10}$$

Therefore we can write the quantum mechanical absorption cross section as follows

$$\int \sigma_{mn} d\omega = \frac{\pi e^2}{2\epsilon_o mc} f_{mn} \tag{3.11}$$

which, apart from the factor of f_{mn} is identical to eqn. 3.7. This not only firms the connection between the classical harmonic oscillator and the atomic system but shows the significance of the oscillator strength. The oscillator strength is a dimensionless number that essentially quantifies the number of quantum oscillators required for the absorption cross section to be equal to that of the classical oscillator. It also serves as an effective means of comparing the relative importance of different transitions within an atom. Finally, the oscillator strengths for simple atoms and ions can be calculated from first principles using well understood physics making them very valuable theoretical tools.

In absorption spectroscopy one measures the intensity of a ray after it has

traversed a medium. The question of interest is how a ray is attenuated after interacting with a macroscopic number of oscillators as described above. For this we must consider the radiative transfer equation in the case of pure absorption, which as expressed for the *specific intensity*, that is intensity per unit frequency, I_ν, is

$$\frac{dI_\nu}{ds} = -\rho\kappa_\nu I_\nu \tag{3.12}$$

where ρ is the mass density and s is distance along the path of the ray. In general the path of a ray may not be straight due to scattering, diffraction or refraction. However, we will assume for the purposes of x-ray absorption that the path is straight and we therefore take $s \to l$, where l is the straight-line-path. It is clear that the constant κ_ν must have units of $cm^2 g^{-1}$ to balance the units in eqn. 3.12. The quantity κ_ν is called the *opacity* of the medium and is simply related to the absorption cross section by

$$\rho\kappa_\nu = n\sigma_\nu \tag{3.13}$$

where n is the number density of absorbers having cross section σ with a contribution at frequency ν. Therefore the opacity at a particular frequency is related to the oscillator strengths of all transitions with contributions at that frequency.

The solution to the transfer equation in this case is

$$I_\nu(l) = I_{o,\nu} e^{-\tau_\nu} \tag{3.14}$$

where $I_{o,\nu}$ is the incident intensity, i.e. at $l = 0$, and τ_ν is the *optical depth*, defined as

$$\tau_\nu = \int_0^l \rho\kappa_\nu dl \tag{3.15}$$

The optical depth is a dimensionless quantity that determines how transparent a medium is to photons of a given frequency. If $\tau_\nu \ll 1$ the medium is said to

be optically thin, or transparent. This means that a typical photon of frequency ν will be able to traverse the medium without being absorbed. If $\tau_\nu \gg 1$ the medium is optically thick, or opaque. In this case a typical photon is likely to be absorbed when traversing the medium.

If the medium is uniform along l then ρ and κ_ν are constants and the integral is trivial. The solution to eqn. 3.12 becomes

$$I_\nu(l) = I_{o,\nu} e^{-\rho \kappa_\nu l} \tag{3.16}$$

yielding the important result that radiation decays exponentially with path length in a uniform medium.

It is also apparent from this form that all of the information regarding the sample properties is contained in the exponent. Therefore, in order to make quantitative use of an absorption measurement one must divide out the incident intensity, thereby obtaining the *transmission* through the sample

$$T_\nu = \frac{I_\nu(l)}{I_{o,\nu}} = e^{-\rho \kappa_\nu l} \tag{3.17}$$

Since l is always a positive distance, and since ρ and κ are by definition positive, it is clear that T_ν will always lie in the range $0 \rightarrow 1$.

3.3 Resonances and Satellites

Now that we know how radiation is absorbed in a medium we must now turn our attention to how this can be exploited to learn about the state of a plasma. To understand this we must first understand one of the most important types of transitions in plasma spectroscopy, the *resonance* transition. A resonance tran-

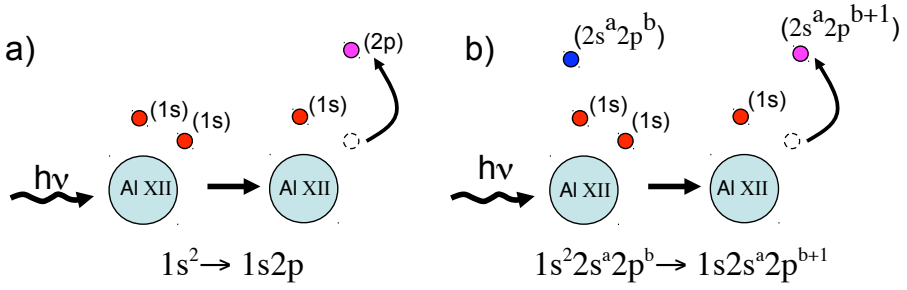

Figure 3.1: Graphical representation of (a) the $He-\alpha$ resonance line transition of Al and (b) a satellite transition of the $He-\alpha$ resonance.

sition is the lowest energy transition from the ground state to an allowed excited state for a given ion. Resonance transitions always have large oscillator strengths and an emission spectrum of a plasma is therefore strongly biased toward these transitions.

For example, the ground state of a He-like Al ion is $1s^2\,{}^1S_o$*. The first excited state is $1s2p\,{}^1P_o$. A transition between these two states has an energy difference of $1598eV$, corresponding to a wavelength of 7.757Å. This transition lies in the soft x-ray range. In addition to being a resonance it is a "K-shell line", meaning it involves the $n=1$ shell. Since it is a transition between $n=1$ and $n=2$ we can further classify it as an α transition. This transition is usually referred to as the $He-\alpha$ line. Using this convention the $He-\beta$ line corresponds to the $n=1$ to $n=3$ transition $1s^2\,{}^1S \rightarrow 1s3p\,{}^1P^o$, and so on for $He-\gamma,\delta$, etc..

Satellite lines occur when additional electrons are added to the ground state configuration that do not participate in the transition. These electrons are called

*The notation used here designates the electron configuration and the angular momentum of the ion. The electron configuration indicates how many electrons are in each shell. In this case $1s^2$ indicates that there are two electrons in the $1s$ shell. The angular momentum information is contained in the term symbol, which takes the form ${}^{2S+1}L_J$. S is the total spin quantum number, J is the total angular momentum quantum number and L is the orbital quantum number in spectroscopic notation: $0 \rightarrow S$, $1 \rightarrow P$[72].

spectators. This process is shown graphically in fig. 3.1, in which an Al ion with two remaining electrons is shown in the ground state in part (a). After absorption of a photon one of those electrons is promoted to the first available excited state, one of the vacancies in the $2p$ shell. In fig. 3.1(b) an Al ion with $2 + a + b$ electrons exists in the ground state. After absorbing a photon with a different frequency one of the innermost electrons, i.e. $1s^2$, is promoted to the next available state, which must be a vacancy in the $2p$ shell because electric dipole transitions from $1s \rightarrow 2s$ are not allowed. The energy of this transition will be smaller than that of the resonance transition. The reason for this is the phenomenon known as nuclear screening (by the spectator electrons).

In the first system, with only two electrons, all of the vacancies in the $2p$ shell have the same well defined energy and therefore any transition from the $1s$ shell to the $2p$ shell will be the same. However, when additional electrons are added to the ion they modify the energy structure. Intuitively, a hypothetical test charge sitting away from the ion sees a charge equal to the number of protons in the nucleus minus the number of electrons bound to the nucleus (assuming the bound electrons are at smaller radii). This nuclear screening modifies the potential of the nucleus, thereby changing the energy structure of the bound states. In reality the screening is more complex because the electrons are distributed probabilistically around the nucleus, and therefore the screening is not complete. So, in the second system, if an electron were to transition from an inner state to the next available excited state it would end up in a state that does not 'see' the entire nuclear charge. The energy difference between these two states is smaller than in the first system because of the lowered, or screened potential.

Various methods have been developed to calculate the energy lowering of

a transition due to screening. It is not possible to solve analytically. However a useful approximation was developed in ref.[45]. In this approximation the energy of the ion is given as

$$E_{ion}(eV) = -13.6 \sum_{n} \frac{Q_n^2 P_n}{n^2} \tag{3.18}$$

where n is the principle quantum number, P_n is the population of electrons in level n and Q_n is the effective charge seen by electrons in level n. The effective charge is given by the approximate relation

$$Q_n = Z - \frac{1}{2}\sigma(n,n) - \sum_{m<n} \sigma(n,m) P_n \tag{3.19}$$

In the above Z is the unscreened nuclear charge and $\sigma(n,m)$ are coefficients tabulated in ref.[45]. The energies of the $1s \rightarrow 2p$ transitions for He- through F-like Al are shown as the blue circles in fig. 3.2. The red squares are the experimentally measured energies of the same ions with the error bars representing the spread in energies of transitions due to the various sublevels in the $2p$ shell, which are not accounted for in the model. The agreement is reasonable for such a simple calculation, but the error grows substantially as the number of electrons increases.

This effect is extremely beneficial because if a sample plasma has a distribution of ions with different charges we can determine not only which charge states exist from the energy differences of these transitions, but in what quantities. We know that in equilibrium the vast majority of the ions will occupy their respective ground states. By illuminating a sample with a broadband source of radiation commonly called a backlighter near the resonance line we will promote an inner electron to an available excited state, thus absorbing photons from the backlight. By measuring how much of the backlight intensity is absorbed, and at what energies, we can determine the population of each of the

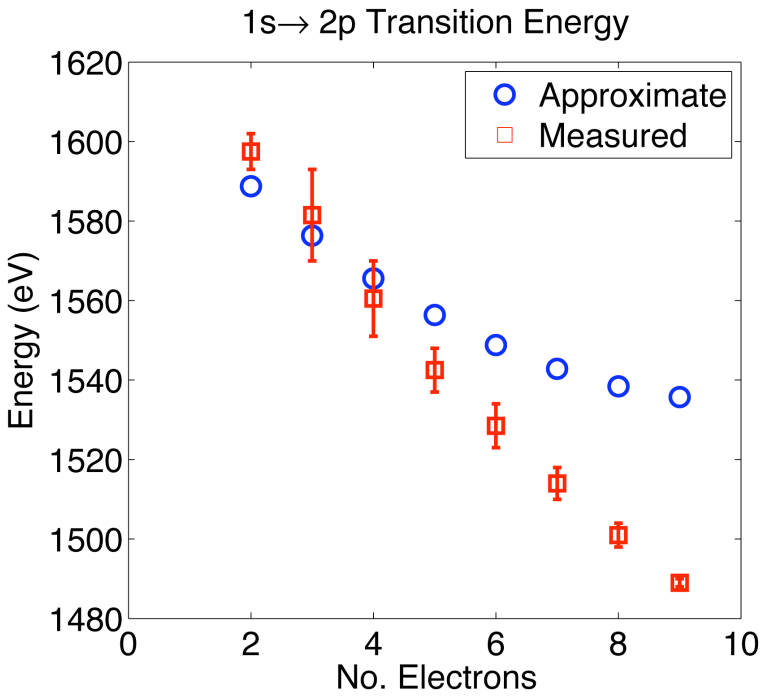

Figure 3.2: The energy of $1s^2 \rightarrow 1s2p$ transitions in various Al ion species as a function of number of electrons bound to the nucleus. The measured energies are shown as the red squares. The square indicates the center of the satellite group while the error bars indicate the spread in energy over which transitions exist. The blue circles represent the approximate shift due to spectator electrons calculated using the screened nuclear charge in eqn. 3.19.

ion species.

We also know that in local thermodynamic equilibrium (LTE) a plasma at a definite temperature and density will have a specific distribution of charge states that can be calculated. Therefore once this is measured one can infer the density and temperature. In fact, for a given Z atom the charge state is extremely sensitive to temperature over a specific temperature range and is therefore a very accurate temperature diagnostic[11]. However, it is sometimes not practical to measure the charge state directly. This measurement may also not

be accurate if a significant fraction of the ions are in excited states, which may be the case with low ionization or in the presence of non-thermal processes. In these cases it may be necessary to compare calculated and measured spectra at each wavelength to determine the plasma conditions.

3.4 Experimental Considerations

Figure 3.3(a) shows the basic elements of an absorption experiment. It consists of the backlighter source, sample to be diagnosed, an optical element to spatially disperse the radiation and a detector. There are countless variations on this basic setup, but each of these elements is required for any type of absorption experiment to be performed. The geometry of the sample is very important. Because the backlighter will traverse a finite thickness (Δl) of the sample, previous experiments have taken great care to insure that the sample is uniform along this dimension. In this case each ray will see the same conditions at every location along the line-of-sight inside the sample. Sufficient uniformity might be accomplished by heating the entire sample volumetrically with an intense x-ray source and constraining the sample with a low-Z "tamper"[44, 2] or by illuminating the sample with a high intensity laser with sufficiently large spot size to produce a uniform plasma over the area being probed[51, 75, 57].

Additionally, it is important that the sample be uniform in the dimension parallel to the dispersion direction, x in the figure. The reason for this is easiest seen in fig.3.3(b). Since the dispersive element for x-rays is a Bragg crystal reflector the wavelength reflected at each point is determined by its angle of incidence, θ, through the Bragg formula, $n\lambda = 2d\sin(\theta)$, where d is the spacing

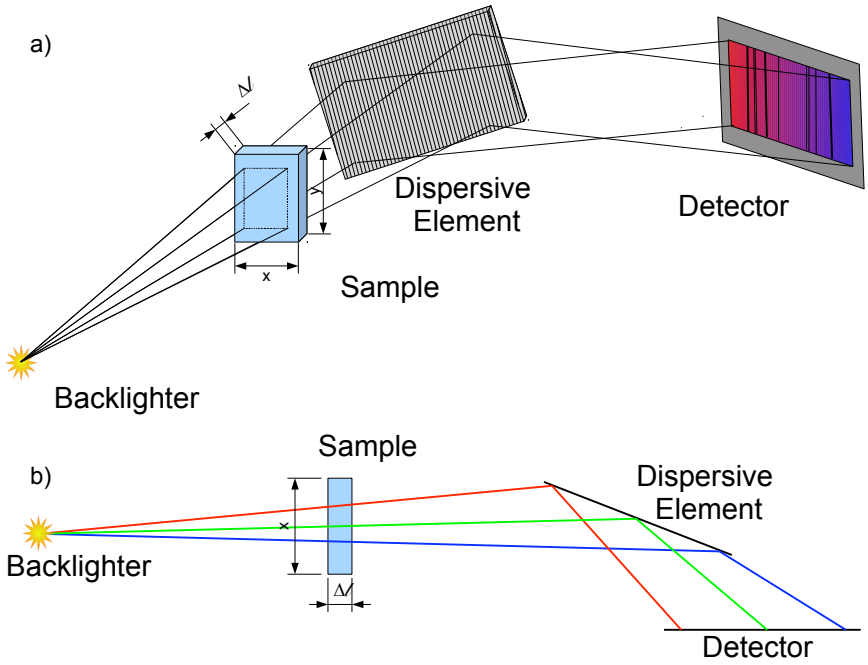

Figure 3.3: (a) A schematic representation of an absorption experiment showing the four basic elements: backlighter, sample, dispersive element and detector. (b) Top view of the same set up. This view illustrates how each single wavelength passes through a unique portion of the sample.

between crystal planes, λ is the reflected wavelength and the integer n is the order of reflection, which we will take to be one. Because of this condition each ray passing through the object at a given x position will transmit only one wavelength to the detector. Therefore having a sample that is uniform along x will insure that each wavelength is probing the same conditions.

These two conditions put severe constraints on the sample since they require that it vary appreciably only in one dimension. In HED experiments this has been accomplished by tamping the samples to constrain them in these two dimensions[2, 52], attempting to volumetrically heat the sample uniformly[42], or by requiring that the area being probed is small compared to the length scales

over which the relevant variables vary[75, 1]. The requirement that the sample be uniform along the line-of-sight can be relieved if some information is known about the sample along this direction, e.g. from another diagnostic or a computer simulation, so that the variation can be unfolded from the spectrum.

Several conditions are required to be met in order to obtain quantitative results from an absorption experiment. These conditions are discussed in detail in ref. [3]. In short, it is required that the film exposure and background levels be calibrated and that the unattenuated backlighter be measured along with the absorption spectrum. This is because the measured quantity that gives information regarding the sample conditions is the *transmission*, not the absorption. The wavelength dependent transmission is obtained using the following formula:

$$T_\lambda = \frac{I_{sample,\lambda}}{I_{o,\lambda}} \tag{3.20}$$

where $I_{sample,\lambda}$ is the wavelength dependent intensity measured after absorption through the sample and $I_{o,\lambda}$ is the intensity of the backlighter measured before absorption through the sample. It is easy to see that in the absence of emission from the sample contaminating the measurement of $I_{sample,\lambda}$, the transmission will always lie between zero and one.

From eqn. (3.20) it can be seen why calibration of the measured intensities is so important: The ratio of two measured spectra must be calculated to obtain the quantity of interest. It is therefore essential that they both be well known in order to obtain meaningful results.

Another complication that can arise experimentally is the presence of spectral features in the backlight source. At first glance it would seem that the features in the backlighter spectrum would be inconsequential since it is divided out. However, this is the ideal case. In a real experiment the measured spectra are convolved with the *instrument function*, $g(\lambda)$. This is usually approximated

as a gaussian with width determined by the measured or theoretical resolution of the spectrometer. Therefore, eqn. (3.20) becomes

$$T_\lambda = \frac{g(\lambda) \otimes I_{sample,\lambda}}{g(\lambda) \otimes I_{o,\lambda}} \tag{3.21}$$

where the $\otimes$ denotes the convolution integral. Writing out the integrals it becomes clear that the instrument functions in the numerator and denominator do not cancel.

$$T(\lambda) = \frac{\int g(\lambda') I_{sample}(\lambda - \lambda') d\lambda'}{\int g(\lambda') I_o(\lambda - \lambda') d\lambda'} \tag{3.22}$$

The consequences of this equation were worked out by Iglesias *et al.* in ref.[31]. In short, the presence of spectral features in the backlight source that are unresolved by the instrument can introduce errors into the calculated transmission spectra $T(\lambda)$. This will, in turn, lead to errors in the measured opacity or the inferred state of the plasma. It is proposed that this source of error could be a significant contributor to unexplained discrepancies between experiment and theory in the work of Iglesias *et al.*, which uses a laser-produced x-ray backlighter[31]. Our experiment circumvents this issue because the x-pinch x-ray source has an extremely smooth spectrum with no identifiable features, as we will see in the next chapter.

CHAPTER 4

DIAGNOSTIC DEVELOPMENT AND CHARACTERIZATION

4.1 The X-pinch X-ray Source

An X-pinch is formed by placing two or more wires between the anode and cathode of a fast rise time current driver, $\geq 1kA/ns$, and crossing them at a point as shown in fig. 4.1(a). This geometry concentrates the current at the cross point, creating approximately n^2 times the magnetic pressure on the exploding wire plasma at the cross point as on the individual wires where n is the number of wires. This dramatically increases the implosion force and plasma heating at that point. After plasma forms, the cross point plasma region is elongated and compressed by the magnetic field, forming a *minidiode* with a small z-pinch in between its two broad plasma electrodes; the length is a few hundred microns. This dense column of plasma is unstable and the neck points created by the instability begin to compress due to the high magnetic field. Eventually one of these necks becomes so dense and so hot that it undergoes "radiative collapse", which allows the plasma implosion to become supersonic preventing plasma in the column from escaping axially. "Radiative collapse" occurs because the density increases, which increases the radiation rate, providing positive feedback for further collapse. The result is an intense and brief burst of continuum and line radiation, the temporal, spectral and spatial characteristics of which depend upon the original wire material[64].

X-pinches have been used for years for point-projection x-ray backlighting to diagnose various plasmas created on pulsed power generators all over the world[16, 6, 7, 9, 40, 22, 5]. The small spot size, $\sim 1\mu m$, and short dura-

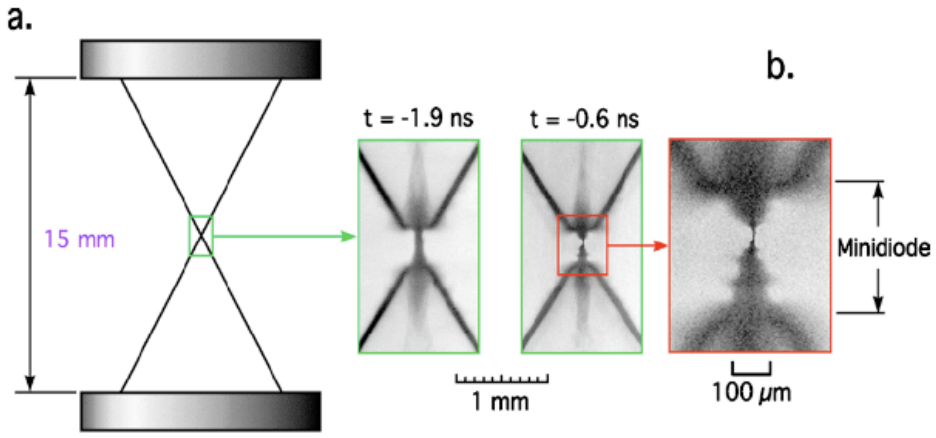

Figure 4.1: (a) Schematic diagram of a two-wire x-pinch. (b) A time series of radiographs showing the collapse of the cross-point during the implosioin of an x-pinch. The expanded inset shows a detailed view of the structure of the minidiode $0.6ns$ before the x-ray burst[60].

tion, $\sim 100ps$, make it an ideal source for x-ray radiography. This is because the maximum achievable resolution in a point-projection radiography setup is determined by the source size. In addition, the short duration of the x-ray burst compared to the dynamical time scales in wire array and x-pinch experiments allows images to be captured with little to no motion blurring.

4.1.1 Source Parameters

The temporal and spatial characteristics of the x-pinch have been well documented in refs. [64, 68, 69]. We will discuss the relevant details from these

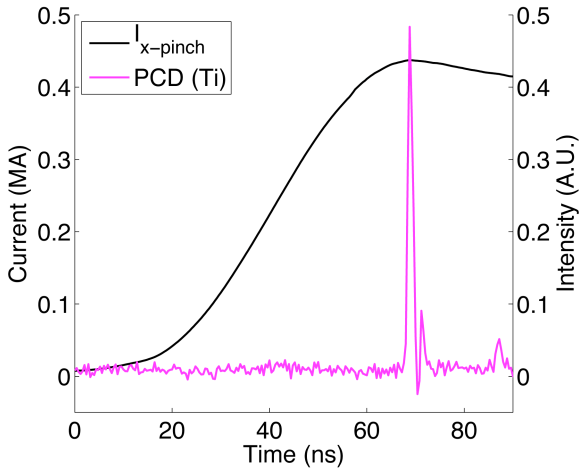

Figure 4.2: Timing signals from XP shot # 5844 showing the x-pinch x-ray burst occurring at 69ns after the start of current, $I_{x-pinch}$, on a 12.5μm Ti foil-filtered PCD.

studies here. The process of radiative collapse that results in the short, intense x-ray burst characteristic of an x-pinch causes extreme parameters to be reached inside a very small volume of plasma. It has been found that molybdenum (Mo) wire x-pinches produce the most reliable and intense x-ray bursts. As such we have used Mo exclusively in these studies.

Figure 4.2 shows signals from a shot on XP where a 4-wire Mo x-pinch was the main load. The PCD (photo-conducting diode) signal shows a clear, single spike at 69ns, indicating the x-ray burst. There is jitter in the timing of when this burst occurs from shot to shot, at least in part because of variations in the current pulse, even using the same wire size from one pulse to the next, but it will reliably be between the peak of $\partial I/\partial t$ and the peak of I. The temporal resolution of the oscilloscope is not adequate to measure the actual duration of the x-ray burst. In order to measure this Sinars *et al.* used a streak camera with $5-10ps$ resolution equipped with a spherically bent crystal spectrometer[69]. They found that the first x-ray burst is the the most intense and is primarily

continuum radiation. This burst lasts considerably less than $100ps$ and the parameters of the emitting region were observed to change on a time scale of a few tens of ps. Subsequent x-ray bursts, if they occur at all, are dominated by line radiation. The ion density and electron temperature were estimated in these subsequent bursts to be about $10^{22}cm^{-3}$ and at least $500eV$[69]. It is expected that the parameters achieved during the initial burst are significantly higher as estimated from the fact that the Ne-like Mo lines are seen immediately after the continuum burst. The tendency of the x-pinch to emit a single burst that is dominated by continuum radiation is one aspect that makes it such a valuable source for radiography and absorption spectroscopy.

Various studies have measured the size of the emitting region. A typical Mo x-pinch has a $3-5keV$ continuum x-ray burst source size of about $1\mu m$ determined using $12.5\mu m$ Ti filters and x-ray optical methods[73, 63], as do Nb and Pd x-pinches[63]. Other materials routinely produce larger source sizes[73]. This is important because the geometrically limited spatial resolution of a point-projection system is proportional to the source size[73, 63].

A new x-pinch configuration known as the hybrid x-pinch has been demonstrated to perform as well or better than the traditional x-pinch and is easier to work with[60]. The hybrid x-pinch is formed by placing two conical electrodes with holes through their centers in the diode. A single wire is strung through the holes, connecting the two electrodes. This scheme, shown in fig. 4.3, delivers all of the current into the short section of wire connecting the two cones. If this section is made short enough, instabilities will result in a single neck region that collapses in a similar manner to the z-pinch in the minidiode of a standard x-pinch. Though the duration of the burst has not been measured with a streak camera it is still too fast to be resolved with PCDs on our fastest tran-

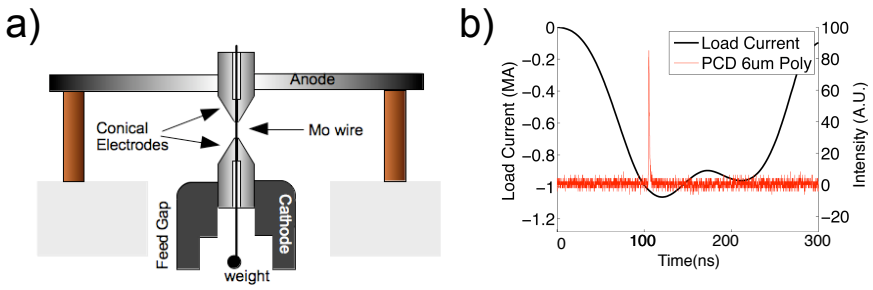

Figure 4.3: (a) Depiction of the hybrid x-pinch configuration as used on COBRA. (b) Timing signals from shot#2030. The x-ray signal recorded from a PCD filtered with $6\mu m$ of polycarbonate is shown in red.

sient digitizer ($3GHz$), implying it is of the same order as the standard x-pinch. Source diameters have been measured to be repeatably $2\mu m$ or smaller using the diffraction patterns produced by an array of narrow slits[60]. It was found that a single, intense continuum x-ray burst was produced more reliably than the standard x-pinch on COBRA. For these reasons we chose to use this configuration for the experimental series conducted on COBRA.

4.1.2 Spectral Characteristics

As discussed in section 3.4, it is important to measure both the unattenuated backlighter spectrum and the absorption spectrum. The measurements presented here are the first measurements of the continuum radiation from Mo wire x-pinches in the $7 - 8.5$Å ($1400 - 1700eV$) range. The spectral characteristics

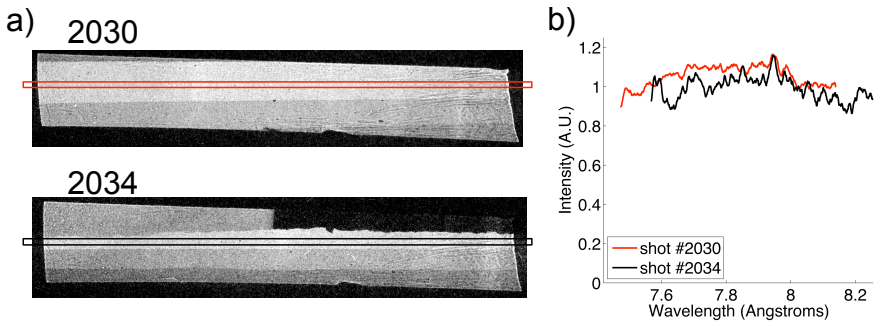

Figure 4.4: (a) Calibration images obtained on COBRA shots 2030 and 2034. (b) Calibrated lineouts of the unattenuated backlighter spectrum taken from the region surrounded by the red (2030) and black (2034) boxes in (a). The lineouts illustrate how smooth the backlighter spectrum is.

of Mo wire x-pinches in other wavelength ranges are discussed in detail in ref. [69]. Two sample spectra from the COBRA experiments discussed in Chs. 5 – 7 are shown in fig. 4.4 along with intensity lineouts plotted on a linear scale.

One of the most striking features of these images is how smooth the spectra are. The lineouts indicate that the average RMS variation over this bandwidth is only ±5% with a peak variation of 25%. The majority of this variations is due to film noise and crystal defects. There are no spectral features that are not resolved by our spectrometer, indicating that the radiation in this region is indeed continuum radiation and not simply poorly resolved line radiation. This is in stark contrast to the backlighter spectra obtained from laser produced pseudo-continuum x-ray sources, which can vary over an order of magnitude or greater over the experimental bandwidth and contain unresolved spectral features [31]. As a result the x-pinch provides a distinct advantage over laser produced x-ray sources.

In addition, the nearly constant intensity of the x-pinch backlighter provides another advantage. The signal-to-noise performance of the film is worse at low exposure and steadily improves with exposure. Therefore the relatively constant intensity over this wavelength band means that the contribution to the error associated with the backlighter intensity will be relatively constant for all absorption lines.

4.2 The Spectrometer

The spectrometer used to implement this diagnostic was designed specifically for use on XP and COBRA and built in house at the Laboratory of Plasma Studies. It is a modification of the Focusing Spectrograph with Spatial Resolution (FSSR)-2D detailed in [54]. This type of spectrometer employs a spherically bent crystal as the dispersive element, which has the advantage of allowing very high spatial resolution, spectral resolution and luminosity. In the current experiments, a quartz $10\bar{1}0$ crystal was used with a radius of curvature equal to $180mm$. Quartz $10\bar{1}0$ has a $2d$ spacing equal to 8.5Å and reflects significantly only in the first order, making it an ideal choice for absorption spectroscopy of Al plasmas since the relevant K-shell lines lie between 6.5 and 8.4Å. The spectrometer is shown in fig. 4.5.

In the FSSR-2D arrangement the source is placed far outside the Rowland circle. The image focuses inside the Rowland circle along the line connecting the source and center of curvature of the crystal, as shown in Fig. 4.6(a). This arrangement allows imaging in both the spectral and spatial directions, hence "2D". However, in the current configuration, the magnification of the image in

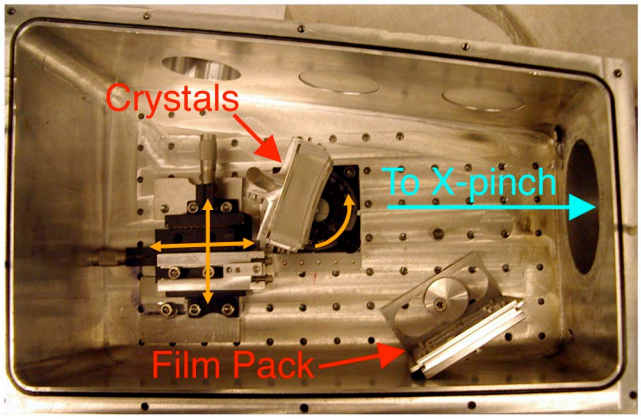

Figure 4.5: Photograph of the spectrometer housing constructed for this diagnostic with the crystals and film in place. The crystals are mounted on a rotation stage which is attached to an $x-y$ translation stage. In addition the pitch angle and height (into and out of the plane of the page) of the crystals are adjustable.

the spectral direction is 3 to 5 times smaller than in the spatial direction. This means that when imaging a small source such as an x pinch the extent of the image in the spectral direction at any given wavelength is negligible.

For absorption spectroscopy we want to image the absorbing object, not the x-ray source. To accomplish this we move the detector away from the focal plane, expanding the image of the source and allowing spatial resolution of the object to be obtained. Also in the interest of imaging, we prefer a uniform magnification of the object along the dispersion direction. This can be achieved simply by rotating the detector with respect to the crystal. This has the effect of equalizing the path lengths traveled by each ray from the source to the detector providing the same magnification at all wavelengths. In principle the optimum position of the detector can be calculated via ray tracing. However, since precise angles and distances are difficult to measure in practice it is simplest to perform this function by eye. A laser pointer with a short focal length lens is placed at the location of the source and imaged onto the film. The film is placed at the

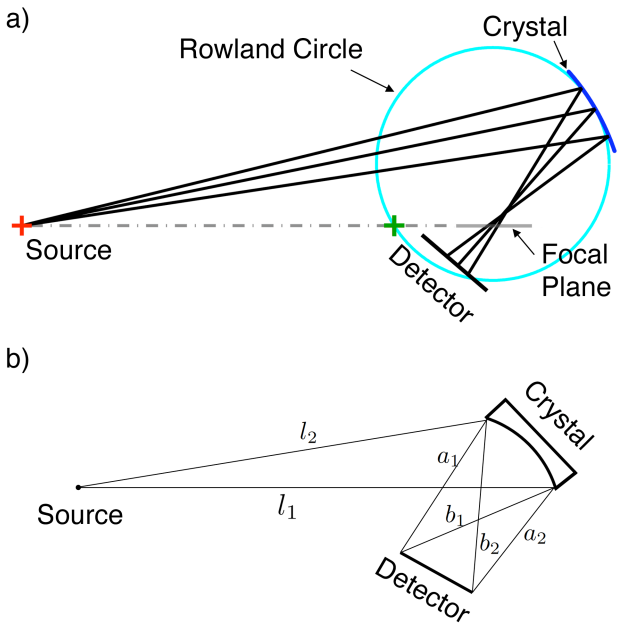

Figure 4.6: (a) A schematic diagram showing the paths of three representative rays through the system. The gray dashed line indicates the focal position in the FSSR-2D system. The green '+' is the center of curvature of the crystal. (b) The six measurements used to characterize the relative locations and orientations of the source, crystal and detector.

focus of the spectrometer and then its position and angle are adjusted until the desired image size and uniformity are achieved.

In order to characterize the spectrometer once it is aligned, six distance measurements are taken which can fully describe the locations and orientations of the crystal, detector and source. These measurements are depicted in Fig. 4.6(b). The six measurements are entered into a ray tracing program that calculates the dispersion curve for the spectrometer. Figure 4.7(a) shows three example dispersion curves calculated for three different sets of parameters used in the experiment, as listed in table 4.1. These curves show the sensitivity of the dispersion to the arrangement of the crystal and detector.

In order to test the accuracy of the dispersion calculation a test shot was per-

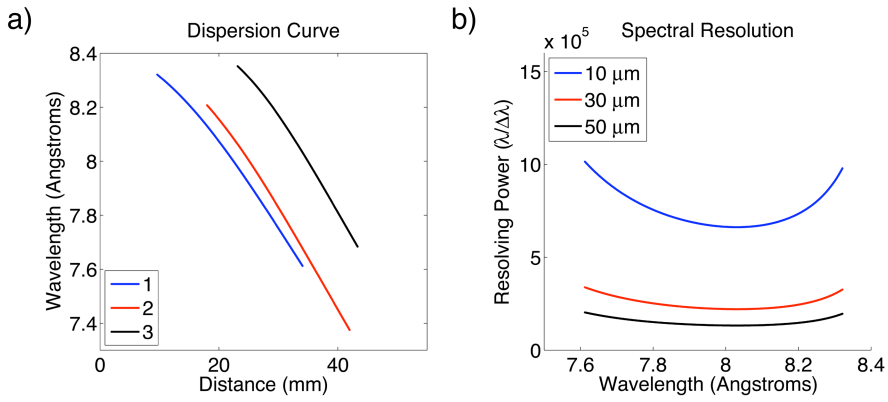

Figure 4.7: (a) Dispersion curves for three different alignment configurations characterized by the six measurements detailed in Fig. 4.6(b). The measurements of each configuration are given in table 4.1, i.e. line 1 corresponds to first set of measurements, line 2 to the second and line 3 to the third. The abscissa is distance on the film along the dispersion direction. (b) Spectral resolution for three different source sizes calculated for alignment configuration 1.

Table 4.1: Values of the six distance measurements used for ray tracing calculations shown in Fig. 4.7(a)

Alignment Configurations						
	l_1 (mm)	l_2 (mm)	a_1 (mm)	a_2 (mm)	b_1 (mm)	b_2 (mm)
1	1038	1056	151	108	141	142
2	1048	1069	150	105	139	135
3	1038	1055	150	105	146	140

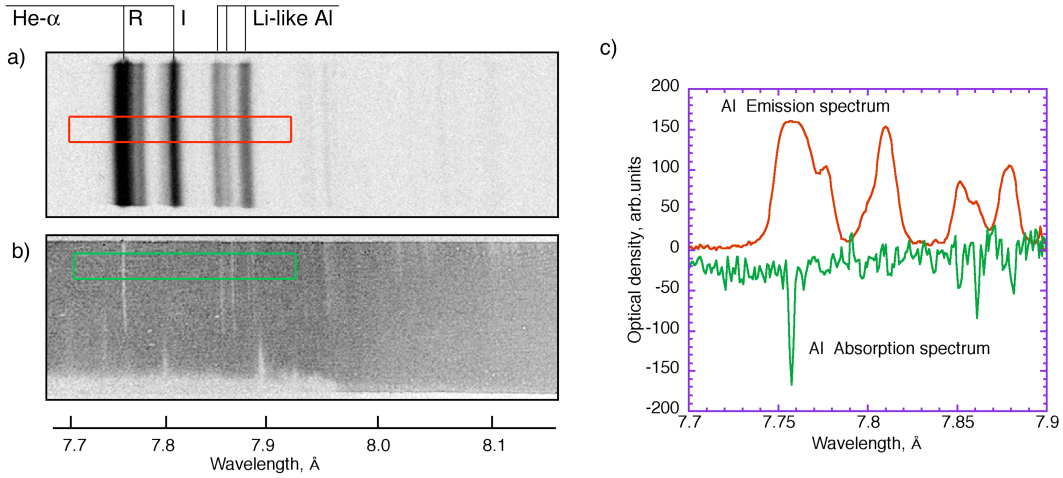

Figure 4.8: (Color Online) (a) Film from the calibration shot performed with the Al x-pinch. The resonance and intercombination lines as well as the Li-like satellite lines are identified. (b) Experimental image of an absorption spectrum from which the spectral resolution was measured. (c) Intensity lineouts taken from within the red box in (a) and the green box in (b).

formed using an aluminum x-pinch and no test object, only thin debris shields. The wavelength scale for this spectrum, shown in Fig. 4.8 (b) and (c), was determined using a single known wavelength and the calculated dispersion curve. The calibration line was chosen to be the $He-\alpha$ intercombination line ($1s^2{}^1S_0 \rightarrow 1s2p^1P_0$) at 7.8069Å, instead of the resonance line because the resonance line is saturated and, therefore, not suitable for use as a wavelength standard. In addition, the x-pinch plasma is more thin to the intercombination line, causing less broadening. Comparison of the wavelengths determined using the calculated dispersion with other known and calculated lines shows good agreement. We estimate this method is accurate to three decimal places.

4.3 Spectral and Spatial Resolution

The spectral resolution can be calculated using the ray tracing results following the methods of [54]. Figure 4.7(b) shows the wavelength dependent resolving power of the spectrometer for three different source sizes. The spectral resolution is excellent even at relatively large source sizes. The calculations suggest that a resolving power, $\lambda/\Delta\lambda$, upwards of 10^5 is possible given the small source size afforded by using an x-pinch. However, these calculations assume an ideal Bragg reflector and are therefore considered only as a guide in designing the spectrometer.

The actual spectral resolution achieved has been estimated using the experimental absorption spectrum shown in Fig. 4.8(c). The full width at half maximum (FWHM) of the $He-\alpha$ resonance line was measured to be about $1.5m$Å. If we assume that this measurement is limited by the instrument then this yields a resolving power of about 5000. To the author's knowledge, this is the best resolution achieved in an HED absorption experiment to date.

A final test was performed to measure the spatial resolution and magnification of the spectrometer. A molybdenum x-pinch was used and a wire mesh was placed $60mm$ from the source. This test image is shown in Fig. 4.9(a). The mesh was 125 lines per inch with wire thickness equal to $33\mu m$. The magnification was measured using the known distance between wires of $200\mu m$ for the smaller mesh and was found to be $M_{spatial} = 4$ in this configuration.

The spatial resolution was estimated by taking a lineout of the mesh across one of the wires and examining its profile. An enlarged region of the mesh is shown in Fig. 4.9(b) with the area of the lineout indicated by the red box. The lineout is shown in Fig. 4.9(c). The spread of the wire edge was measured, us-

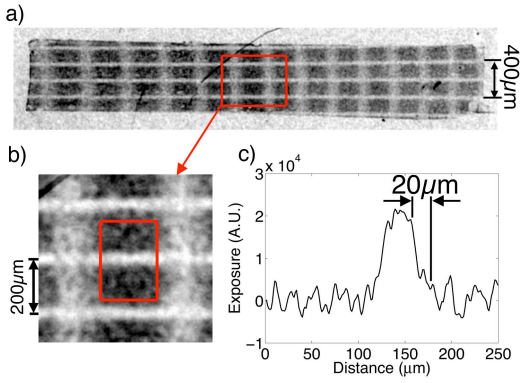

Figure 4.9: (a) Image obtained using the 125 lines per inch fine wire mesh and a Mo x-pinch. (b) expanded portion of the image outlined in red. (c) Lineout of one wire of the mesh taken from within the red box in (b). The 90% to 10% spread of the wire edge was measured to be 20μm giving an estimate of the spatial resolution of the system.

ing the 90% and 10% exposure values as thresholds, to be approximately 20μm. We can take this measurement to be an upper limit of the spatial resolution of the system. In a standard point-projection geometry we would expect the resolution to be significantly better than this with a source size of about 5μm. This means that either the source size is larger than expected or the crystal is degrading the resolution. It is likely that the crystal is at least in part responsible for degrading the resolution since small defects are evident and bending induces large stresses inside the lattice. In addition, the film being used has a rather large grain size which can be seen in the expanded portion of the mesh image. This is also a likely contributor to the resolution.

CHAPTER 5

EXPERIMENTAL METHODS

5.1 Experimental Setup

Absorption spectra were obtained using three different experimental configurations. The diagnostic system was first implemented on XP, where the higher shot rate facilitates varying the geometry to investigate the operation of the diagnostic. As a result improvements were implemented when the diagnostic was moved to COBRA. Figure 5.1 shows the basic setup of the experiment on both XP and COBRA indicating the relative positions of the x-pinch backlighter, the parallel pair of exploding wires, the spherically bent crystal and the film. Only the values y and p were changed from one test series to the next. In all the experiments in which absorption spectra were obtained the x-pinch was driven by the entire generator current and the sample was driven by a portion of the current by making it one of several return current paths.

In all of the experiments presented the z-direction of the object (i.e. parallel to the wires) is aligned with the dispersion direction of the crystal. This was chosen because the object is expected to be most uniform along this direction. The x-axis at the object corresponds to the line connecting the two wire centers that is perpendicular to the wires. The quartz crystal is aligned to allow spatial resolution along this dimension, where the gradients of interest exist. Given this geometry the field of view at the object can be approximated as

$$FOV_{x,z} = L_{x,z}\frac{y}{y+p}$$

where $L_{x,z}$ is the dimension of the crystal along the x and z directions as defined at the object plane and p and y are as defined in Fig. 5.1. The crystal dimensions

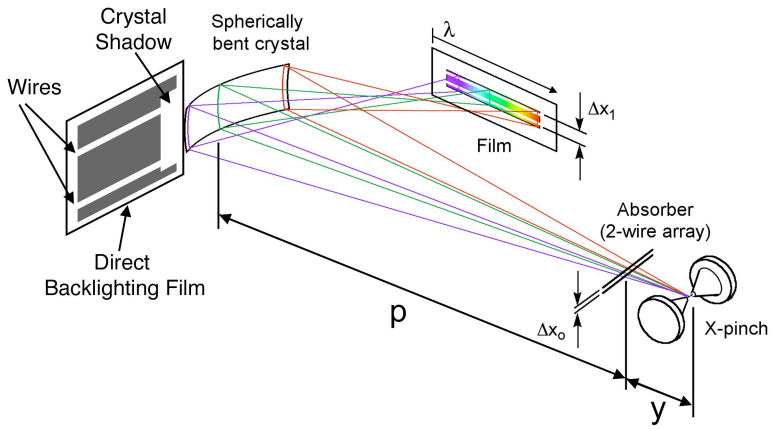

Figure 5.1: A schematic diagram of the experimental setup showing the x-pinch backlighter, the absorber, the crystal, and both the spectrometer and direct backlighting films. A series of thin polypropylene debris shields totaling 16μm thickness, not shown, are placed in front of the crystal.

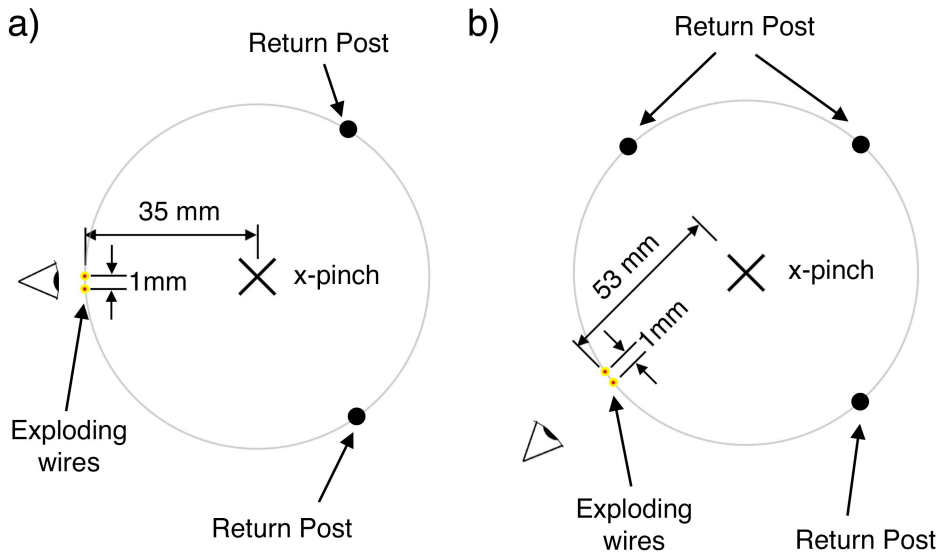

Figure 5.2: A top view of the load configuration for (a) the XP experiments and (b) the COBRA experiments showing how current is divided in the return current path by the posts and the exploding wires. In both cases the eye indicates the direction of view of the absorption spectrometer.

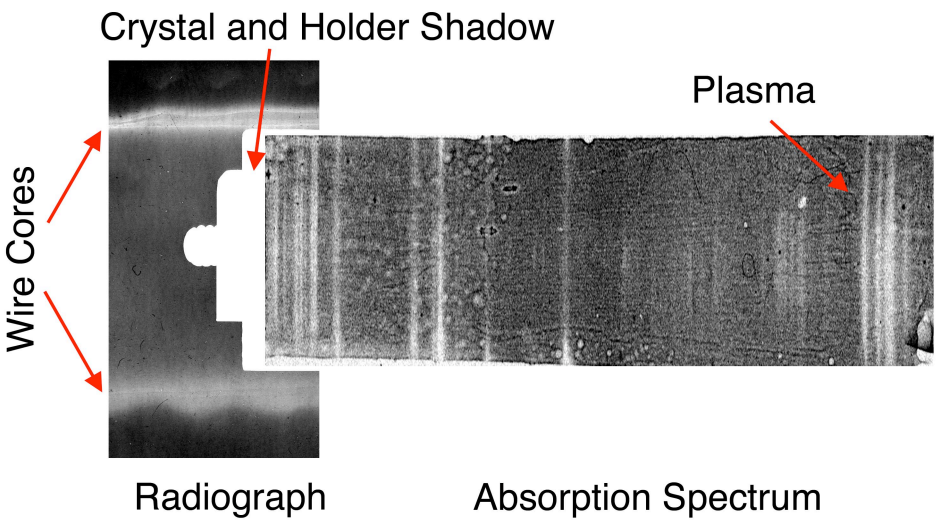

Figure 5.3: Experimental radiograph and absorption spectrum obtained on XP shot 5790 illustrating how the radiograph can be used to locate the field of view with respect to the wires.

are $16mm \times 52mm$. In addition to the absorption spectra, direct x-ray backlighter images of the parallel exploding wires were also obtained using a film filtered with a $12.5\mu m$ Ti foil that was placed behind the crystal as shown in fig. 5.1. The image obtained on this film is useful for determining the location of the wires relative to the crystal since shadows of each object can be seen. It is also potentially useful for placing upper or lower bounds on the aerial density of the wire cores and coronal plasma by using the absorption on the direct backlighter radiograph. A direct backlighter radiograph is shown in fig. 5.3 together with an absorption spectrum , both from XP shot 5790, to illustrate how the radiograph can be used to locate the position of the wires in the spectrum.

Experiments were conducted on XP with the wires at two distances, $y = 35mm$ and $y = 100mm$, from the x-pinch. In both cases the crystal was $830mm$ from the x-pinch. The wires shared the return current with two $12.5mm$ diameter copper posts. The locations of the posts are shown in fig. 5.2(a). An integrating Rogowski coil monitored the current through the sample. The wires were

initially placed at $y = 100mm$ in order to achieve a large field of view. However, since current is inductively divided between the return paths, placing the wires at that distance increases the inductance of that path relative to the posts. This limited the current through the wires to $< 8kA$, which was so little that no plasma was visible around the wires in the absorption spectra.

The wires were then placed at $y = 35mm$ in order to increase the current through them to about $95kA$. This current created plasma around the wires and these current carrying plasmas were driven towards the centerline between the two wires by the $\mathbf{J} \times \mathbf{B}$ force as discussed in sec. 2.2.2. In this geometry the field of view was $0.7mm \times 2mm$, i.e., $0.7mm$ at the object in the spatial direction. Since $1mm$ was the closest we were able to space the wires reproducibly this prevented viewing both wires in an absorption spectrum - they were too far apart. The $2mm$ field of view in the spectral (axial) direction should introduce some nonuniformity due to the axial instability which has a wavelength of approximately $500\mu m$[36]. However, fig. 5.4 shows that their is little variation in the z-direction between the two wires at $t = 100ns$. The effect of the instability is primarily visible on the outside of the wires. Therefore, we anticipate that the axial instability will have negligible impact on the data analysis.

The x-pinch timing was monitored with a set of three filtered photoconducting diamond (PCD) detectors mounted on a port on the main vacuum chamber. One PCD was filtered with $12.5\mu m$ Ti, allowing photons with energies in the range of $3 - 5keV$ to be detected. This was chosen because the Ne-like Mo lines that exist over long time scales are below $3keV$. This means that only continuum radiation from the x-pinch will be seen by this detector, allowing the time of the continuum burst to be discriminated from other bursts. The other PCD's were filtered with $8\mu m$ polypropelene and $25\mu m$ Be foils respectively. The latter

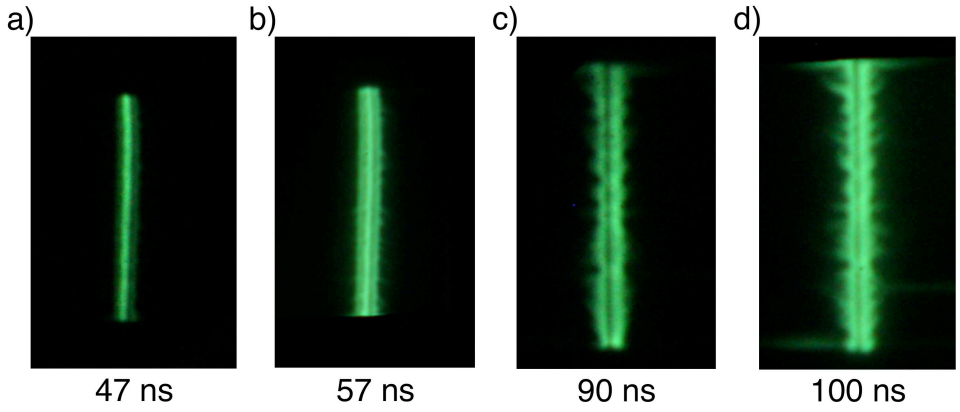

Figure 5.4: Evolution of the exploding wire pair as seen in XUV self-emission. (a) Image from COBRA shot 2030 taken 47ns after the start of current. (b) Image from COBRA shot 2030 taken 57ns after the start of current. (c) Image from COBRA shot 2034 taken 90ns after the start of current. (d) Image from COBRA shot 2034 taken 100ns after the start of current.

is most relevant to the experimental spectra. These filters allow lower energy photons to pass, giving the time history of all of the radiation above 1keV emitted by the x-pinch. In addition an unfiltered x-ray diode (XRD) was used to monitor the emission from the sample wires. The XRD is sensitive to ultraviolet and higher energy photons. Since breakdown of the wires is accompanied by a burst of ultraviolet radiation this detector allows us to measure when the wire sample initiates and becomes plasma.

Two important changes were made to the spectrometer when it was moved to COBRA. A second crystal was added to detect the backlighter radiation over the same spectral band but without having it pass through the exploding Al wire plasmas; instead a step wedge was added to the front of the film in order to enable calibration of the film on each shot. This process will be described in sec. 6.1. The second crystal was placed adjacent to the first one, as shown in fig 5.5(a) ensuring they were the same distance from the source. Both crystals were mounted on the same rotation and translation stages, allowing them to be

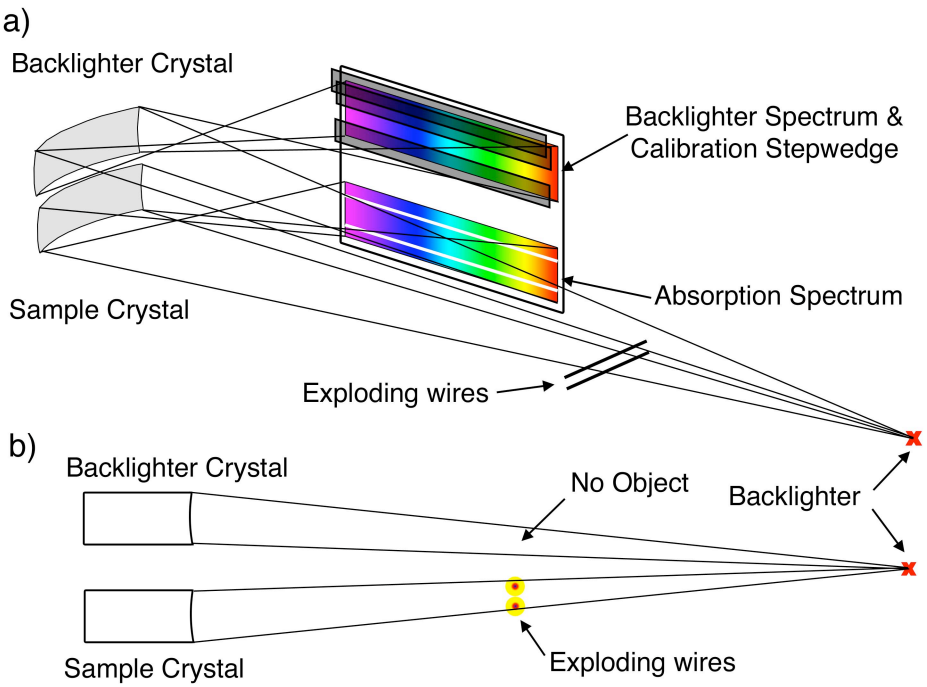

Figure 5.5: (a) View of the improved experimental setup implemented on COBRA showing the two crystals nearly colocated, the placement of the calibration stepwedge and the single film used to detect both spectra. (b) A side view showing how one crystal sees the wire plasma sample while the other does not.

aligned identically. The difference is that the second crystal is not along a line of sight containing both the x-pinch and the wires. This is easiest to see in the side view shown in fig 5.5(b). The spectrum reflecting from the top crystal is filtered using the step wedge mentioned above and described in sec. 6.1. In addition, the spectra reflected from the two crystals were collected on the same film, which helps alleviate errors that could be introduced by development processes.

For the COBRA experiments the crystals were placed at a distance of $1000 \pm 5mm$ from the x-pinch. This placement allowed the use of three polypropelene debris shields totaling $16\mu m$ in thickness. The distance from the x-pinch

to the object is $53mm$, thereby giving $p = 947mm$ and $y = 53mm$. This resulted in a field of view equal to $0.85mm \times 2.7mm$. In all of the COBRA experiments two $40\mu m$ Al wires spaced $1mm$ apart were used to generate the absorption object plasma. These two wires shared the return current with three $12.5mm$ diameter return posts as shown in fig. 5.2(b). As mentioned previously in sec. 4.1.1 the new hybrid x-pinch configuration was used during the COBRA experiments, because of the improved reliability and ease of use compared with other x-pinch configurations tested on COBRA[62, 67]. Previously, the most successful x-pinches fielded at the $1MA$ current level were so called *nested* x-pinches[62]. This configuration requires the use of 19 wires and is considerably more time consuming to implement on COBRA than the hybrid x-pinch configuration.

5.2 Identifying Spectral Features

The first step in the data analysis is to identify spectral features reliably. Since the Al emission spectrum is well known we began by using an Al x-pinch with no absorbing object, other than the Be and polypropylene filters, to calibrate our spectrometer alignment. The raw recorded spectrum from this shot is shown in fig. 5.6(a). The image is a negative, i.e. dark areas are where emission was recorded, and the contrast has been adjusted to bring out the details.

The two primary lines in the He-like Al spectrum that were used to calibrate the spectrometer, the He-α resonance (R) and intercombination (I) lines, are labeled in fig. 5.6. Their wavelengths are well known both experimentally and theoretically. Immediately to the right of the resonance line is a group of satellites that tend to merge together. The fact that we can see this group clearly, well

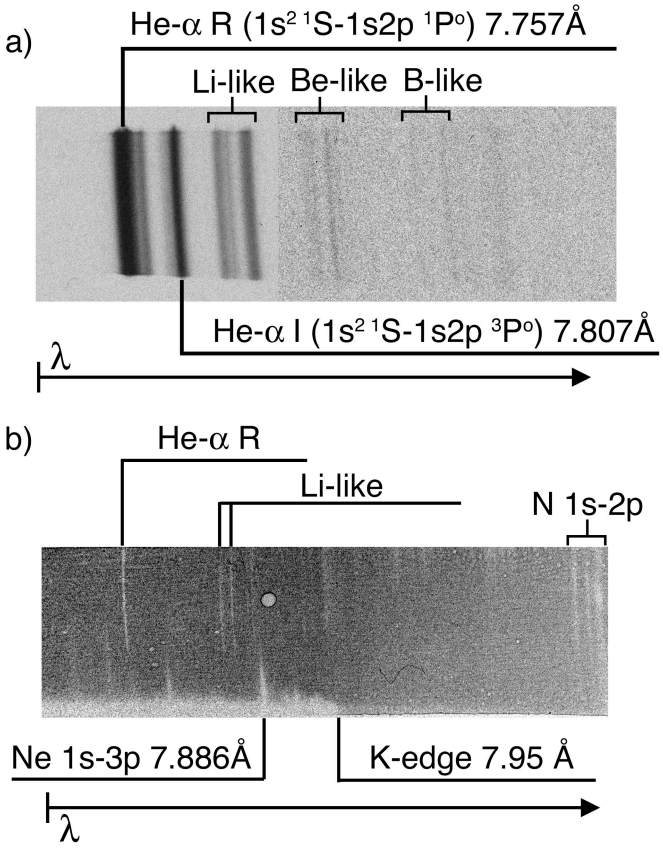

Figure 5.6: Same as fig. 4.8(a) and (b) with more lines identified. (a) Al emission spectrum obtained from an Al x-pinch. The resonance (R) and intercombination (I) lines are labeled as well as the approximate locations of the Li-,Be-, and B-like Al satellite groups. (b) Absorption spectrum obtained on XP shot# 5754 using the same alignment as (a).

separated from the resonance line, is evidence of the high resolution of our system. In addition to the resonance and intercombination lines, the approximate locations of the Li-, Be- and B-like satellite groups are marked. The intensity of emission from these groups is seen to die off quickly as the ion charge decreases. This is because plasmas that produce an abundance of He-like Al emission are too hot for the lower charge states to exist at the densities of interest here. Because of their low intensities, it is not practical to try to use this spectrum to identify each of the lines in these satellite groups unambiguously.

The spectrometer was left aligned exactly the same way and several more shots were fired with a Mo x-pinch and the two parallel Al wires. The results of one of these shots is shown in fig. 5.6(b). By comparing these two images we can immediately identify the resonance line and the Li-like satellites. Two interesting features are immediately apparent. First, there is no intercombination line in the absorption image. Second, the longest wavelength Li-like satellites are missing. If we assume that we have a completely uniform backlighter spectrum so that photons exist at all possible transition energies, which we showed to be true in sec. 4.1, it can be concluded that the optical depths for these transitions are negligible. This may be because the corresponding absorption cross sections are negligible compared to the transitions we do see or that these transitions result from non-thermal processes, such as electron beam excitation, which are present in the Al x-pinch but not in the absorption sample.

There are more features visible in the absorption spectrum than in the emission spectrum. At the bottom of the absorption image a region of broadband absorption is visible. A point is seen where this absorption transitions from nearly complete at shorter wavelengths to very weak at longer wavelengths. This is indicative of the cold K-edge at $1560eV$ (7.95Å). The K-edge is sharp only in very weakly (one or two times) ionized and dense material. This indicates that we are seeing the residual wire core. By comparing spectra generated by the SCRAM calculation and published in [75] we determined that the prominent feature stemming from the wire core at the bottom of the image is the Ne-like Al $1s - 3p$ line at $1572eV$ (7.886Å).

Using these known points we can estimate a dispersion curve which will allow us to identify the other spectral features in the image. This method allowed us to determine that the prominent absorption lines on the long wavelength side

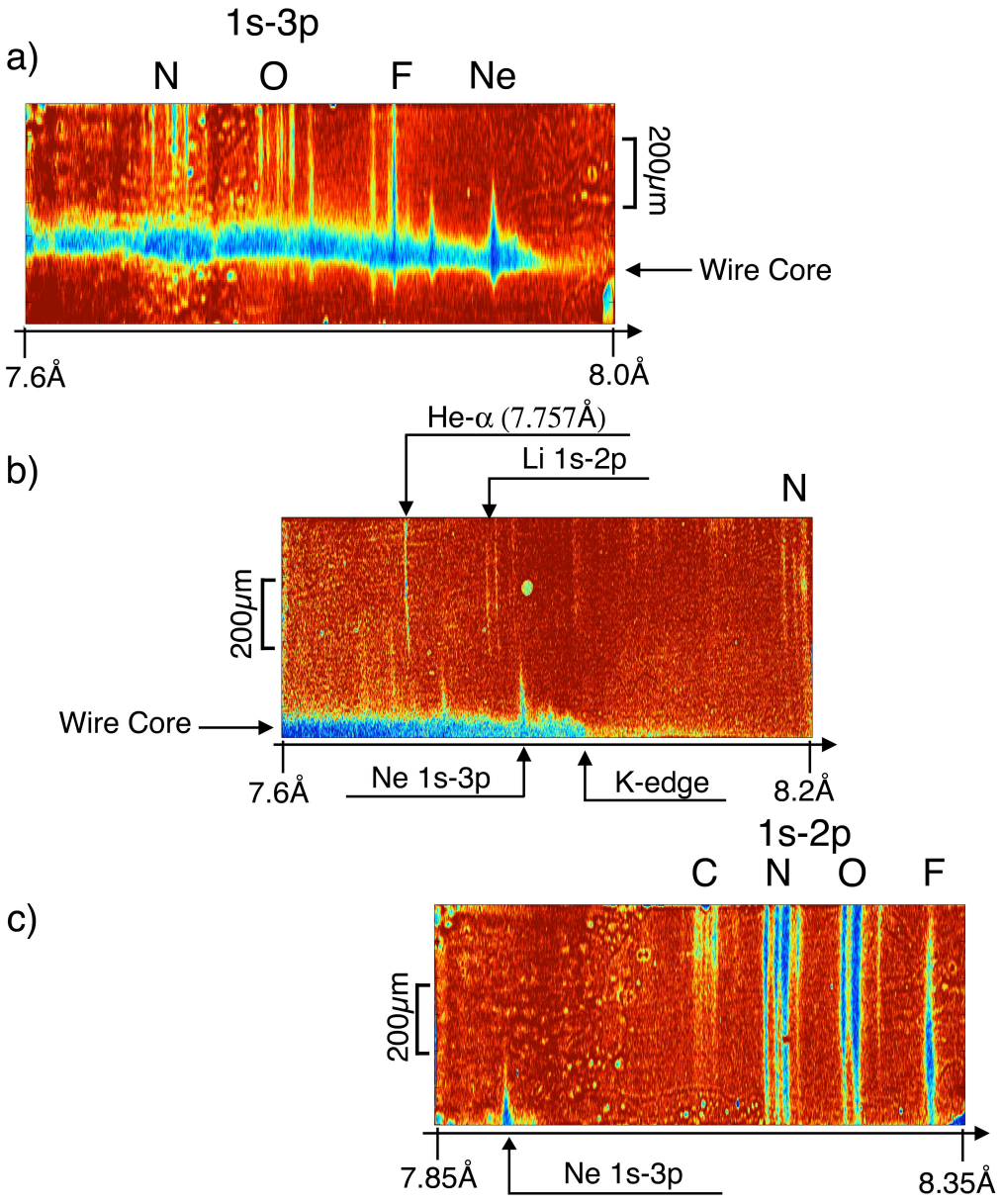

Figure 5.7: (Color) (a) Transmission spectrum showing the N-, O-, F- and Ne-like $1s - 3p$ satellite lines. The location of the inside edge of the wire core is shown to the right of the image. (b) Transmission spectrum showing the Ne-like $1s - 3p$ lines, the He-α resonance line (7.757Å) and the K-edge (7.95Å). (c) Transmission spectrum showing the Ne-like $1s - 3p$ line at 7.886Å and the C-, N-, O- and F-like Al $1s - 2p$ satellite lines.

of the image are from N-like Al. Once the features were identified we consulted the SCRAM calculation to get exact predicted wavelengths for transitions that are not tabulated or well documented, such as the N-like lines. We repeated this process while changing the alignment of the spectrometer to map out the spectral locations of all the visible features, using the few known wavelengths mentioned above as fiducials to identify and locate further unknown features. Figure 5.7 shows a set of three shots from the XP series of experiments that bracket the total wavelength range we investigated in these experiments. These images have been calibrated and converted to transmission using the processes that will be described in sec. 6.1. 100% transmission is shown in red while 0% transmission is shown in blue.

In fig. 5.7(a) we can see the Ne-, F-, O- and N-like $1s - 3p$ satellite transitions along with the cold K-edge. Figure 5.7(b) is the same as fig. 5.6(b) except it has been converted to transmission. Figure 5.7(c) shows the Ne-like $1s - 3p$ transition again along with the F-, O-, N- and C-like $1s - 2p$ satellite groups. These groups are the absorption features that have been studied most intensely in HED Al plasmas. Their dependence on temperature is relatively well understood and they have been used previously to determine the temperature of various plasma samples[1, 11, 44, 51, 57]. However, the resolution afforded by our spectrometer allows us to see the lines in much better detail than previously reported.

CHAPTER 6

ANALYSIS METHODS

6.1 Film Calibrations

In this section we discuss in detail each of the steps required to calibrate and analyze the experimental absorption spectra. Some of the shots, particularly those performed on XP have no calibration available for the film, and so certain assumptions are made in order to extract quantitative information from these spectra. Justifications and consequences of these assumptions will be discussed. All of the data was recorded on BioMax Maximum Sensitivity (MS) medical x-ray imaging film. BioMax is a high sensitivity film, almost as sensitive as DEF, the standard scientific imaging film before it was discontinued about ten years ago, in the energy range of interest, $1.4keV - 1.8keV$[37, 10]. The high sensitivity of BioMax makes it ideal for applications such as ours in which exposure levels can be relatively low. This high sensitivity, however, makes it highly susceptible to noise and unwanted exposure, including low levels of background x-rays, which we must take into account in order to properly analyze the spectrum.

6.1.1 Film Exposure and Background Levels

The first step in calibrating the film is to subtract the background exposure level. This is the exposure that is visible in areas of the film that were not directly exposed by the x-pinch. This can be due to a number of factors including crystal and hardware fluorescence and high energy x-ray background[51]. This type of

exposure generally has a gradient and therefore can introduce systematic errors in the analysis if it is not taken into account. In addition, it is necessary to take into account film fogging due to errors in the development process, which is also treated as a background exposure.

The exposure level on all sides of the spectrum is sampled randomly at 200 points and interpolated across the entire image using radial basis functions. Radial basis function (RBF) interpolation is a technique which provides robust interpolation when sparse, nonuniformly distributed points are used[49]. In this method a linear combination of suitable radially symmetric basis functions, in our case gaussian, is used to approximate the underlying surface described by the sampled points. The RBFs are centered at each sample and the coefficients are determined using the condition that the surface have continuous first derivatives. This process is able to capture low frequency variations across the image quite well and ignore the high frequency noise. Figure 6.1 shows an experimental image before and after background subtraction along with the interpolated background exposure surface that is subtracted from the raw (digitized) absorption spectrum.

As was mentioned in Sec. 5.1, two crystals placed adjacent to each other were used on the COBRA experiments (see fig. 5.5). One crystal was aligned to have a view of the x-pinch through the sample while the other was aligned so as to see only the x-pinch. This way we could, in principle, measure the backlighter spectrum directly, taking advantage of the available calibration for BioMax[37]. However, development procedures must be strictly controlled if this calibration procedure is to be used, and the optical density of the film must be determined by a calibrated microdensitometer or equivalent[29]. Since we do not have access to a microdensitometer this procedure cannot be used. In-

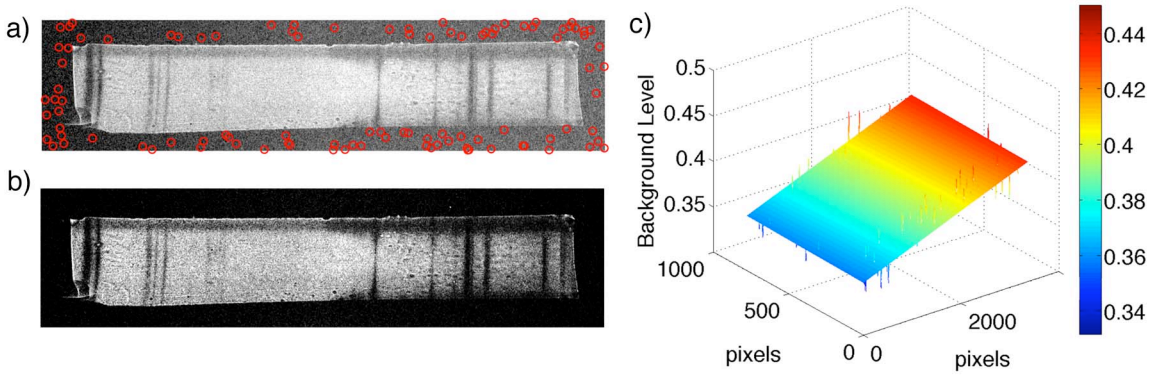

Figure 6.1: (a) Raw recorded spectrum with red circles showing the randomly selected points to use in interpolation. (b) Image with background subtracted. (c) Surface map of the inferred background exposure.

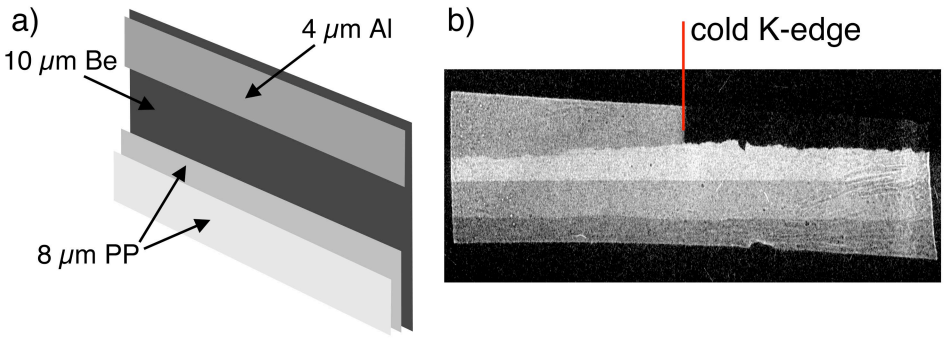

Figure 6.2: (a) The step wedge configuration used to calibrate the films. Two layers of 8μm polypropylene (PP) and one layer of 4μm Al on top of the 10μm Be x-ray filter provide known attenuation steps for the backlighter x-rays. (b) Experimental image from COBRA shot# 2034 showing the attenuation from each of the filters. The cold Al K-edge can be seen in the Al step which provides a wavelength fiducial.

stead, we have placed a step wedge on the x-ray filter for the backlighter film.

A schematic of the step wedge is shown in fig. 6.2 (a). Two layers of 8μm polypropylene and one layer of 4μm Al provide three known attenuation steps. Tabulated transmission data for polypropylene and Al were obtained from the Center for X-Ray Optics(CXRO)[28].

If we assume that the intensity resulting in a given film exposure follows the functional form suggested in[29] we can write

$$I_{film} = \alpha(e^{\beta E} - 1) \tag{6.1}$$

where E is the measured exposure level and α and β are unknown coefficients. Since we know the transmission of each of the filters in the step wedge and we measure the exposure levels on the film we can fit the coefficients to this function via a least squares method.

6.1.2 Transmission Error Estimation

There are two main types of error we must consider. The first, and more concrete of the two, is the error in measured transmission. The second, which we will discuss in Sec. 6.2.4, is error in inferred temperature and density values. Error in the transmission measurement is governed by one's ability to measure exposure levels on the film accurately, and to relate this to x-ray fluence at the film. There are many factors which contribute to uncertainty in this measurement, including chemical fog, calibration procedure, background subtraction, noise on the film and wavelength calibration. Each of these sources should be defined and quantified for both the backlighter spectrum and absorption spectrum and then compounded to determine the final error in transmission.

We are able to measure two quantities, noise and transmission through a known amount of Al, which we feel together allow us to assess the error in measured transmission. The calibration step wedge includes a filter, $4\mu m$ Al, that is not used in the calibration procedure, but only as a wavelength fiducial. Once

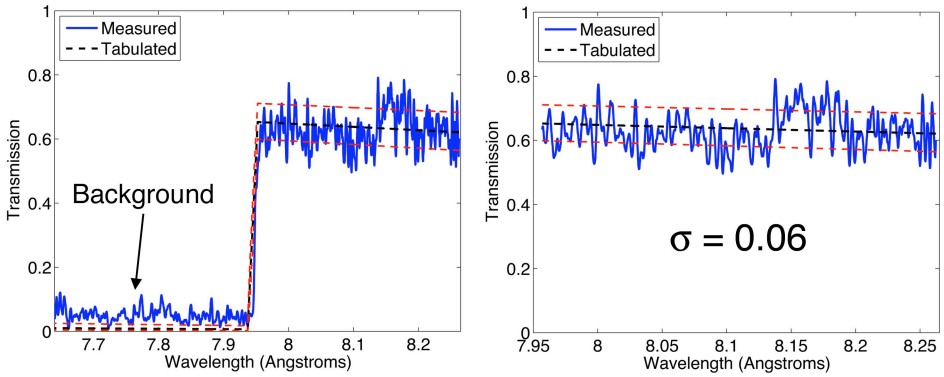

Figure 6.3: (a) Measured transmission through the $4\mu m$ Al filter shown in blue. The dashed black line is the tabulated transmission through a $4\mu m$ Al foil. The red lines show the transmission expected through $3.2\mu m$ and $4.8\mu m$ foils. The filter is completely absorbing below the K-edge so the measured value in this range is representative of the error in the background subtraction method. (b) same as (a), but showing just the spectral region above the K-edge.

the image of the backlighter has been calibrated we can calculate the absolute transmission through the Al filter

$$T_{Al} = \frac{I_{Al}}{I_o} \tag{6.2}$$

where I_{Al} is the measured fluence through the Al filter and I_o is the unattenuated backlighter fluence. This quantity is shown in fig. 6.3(a) with the tabulated transmission data shown in black.

We can see that above the K-edge, 7.95Å, the agreement is quite good and the variation about the mean in the measured transmission is generally within the change in transmission due to ±20% uncertainty in the filter thickness. The agreement below the K-edge is not as good. This is due to the background subtraction discussed in Sec. 6.1. However, we expect the agreement to be worse at low exposure levels because the film response is highly nonlinear in this regime. Figure 6.3(b) shows the transmission above the K-edge only. If we subtract the

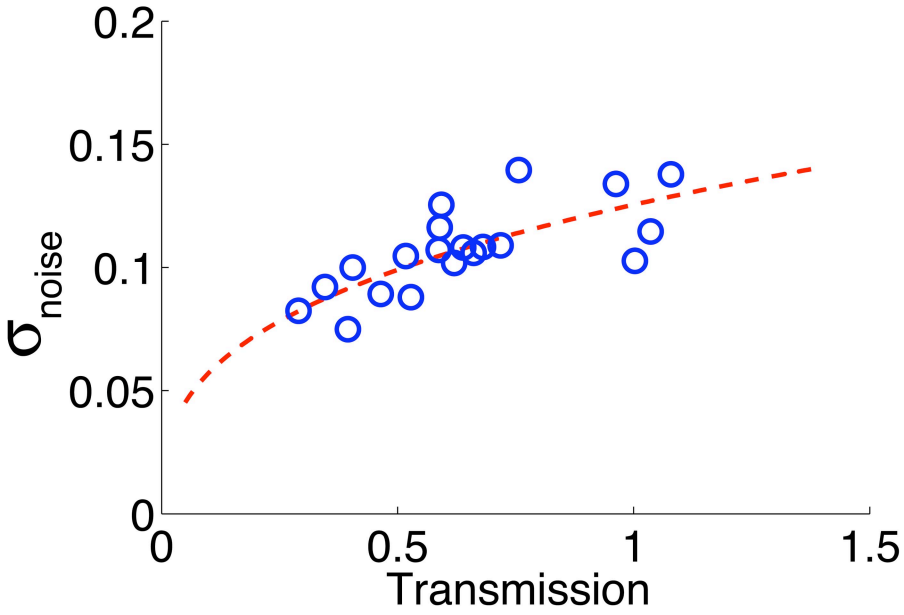

Figure 6.4: Measured standard deviation of noise as a function of transmission (blue circles) and the power law fit (red dashed line). The points indicating transmission greater than one are due to noise.

tabulated transmission from the measured transmission we find it has a standard deviation of about 0.06 corresponding to a relative error of about 9%. The standard deviation below the K-edge is about 0.02. Since we only have two points we can use a line to approximate this error as a function of transmission. Though this is only accurate if the film exposure lies in the linear regime, we argue that this represents a reasonable approximation to the error in *transmission* due to film calibration, wavelength calibration and background subtraction which we will refer to as calibration error.

We are also able to quantify the effect of film noise on the measured transmission by converting the calibrated step wedge image to transmission by dividing the fluence through each step by the unattenuated backlighter fluence. Anticipating that the noise will vary with exposure, we can measure the vari-

ance of the the transmission at different locations of the image corresponding to the different filter steps. Using these discrete steps we then perform a power law fit to the standard deviation as a function of transmission. The measured deviations and fit are shown in fig. 6.4. Since the step wedge image and the absorption image are on the same film we know they were subject to the same development procedure and we can reasonably assume that the noise on each image has the same standard deviation, allowing us to estimate the error due to noise on the absorption spectrum.

Standard error propagation procedures must be implemented in order to estimate the total error of the transmission measurement. We assume that the individual sources of error add as the square root of the sum of the squares, or

$$\delta T = |T| \sqrt{\left(\frac{\delta X}{|X|}\right)^2 + \left(\frac{\delta Y}{|Y|}\right)^2} \tag{6.3}$$

where δT is the absolute error in transmission. Since both sources of error discussed are error in transmission we see that the denominators in eqn. 6.3 cancel the factor of $|T|$ in front. Therefore the expression for total error becomes

$$\delta T = \sqrt{\sigma_{cal}^2 + \sigma_{noise}^2} \tag{6.4}$$

Using the two expressions obtained for error due to calibration and error due to noise we can generate an approximate function describing the total transmission error for our experiments. This curve is shown as the blue trace in fig. 6.5. The black and red traces show the contributions due to noise and calibration, respectively. We can see that noise is the dominant contribution to the error and therefore we expect the total error could be improved greatly by increasing the backlighter intensity which would enable use of a different film. Except at the lowest transmission levels, the absolute error is between about 0.1 and 0.15. By averaging the relative error in this range we can roughly approximate the relative error in transmission to be about 17%.

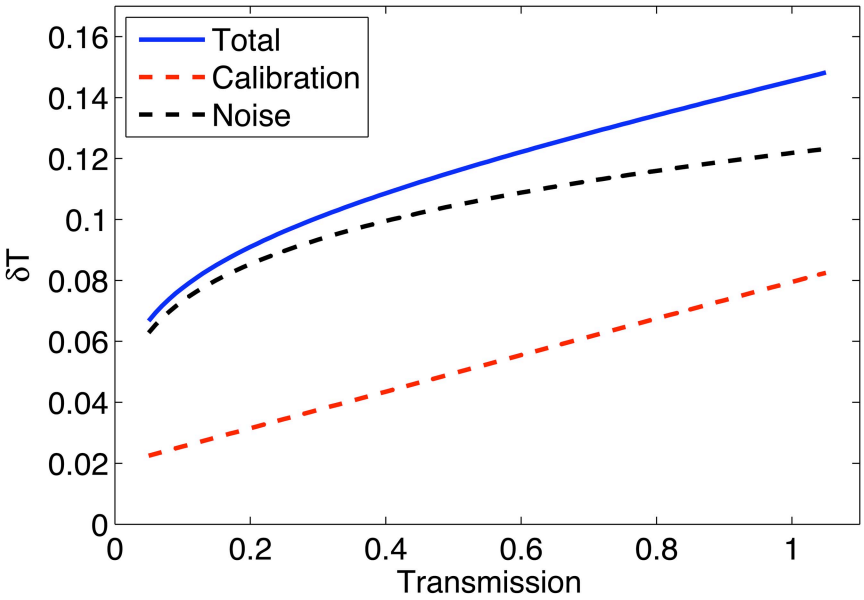

Figure 6.5: Total calculated transmission error as a function of transmission (solid blue line). The contribution due to noise (black dashed line) and calibration (red dashed line) are also shown.

The experiments on XP did not include a second crystal for calibration. For these experiments fluence is assumed to be linearly proportional to exposure. This also means that we have no measurement of the unattenuated backlighter spectrum. To circumvent this limitation, we sample the film exposure in regions that were not attenuated by plasma. We can then exploit the smoothness of the backlighter by fitting a quadratic to the sampled portions of the spectrum. This gives us an estimate of the backlighter fluence at all wavelengths, which we can then use to compute the transmission via eqn. 3.20. By comparing the transmission measured using the calibrated procedure above to the uncalibrated procedure just described we estimate that this procedure will introduce an additional 10% error in the transmission, bringing the total error up to about 20% for the uncalibrated shots in the linear range of the film. Because of these approximations and the additional error, estimates of plasma param-

eters are considerably less accurate from the XP shots. We can however infer densities and temperatures using the same procedures as we would with the calibrated COBRA images, recognizing that the results are more uncertain.

6.2 Fitting Models to Experimental Data

Ever since it has become practical to use computer simulations to calculate detailed expected spectra ("synthetic spectra") at a given set of plasma conditions, the direct comparison of synthetic to experimental spectra has been a popular method for interpreting spectroscopic data. There are inherently many sources of uncertainty in this method, but much progress has been made in this field over the last 10 years by improving the completeness of the models and comparing them with benchmark quality data. The comparison can be accomplished by several approaches that depend upon the quality of the experimental spectrum. For example, fitting can be based upon a particular line ratio or set of ratios, line widths, absolute values of the peak intensities of lines, or by fitting the absolute intensity of the spectrum at each point. In any case, some fitness function must be defined in order to assess the quality of the fit and converge on a set of parameters that best represent the plasma that produced the spectrum. In many cases, including this work, a reduced chi-squared (χ_r^2) fitness function is chosen. This function is written

$$\chi_r^2 = \frac{1}{N}\sum_i^N \frac{1}{W_i}\left(y_{i,exp} - y_{i,theor}\right)^2 \tag{6.5}$$

where N is the number of points, $y_{i,exp}$ and $y_{i,theor}$ are the experimental and theoretical values being compared and W_i is a weight, typically chosen to be a mea-

sure of the error at each point. In our experiments, N is typically a few thousand total which corresponds to several tens of points in a single line. If the weights are representative of the noise distribution on the data $\chi_r^2 = 1$ represents an optimal solution. Therefore in this case one minimizes $f = \chi_r^2 - 1$, where f is the fitness function. Once the fitness function and set of experimental values are defined, an optimization technique can be applied to search the parameter space and choose a suitable set of parameters to describe the state of the plasma.

In this study we have chosen to compare measured and theoretical transmission spectra at every point in large portions of the spectrum. We have chosen a set of wavelength windows to use, each of which contains a specific line or group of lines. The line group and maximum and minimum wavelengths of each of the windows used is shown in table 6.1. This set varies from shot to shot depending on what bandwidth is being imaged and the quality of the image. In this way we can choose to reject regions of the spectrum that don't have useful diagnostic information or that contain defects or a high noise level. In addition, we can account for small discrepancies in the positions of lines by allowing each window to shift slightly in wavelength. Finally, this allows us to use only well understood lines for the fitting and then see how well the model compares with less understood lines once the fit is optimized. The weight has been chosen to be the square of the error in the transmission measurement as defined by eqn. 6.4.

The model used in this study to calculate the opacity as a function of density and temperature is a hybrid collisional radiative model known as SCRAM[27]. The approach taken in this code composes the level structure using a small set of fine structure levels accessible using a coronal approximation and supplements this with a complete set of configuration- and superconfiguration*averaged lev-

Table 6.1: Maximum and minimum wavelengths used to window the spectra about each line group.

Satellite Group	$\lambda_{\mathbf{min}}$ (Å)	$\lambda_{\mathbf{max}}$ (Å)
O-like $1s - 3p$	7.52	7.65
F-like $1s - 3p$	7.67	7.77
Ne-like $1s - 3p$	7.83	7.95
B-like $1s - 2p$	7.98	8.07
C-like $1s - 2p$	8.07	8.15
N-like $1s - 2p$	8.16	8.2
O-like $1s - 2p$	8.24	8.28
F-like $1s - 2p$	8.3	8.35

els. Where previous models fail in certain regimes, i.e. high density, low temperature, etc., this method allows high accuracy to be achieved under a variety of plasma conditions in much less computational time than standard relativistic configuration and fine structure models[27]. These advantages make SCRAM particularly well suited for diagnostic use in HED plasmas.

Dr. Stephanie Hansen of Sandia National Laboratories performed a set of calculations specifically for the analysis of the spectra obtained in the experiments detailed in sec. 5.1. The standard SCRAM model was supplemented with additional fine structure data in order to get better agreement with the $1s - 3p$ transitions which have been studied less rigorously in the past. This model has about 4×10^5 levels among the 13 Al ionic states plus neutral Al (Al-

*A superconfiguration (SC) is a compact form of completely representing the state of a multi-electron ion. The state of the ion is denoted by the principal quantum number of each occupied shell, (n_s), and the number of electrons occupying that shell, N_s, in the form $(n_s)^{N_s}$[4]. For example the ground state SC for O-like Al is $(1)^2(2)^6$, where the actual distribution of electrons within the $n = 2$ shell is treated statistically instead of explicitly. A possible excited SC of O-like Al is $(1)^1(2)^7$.

like through H-like) and of order 1×10^9 transitions coupling the levels. The model includes continuum lowering effects. A Maxwellian electron distribution was used to calculate the NLTE radiative and collisional decay rates which then enables the set of rate equations to be solved giving the level populations as a function of electron temperature and mass density. The wavelength dependent opacity and emissivity are then obtained assuming a Voigt profile which includes natural, collisional, temperature (assuming $T_i = T_e$) and approximate Stark broadening. Stark and polarization, which is due to the spatial variation of the electric potential due to the free electron distribution[56], shifts are also included. The plasma is assumed to be optically thin to its own emission in the calculation which means that the spectra will be geometry independent. This allows us to use the opacity to determine the transmission spectra for arbitrary plasma thickness, assuming a planar geometry, using eqn. 3.16.

A table of opacities at discrete densities and temperatures was compiled and used as the primary theoretical spectral data in our analysis. The temperature and density were logarithmically spaced on the intervals $1 - 100eV$ and $0.00027 - 2.7g/cm^{-3}$ respectively. Two points per decade were used in density, giving 9 points total. 16 points were used for the temperature ($T = 1.36^n$, where $n = 0, 1, ...15$) since absorption spectra are known to be more sensitive to temperature than density. Thus, the grid spacing was a limiting factor to the accuracy achievable with this diagnostic up to the time that the analysis in the this thesis was done.

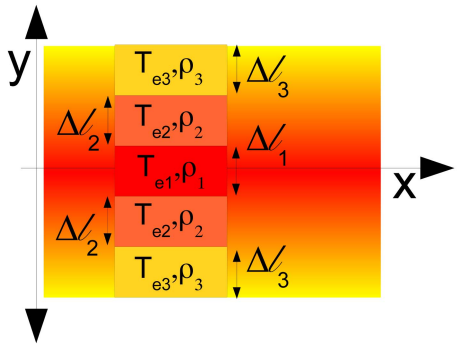

Figure 6.6: (Color)(a) A hypothetical smoothly varying plasma along with the set of uniform plasma regions that has been used to approximate the presumed actual profile.

6.2.1 The Need for Multiple Temperatures and Densities

As was mentioned in sec. 3.4 it is desirable that the sample being probed is uniform along the line of sight of the diagnostic. In the case of exploding parallel wires, as used in this experiment, this is not correct. Gradients exist in the plasma in all directions, and cylindrical symmetry cannot be assumed, ruling out the use of Abel inversion, even close to the individual wires. However, to first order the plasma is uniform along the z-axis (i.e. parallel to the wires).

In order to accommodate the nonuniformity along the line of sight we have incorporated the ability to include multiple plasma regions in the fitting algorithm. As shown in fig. 6.6(a), a plasma with continuously varying temperature and density as a function of space is being approximated by discrete regions of uniform density and temperature. The challenge is to choose an appropriate thickness, density and temperature for each of these regions in order to accurately describe a real plasma.

Given the rapid variation in density and temperature expected in the $x - y$ plane, it is reasonable to analyze the experimental images to see if a single density/temperature region can account for the observed absorption as represented

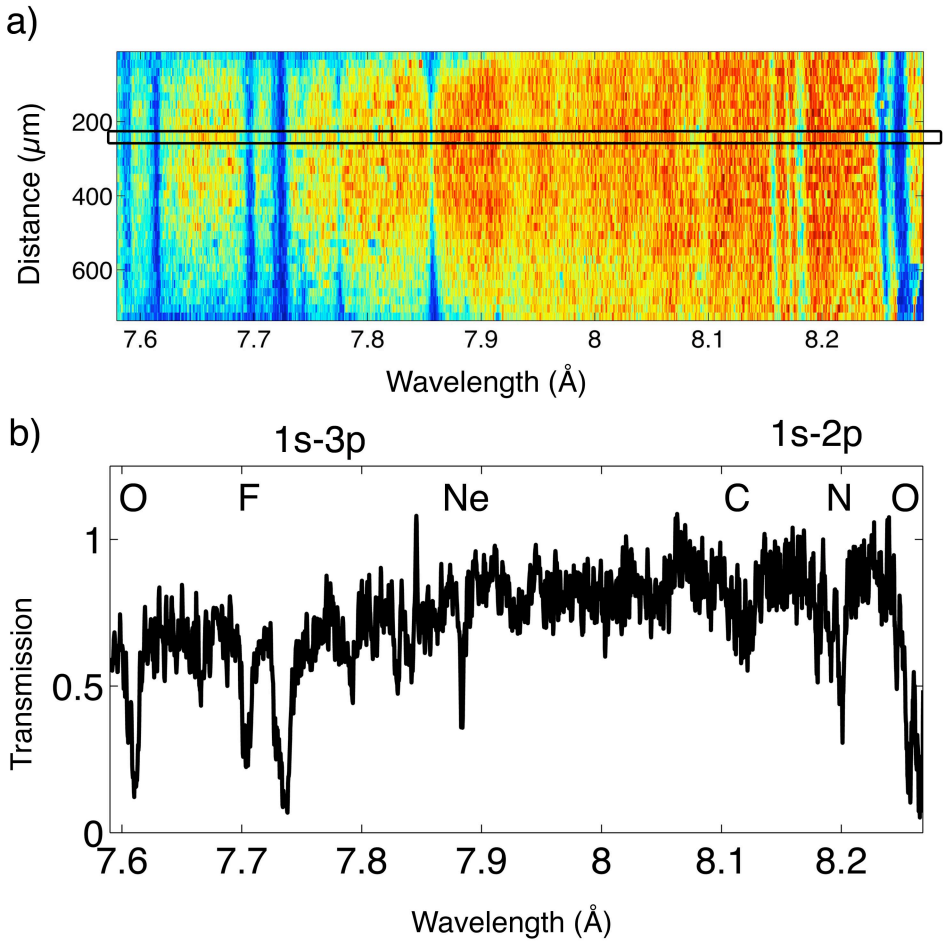

Figure 6.7: (Color)(a) Experimental transmission spectrum obtained from COBRA shot 2034. (b) A lineout of the spectrum at the position indicated by the black box in (a). The locations of the Ne-,F-,O-,N- and C-like Al lines are noted along with the type of transition, i.e $1s-3p$ or $1s-2p$.

by the spectra or if it is necessary to include multiple regions in order to adequately represent the spectra. Taking, for example, the transmission spectrum obtained from COBRA shot 2034, shown in fig. 6.7(a). If we take a lineout along the spectrum at an arbitrary position, designated by the black box , we see in fig. 6.7(b) that Al ions from C-like to Ne-like all exist at the same location. Using the non-LTE ionization balance calculated by PrismSPECT[32] in the parameter ranges of interest we can look at the abundances of the individual ions to see if

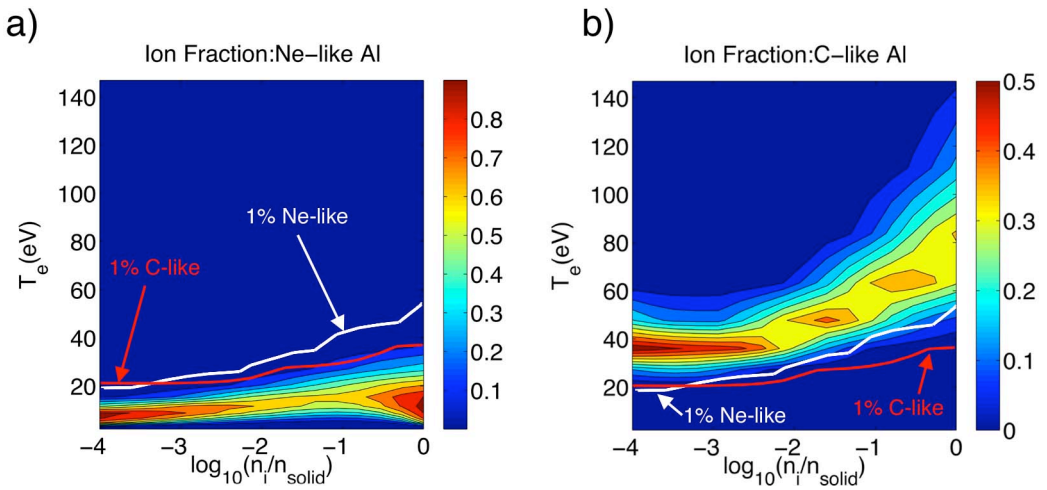

Figure 6.8: (Color)(a) Contour map of the population fraction of Ne-like Al versus density and temperature. The white line indicates the location of the 1% Ne-like Al contour. (b) Contour map of the population fraction of C-like Al. The red line indicates the location of the 1% C-like Al contour.

it is possible to reproduce this absorption spectrum with a single density, temperature and thickness in the *y*-direction as a function of x. To simplify things we will look at the Ne-like and C-like Al population fractions since they are the farthest apart in ionization level and are therefore the most difficult to match with a single density and temperature.

Figure 6.8 shows the population fractions of Ne-like Al in part (a) and C-like Al in part (b) as a function of density and temperature. On both plots the contours corresponding to 1% Ne- and C-like populations are drawn. This shows that, generally speaking, these two ions cannot exist at the same density and temperature at levels of more than a percent or two. As the plasma approaches solid density the ion distributions broaden somewhat. However, the simultaneous levels of each are still below 10%.

Figure 6.9(a) shows the C-like and Ne-like portion of three transmission spectra calculated using PrismSPECT at $6\times10^{19} cm^{-3}$ ion density, thickness equal

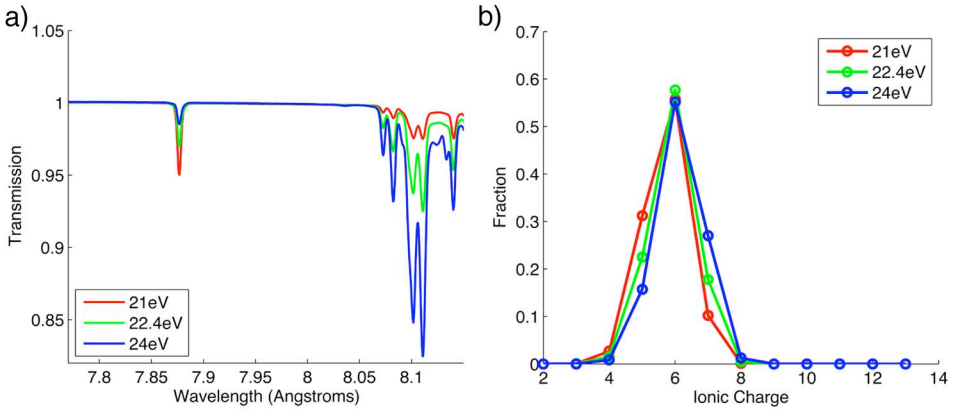

Figure 6.9: (Color)(a) Transmission of the Ne- and C-like satellite lines calculated in non-LTE using PrismSPECT at $6 \times 10^{19} cm^{-3}$ ion density and temperatures ranging from $21eV$ to $24eV$. (b) Ion population distribution at the same conditions shown in (a).

to $200\mu m$ and different temperatures. The three spectra all show absorption from the C- and Ne-like lines that is much less than that seen in the fig. 6.7(b). In fact the most absorption seen by both charge states simultaneously is only about 5%, which would be impossible to discern above the noise in our spectra. In figure 6.9(b) we see the computed charge state distribution at each of the conditions shown in fig. 6.9(a). These distributions show that, as suggested above, the Ne-like and C-like ions do not exist together at levels above a few percent. In fact, any quantity sufficient to produce enough absorption from one ion to be measurable would require that there be virtually none of the other ion left. All of this taken together suggests that a single density and temperature could not produce the level of absorption seen simultaneously in the Ne- and C-like satellite lines in fig. 6.7. Therefore, we need multiple regions to model our plasma.

It is important to note that PrismSPECT calculates the ionization balance assuming a steady state, which may not be valid. If we assume that the plasma can be divided into regions of uniform density and temperature, this assumption certainly would be violated if the lifetime of an ion in a particular ioniza-

tion state in a give region is longer than the time it takes the ion to traverse that region. We know that there are flows in the plasma, so this is a conceivable scenario.

For example, if a F-like Al ion is "born" near the wire core and has a velocity imparted to it by the magnetic force it will move towards the centerline between the two wires. As it travels it will be part of a fluid element that has varying density and temperature. To assume steady state at each position, the local charge state distribution must equilibrate with the local electron temperature in a time that is short compared to the time this ion spends traveling from one region to the next. In order to determine if this is true, we must estimate the flow velocity and the lifetimes of the ions in a particular ionization state.

Using PrismSPECT we can calculate the time-evolution of the ion populations in a plasma in which we instantaneously change the electron temperature while keeping the density constant. In order to model our system we initialize the populations of each ion to be the LTE populations at $8eV$ and $6 \times 10^{19} cm^{-3}$ ion density, representing conditions near the wire core. We then instantaneously change the plasma temperature to $29eV$ keeping the density constant, representing conditions found between the two wires in the analysis of a particular shot to be discussed in Sec. 7.2. The populations then evolve from their initial state to a final state.

This evolution is shown in fig. 6.10(a). We can see that the populations stabilize approximately $300ps$ into the calculation. At this time the ion distribution is peaked at N-like Al, as shown in fig. 6.10(b). If we estimate the flow velocity of material in the coronal plasma to be $\sim 100km/s$ as found in other related experiments[8, 39, 38], then it would take material from the core about $5ns$ to reach the center line between the two wires. This time is much longer than the

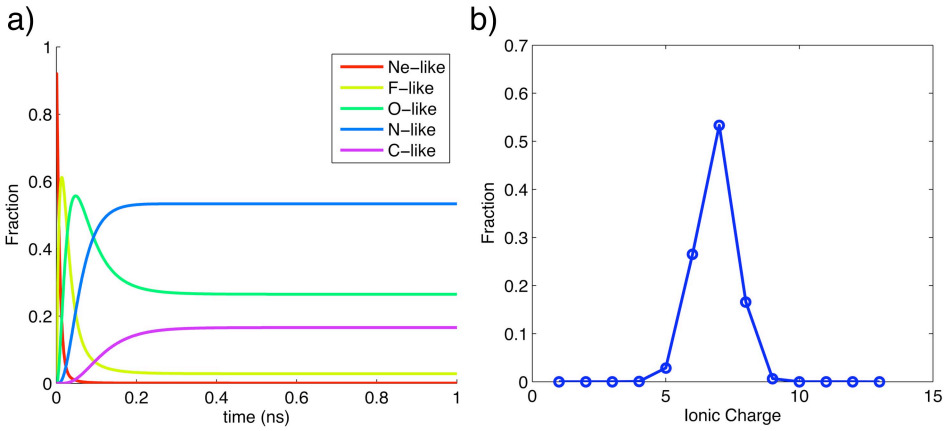

Figure 6.10: (Color)(a) Time evolution of the population fractions of Ne-like through C-like Al. (b) Final ion distribution after the plasma has reached equilibrium.

equilibration time given by the calculation. Therefore we expect the ionization state to be determined locally by the electron temperature. Because of this we believe that it is reasonable to approximate the plasma as a set of discrete uniform plasma regions, each in steady-state.

6.2.2 The Genetic Algorithm

The algorithm we have chosen to use to optimize our solution and generate the best fit for each absorption spectrum is a genetic algorithm (GA). The GA is a stochastic optimization technique which uses the principles of natural selection to search the solution space and iterate to an optimal solution[58]. GAs are a general search technique that can be applied to nearly any problem. We have used a toolbox developed for use with MatLab® by the evolutionary computation research team at the University of Sheffield, UK[12].

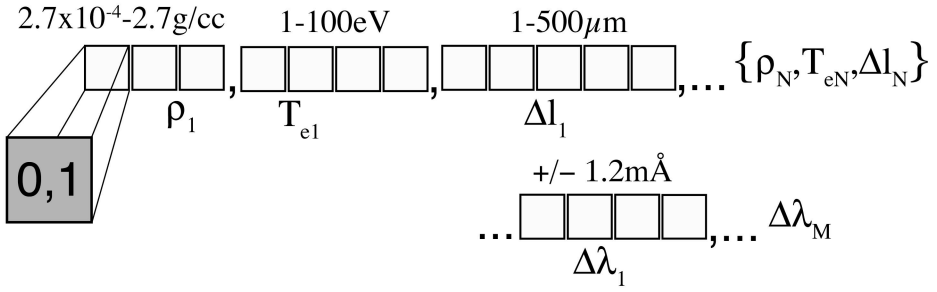

Figure 6.11: Representation of the chromosome used to encode the density, temperature, path length and wavelength shifts for use in the GA. Each box holds a zero or a one. The entire chromosome creates a single binary string which is acted on by the GA. The individual pieces of information are only extracted when evaluating the fitness.

The GA operates simultaneously on a population of potential solutions, or "individuals", assessing each one for its fitness in the problem domain. The set of solutions are "bred together" according to their fitness in a process that mimics natural selection and a new generation of solutions is born. Each generation breeds a population that is better suited to its environment than its predecessors[70]. If the problem is formulated well this will result in an optimum solution.

The individuals in the population are encoded in a chromosome which is acted on by the selection and breeding processes. The chromosome represents all of the relevant information needed to model the spectrum at a single *x* position. Each *x* position in the image is optimized separately. This encoding, done in binary, maps the chromosome to the real values associated with the problem. The encoding used in this work is depicted in fig. 6.11. Each plasma region has a temperature, represented by a 4-bit string, and density, represented by a 3-bit string, associated with it. The number of regions per *x* position is potentially a variable, but we have settled on three regions as a balance between compu-

tation time and accuracy. When decoded the density and temperature become integers, 1 – 16 for temperature and 1 – 8 for the density, and are used as indeces for the table of parameters for which calculations were made. The path length for each region is represented by a 5-bit string which is converted to a distance. In our case, the coarseness used to represent the density and temperature is dictated by the values for which the SCRAM model was run. The path length is set to be within reasonable limits as determined by previous experiments and simulation results.

A final piece of information has been encoded into the chromosome. As mentioned in sec. 6.2 we wish to divide the spectrum into a subset of discrete wavelength (or energy) intervals and use only these to fit the spectra. Each of these intervals is allowed a shift, $\Delta\lambda$, to account for any uncertainties in the experimental wavelength assignment or distortions in the image. The allowed shift is in the range $\pm 1.2m$Å inclusive. All of these parameters are encoded in binary and strung together to create the chromosome. The parameters for a single plasma region are grouped together as shown in fig. 6.11 and successive regions are added on. The shift for each spectral window is added to the end of the string. It is this binary string that gets acted on by the machinery of the GA.

To initialize the GA, a population of chromosomes is randomly generated. The fitness of each member of the initial population is assessed using the χ^2_r function, eqn. 6.5. The members are then ranked according to their relative fitness levels and members are selected for breeding with a probability proportional to their rank[70]. Breeding is accomplished by a process called recombination where portions of an individual's genetic code are exchanged with that of another. The amount of information exchanged, and where in the chromosome this exchange occurs is varied randomly to mimic natural processes[70].

Finally, a portion of the newly created individuals are mutated by changing the state of a single bit at random. The probability of mutation is low, about 0.01, but it serves to introduce variation in the population which helps search the entire solution domain and prevent early convergence[12]. This new batch of individuals must be inserted into the population to produce the new generation, but to keep the population size the same, old members are replaced by new ones. This is accomplished by ranking the new individuals against the old generation and replacing the least fit members.

A new generation is now complete. Each individual is ranked again using the same criteria and the breeding process restarts. By mimicking natural selection we expect the average fitness of each successive population to increase since the fittest members of the previous generation are retained while the least fit members are eliminated[58]. After a specified condition is met, such as a certain number of iterations or meeting certain convergence criteria, the algorithm is terminated and a solution is reached. This solution may not be *the* optimum and running the algorithm again may produce a different result with the same, better or worse fitness. Because of this the GA requires an element of human intervention. In this work the GA is run many times on the same data and the various solutions are compared. In addition to producing a good fit in the χ_r^2 sense the solution must fit well "to the eye" and be physically reasonable. Clearly, the solutions generated by a GA are not unique, but they fit two ultimate criteria: they are fittest solutions with respect to their population and they look right.

Other conditions can be incorporated into the algorithm to help constrain the solutions and ensure that they make physical sense. The first method we employ exploits the fact that the experimental spectra are smoothly varying func-

tions of space. Taking the image in fig. 6.7(a) as an example we see that the absorption in all of the lines increases and decreases smoothly from one spatial location to the next. From this observation we can infer that the parameters also vary smoothly. To help accommodate this condition we seed the GA at each x position with the solution from the previous position as well as similar solutions. To accomplish this we take the previous x position's solution and perturb it randomly by ± 1 point in the discretized solution space, i.e. $+35\%, -25\%$ in temperature and $10^{\pm 0.5}$ in density, leaving the wavelength offsets untouched. A randomized initial population is generated as in the startup phase of the GA, but half of this population is replaced at random with the perturbed solutions from the previous step. By doing this we bias the solution towards similar solutions while allowing an exploration of the entire solution space through the random portion of the population.

The second condition we enforce comes from prior knowledge of the behavior of wire array plasmas. Since the $\mathbf{J} \times \mathbf{B}$ force tends to focus plasma to a geometric axis we assume that the highest density will be along the axis of symmetry. Figure 6.12(a) shows an axial radiograph from an $8 \times 18 \mu m$ W wire array z-pinch experiment performed on COBRA provided by Mr. Isaac Blesener. The details of this experiment are described in ref. [6]. This view allows us to see the distribution of plasma density perpendicular to the ablation stream. Figure 6.12(c) shows lineouts of the ion density taken perpendicular to the ablation stream at the locations indicated in (b). The density is peaked at the center of the stream, $y = 0$, along the entire length of the stream and is approximately symmetric about the x-axis. If we let region one be the region that straddles the $y = 0$ plane we can easily enforce the condition that the density be highest there by checking each possible solution to see if region one has the highest density.

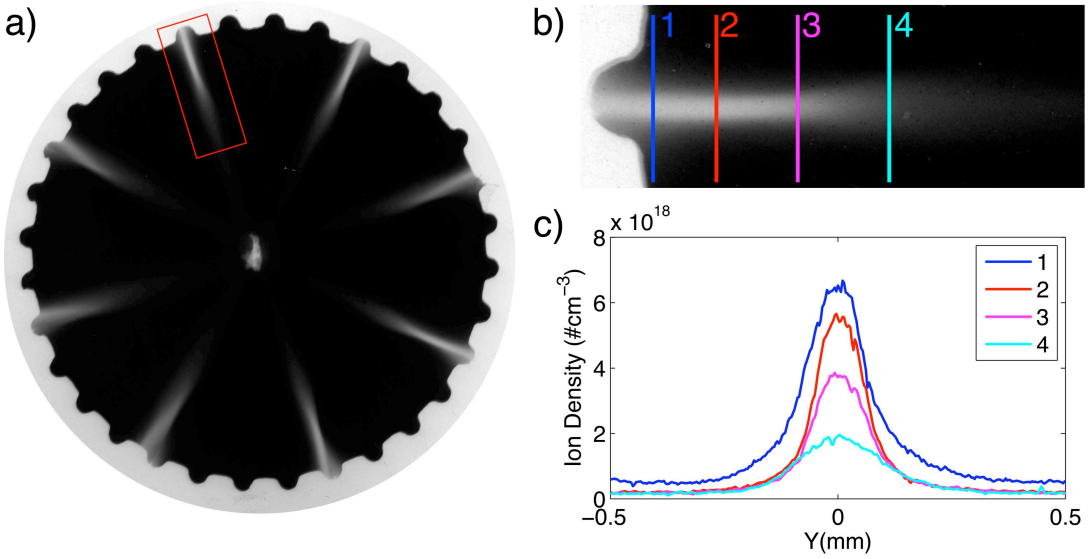

Figure 6.12: (Color) (a) Axial x-ray radiography image of an $8 \times 18 \mu m$ W $10mm$ diameter wire array. Black regions of the film indicate high exposure, meaning there is no mass attenuating the x-rays. Light regions indicate the presence of array material. (b) Close up of the portion of (a) highlighted by the red box. (c) Calibrated lineouts taken at the location taken at the locations indicated by the vertical lines in (b). The lineouts show the mass density as a function of distance from the center of the stream.

If this is not true then we artificially add to the fitness value of that solution to make it undesirable.

The final condition employed to bias the GA stems from the above condition on the plasma density. We expect that regions of highest density will have the shortest path lengths. This is because absorption is exponential with the product of density and path length, so a combination of high density and long path length will lead to unreasonably large absorption in a given region. To enforce this condition in the algorithm we simply limit the search space for each region by assigning a different range of path lengths to each region. Region one is allowed to vary between $1 \mu m$ and $100 \mu m$. Region two is allowed to vary between

$20\mu m$ and $200\mu m$ and region three is allowed to vary between $60\mu m$ and $500\mu m$. As we will see in the analysis presented in Sec. 7.2, the GA never converged to a solution at the limits of the allowed path length ranges, suggesting that the imposed limits are not artificially restricting the solution. The path lengths of each region are then divide by two so that they can be mirrored about the x-axis.

6.2.3 Accuracy and Convergence Tests

A number of tests can be performed to see how well the GA converges on a solution to a given problem. However, to assess success one needs to know the answer before the test is performed. To accomplish this we have designed a series of tests that use synthetic spectra with artificially generated noise.

The first test is the simplest. We input a synthetic spectrum generated from a single density and temperature region with a given thickness and ask the algorithm to find the spectrum that fits best. We have added noise that is proportional to transmission using eqn. 6.4. We initialized the population using 100 individuals and allowed it to run for 80 generations before terminating. We did this, varying the amplitude of the noise above and below a level comparable to that on the film and ran each case 100 times. The results of these tests are summarized in table 6.2.

The accuracy is quite good for noise levels equal to or less than that of the film. As the noise grows larger than that on the film the reliability becomes somewhat worse. However, it should be noted that the runs that failed to converge to the proper solution had χ_r^2 values that were worse than the successful solutions. This means that even though the GA may not give the correct solu-

Table 6.2: Table summarizing the results of the single (ρ, T_e) accuracy tests. The first column is the fraction of noise added to the synthetic spectrum compared to the experimental noise. Column two gives the number of times the GA converged to the correct solution in a test problem and column three gives the average fitness value for the correct solutions.

σ	% **Correct**	$\langle \chi_r^2 \rangle$
0.25	76	1.03
0.5	72	1.024
0.75	79	1.0036
1.0	81	1.024
1.25	60	1.0028

tion every time, one should be able to tell by comparing a family of solutions which ones are best.

An example of one of the successful runs is shown in fig. 6.13(a). The best fit is shown in red and the input synthetic spectrum with noise is shown in black. Figure 6.13(b) shows the fitness value of the "best" individual at each generation. Convergence does not occur until generation 71 in this particular example. However it often occurs as early as ~ 30 generations.

Having shown that the GA reliably converges to the proper solution under realistically noisy conditions in this simple example we can now test its performance on a more difficult case. We wish to model a smooth distribution of density and temperature using a small number of regions. We set up a smooth distribution, shown in fig. 6.14, using points in our opacity table. Then we generate a transmission spectrum from the sample plasma distribution and add noise to it as before.

The GA then fits three regions to the spectrum. A sample result of this test

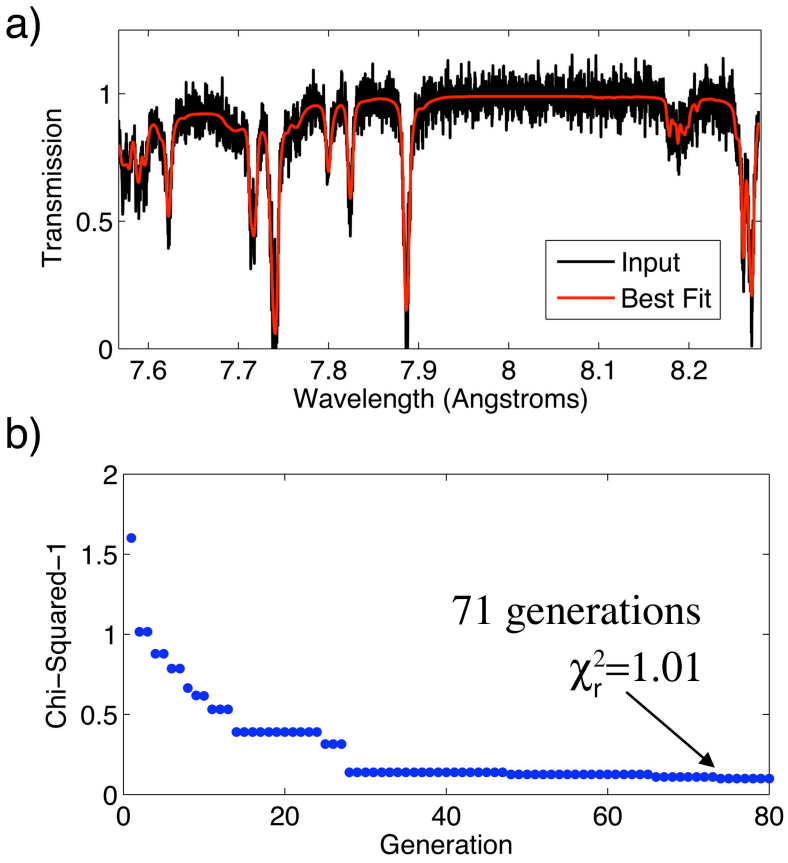

Figure 6.13: (Color) (a) Best fit spectrum showing convergence to the correct solution for a single density and temperature. (b) The fitness of the best fit individual at each generation. It took 71 generations to reach the solution.

is shown in fig. 6.15. Figure 6.15 (a) shows the input spectrum in black along with the fit generated by the GA in red. The χ_r^2 value is about 1.13. Visually, it is easy to see that the relative intensities match well for the majority of the lines. Figure 6.15 (b) and (c) show the density and temperature distributions generated by the GA respectively. The large grey blocks show the three regions with the height indicating the value of density or temperature and the width indicating the path length of the region. The center location of each region is then used to interpolate a smooth distribution from the three points. The agreement

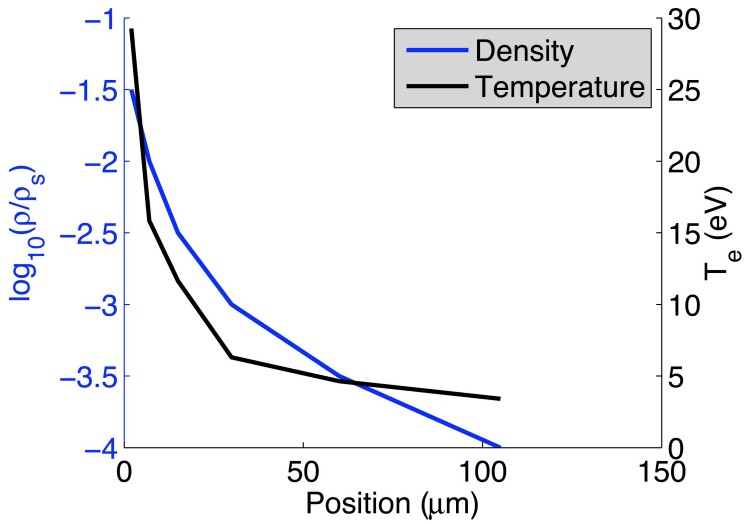

Figure 6.14: (Color) Sample density (blue) and temperature (black) distributions used to test the GA.

is quite good considering only three points have been used and no information about the original distribution is known. The only assumptions used are that the density should be highest at the origin and that the path length should be successively larger moving away from the x-axis. The author believes that the success of these two tests indicate that this algorithm will be able to converge to a physically meaningful solution using the experimental spectra.

6.2.4 Estimating Error in Plasma Conditions

There is still one more type of error we need to discuss. This is the error in the plasma conditions which are determined by the GA. This type of error is ambiguous, since the only way to estimate it is to have independent measurements

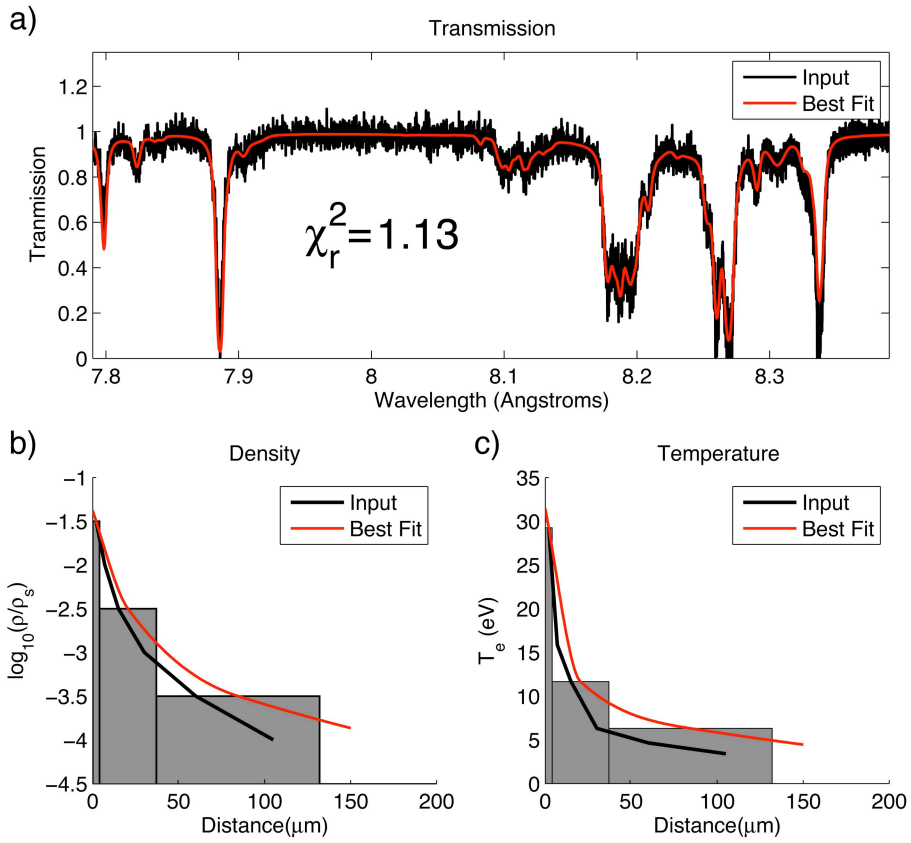

Figure 6.15: (Color)(a) Synthetic spectrum generated from density and temperature distribution shown in fig. 6.14 in black along with the best fit as determined by the GA using three regions in red. The fit has a fitness value $\chi_r^2 = 1.13$. (b) Original density profile (black), location and density of each region (grey blocks) and interpolated density distribution (red). (c) same as (b) but for plasma temperature. Region 1 is $4\mu m$ wide.

of the parameters with their own independent error bars. Without this, the inferred conditions and associated errors will be dependent on the model used to compute the synthetic spectra, the assumptions made on allowed solutions, the optimization routine and the accuracy of the transmission measurement. As mentioned previously, the results of the GA are not unique, though we believe they represent a physically reasonable solution.

Further complicating our desire to quantify the error is the fact that we are

using opacities calculated at specific density and temperature points to compute the synthetic transmission spectra. For example, the temperature grid is evenly spaced on a log scale with inevitable uncertainties of $-25\%/+35\%$.

The absorption spectra are most sensitive to temperature because the diagnostic directly probes the ionization distribution of the plasma. As such we are most confident in the values of temperature quoted. A sensible approach to determining the error in inferred plasma temperature is to perturb the optimum solution and see how far away one needs to be to produce a spectrum that does not agree with the data. However, without additional points on the grid it is impossible to do this. We can say only that using the nearest temperature point available produces clearly "less fit" results in our analysis. Since the spectra are so sensitive to temperature we think it is reasonable to go further and use the smaller of the two increments, i.e. say that we believe our temperature measurement to a level of $\pm 25\%$.

The density grid is spaced evenly on a log scale with half an order of magnitude between points. This works out to approximately a factor of three separating points on a linear scale. This was done anticipating a large range of density in the experiment and that the spectra will not be terribly sensitive to density. Still, we can say with confidence that changing the density by one point on the grid results in unacceptable agreement between measured and synthetic spectra. For this reason we believe that we can say that the measured density using our technique is accurate within a factor of 2, or $-50\%/+100\%$.

The path length determined by the GA for each region does not affect the ionization balance and therefore only affects the depth of the absorption lines. We do have direct access to this and can check the sensitivity of the solution to this parameter. By manually modifying the solution and perturbing the path

lengths we believe them to be accurate within ±40%.

CHAPTER 7

RESULTS AND DISCUSSION

7.1 Trends in the Data

Many shots were taken on XP in order to understand the function of the spectrometer and the spectral features. Table A.1 comprises a list of those shots for which absorption spectra were obtained. As stated in sec. 6.1 there was no separate measurement of the backlighter spectrum or film calibration available for these shots. However, as discussed in sec. 6.1.2, it is possible to obtain semi-quantitative information from these data without a calibration. For example, by exploiting the smoothness of the backlighter spectrum we are able to determine the grey-scale level of the film corresponding to the backlighter fluence using portions of the radiation that were not attenuated by plasma. This leads to a relatively small additional error in the absolute transmission while still allowing us to discern trends in the properties of the exploding wire plasmas from the absorption spectra.

In the sections to follow we will look at the behavior of certain spectral features as well as the wires and wire plasmas. We will use the opacity and transmission calculated using SCRAM to study the properties of the plasma through which the backlighter x-rays are passing by calculating the expected line spectrum and K-edge profile as a function of mass density and electron temperature and relating this to the experimental spectrum as a function of position. We use the ion population fractions that give the best match to the absorption spectrum to estimate the density and temperature of the sample.

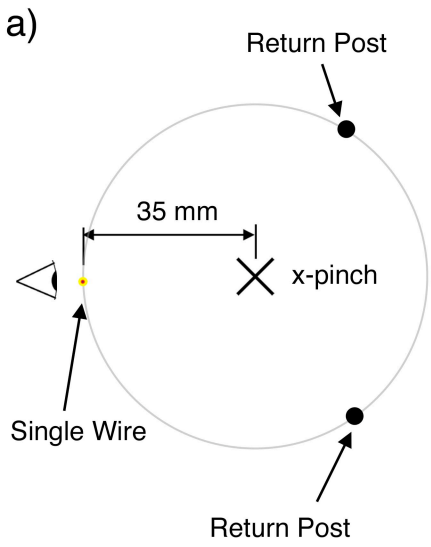

Figure 7.1: Top view of the single wire experiment showing the locations of the x-pinch, return current posts and single exploding wire sample. The eye indicates the line of sight of the spectrometer.

7.1.1 K-edge and the Wire Core

A small number of shots were taken using a single exploding Al wire plasma as the absorbing object, shown schematically in fig. 7.1, because the near cylindrical symmetry simplifies analysis. However, a single wire carrying $95kA$ inevitably pinches at at least one axial location and emits x-rays in the spectral region of interest, thus partially spoiling the absorption spectrum. Figure 7.2 shows the absorption spectrum along with the direct backlighting radiograph obtained on XP shot 5786. The radiograph clearly shows pinching in one region of the wire. The emission lines from the exploding Al wire are labeled at the top of the image. The emission lines are in focus in the spectral direction due to the focusing properties of the spherically bent crystal and, therefore, do not spoil the entire image. This leaves a good deal of the spectrum suitable for analysis.

Consider first the structure of the K-edge in these spectra, because it shows

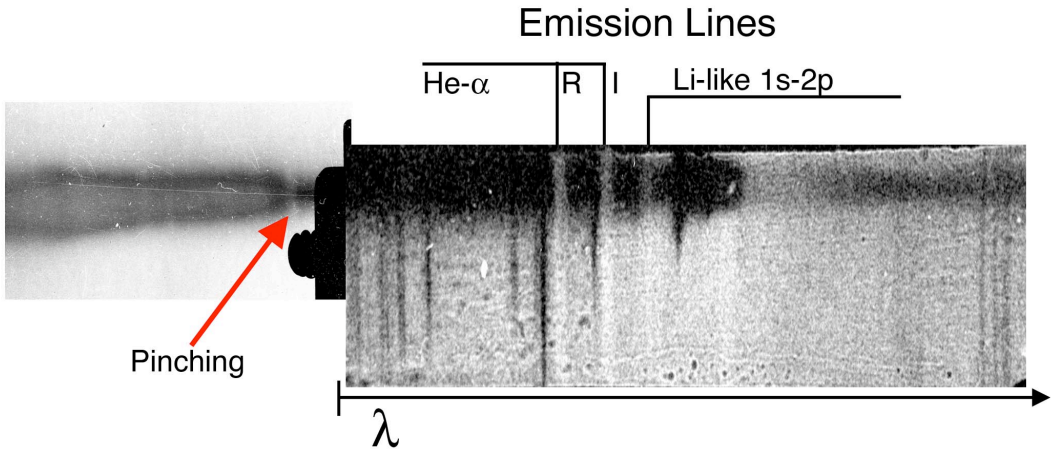

Figure 7.2: Experimental radiograph and absorption spectrum obtained on XP shot 5786. On the absorption spectrum the emission lines from the single exploding wire are labeled.

interesting features and it is unaffected by the self-emission of the wire. Shot numbers 5755, 5756, 5783, 5785 and 5786 were all single wire tests. 5783 and 5785 used 38μm wires made from Al alloy 1199, which is at least 99.99% pure Al. The others used 40μm wires made from Al alloy 5056 which is 95% Al and 5% Mg with trace amounts of Mn and Cr. There is a clear difference in the shape of the K-edge as a function of space between these two types of wire. The two single wire pure Al tests show a very similar radial profile of the K-edge. However the x-pinch x-ray burst was weak on shot 5783, resulting in poor image quality, and so we will focus our attention on shot 5785. Likewise, the three Al alloy 5056 tests showed similar profiles. We will focus our attention on shot 5786 because it produced the best image and was taken closest in time to the image from shot 5785.

The total current pulses for shots 5785 and 5786 are similar (fig. 7.3), albeit not the same, and the configurations were identical. Therefore, although we did not have a separate current monitor on the exploding wires, it is reasonable to

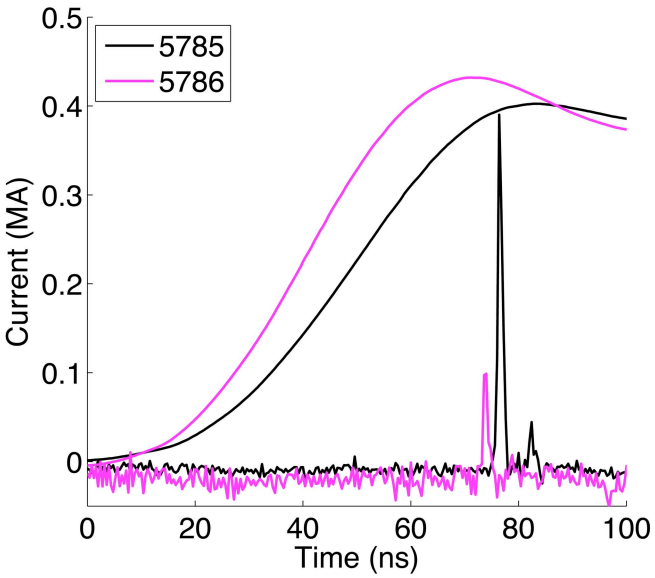

Figure 7.3: (Color) Load current and x-pinch radiation burst monitored using a Ti filtered PCD for XP shot numbers 5785 and 5786.

expect that they were subject to similar drive conditions. In addition, the x-ray burst timing is similar, as shown in fig. 7.3. Figure 7.4 shows the absorption spectra obtained on these two shots. There is a clear difference in the absorption in the vicinity of the K-edge (7.95Å).

In fig. 7.4(a), we see the K-edge is virtually non-existent. In the central $10 - 20\mu m$ of the wire the edge is very extended. Instead of sharply dropping to very low absorption at longer wavelengths, the transition occurs over about 0.06Å. Moving to larger radius the cold material absorption transitions over a radial range of $50 - 60\mu m$ to absorption by Mg-, Na- and Ne-like lines. The lineouts at different radial positions, shown in fig. 7.5(a), depict this behavior. The top lineout, taken along the wire axis, shows the smooth transition in absorption as compared to the cold Al absorption shown as the dashed grey line. $50\mu m$ away from the axis we see the presence of Mg-like lines indicating the tempera-

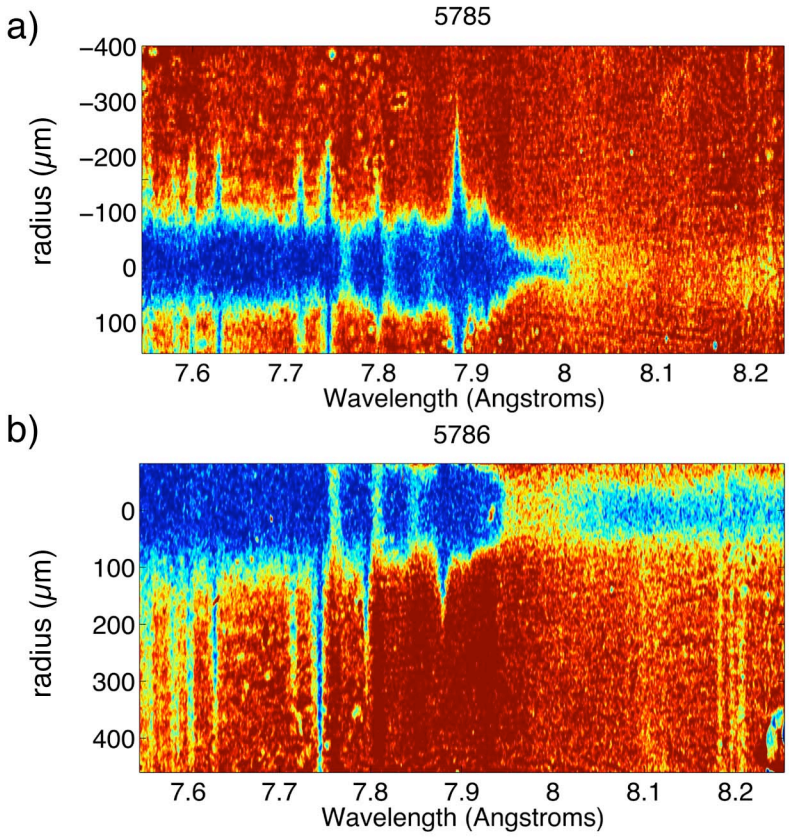

Figure 7.4: (a) Absorption spectrum obtained on XP shot# 5785. (b) Absorption spectrum obtained on XP shot# 5786.

ture is increasing. Further out Na- and Ne-like lines appear and the continuum absorption has disappeared, indicating the temperature is higher still. Previous studies of Al in the WDM regime and of shock-compressed Al targets have observed shifts and broadening of the K-edge[41, 42, 25]. In particular, broadening of the edge occurs at or near solid density as the temperature is increased from zero to a few eV[42]. This broadening could potentially explain the shallow slope observed here, although, the material in the exploding wire core is much less dense, $\sim$ 1/10 solid density or less, than the samples considered in that work. If this behavior were to hold true under these conditions, a temperature greater than a few eV would explain the smooth transition from strong to

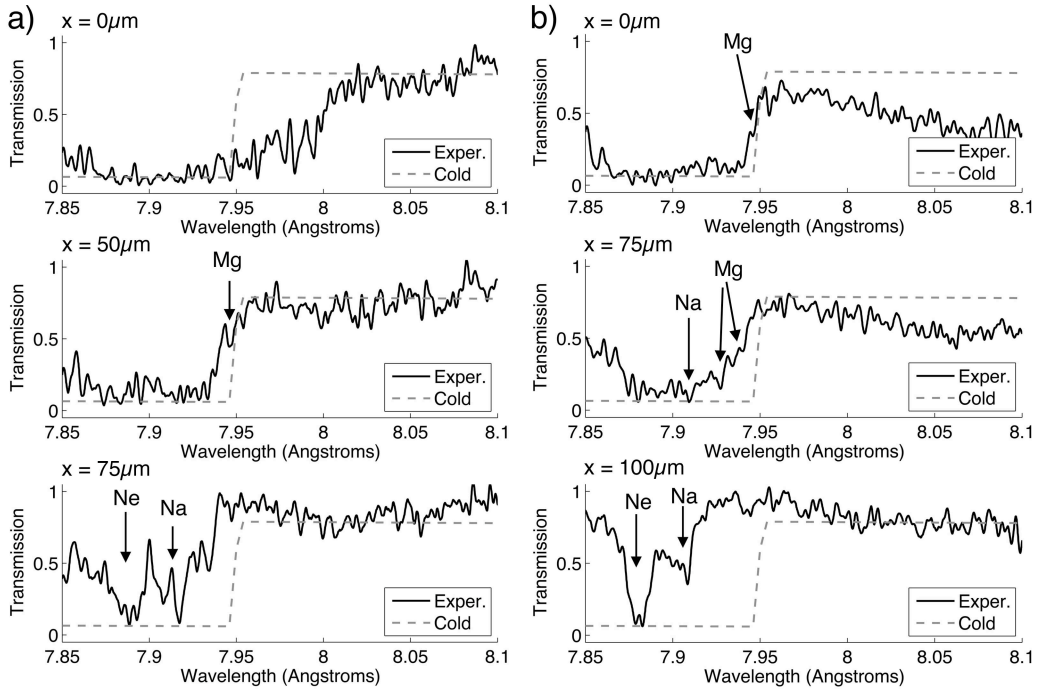

Figure 7.5: (a) Lineouts of the transmission spectrum obtained on XP shot 5785 at $x = 0\mu m$, $50\mu m$ and $100\mu m$. (b) Lineouts of the transmission spectrum obtained on XP shot 5786 at $x = 0\mu m$, $75\mu m$ and $100\mu m$. On each plot the transmission through a cold Al sample with aerial density $n_i l = 1.5\times10^{19} cm^{-2}$ is shown for comparison.

weak absorption in the central region of the wire in fig. 7.5(a).

In contrast, the image in fig. 7.4(b) shows a transition from strong absorption below 7.95Å to weak absorption above 7.95Å out to a radius of about $50\mu m$. This indicates that the material inside the wire core is relatively cold and dense out to a radius of about $50\mu m$. Comparing a lineout taken in this region to the absorption of cold Al, fig. 7.5(b), we see a very similar absorption profile. At the edge of the core there is a region of approximately $30\mu m$ over which the absorption transitions from the cold absorption to absorption by Na- and Ne-like line features, shown in the lower plots in fig. 7.5(b). We will see in the next two sections that this transition region bears the hallmarks of a steady increase in temperature and a rapid decline in density. This region may be where most of

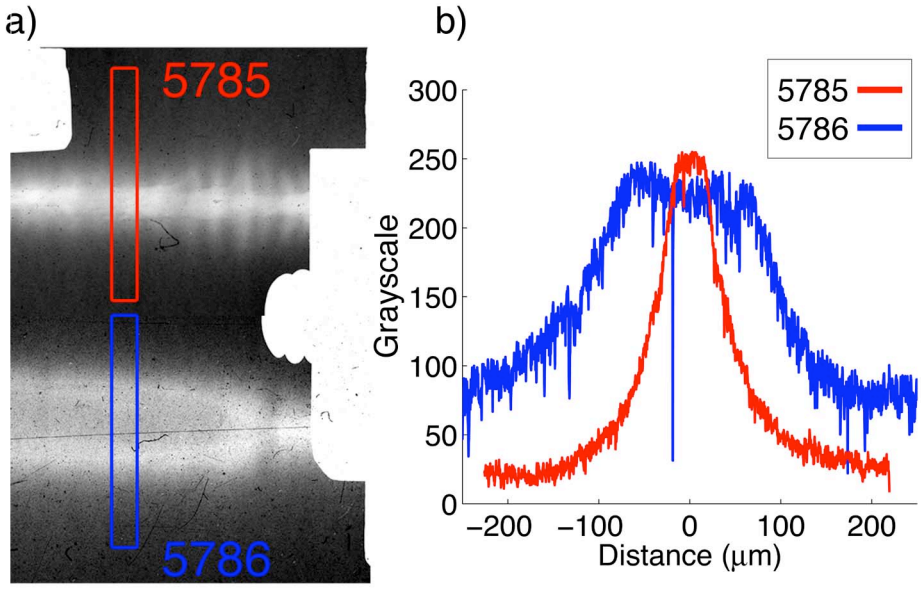

Figure 7.6: (a) Direct radiographs obtained on shots 5785 (top) and 5786 (bottom). (b) Lineouts taken across the wire cores in (a). The area of the image from which the lineouts are taken is designated by the red and blue boxes.

the transfer of energy from the coronal plasma, which is heated by current flow, to the wire core core, which carries very little current, takes place. The increased absorption above 8Å is currently not understood. It may be due to the presence of other materials in the alloy, although using the tabulated transmission data we were not able to reproduce this, or to an increase in density at the corresponding axial position caused by pinching of the wire.

The direct radiographs obtained on these two shots illustrate additional differences between the exploding Al alloy wires and pure Al wires. Figure 7.6 (a) shows the experimental radiographs from shots 5785 (top) and 5786 (bottom). The pure Al wire core has a dense column in the center with a diameter of about $40\mu m$ surrounded by a more tenuous and axially nonuniform plasma. The axial structure has a wavelength of about $20\mu m$. The lineout shown in fig. 7.6(b) of shot 5785 shows a flat density profile that is $\sim 100\mu m$ in diameter and a decreas-

ing density with increasing distance from the wire center. In contrast, the alloy wire core appears to have a diameter of about 200μm and a tube-like, or hollow structure. This structure has been seen in the past[53] and is repeatable in our experiments with Al alloy 5056. By contrast, the pure Al wire shots do not exhibit this behavior, with both single wire pure Al shots showing a wire core density profile that peaks on axis. As previously noted, the absorption spectra of these wires also all show the K-edge radial profile similar to that shown in fig. 7.4(a).

All of the shots, including those with more than one wire, show a correlation between the radial profile of the K-edge in the absorption spectra and the structure of the exploding wire. Figure 7.7 shows a sampling of absorption spectra along with the corresponding radiographs of experiments using two Al 5056 wires spaced 1mm apart. All of the spectra that showed the sharp edge also showed the tube-like wire core, as seen in fig. 7.7(a). Though we can see only half of the wire core in the absorption spectrum, a clear edge is visible.

There were however Al 5056 experiments that showed the same extended K-edge as the pure Al. Figure 7.7(b) and (c) shows this behavior in the two-wire Al 5056 arrays. In fig. 7.7(b) we see a very extended K-edge, though it is asymmetric in the spatial direction. There is a dense band visible that fades smoothly into the background towards the top of the image (i.e. towards the second wire). Towards the bottom of the image there is a sharper transition to lower density and a fade to the background exposure level. This asymmetry in the density profile is directly related to the presence of the second wire and will be discussed more in sec. 7.1.3.

Figure 7.7(c) shows a very late stage in the evolution of the exploding wires, which was obtained by using two 17μm Al alloy 5056 wires with the same mass

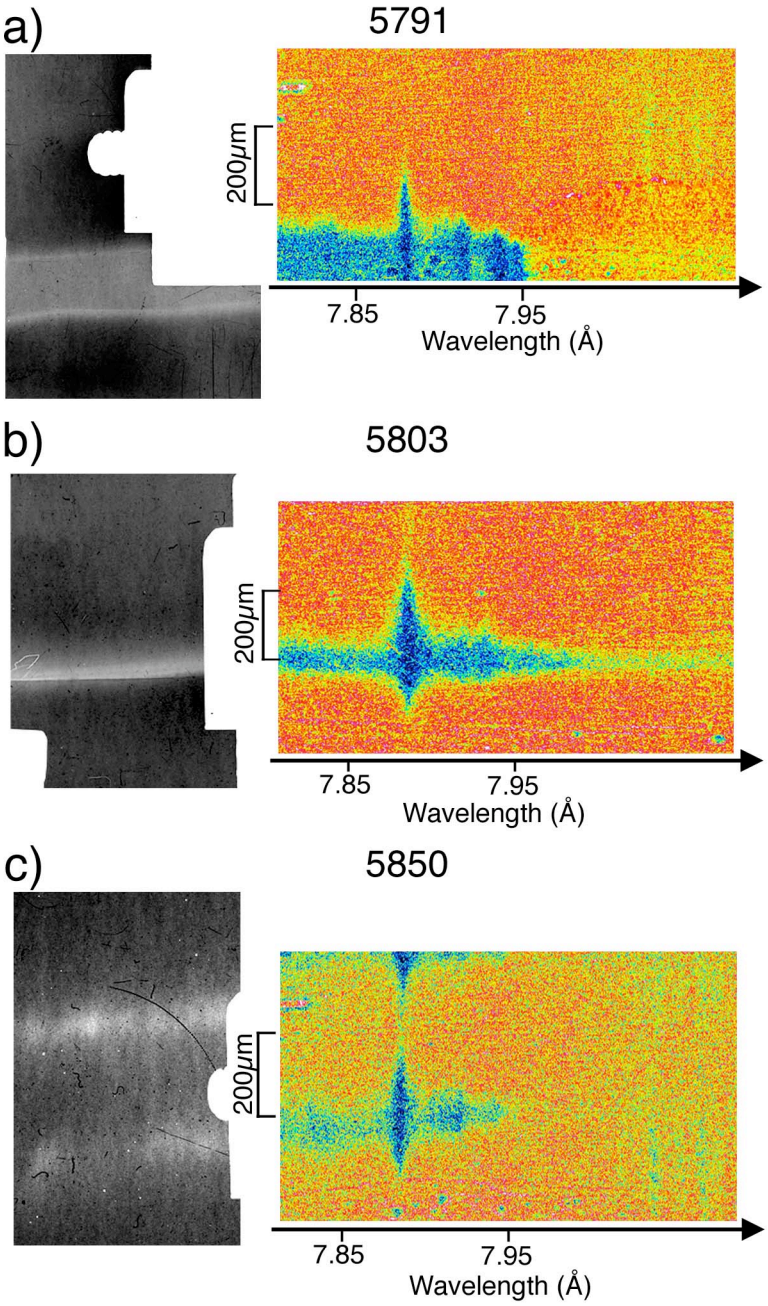

Figure 7.7: Comparison of the shape of the K-edge and the structure of the wire core on three shots using two Al 5056 wires spaced 1*mm* apart. The wires in (a) and (b) were 25μm, while the wires in (c) were 17μm.

X-pinch as used for 5803. Since there was less initial mass than in the shots shown in the other images, it ablated faster, allowing us to see this late stage. The radiograph shows very little mass left at the original wire position, as does the absorption spectrum. The K-edge is barely evident in the absorption spectrum since the bulk of the wire mass has ablated off of the wire core and what remains is diffuse and axially non-uniform according to the radiograph.

From these images we hypothesize that the extended K-edge is a result of conditions reached as more and more wire material is ablated from the wire core into the coronal plasma and the temperature increases. As the wire core loses mass the state of the material changes, as evidenced by both the radiographs and the spectra. The residual core becomes hotter and less dense. Eventually there is very little material remaining and the wire core develops gaps, resulting in an absorption spectrum like that shown in fig. 7.7(c). It appears that the pure Al wire initiates differently than the alloy wire, leading to the aforementioned "late" stage behavior occurring earlier in time.

From this point forward we will be discussing only wire pairs made using Al alloy 5056 wires, which will be referred to simply as Al, although they have 5% Mg.

7.1.2 $1s - 2p$ Transitions

To date, the $1s - 2p$ absorption lines are the most commonly used portion of the Al absorption spectrum for laser plasma diagnostics. One reason for this is that even with moderate spectral resolution the satellite groups can be distinguished from one another, making determination of the temperature relatively

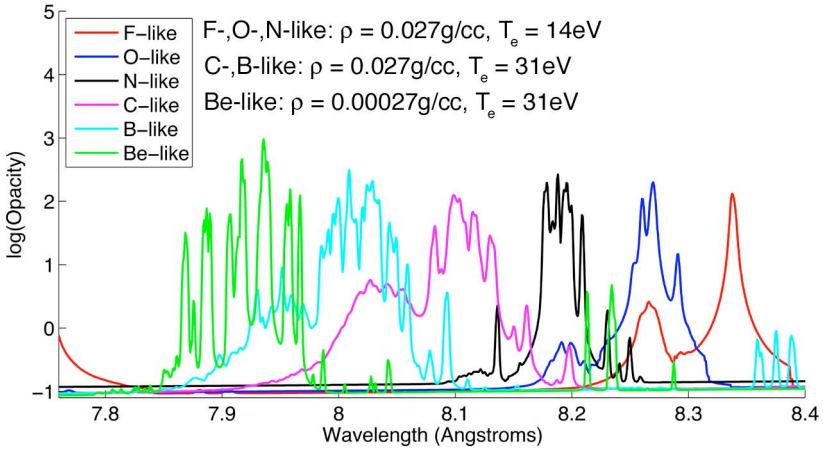

Figure 7.8: (Color) Opacity of $1s-2p$ satellite lines of Al ionization stages F-like through Be-like calculated using SCRAM. F-, O-, and N-like opacities are calculated at $\rho = 0.027g/cc$ and $T_e = 14eV$. C- and B-like opacities are calculated at $\rho = 0.027g/cc$ and $T_e = 31eV$. The Be-like opacity is calculated at $\rho = 0.00027g/cc$ and $T_e = 31eV$. Opacities are artificially shifted to have the same base line for clarity.

simple. Additionally, the $1s-2p$ transitions are simpler to model than higher n transitions. $1s-2p$ satellites of the He-α resonance exist up to F-like Al allowing temperatures below $10eV$ to be measured. Because Ne-like Al is a closed shell ion (i.e.l the $2p$ shell is filled), a ground state $1s$ electron cannot transition to the $2p$ shell. Therefore Ne-like satellites generally exist only for $1s-3p$ or higher transitions.

Figure 7.8 shows opacities of the satellite groups of each of the Al ions from Be-like through F-like calculated in non-LTE by SCRAM at different densities and temperatures. In this way we can see exactly what features result from which ions. We see immediately that the F-like spectrum is the simplest, consisting of only one feature that is made up of two lines, separated by only $2m$Å according to the calculations of Ref. [11]. These lines are blended together by various broadening effects that are included in the model. As the Al ion loses

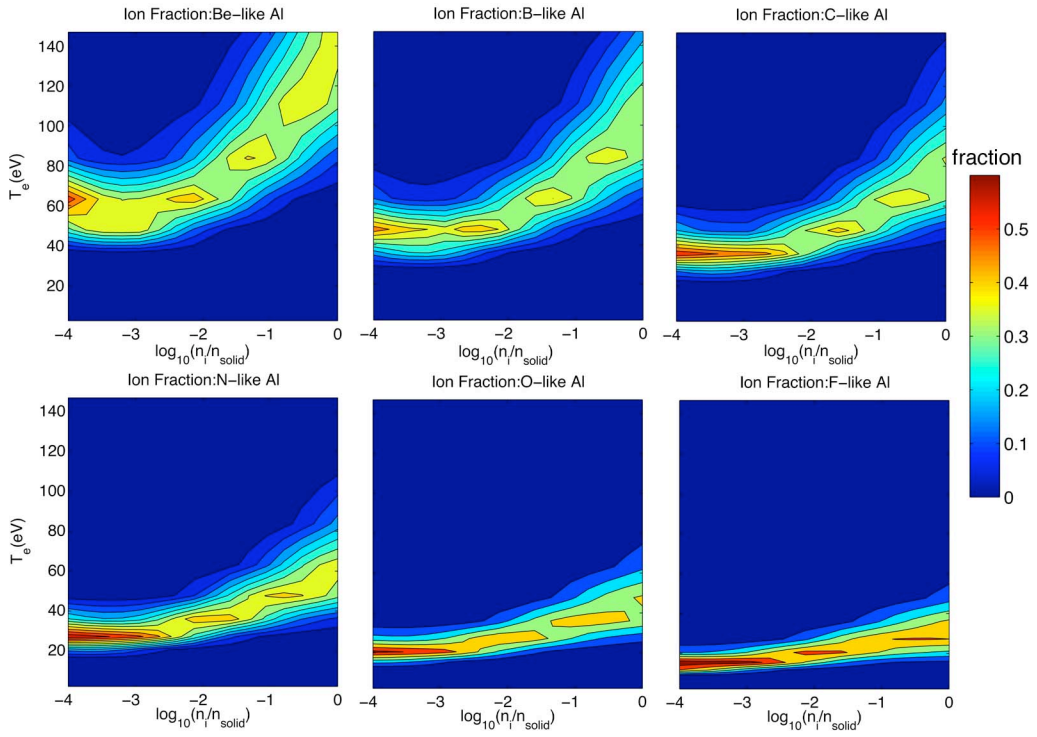

Figure 7.9: Contour plots of the population fraction of Be-like through F-like Al as a function of ion density and temperature.

more electrons the spectrum becomes more complex. The reason for this is simply that as electrons are removed there are more vacancies available in the $2p$ shell which increases the possible number of transitions to a $2p$ level that a $1s$ electron can undergo as a result of absorption of a photon.

The dominant opacity features of each ionization state are well separated from each other. However there are features that can be seen on the short wavelength side of each satellite group that overlap with the next ionization stage. These features are due to excited spectator electron effects and are typically at least an order of magnitude smaller than the dominant features in that group.

In order to use the ionic populations to help determine plasma conditions using absorption spectra, we show the calculated non-LTE population fractions for Be-like through F-like Al in fig. 7.9 as a function of density and temperature.

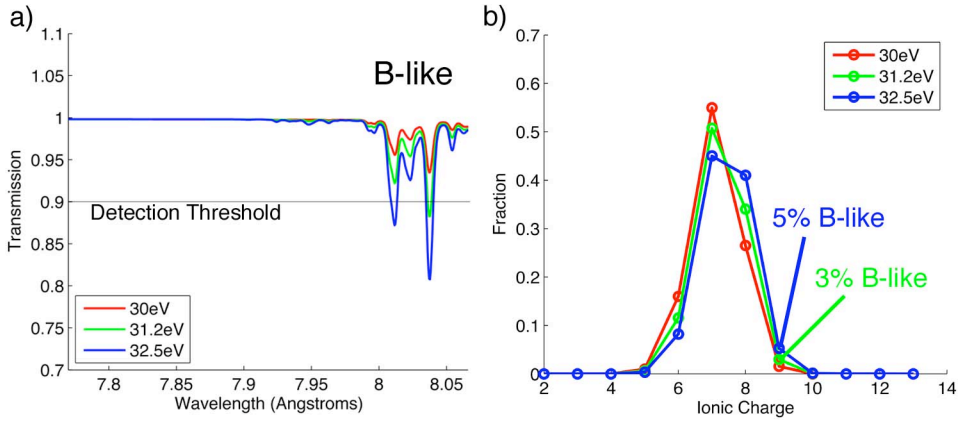

Figure 7.10: (Color)(a) Transmission of the B-like $1s - 2p$ satellite lines at $30eV$, $31.2eV$ and $32.5eV$. The 10% absorption detection threshold is marked on the plot. (b) The ion distribution at the same three temperatures. The percentage of B-like Al is shown explicitly at $31.2eV$ and $32.5eV$.

These plots show in what region of parameter space the different ions exist. By noting which ions are present in a particular spectrum, we can place upper or lower bounds on the temperature by cross referencing with the contour plots. With our spatially resolved data, one can see the variation in charge state, and therefore possible temperature range, with little or no analysis. Although this method is only semiquantitative, it offers very useful, and immediate insight into the properties of the plasma as a function of position.

First, we must estimate at what fraction a given ion must be present to result in a detectable amount of absorption on the film. We claim that due to the noise in the recorded spectra, absorption less than 10% will not be reliably detectable. Assuming an aerial density of $2 \times 10^{17} cm^{-2}$, which is consistent with the aerial density of the innermost plasma region determined by the GA in sec. 7.2, we can use PrismSPECT to estimate this population fraction for B-like Al, for example. In fig. 7.10(a) we see that the absorption from B-like Al crosses the detection threshold when the electron temperature is between $31eV$ and $33eV$.

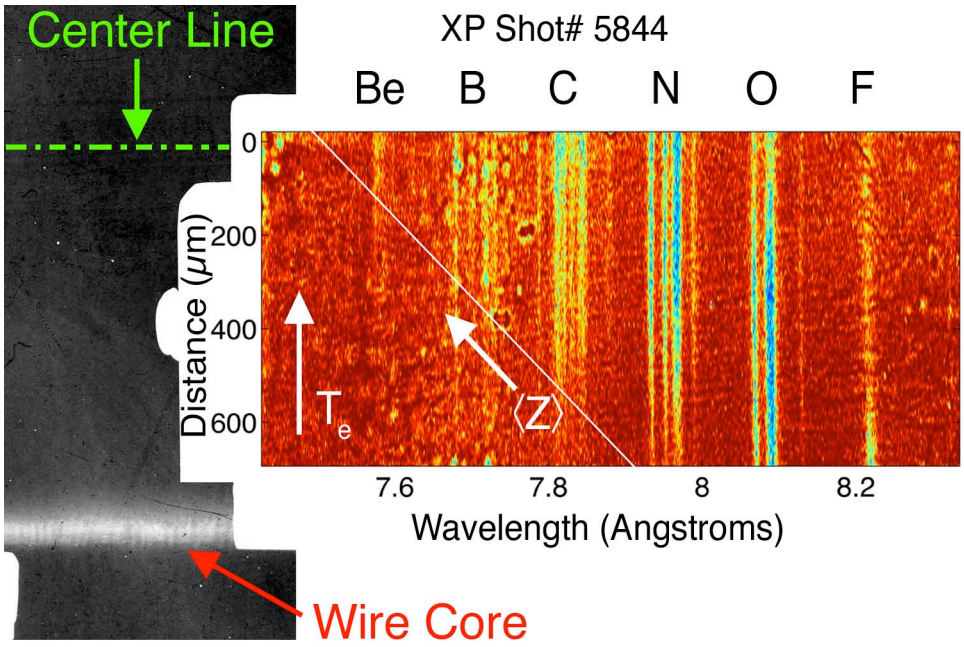

Figure 7.11: (Color) Experimental transmission spectrum obtained on XP shot 5844 is shown along with the direct radiograph. The two images are aligned in the vertical direction (spatial for the spectrum) and their spatial scales are the same. The location of the one visible wire core and the center line are shown on the radiograph. The line crossing the image at an angle marks the approximate location of the appearance of new ionization states as a function of position. Average ionization increases going up and to the left. This indicates that the temperature increases going up the image, as indicated by the arrow on the left.

In fact, at $32.5eV$, two of the peaks are above the threshold which increases the likelihood that the signal will be seen above the noise. The ion distribution in fig. 7.10(b) shows that this corresponds to an abundance of 5% B-like Al. From this we can estimate that detection of a given ionization stage is likely when it makes up greater than 5% of the population.

In fig. 7.11, for example, we show the $1s - 2p$ transmission spectrum from the plasma between two Al wires spaced $2mm$ apart. One of the wires is just out of the field of view at the bottom of the image and the center line between

the two wires is approximately at the top of the image. We expect the plasma temperature to be lowest near the wire core which is where we see the F-like ions absorbing the strongest. As we move up the image, i.e. away from the wire, absorption of the F-like line decreases and the O-like absorption increases. In this region of the image N-,O- and F-like Al are all present, but there is no absorption from C-like Al. Therefore, the contour plots in fig. 7.9 suggest that the temperature is about $20eV$. However we do not learn anything about the plasma density with only this information.

Approximately $100\mu m$ from the bottom of the image C-like Al begins to absorb significantly, indicating the average ionization of the plasma, and therefore the temperature, is increasing. Because there is no absorption from B-like Al we can say that the temperature is no more than $30eV$. Closer to the center line between the two wires B-like and finally Be-like Al begin to absorb. The existence of Be-like Al suggests a temperature of at least $35eV$. The reason the lines from lower charge states appear to extend all the way to the middle despite the higher temperature is that they actually come from a cooler plasma region away from $y = 0$ as will be discussed in detail in sec. 7.2.

For comparison we can conduct the same analysis on the absorption spectrum from XP shot 5790, shown in fig. 7.12. This shot was exactly the same as 5844 except the wires were separated by $1mm$. In this image we can see the center region between the two wires while the wire cores are just off the top and bottom of the image. The spectrometer alignment was such that the O- and F-like absorption features were not recorded. The spatial profiles of the Li-through C-like spectral features clearly show that the temperature increases towards the center of the image. Following the same process as above we can say that the peak temperature in the $\sim 100\mu m$ region on the center line is about $45eV$.

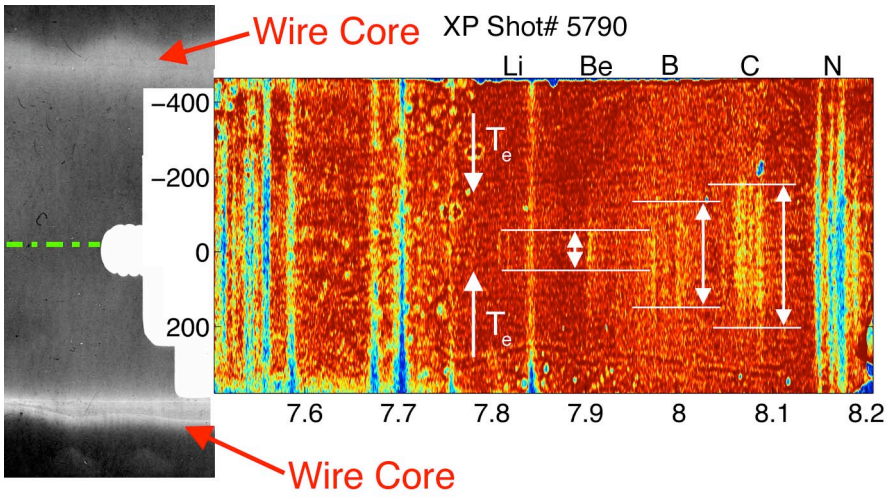

Figure 7.12: (Color) Experimental transmission spectrum obtained on XP shot 5790 along with the direct radiograph. The location of the wire cores are noted. The center line between the two wires is noted on the radiograph by the dashed green line. The arrows indicate the spatial extent over which each of the ionization states exists. The ionization stages are labeled at the top of the image.

Only $200\mu m$ from the center line, the temperature drops to no more than $20eV$.

We have shown that the spectra indicate the temperature is highest near the centerline between the two wires and lowest near the wire core. This indicates that the two wire system behaves similarly to a cylindrical wire array z-pinch. in that configuration, plasma flows toward the axis in the form of ablation streams from each wire, and collects on axis where the radially inward kinetic energy imparted via the $\mathbf{J} \times \mathbf{B}$ force thermalizes, contributing to a higher temperature on axis than in the streams[8, 13]. However, there is no clear evidence found through the above semi-quantitative analysis that the density increases on the axis, as is known to occur in cylindrical wire arrays[7, 38]. The spectra transition smoothly from low temperature to high temperature indicating there are no shocks or other discontinuities present.

7.1.3 $1s - 3p$ Transitions

To our knowledge there is no detailed experimental data on the $1s - 3p$ satellite lines of Al. The only line that has been reported and used diagnostically in the past is the Ne-like $1s - 3p$ line at 7.886Å[75, 1, 41]. The $1s - 3p$ transitions occur when a $1s$ electron absorbs a photon and transitions to a vacancy in the $3p$ shell. Since all of the ions we are considering have no electrons in the $3p$ shell when in the ground state there will be more transitions available to the $1s$ electrons than in the case of the $1s - 2p$ satellites. Therefore we expect these spectra to be more complicated. In addition there could now be features due to Ne-, Na- and Mg-like Al. The possibility of these features allows the inference of plasma temperature from absorption spectra to be extended to lower temperatures than if only the $1s - 2p$ lines are used. The Ne-like line at about 7.886Å noted above is present in our spectra. This line has been shown to be sensitive to stark broadening and has been used in the past as a density diagnostic[75, 1]. The opacities of the Ne-, F-, O- and N-like $1s - 3p$ satellite groups are shown in fig. 7.13 calculated using SCRAM at $\rho = 0.027 g/cc$ and $T_e = 14 eV$.

The calculations show a more complicated structure than the $1s - 2p$ satellites, as expected. However the same basic trends apply. The spectra are more complicated as ionization increases, with the Ne-like being the simplest. Each satellite group has a spectral structure similar to the $1s - 2p$ satellites. There are prominent features at long wavelengths and smaller features on the short wavelength side of each group. However, these shorter wavelength features are stronger relative to the most prominent satellite feature than in the case of the $1s - 2p$ satellites. The prominent features remain relatively well separated from each other, but the increased magnitude of the shorter wavelength features causes the spectra to appear overlapped. As one looks to even shorter

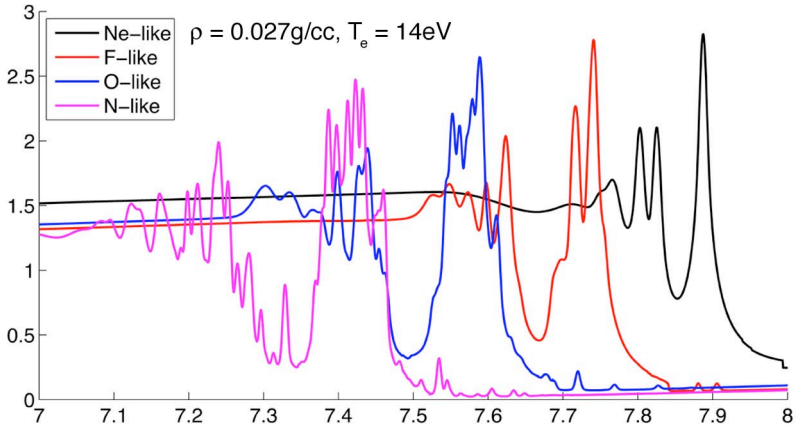

Figure 7.13: (Color) Opacity of the $1s - 3p$ satellite lines of Al ionization stages Ne-like through N-like calculated using SCRAM. Opacities are calculated at $\rho = 0.027 g/cc$ and $T_e = 14 eV$ and artificially shifted to have the same base line for clarity.

wavelengths, the line dominated opacity features turn into continuous absorption. This is the modification of absorption above the K-edge in cold, neutral Al that occurs when the material heats.

Figure 7.14 shows the absorption spectrum obtained on XP shot 5804 which was aligned specifically to see the $1s - 3p$ transitions. In this shot the absorbing plasma was produced by a pair of $25 \mu m$ Al wires spaced $1 mm$ apart. Satellite lines from N-like through Ne-like are prominent. In addition, features due to Na- and Mg-like Al are present very near the wire core where the density is highest and, as was shown in the previous section, the temperature is the lowest. Overall, the spatial profiles of these transitions are consistent with the $1s-2p$ transitions. The Ne-like lines absorb less and the O-like and N-like groups begin to absorb more as we move away form the wire core, indicating the temperature is increasing. These transitions are, thus, also valuable as a temperature diagnostic, but the spectra are more complicated, making the modeling needed to obtain quantitative temperature determination more challenging.

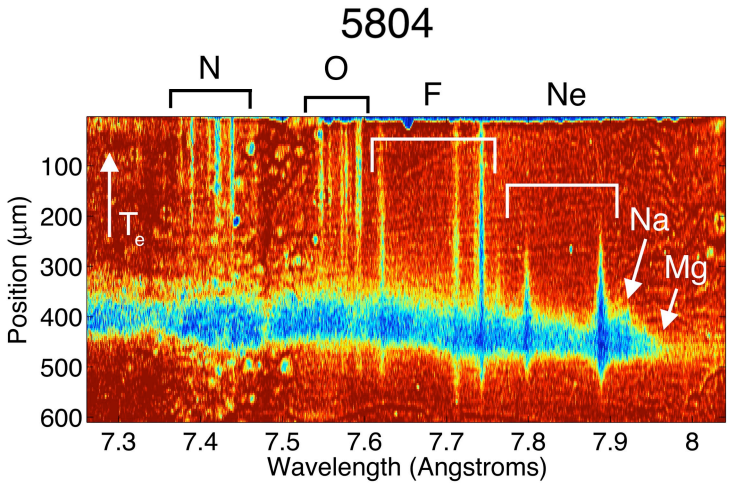

Figure 7.14: (Color) Experimental transmission spectrum obtained on XP shot 5804 showing the $1s-3p$ transitions. The ionization states are labeled at the top of the image. Each portion of the spectrum occupied by each state is indicated by the horizontal bars. The Na- and Mg-like features are labeled directly at the right of the image. The upward pointing arrow at the left of the image indicates that temperature is increasing moving toward the top of the image.

The transmission spectra, calculated using SCRAM, in the vicinity of the Ne-like line at 7.886Å at a temperature of $T_e = 4.6eV$ and densities ranging from $0.27g/cc$ to $0.00854g/cc$ is shown in fig. 7.15(a). A density dependence to the structure is quite evident. The path length has been changed for each density to keep the aerial density constant.

The blue line, corresponding to 1/10 of solid density, shows a feature, due primarily to absorption by Na-like Al ions, that appears to be similar to the broadened K-edge observed in the experiment. Additional broadening on the long wavelength side is due to absorption by Mg-like Al. The cutoff of this feature lies at about 7.95Å which is the location of the cold Al K-edge. On the short wavelength side there is a broad hump due to Ne-like Al. As the density is decreased all of these features shift to shorter wavelength and become sharper.

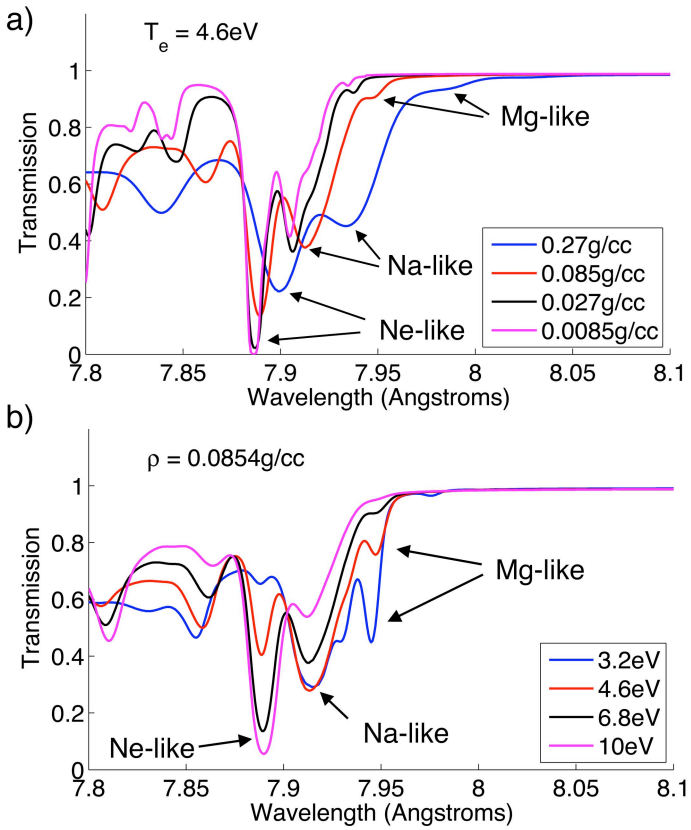

Figure 7.15: (Color)(a) Calculations of the transmission through an Al plasma at $4.6eV$ and varying density. The path length has been changed to keep the aerial density constant at $0.95gcm^{-2}$. The prominent Ne-like, Na-like and Mg-like $1s-3p$ features are also noted. (b) Transmission at $0.085g/cc$ and varying temperature. The same features are noted.

The shift is due to the plasma polarization shift and the change in width is due primarily to the Stark effect.

Figure 7.15(b) shows the temperature dependence of these same features at $\rho = 0.085g/cc$. We can see that, similar to the temperature dependence of the $1s-2p$ transitions, it is mostly the strength of absorption that changes because the population fractions change. At $3eV$ there is a prominent Mg-like absorption peak located at 7.95Å. As the temperature increases the Mg-like absorption de-

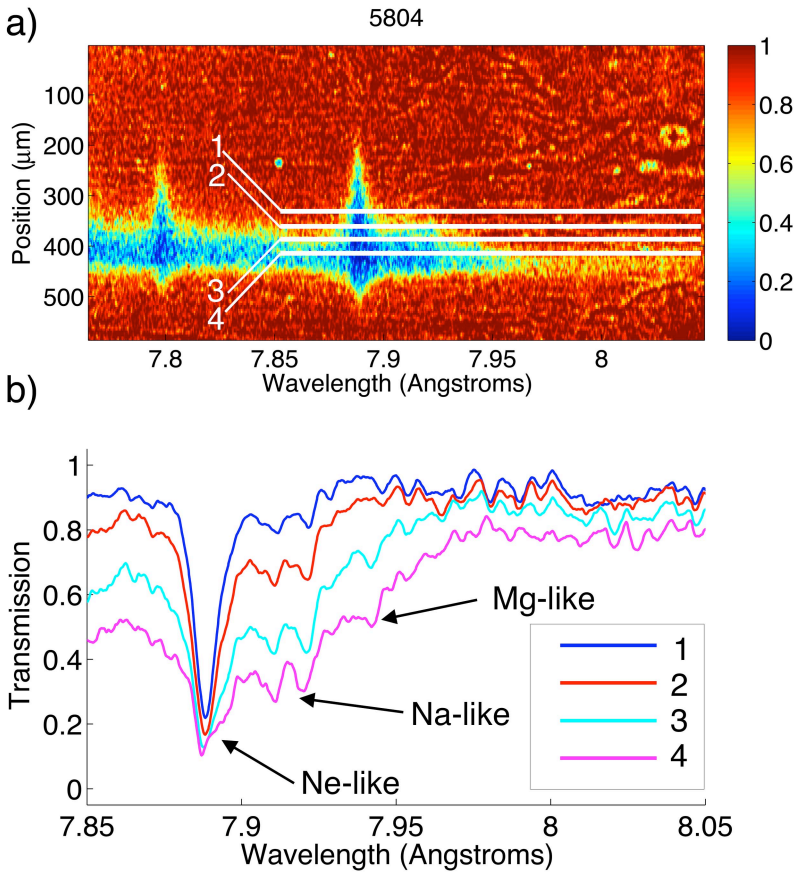

Figure 7.16: (Color) (a) Expanded view of the region surrounding K-edge in the transmission spectrum obtained on XP shot# 5804. (b) Lineouts of the transmission taken at the locations noted by the white lines in (a). The Mg-,Na- and Ne-like features are noted.

creases and the Ne-like absorption increases. At $7eV$ the Mg-like feature nearly disappears and the Na-like feature begins to shrink. Taken together, the temperature and density dependence of these lines provide valuable qualitative and quantitative information about the plasma near the wire core, where the density is high and the temperature is low.

Figure 7.16(a) shows an expanded portion of fig. 7.14 from 7.75Å to 8.1Å. The Ne-like line at 7.886Å is narrow furthest from the wire core and becomes

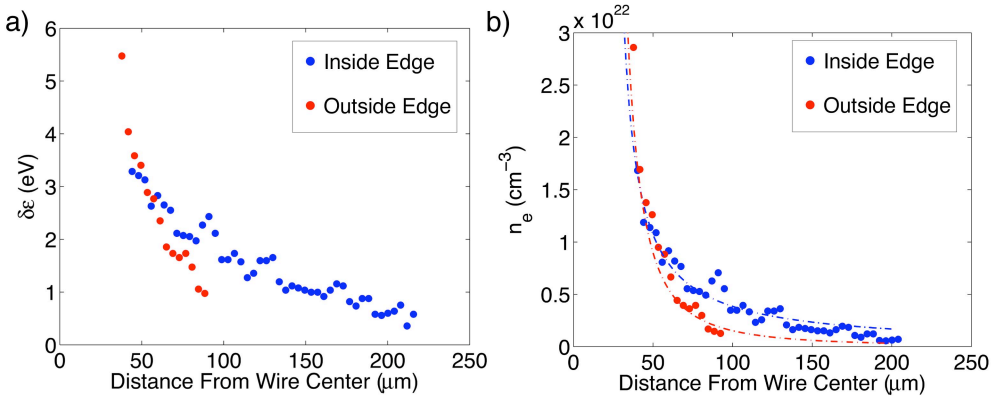

Figure 7.17: (Color) (a) Full Width at Half Maximum (FWHM) of the Ne-like $1s - 3p$ line measured in eV on the inside (blue) and outside (red) edges of the wire in the absorption spectrum from XP shot 5804. (b) Order of magnitude estimate of the electron density assuming the entire line width measured in (a) is due to stark broadening. The curves in (b) suggest that the density falls as $\sim 1/r$ on the inside and $\sim 1/r^2$ on the outside.

wider closer to the wire core, where it eventually saturates near the line center. This is shown quantitatively in the lineouts in fig. 7.16(b). This is a clear indication that the density is decreasing as we move further from the wire core. Also evident in the lineouts is that as we approach the wire core center, the Na-like features, and eventually Mg-like features, become more prominent. This is an indication that the temperature is falling as the density increases. In fact, the shape of the Mg-like feature in lineouts 3 and 4 is very similar to those in the spectra shown in fig. 7.15(b) for temperatures $T_e = 3eV$ and $4.6eV$. This implies that the temperature in the wire core is less than $5eV$ and the density is $\sim 1/30$ solid density at the time this spectrum was obtained.

The obvious asymmetry in the spatial profile of the Ne-like line, i.e. the line extends much farther towards the top of the image than towards the bottom, is due to the asymmetry of the configuration. The top of the image is in the direction of the center line between the two wires, which we will call the inside of

the two wire array, while the bottom of the image is away from the other wire, which we will call the outside. In fig. 7.17(a) we have plotted the FWHM of this line as function of distance from the center of the wire core. On the outside of the wire the width of the line decreases approximately three times faster than on the inside. If we assume Stark is the dominant broadening mechanism the density is falling much more rapidly outside the wire than inside. On the outside of the array the magnetic field acts to push plasma towards the center line of the wire pair, thereby causing the density to drop off much more quickly outside the wire. This behavior has been seen before, notably by Douglass et al. who found in W wire arrays that the coronal plasma density falls off roughly as $1/r^2$ outside the array and $1/r$ in the direction of the injected plasma streams[17]. We have plotted such curves in fig. 7.17 (b) for comparison with the data momentarily.

Using a simple Stark broadening model developed for K-shell transitions with even Δn[56] we can generate an order of magnitude estimate of the electron density if we assume that the only broadening mechanism is Stark. The equation for the FWHM of the line in energy units is

$$\delta\epsilon_s = 4.3\frac{n^2}{Z_{nuc}}\left(\frac{n_e}{10^{22}}\right)^{0.58} \tag{7.1}$$

where n is the principal quantum number of the upper level, i.e. $n = 3$, Z_{nuc} is the nuclear charge and n_e is the electron density in cm^{-3}.

Figure 7.17(b) shows the electron density estimated using this formula. It is important to note that this is merely an upper estimate used to understand the trend in density versus distance form the wire core. Other processes contribute to broadening and a detailed calculation is required to obtain an accurate density determination.

More work is needed, both experimentally and theoretically, to make the

broadening of the Ne-like $1s-3p$ line a credible quantitative density diagnostic. For instance, we have implicitly assumed that the absorbing region is uniform in density and temperature. In reality the previously mentioned plasma polarization shift as well as the increased presence of Na-like features at lower temperatures can contribute to the perceived broadening. In addition, at lower densities further away from the wire core Stark may not be a dominant broadening mechanism. The higher temperatures in this region can increase the magnitude of thermal broadening. We can easily estimate this effect using the formula

$$\Delta\epsilon_{th} = \frac{\Delta E}{20,000}\sqrt{\frac{T_{ion}}{Z_{nuc}}}$$

where ΔE is the transition energy, Z_{nuc} is the nuclear charge and T_{ion} is the ion temperature. All temperatures and energies are expressed in eV. Calculating this width for the same Ne-like Al line, and assuming $T_e = T_{ion}$, we can see that for temperatures below $\sim 25eV$ it is small, $\leq 0.1eV$, compared to the stark broadening estimated above . Therefore we can safely ignore thermal broadening for temperatures where Ne-like Al is prominent. Finally, if the optical depth of the line is large then saturation of the absorption can lead to artificial broadening that is not related to density. Nevertheless, we believe that the dependence of density on position in the vicinity of the wire core found from this semi-quantitative analysis is giving the correct trend.

7.2 Quantitative Analysis

Using the genetic algorithm presented in sec. 6.2.2 we are able to infer more accurate spatially resolved density and temperature from properly calibrated

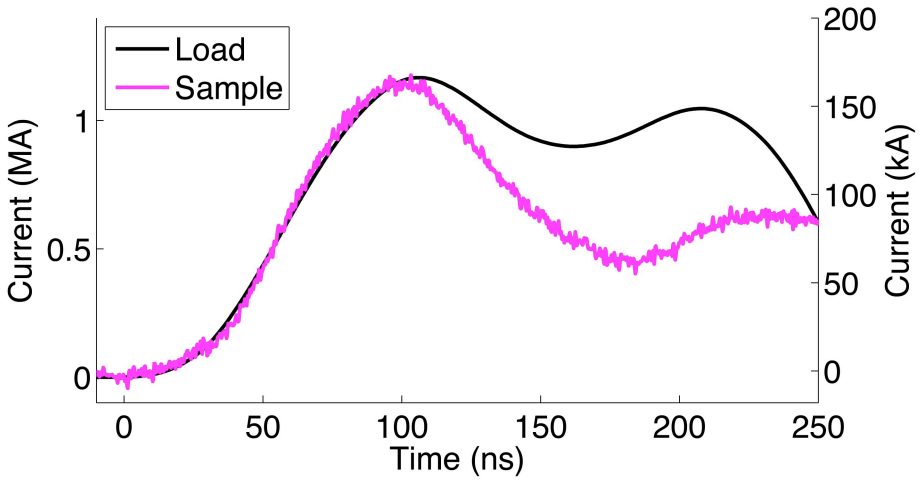

Figure 7.18: (Color) Main load current and current through the exploding wire pair (which was the "load" in place of one return current post) on COBRA shot 2036.

absorption spectra. This analysis enables us to infer physically reasonable, if not unique, spatially resolved density and temperature from absorption spectra obtained from two-wire configurations on COBRA. In the remainder of this chapter we will show the data along with the results of the analysis of two shots from the series of experiments performed on COBRA that included the calibration step wedge described in sec. 6.1. For these shots we are able to carry out rigorous quantitative analysis, including estimates of the measurement error. We have also used the GA to analyze one XP shot, for which we have only an estimated calibration as previously discussed, and this is discussed at the end of the chapter. The purpose is to see if the resulting analysis yields plasma conditions that are in agreement with the semi-quantitative analysis presented in sec. 7.1.2

In all of the COBRA shots the absorption sample was the plasma produced from a pair of $25\mu m$ Al 5056 wires spaced $1mm$ apart, the "object plasma" in the remainder of this section. On two of the shots a Rogowski coil was placed

around the sample to measure the current through it. Figure 7.18 shows the entire load current as well as the current through the two wires. The peak current through the absorption sample was about $150kA$ with a rise time of about $100ns$. The Rogowski coil blocked the line of sight of the spectrometer so we were unable to measure the current on shots when absorption spectra were obtained. However, we can see that up to peak current the load current and sample current track very well. This strongly suggests that there were no time varying impedance effects that would cause the division of current between the sample and the return posts to change in the shots without a Rogowski coil. Therefore we believe it is appropriate to estimate that the sample carries a fixed fraction of the load current up until the time of peak current, by which time the absorption spectra were obtained in the following tests.

7.2.1 **COBRA Shot** 2034

Figure 7.19(a) shows the load current and x-ray signals from this shot. The x-pinch x-ray burst occurred at $112ns$ after the start of current rise. The first peak in the signal from the $12.5\mu m$ Ti filtered diode is spurious. The second peak, where the diode saturates is when the x-pinch fired. There was a problem with the $25\mu m$ Be filtered PCD on this shot, which is why it is not shown. We can see from the open pinhole camera images in fig. 7.20 that there was only one hot spot formed and therefore only one continuum x-ray burst. The detector for the open pinhole camera consists of two layers of film. The first layer is Kodak DR-50, and the second is BioMax-MS. The first layer acts as a spectral filter allowing only the harder photons to expose the rear film. The front film shows a large

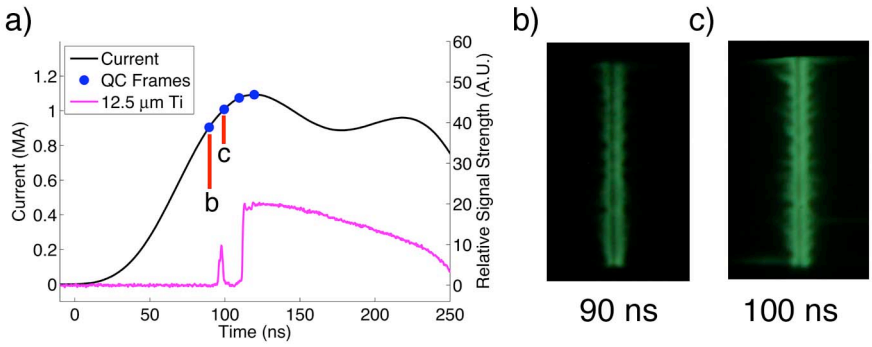

Figure 7.19: (Color) Main load current and 12.5μm Ti filtered Si diode signals from COBRA shot 2034. The blue circles indicate the times at which the MCP framing camera was triggered. (b) MCP framing camera image of the object plasma taken at 90ns, (labeled 'b' in (a)) after the start of current rise. (c) MCP framing camera image of the object plasma taken at 100ns (labeled 'c' in (a)).

emission region, while the rear film shows only a single small region. If there was more than one hot spot formed we would see multiple such images on the rear film. The blue dots in fig. 7.19(a) indicate the times at which XUV framing camera images were obtained. Because the two-wire plasma is not in the center of the chamber the XUV framing camera was able to image it in only two of the frames, labeled 'b' and 'c' in fig. 7.19(a). Both show the parallel wires separated by a dim region in the center.

Figure 7.21 shows the experimental transmission spectrum obtained on COBRA shot 2034. The backlighter and absorption spectra were calibrated as described in sec. 6.1 resulting in an error in the transmission measurements in the following discussion of about ±17%. The wire cores are not visible in this spectrum. However we are able to see all of the plasma from just inside each of the wire cores to the center line between the wires. The O-, N- and C-like $1s - 2p$ satellites are visible as well as the Ne- and F-like $1s - 3p$ satellites.

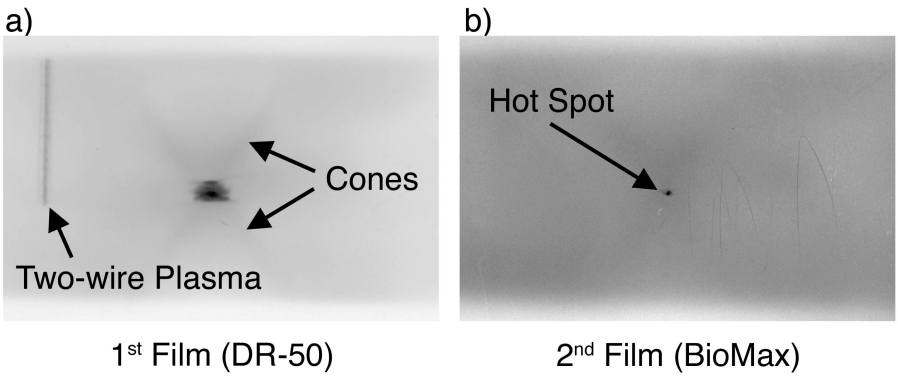

Figure 7.20: (Color) Unfiltered (open) pinhole camera images of the x-pinch and two wire sample plasma. (a) Front film. On the left, the two-wire object plasma is visible. The dark spot in the center of the image is emission from the hot spot and surrounding plasma. Emission and/or scattered photon from the cones that make up the electrodes of the hybrid x-pinch are faintly visible. (b) Second film. One small emission region indicating only one hot spot occurred on this shot.

The spectrum shows increasing ionization towards the center line between the wires, as we have seen before. The O-like $1s-2p$ and the F-like $1s-3p$ satellite absorption lines are approximately constant in intensity across the entire image. All of the variation with position in the spectrum occurs in the Ne-like $1s-3p$ and the N- and C-like $1s-2p$ satellites. As we approach the edges of the image, near the wire cores, the Ne-like $1s-3p$ line absorbs more strongly and broadens, indicating a density increase similar to that observed in sec. 7.1.3. Towards the center line between the two wires, the absorption of the N- and C-like satellites increases. There is no clear evidence of the presence of B-like Al above the noise in the image.

Figure 7.22 shows, below the experimental spectrum, the best fit transmission spectrum obtained using three plasma regions by the GA. Qualitatively, the trends in the image are captured very well by the GA. The F- and O-like lines are nearly constant across the entire image with the exception of the F-like lines

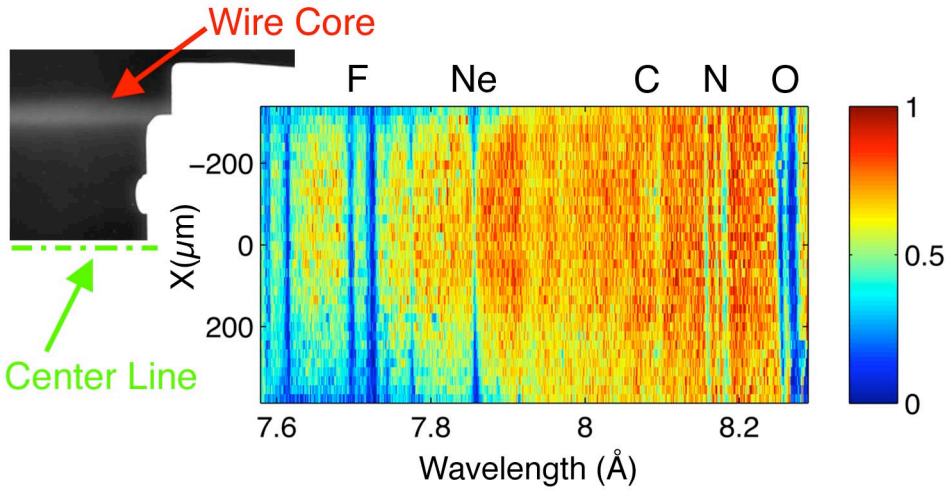

Figure 7.21: (Color) Experimental transmission spectrum obtained on COBRA shot# 2034 along with the direct radiograph. The location of one wire core and the center line between the two wires are noted. The color bar on the right shows the level of transmission from zero to one.

on the far left. These lines decrease in intensity near the core in the calculated spectrum, which is likely due to the tradeoffs made in fitting a finite number of regions to a continuous distribution and not to inaccuracies in the atomic model. The variation with position in the Ne-like line at 7.886Å is captured well. It is weakest in the center and increases in absorption as we look toward the top and bottom of the image (i.e. closer to the wire cores). Closest to the cores the bound-free absorption between lines is captured well below 7.9Å. The increase in absorption of the N- and C-like satellite lines is not captured as well. The general trend of increasing ionization is shown, but it occurs in discrete jumps as a result of the coarseness of the temperature/density grid we used.

Figure 7.23(a) shows a comparison of the experimental and calculated spectra at $x = -220\mu m$. Overall the major features of the spectrum match well, particularly the peak absorption of the O-like satellite lines, the two F-like lines between 7.70Å and 7.77Å and the primary Ne-like line at 7.886Å. The peaks of

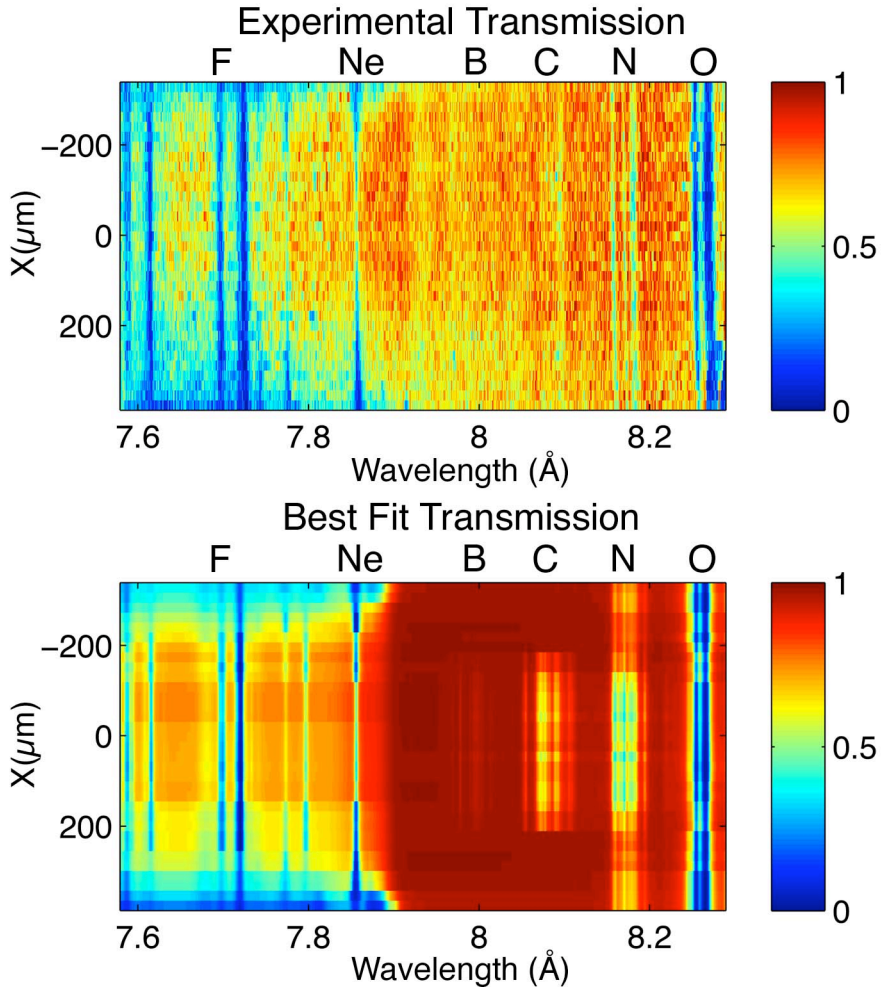

Figure 7.22: (Color) (a) Experimental transmission spectrum from COBRA shot# 2034. (b) Synthetic transmission spectra generated by the genetic algorithm. In both spectra $x = 0$ corresponds to the center line between the two wires.

the C-like lines and the F-like line at 7.62Å are low in the calculation. The discrepancy in the C-like satellites may be due to a small underestimation of the temperature in the central region.

The continuum absorption between satellite groups at wavelengths greater than 7.95Å does not agree well with the experiment, although, below 7.95Å it matches quite well. This could be due to experimental errors, such as crystal defects or errors in the transmission measurement. However, this seems unlikely

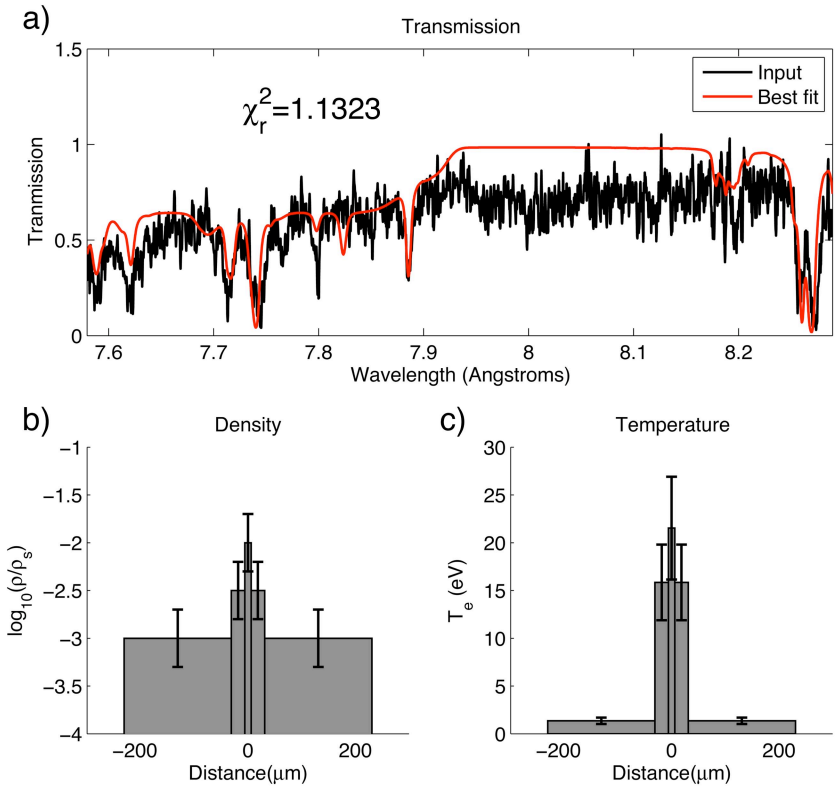

Figure 7.23: (Color)(a) Comparison of the experimental and best fit synthetic transmission spectra from $x = -220\mu m$. The experimental spectrum is shown in black and the fit is shown in red. (b) Mass density of the three regions determined by the GA. We have taken advantage of the assumed symmetry along the line of sight and reflected each region about the y-axis. Density is shown on a log scale normalized to solid density, $\rho_s = 2.7g/cc$. The $-50\%/+100\%$ error is shown. (c) Temperature of the three regions determined by the GA with the ±25% error shown for each region.

because it is not systematic as will be seen in the next section. The discrepancy is likely due to known inaccuracies in the model at low temperature[26].

Figure 7.13 shows that the SCRAM calculation predicts three Ne-like features, at 7.755Å, 7.798AA and 7.824Å, below the prominent line at 7.886Å . However the experimental spectrum shows evidence of only two. Figure 7.24 shows a close up of this portion of the spectrum. We can see that the location of the line

labeled "ii" is close to an experimentally observed line, although the intensity is not well predicted. However, there is no line visible above the noise at the location of the line labeled "iii". In the calculation there is a Ne-like line near the experimental location of the line labeled "i", but in the calculation it is very low intensity and appears much closer to the F-like line at 7.74Å. Discrepancies here are no surprise since virtually no data exist regarding the placement and relative intensities of these lines. This data set and these calculations comprise a first effort at obtaining such information about these lines. Considering this, the current level of agreement is quite good.

Figure 7.23(b) and (c) show the density and temperature distributions determined by the GA at this location, 220μm from the center line. The density and temperature both peak on the x-axis reaching values of $0.027 g/cc$ ($6 \times 10^{20} cm^{-3}$ ion density)$+100\%/-50\%$ and $21 \pm 5eV$ respectively. The error bars shown here and in subsequent figures are due primarily to the grid spacing used in the SCRAM model. Further work could potentially improve on this. The width of the innermost plasma region is $15 \pm 6\mu m$, while region two is $50 \pm 20\mu m$ and region three is $400 \pm 160\mu m$. Both the temperature and the density fall by about an order of magnitude over a distance of $200\mu m$.

The theoretical spectrum at $x = 24\mu m$ shown in fig. 7.25 suggests that the plasma temperature peaks at about $29 \pm 7eV$ and the mass density peaks at about $0.085(+0.085/-0.043) g/cc$ with a path length of $10 \pm 4\mu m$. It fits the experimental spectrum in fig. 7.25(a) well except for the absorption level between the lines above the K-edge. The primary difference between the spectra at $x = 24\mu m$ and $x = -220\mu m$ is that at $x = 24\mu m$ the C-like lines appear, the N-like lines are more intense and the Ne-like lines are weaker, all of which indicate a higher temperature.

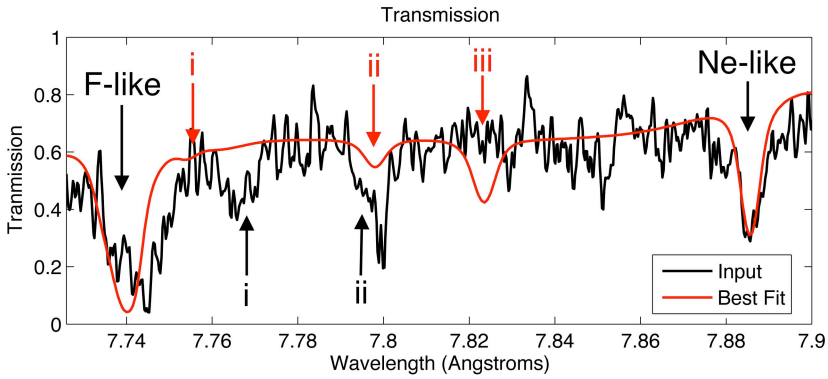

Figure 7.24: (Color)Expanded portion of the spectrum showing the Ne-like lines at at 7.755Å, 7.798*AA* and 7.824Å labeled i, ii and iii respectively.

The GA has determined each of the three plasma region conditions in order to fit the observed spectrum well and satisfy the constraints detailed in sec. 6.2.2, namely that the density is highest along the x-axis and that the parameters vary smoothly along the spatial dimension. This results in a coarse distribution of density and temperature unevenly distributed across the $x - y$ plane, where the y-dimension is along the line of sight of the spectrometer and contains the three regions, which are symmetric about $y = 0$. Figure 7.26 shows this grid with the dots marking the centers of each region and the error bars denoting the spatial extent of each region. We can use the centers of each of these regions as anchor points to interpolate the density and temperature on a uniform grid. The red points along the edges in fig. 7.26 are there to mark the boundary of the interpolation region. We will set $T_e = 0$ and $\rho = 1 \times 10^{-5}\rho_s$ at these points to constrain the interpolation and avoid oscillations.

Figures 7.27(a) and (b) show the results of this interpolation for the electron temperature and mass density respectively. Density is again shown on a log scale normalized to solid density (ρ_s). It is immediately clear that the temperature is highest near the center line where streams from each of the wires

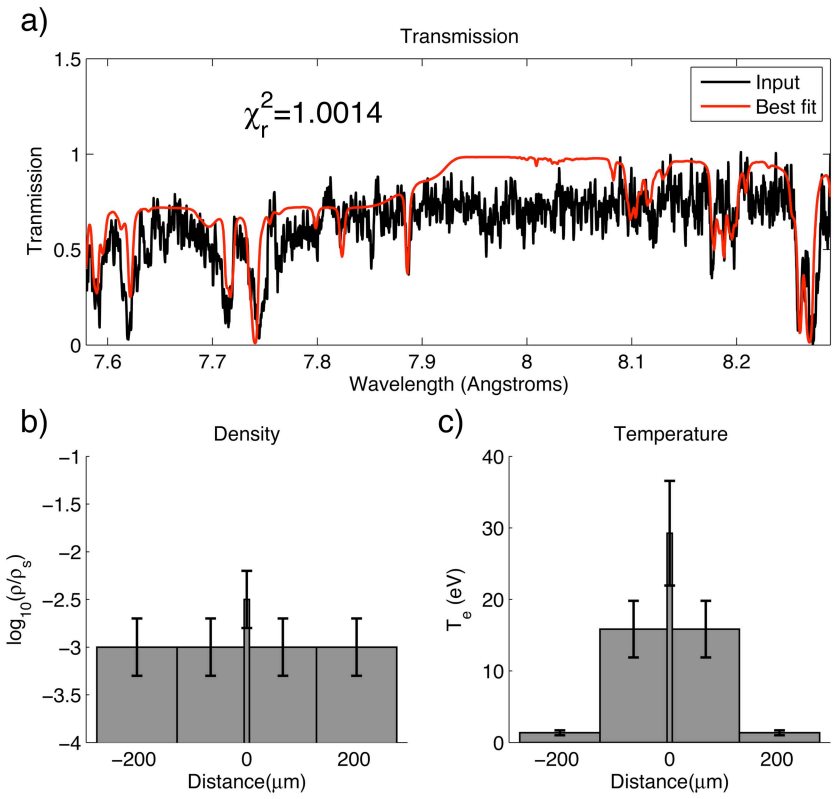

Figure 7.25: (Color)(a) Comparison of the experimental and best fit synthetic transmission spectra from $x = 24\mu m$. The experimental spectrum is shown in black and the fit is shown in red. (b) Mass density of the three regions determined by the GA. Density is shown on a log scale normalized to solid density, $\rho_s = 2.7g/cc$ ($6 \times 10^{22} cm^{-3}$). Error bars are shown. (c) Temperature of the three regions determined by the GA with error bars shown.

collide, reaching $29eV$. According to the density map, there is no evidence of an increase in density at the centroid of the system ($x = 0$, $y = 0$) as one might suspect. However, this diagnostic is much less sensitive to density than to temperature so there may be an increase in density that we cannot detect. In particular, a factor of 2 could be undetectable because of the SCRAM grid spacing. Future analysis could eliminate this possibility. We do see an expansion of the hot plasma in the center. It may be that once the plasma becomes hot enough on

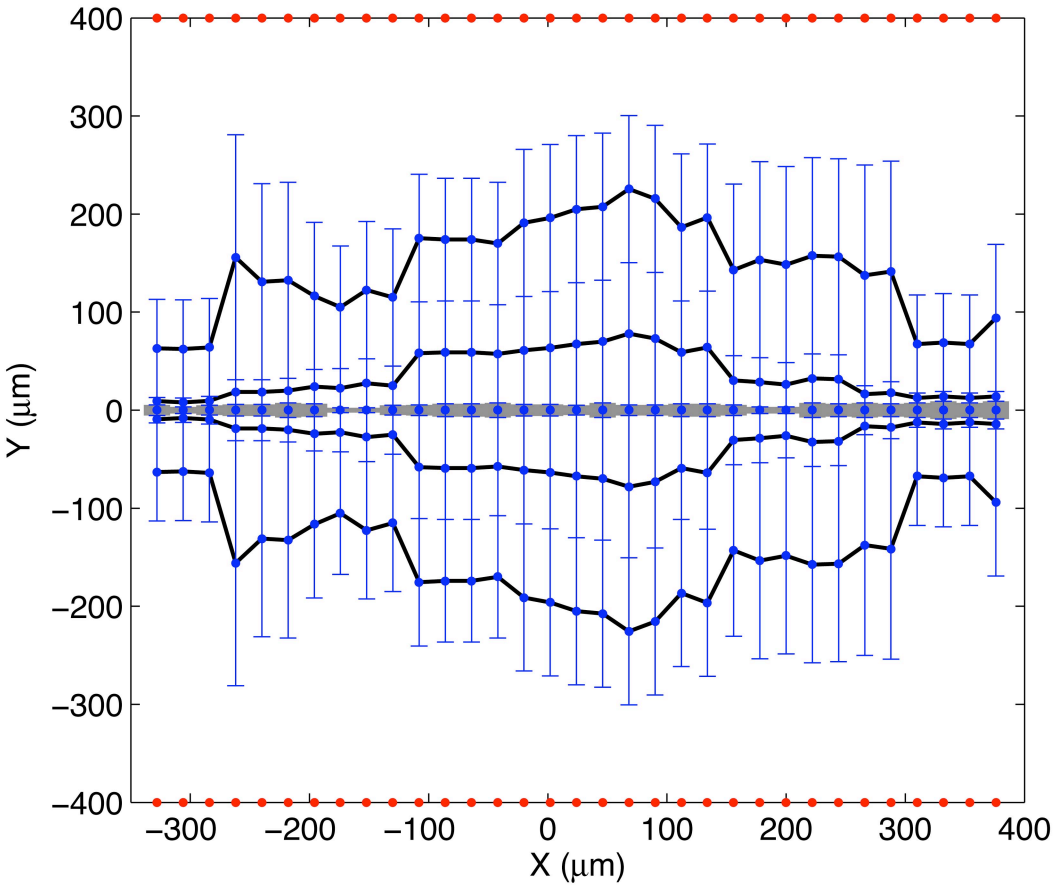

Figure 7.26: (Color)The location and size of each of the regions of plasma chosen by the GA to model the experimental transmission spectrum obtained on COBRA shot 2034. The dots indicate the center of the region and the error bars indicate the extent. The red dots on the upper and lower edges are inserted artificially to act as boundary conditions for the interpolation. The extent of region one is shaded in grey, while the centers of regions two and three are connected with the black line.

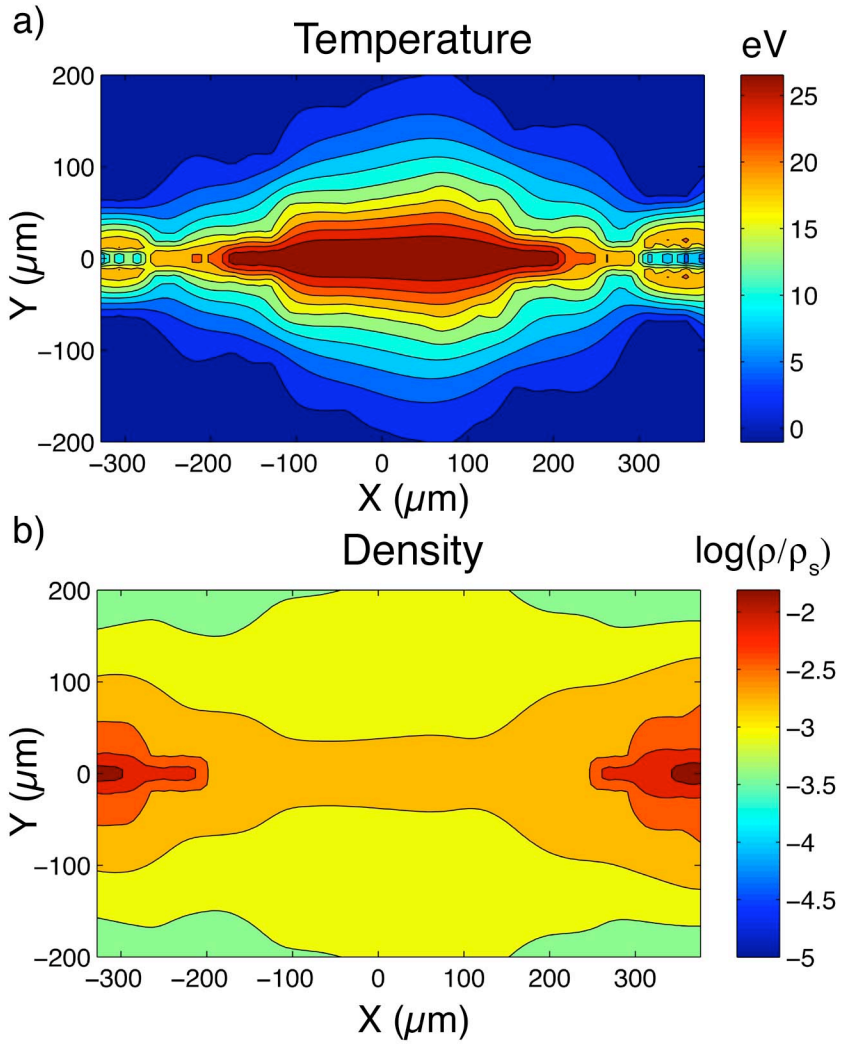

Figure 7.27: (Color) (a) Temperature map constructed by interpolation of the optimum points determined by the GA. (b) Density map constructed by interpolation of the points determined by the GA. Density is shown on a log scale normalized by solid density, $\rho = 2.7 g/cc$.

axis the magnetic field is not sufficient to confine it because of the low current, $\sim 150 kA$. Then the plasma can expand and the density is unable to increase in the center.

The density increases near the wire cores where the temperature drops, in a similar way to the pattern observed in the previous sections. In the temperature

map we see a higher temperature plasma surrounding the colder material near the wire core. This is consistent with the model presented previously in sec. 2.2.2 in which a sheath of hotter, more tenuous plasma surrounds the wire core and carries virtually all of the current. As plasma is redirected to the center between the two wires the hotter current carrying plasma converges on the x-axis, closing off the cold, dense plasma. This gives rise to the "island" of cold plasma on either side of the temperature map.

7.2.2 **COBRA Shot** 2030

COBRA shot 2030 was also obtained with an adequate calibration image as well as x-pinch x-ray burst intensity. The signals from this shot are shown in fig. 7.28 along with two images from the XUV framing camera. The x-pinch x-ray burst occurred $105ns$ after the start of current rise. The XUV images in fig. 7.28(b) and (c) are much earlier than this, occurring at $47ns$ and $57ns$. They do show that even at these earlier times there is plasma collecting at the center of the two wires. In fig. 7.28(b) we can see a distinct band of emission on the axis that is far brighter than the plasma at the wire locations. This suggests that the plasma is hotter at this location. In fig. 7.28(c) the entire system is brighter, but this is especially true of the coronal plasma around the wires.

Figure 7.29 shows the experimental transmission spectrum obtained on this shot alongside the direct radiograph. At the top of the image the edge of one wire cores is visible. The center line between the two wires is approximately $50\mu m$ above the bottom of the image. In this shot the spectrometer was aligned to view shorter wavelengths so the O-like $1s - 3p$ satellites are in view but the

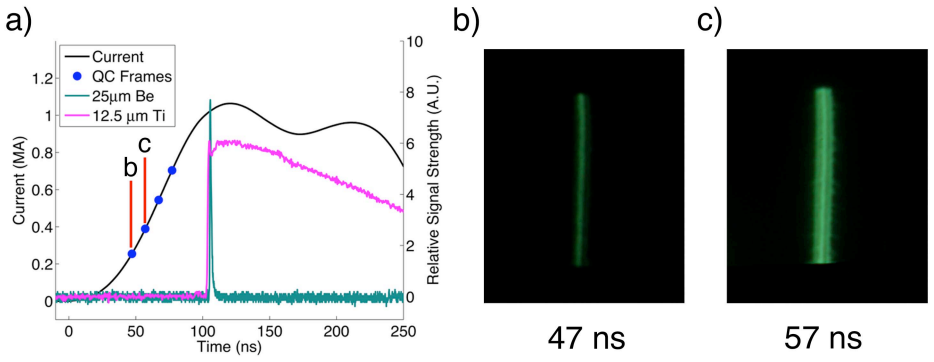

Figure 7.28: (Color) Main load current, $25\mu m$ Be filtered PCD and $12.5\mu m$ Ti filtered Si diode signals from COBRA shot# 2030. (b) MCP framing camera image of the object plasma taken at $47ns$, (labeled 'b' in (a)) after the start of current rise. (c) MCP framing camera image of the object plasma taken at $57ns$ (labeled 'c' in (a)).

O-like $1s - 2p$ satellites are not.

The temperature again is lowest near the wire core where the Ne-like line is most prominent and the Na-like line is present. The line is also broadened somewhat very near the core indicating the density is higher there.

The transmission spectrum in fig. 7.29 has more variation than that in fig. 7.21. Whereas in shot 2034 the F- and O-like lines were roughly constant across the image, in shot 2030 there is significant variation. The O-like lines do not appear until about $300\mu m$ away from the wire core, where the Ne-like lines disappear completely. This suggests that the temperature gradient along the x-direction is more severe than in shot 2034.

The synthetic spectrum resulting from the GA is shown in fig. 7.30. The basic trends in the experimental spectrum are reproduced well. The primary difference is that the O-like lines appear much nearer to the core than in the experimental image. However, we believe that this is reasonable. If we look, for example, at $x = -300\mu m$ in both the experimental and synthetic spectra we

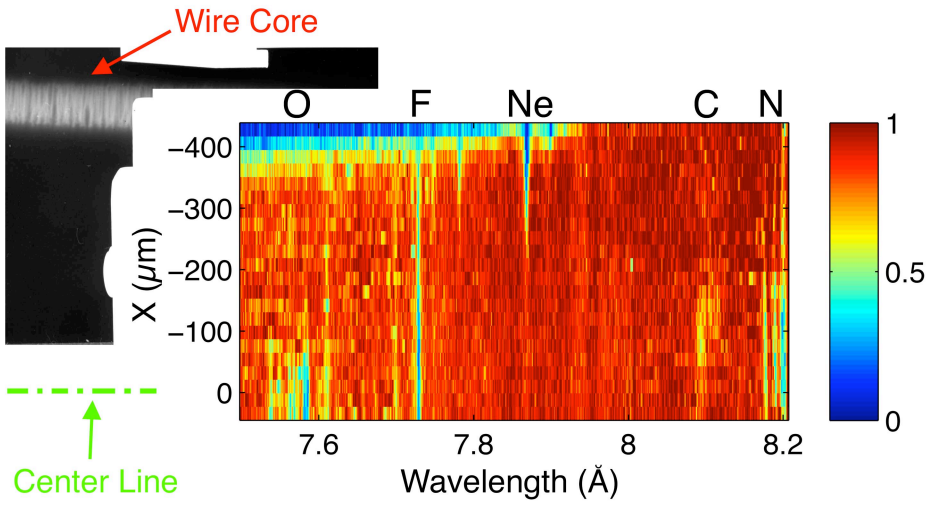

Figure 7.29: (Color) Experimental transmission spectrum obtained on COBRA shot# 2030 along with the direct radiograph. The location of one wire core and the center line between the two wires are noted. The color bar on the right shows the level of transmission from zero to one.

can see at the far right of the image the presence of N-like Al in addition to Ne- and F-like Al. We would expect that if Ne-, F- and N-like Al are all present in a plasma then O-like Al should be present as well. The absorption of the O-like lines predicted in the synthetic spectrum is low and so would easily by obscured by noise on the film or defects in the crystal.

In fig. 7.31(a) we compare the synthetic and measured absorption spectra at $x = -400\mu m$, corresponding to a location very near the wire core. The fit, shown in red, agrees very well with the measured spectrum, particularly capturing the shape of the Ne-like line at 7.886Å well. The Na-like line is not quite as sharp in the calculation and the peak is closer to the Ne-like line than in the experiment.

At the short wavelength side of the spectrum, the continuum absorption is underestimated in the calculated spectrum. This is likely an experimental issue. In the radiograph in fig. 7.29 we can see that the wire is not perfectly straight with respect to the crystal. This would cause the location of the residual dense

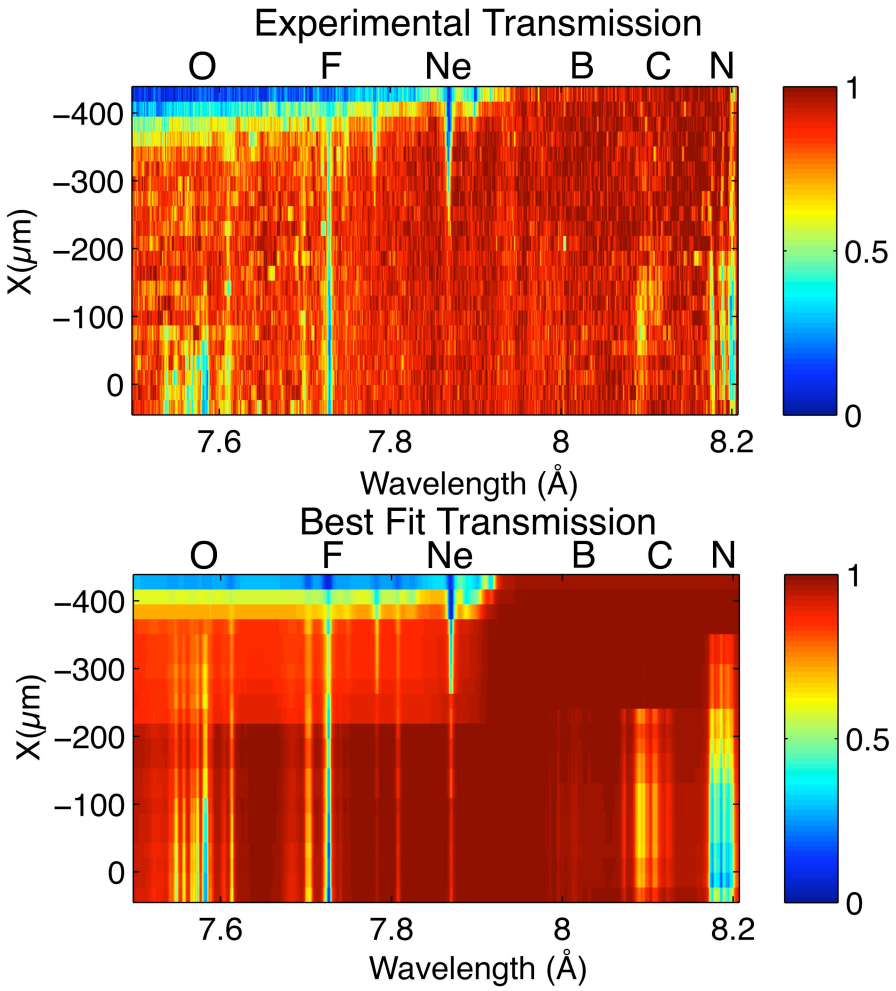

Figure 7.30: (Color) (a) Experimental transmission spectrum from COBRA shot 2030. (b) Synthetic transmission spectrum generated by the genetic algorithm. In both spectra x=0 corresponds to the center line between the two wires.

wire core to change along the spectral direction, see fig.3.3(b), which could account for the increased absorption below 7.7Å. We do not expect this to have much impact on the plasma between the wires since this plasma is strongly influenced by the magnetic field resulting from the combination of the two wires once it leaves the wire core.

Figures 7.31 (b) and (c) show the density and temperature profiles inferred by the GA. We can see at $x = -400\mu m$ that the highest density is not asso-

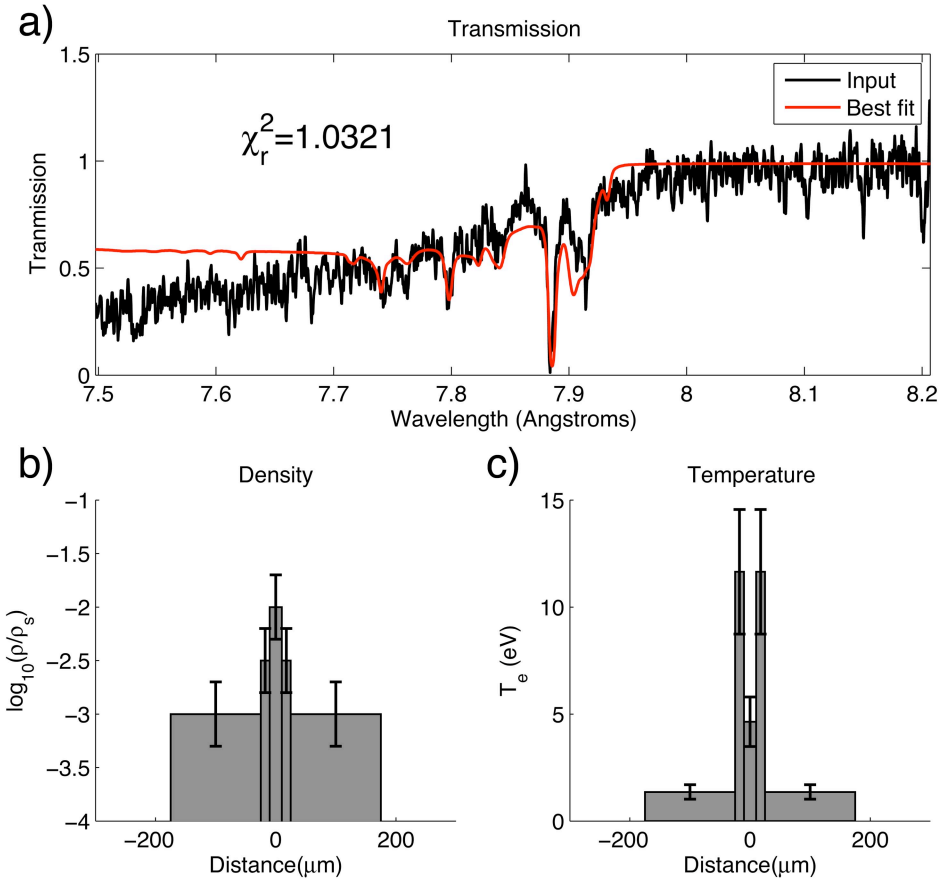

Figure 7.31: (Color)(a) Comparison of the experimental and best fit synthetic transmission spectra from $x = -400\mu m$. The experimental spectrum is shown in black and the fit is shown in red. (b) Mass density of the three regions determined by the GA with $-50\%/+100\%$ error bars shown. Density is shown on a log scale normalized to solid density, $\rho_s = 2.7g/cc$ ($6 \times 10^{22} cm^{-3}$). (c) Temperature of the three regions determined by the GA with $\pm 25\%$ error bars shown.

ciated with the highest temperature. This is indicative of the cold "island" seen in the previous section where a more tenuous plasma surrounding the dense central region is hotter and therefore likely carrying the current. Figure 7.32 shows a comparison of the calculated and measured spectra along with the density and temperature profiles inferred by the GA at $x = -10\mu m$, corresponding to a location in the vicinity of the center line between the two

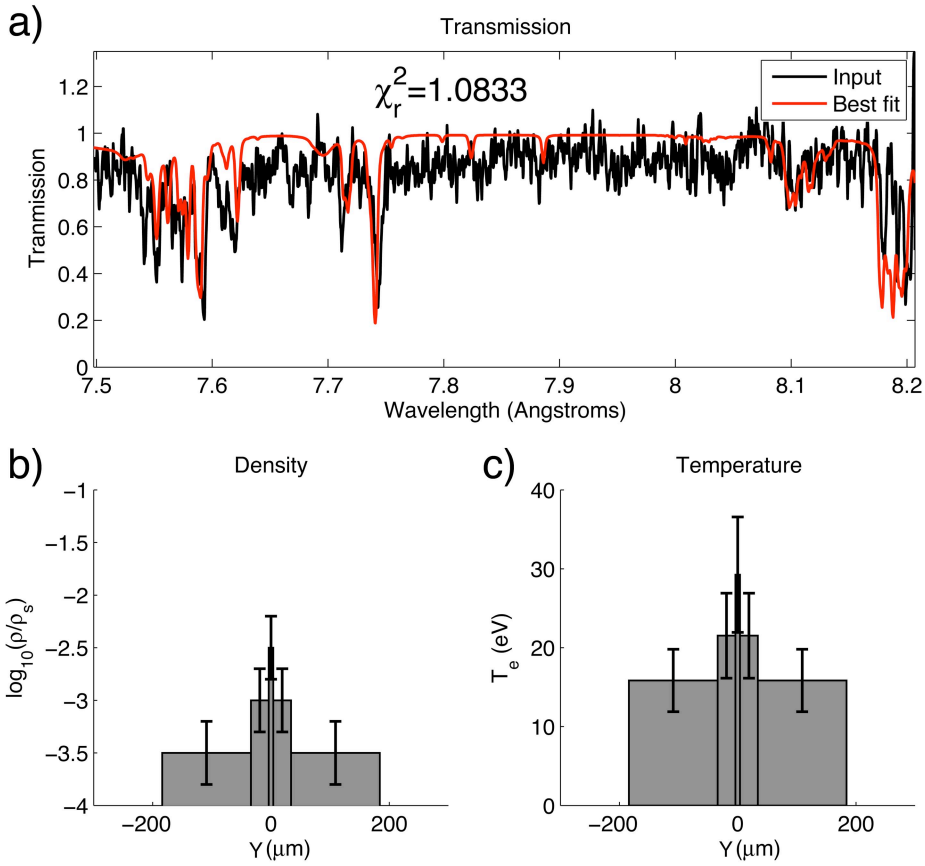

Figure 7.32: (Color)(a) Comparison of the experimental and best fit synthetic transmission spectra from $x = -10\mu m$. The experimental spectrum is shown in black and the fit is shown in red. (b) Mass density of the three regions determined by the GA with $-50\%/+100\%$ error bars shown. Density is shown on a log scale normalized to solid density, $\rho_s = 2.7g/cc$ ($6 \times 10^{22} cm^{-3}$). (c) Temperature of the three regions determined by the GA with $\pm 25\%$ error bars shown.

wires. We see that now the density and temperature are both highest on axis at $\rho = 0.085(+0.17/-0.043)g/cc$ and $T_e = 30 \pm 7.5eV$ respectively. If we compare this spectrum with those obtained in COBRA shot 2034 we see that there is not as much of a discrepancy in the absorption between the satellite groups. We attributed that discrepancy to the low density, low temperature plasma ($\rho = .0003(+5.4 \times 10^{-4}/-1.3 \times 10^{-4})g/cc, T_e = 2 \pm 0.5eV$) that was found to sur-

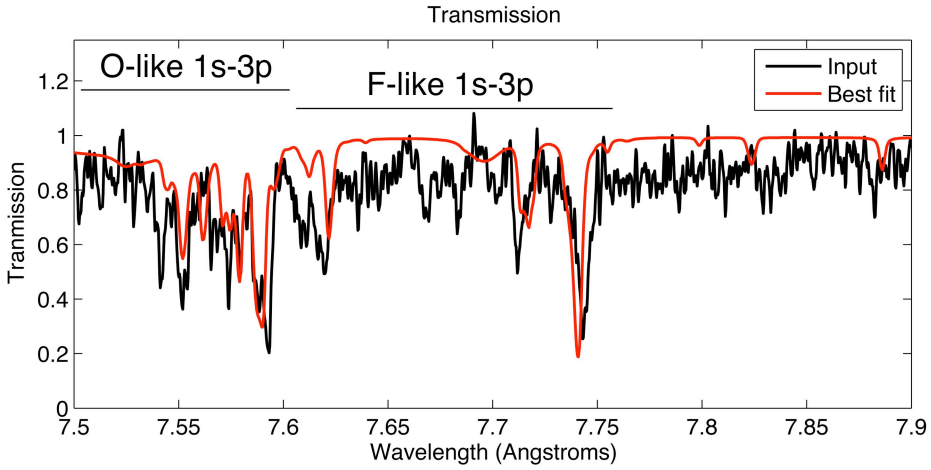

Figure 7.33: (Color) Expanded portion of the spectral range including the $1s-3p$ transitions from $x = -10\mu m$. The experimental spectrum is shown in black. The best fit synthetic spectrum is shown in red.

round the entire system. In shot 2030 we do not see this, and as a result the transmission between the satellite groups is about one, which agrees well with the experiment.

As was stated in sec. 7.1.3 the $1s-3p$ lines are poorly understood, so it is useful to look closely at the experimental and synthetic spectra to see how well the model reproduces the structure of these lines. Figure 7.33 shows the O- and F-like Al $1s-3p$ satellites in 7.32(a) between 7.5Å and 7.9Å. The locations of the lines in the theoretical profile are in general agreement with the experimental spectrum. The general shape of the O-like group of lines between 7.5Å and 7.6Å is reproduced quite well by the calculation, though the details of the intensity and location of each feature are not. Overall the predicted $1s-3p$ satellite profiles show surprising agreement with the experiment.

The two dimensional density and temperature maps reconstructed from the GA output are shown in fig. 7.34 for COBRA shot 2030. For $x \leq 375\mu m$ the cold material at the edge of the wire core is surrounded by hotter coronal plasma.

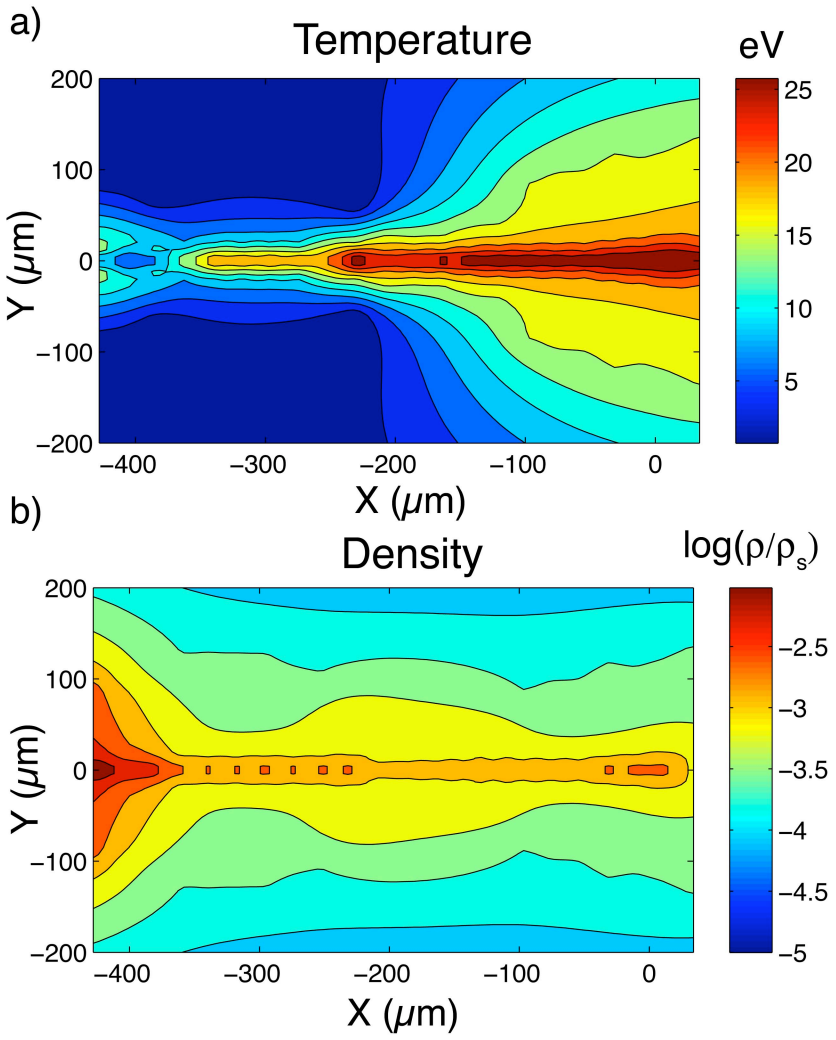

Figure 7.34: (Color) (a) Temperature map constructed by interpolation of the points determined by the GA. (b) Density map constructed by interpolation of the points determined by the GA. Density is shown on a log scale normalized by solid density, $\rho = 2.7$

On the x-axis the temperature steadily increases for $x > 375\mu m$. The density is roughly constant on the x-axis, except for isolated regions of higher density which are artifacts of the interpolation. The width of the hottest and most dense region of plasma straddling the x-axis is relatively constant with position, about $30\mu m$.

The width of the the plasma having temperature $10eV$ and above is about three times larger near $x = 0$ than near $x = -300$. However the density map does not reflect this behavior. There is some expansion visible in the plasma with density $\rho < 0.0027g/cc$. However, the densest material in the center appears to stay confined. We know that the collision of plasma at the center causes thermalization of the x-directed kinetic energy which can lead to expansion of the plasma in the y-direction. The only confinement mechanism available is magnetic, and we have no information about the distribution of the magnetic field and current density. By using the measured density and temperature we can estimate that $\nabla p \sim 10^{13} Nm^{-3}$ and, therefore, to maintain confinement $\mathbf{J} \times \mathbf{B}$ must be equal and opposite. If we assume that there is magnetic confinement in the y-direction at $x = 0$ we require that $p + B^2/2\mu_o$ is constant on this line. Therefore, using the measured peak pressure at the center, where $B = 0$, of $6 \times 10^9 Pa$, we can estimate the maximum value of B along the y-axis to be $\sim 100T$.

7.2.3 **XP Shot** 5844

Although we can't be as accurate with the XP data as with the COBRA data, it is still important to analyze some of the XP data using the GA to see if it agrees with the semi-quantitative analysis presented in sec. 7.1.2. This will provide a

consistency check on both methods. XP shot 5844 is a good candidate for this analysis because the alignment enabled all of the $1s - 2p$ satellites to be seen.

In the spectrum obtained on this shot, shown in fig. 7.35(a), only the streaming plasma between the wires is visible. The best fit transmission spectrum, fig. 7.35(b), shows very good agreement with the experimental spectrum, apart from the abrupt change in absorption of the F- and B-like lines at $x = 200\mu m$. These are due to the coarseness of the opacity table and would be smoother if more temperature points were available.

In the temperature map, fig. 7.36(a), we can see that the peak temperature is $39eV$, somewhat higher than the peak temperatures found on COBRA. The peak temperature occurs within $100\mu m$ of the center line between the two wires, $x = 0$. The density map, fig. 7.36(b), shows somewhat lower density than was found on COBRA in the streaming plasma, with the peak density occurring in the same location as the peak temperature. This density enhancement suggests that we are seeing compression of the streaming plasma as it stagnates at the center.

The errors in absolute absorption are higher in this case due to the approximations used to infer transmission from the absorption spectra. We expect that the total error is about 20% as discussed in sec. 6.1.2. This results in less confidence in the inferred density and temperature than in the case of the calibrated shots. However, the peak temperature as a function of x position determined by the GA agrees well with the semi-quantitative analysis performed on fig. 7.11 in sec. 7.1.2. This suggests that the results are generally sound, but the error is unknown.

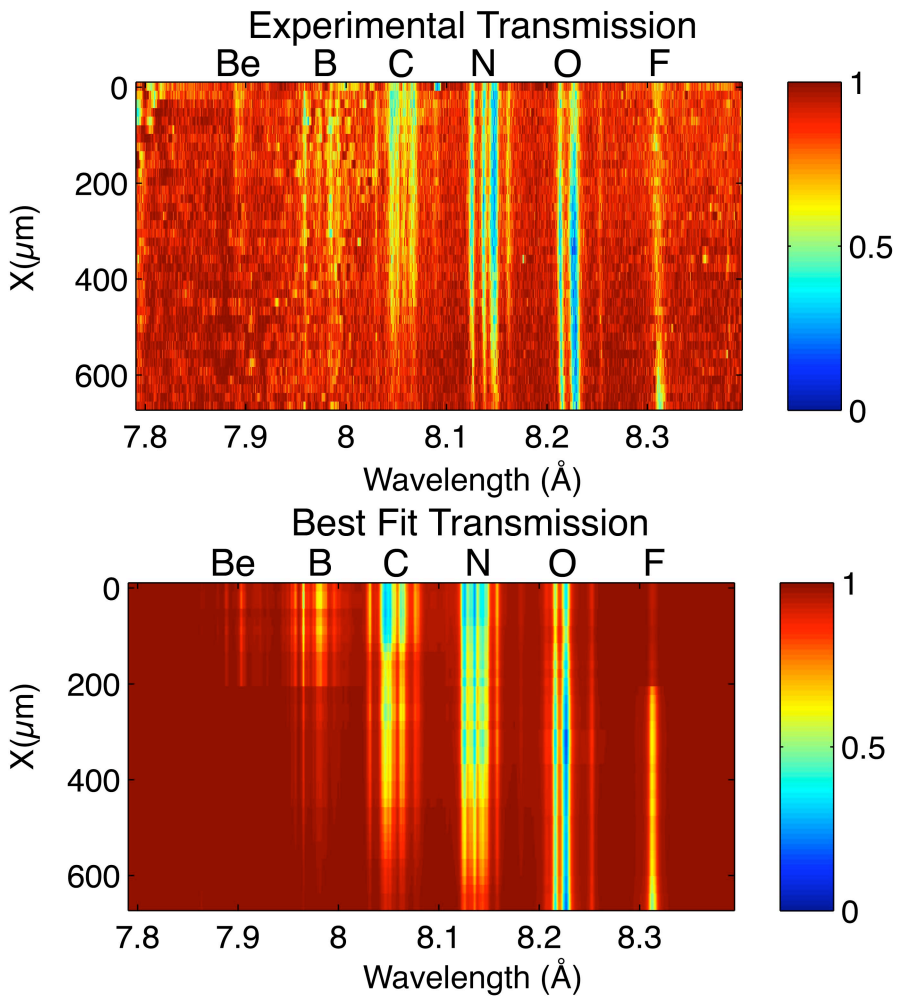

Figure 7.35: (Color) (a) Experimental transmission spectrum from XP shot 5844. (b) Synthetic transmission spectrum generated by the genetic algorithm. In both spectra x=0 corresponds to the center line between the two wires.

7.3 Comparison With Simulation Results

In order to gain more insight into the plasma under study, we ran a series of simulations using the extended MHD (XMHD) simulation code PERSEUS written by Drs Matthew Martin and Charles Seyler[47, 59]. This code includes so-called two-fluid physics, including the Hall and electron inertia terms in the generalized Ohm's law.

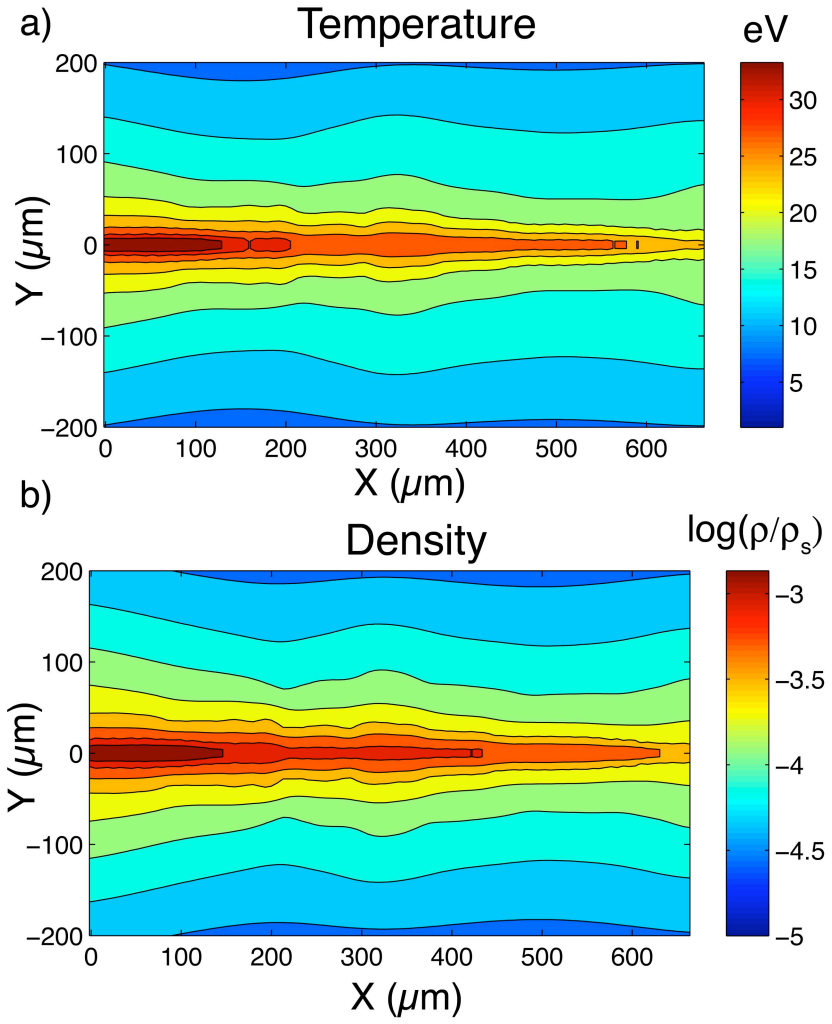

Figure 7.36: (Color) (a) Temperature map constructed by interpolation of the three points determined by the GA. (b) Density map constructed by interpolation of the three points determined by the GA. Density is shown on a log scale normalized by solid density, $\rho = 2.7 g/cc$.

We are using a two dimensional cartesian ($x - y$) version of PERSEUS that simulates the evolution of the exploding wire pair in the plane perpendicular to the wires. This allows direct comparison with the experimental data from the previous section. At the moment PERSEUS does not include any loss mechanisms. Most notably missing, given our multiply ionized Al plasma, is the component of internal energy due to ionization. We can estimate the effect this will have on the plasma by looking at the entropy equation used in PERSEUS

$$\frac{\partial s}{\partial t} + \nabla \cdot (\mathbf{u}s) = (\gamma - 1)\eta\rho^{1-\gamma}J^2 \tag{7.2}$$

where $\mathbf{u}$ is the fluid velocity, η is the plasma resistivity, γ is the adiabatic index, which is uniform in space and constant in time in the simulation, and s is the entropy density, which is given by $s = P/\rho^{\gamma-1}$. We can see that the only entropy source is due to ohmic heating, ηJ^2. Loss terms, such as radiation and ionization would appear as negative terms on the right side of eqn. 7.2. The fact that ionization is not accounted for implies that the energy delivered by the driver current will go into increasing the entropy and therefore the temperature.

This effect can be compensated for partially by adjusting γ. It is known that including the effects of radiation and ionization in the thermodynamic description of the plasma reduces the adiabatic index compared to the ideal gas value of $\gamma = 5/3$[18]. This still cannot capture all of the necessary physics and account for all of the expected discrepancy in the internal energy, partially because γ is neither uniform nor constant in the experiment.

The impact the losses will have on the global dynamics will be largely dependent upon the balance between the various components of the total plasma energy density, ϵ_{Tot}, given by

$$\epsilon_{Tot} = \epsilon_{kin} + \epsilon_{int} + \epsilon_{mag} \tag{7.3}$$

where ϵ_{kin} is the kinetic energy density, ϵ_{int} is the internal energy density and ϵ_{mag} is the magnetic energy density. Each of the components of the total energy as modeled in the code are expressed with respect to the relevant dynamical variables below

$$\epsilon_{kin} = \frac{1}{2}\rho u^2 \tag{7.4}$$

$$\epsilon_{int} = \frac{p}{\gamma - 1} = \frac{1 + Z}{\gamma - 1} n_i k_B T_e \tag{7.5}$$

$$\epsilon_{mag} = \frac{1}{2\mu_o} B^2 \tag{7.6}$$

where quasi-neutrality has been invoked and the electron and ion temperatures have been assumed to be equal in eqn. 7.5.

The energy invested into ionization and the energy density of the radiation field are typically assumed to be part of the internal energy and would therefore be added to eqn. 7.5. It seems reasonable to assume that in a regime where the magnetic and momentum energy densities are dominant, the plasma dynamics will be relatively insensitive to the details of the internal energy, such as in a hydrogen plasma. We can use what we know about our plasma from the previous section to estimate which energy sources are important.

We can easily estimate the contribution of radiation by assuming a planckian source and using the well known formula for the energy density of a blackbody radiation field[21]

$$\epsilon_{rad} = \frac{4\sigma}{c} T^4 \tag{7.7}$$

where σ is the Stefan-Boltzmann constant, c is the speed of light and T is the plasma temperature. Using the peak temperature measured in the COBRA experiments, $T_e = 29eV$, gives $\epsilon_{rad} \sim 10^7 Jm^{-3}$.

The ionization energy can be estimated using a hydrogenic atom model which yields an approximate ionization potential $\chi_i = E_H Z^2$, where $E_H = 13.6eV$

is the excitation energy of hydrogen and Z is the net charge on the ion[18]. Then to compute the energy invested in ionization we evaluate

$$\epsilon_Z = n_i \sum_{k=0}^{Z} \chi_k \tag{7.8}$$

$$\approx n_i E_H \sum_{k=0}^{Z} k^2 \tag{7.9}$$

using $n_i = 10^{26} m^{-3}$, a typical value found between the wires, and $Z = 5$, corresponding to O-like Al. This yields $\epsilon_Z \sim 10^{11} Jm^{-3}$. However, the hydrogenic model overestimates the ionization potential at moderate ionization and continuum lowering has not been accounted for, which will be shown to have a non-negligible effect in sec. 7.3.3, so this contribution to the internal energy is likely lower, say $\sim 10^{10} Jm^{-3}$. It is clear that the radiation energy density is negligible compared to the internal energy density associated with ionization. Finally, we can estimate the internal energy due to the plasma pressure assuming $Z = 5$, $n_i = 10^{26} m^{-3}$ and $T_e = 30eV$ using eqn. 7.5 which yields $\epsilon_{int} \sim 5 \times 10^9 Jm^{-3}$.

The magnetic energy and kinetic energy are generally thought to be more dynamically significant than the internal energy in wire array z-pinches. Using the same density as above and estimating the flow velocity to be $100 km/s$, the kinetic energy density is found to be $\epsilon_{kin} \sim 10^{10} Jm^{-3}$. The magnetic energy is more difficult to estimate since the distribution of current is unknown in our plasma. If we assume each wire is carrying half of the current we can estimate the magnetic field at a given distance. Close to the wires, say $r = 150 \mu m$, the field will be similar to that of a single wire, so we can estimate $B = (\mu_o / 2\pi r)(I/2)$. This gives $B \approx 100T$, which results in a magnetic energy $\epsilon_{mag} \sim 10^9 Jm^{-3}$. The real value is most certainly smaller than this because the current is distributed throughout the plasma, not confined to the wires.

This shows that, at the temperatures measured in the experiment, radiation

is a small component of the internal energy density compared to the kinetic and ionization energies. Thus, ionization and the radiation associated with ionization must be taken into account to properly describe our experiments. We will see that this results in calculated plasma temperatures that are considerably higher than those found in the experiment with associated effects on the plasma dynamics.

7.3.1 Simulation Setup

To simulate our two-wire plasma we initialize our domain with a uniform floor density, $\rho_{floor} = 2.7 \times 10^{-9} g/cc$, everywhere except at the wire locations. The domain is $3mm \times 3mm$ with a resolution of $\delta x = \delta y = 10\mu m$. The wires in the experiment are $40\mu m$ diameter which corresponds to a cross-sectional area of $A = 1.25 \times 10^3 \mu m^2$. We initialize a cluster of 12 cells, as shown in fig. 7.37(a) to contain solid density plasma at $T = 0.14eV$, corresponding to a cross-sectional area of $1.2 \times 10^3 \mu m^2$. The two wires are placed $1mm$ apart and the line connecting the two wires lies on the x-axis as shown in fig. 7.37(b).

The plasma resistivity is modeled using an analytic approximation for the Lee-More-Desjarlais resistivity model[15]. This model captures the behavior of high energy density plasmas far better than Spitzer resistivity, particularly in the low temperature, high density regime[15]. The driver current was set to a peak value of $150kA$, corresoding to the COBRA experiments, with a zero-to-peak rise time of $120ns$. A time-varying magnetic field corresponding to the driver current is applied on the boundary which drives the current through the plasma. All boundary conditions were set to allow outflow of all fluid quanti-

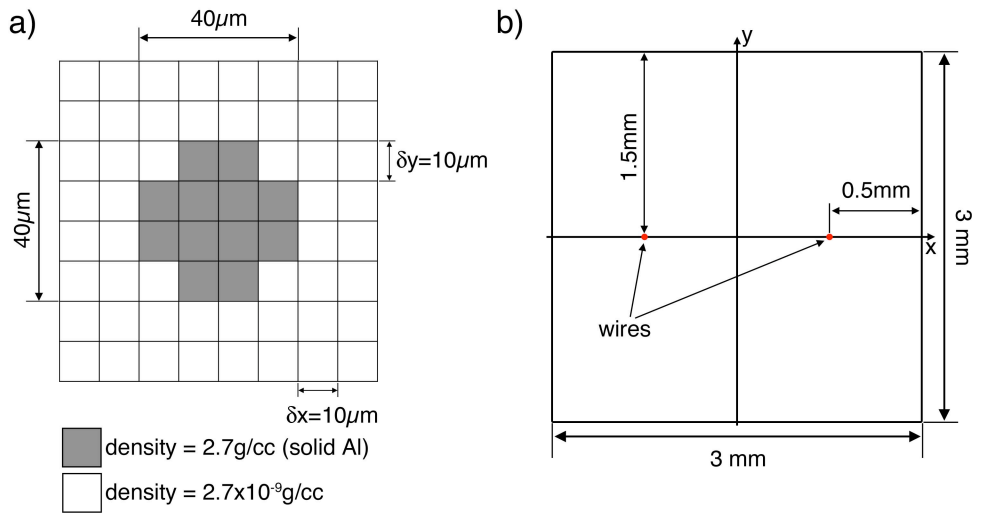

Figure 7.37: (Color) (a) Arrangement of cells used to initialize the wire density. White cells are empty. Grey cells are initialized to solid density. Each cell is $10\mu m \times 10\mu m$. (b) Setup of the simulation domain with placement of the wires (red dots) shown. The domain is $3mm \times 3mm$. x and y axes are shown with the origin in the center of the simulation domain.

ties. Since no ionization model is implemented we must set the ionization state for the fluid which remains uniform in space and constant in time. We chose $Z = 3$ to be a suitable average ionization state since this lies in the middle of the range observed in the COBRA experiments. The speed of light was artificially reduced by a factor of 20 to speed up the computation time.

The adiabatic index was chosen to be 1.15 and 1.67 in two different simulations that were otherwise identical. The latter was chosen because it is the upper limit of γ. The former was computed with representative experimental values of density and temperature using the formulae in ref. [18] which include approximate corrections for ionization and density effects. By running identical simulations with different values of γ we can estimate the sensitivity of the plasma dynamics to the inclusion of the loss processes that contribute to reducing γ.

7.3.2 Simulation Results

Figures 7.38 and 7.39 show the density and temperature maps computed by PERSEUS at $t = 60ns$, $80ns$ and $100ns$ for runs where $\gamma = 1.15$ and $\gamma = 1.67$, respectively. It is obvious from these images that the dynamics are qualitatively different between the two simulations. In both simulations material gathers at the center line between the wires ($x = 0, y = 0$) early in time. This material heats dramatically and explodes outward. With $\gamma = 1.15$ some mass remains near the center line after the explosion with $n_i \sim 6 \times 10^{19} cm^{-3}$, and peak temperatures are about $120eV$. However, with $\gamma = 1.67$ the explosion clears out almost all of the density in the center, $n_i \lesssim 6 \times 10^{18} cm^{-3}$, leaving a void behind. The peak temperatures exceed $300eV$.

Clearly, in the regime relevant to our experiments the plasma dynamics predicted by PERSEUS are very sensitive to the particular value of γ chosen. Particularly, the expulsion of material from the central region is likely due to thermal expansion, which would be significantly lower if ionization were included. When γ is low the plasma stays smaller and the density remains higher near the center line. When the plasma is approximated as an ideal gas the material cannot be confined and by $t = 100ns$ it has nearly reached the edge of the simulation domain. All of this suggests that the various processes that can contribute to reducing γ are important in a dynamical sense, i.e. not simply for predicting temperature and density.

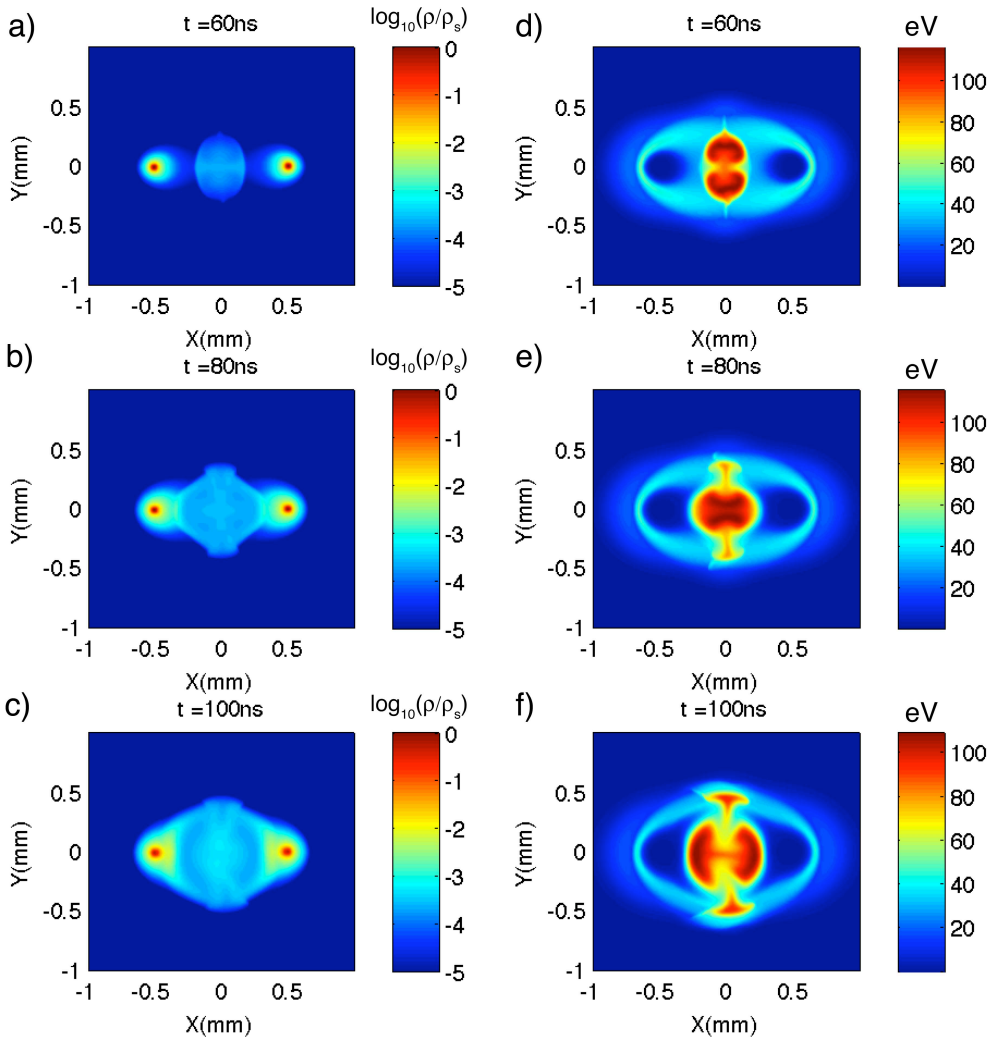

Figure 7.38: (Color) Results of the PERSEUS simulation with $\gamma = 1.15$. Log of the density for $t = 60ns$ (a), $t = 80ns$ (b) and $t = 100ns$ (c). Temperature for $t = 60ns$ (d), $t = 80ns$ (e) and $t = 100ns$ (f).

7.3.3 Comparison With Experimental Results

Figure 7.27 makes it very clear that neither of the simulations presented above represent the data. There are no clearly defined ablation streams, and the density is lower than measured in the experiment. With $\gamma = 1.15$ the temperature is a factor of $2 - 3$ higher than the measured values and the peak temperature is not located at the center line as inferred by the GA. This is still better than the

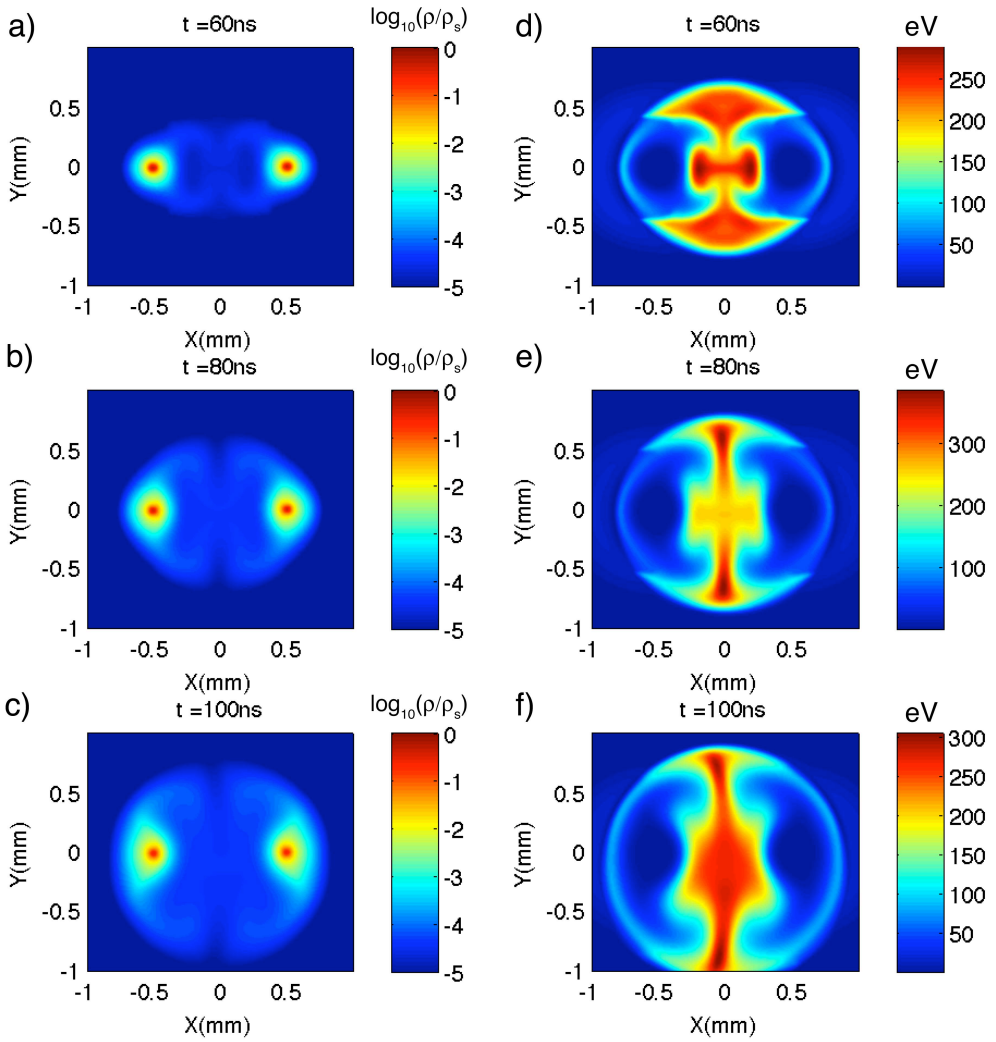

Figure 7.39: (Color) Results of the PERSEUS simulation with $\gamma = 1.67$. Log of the density for $t = 60ns$ (a), $t = 80ns$ (b) and $t = 100ns$ (c). Temperature for $t = 60ns$ (d), $t = 80ns$ (e) and $t = 100ns$ (f).

results from the simulation in which $\gamma = 1.67$ which overestimates the temperature by a factor of ~ 10.

Since the values of density and temperature are not in agreement with the experiment, we use the data to calculate the internal and ionization energies to compare with the internal energy of the plasma in the simulation. For each of these quantities we must know the average ionization, Z. Fortunately, this is calculated by SCRAM, and we therefore know Z everywhere that we know the

density and temperature from the GA. We know n_i, T_e and Z and, from eqn. 7.5, we can see that the adiabatic index is the only unknown parameter needed to determine the internal energy of the fluid. We have chosen to use the ideal gas value, $\gamma = 5/3$. We can use eqn. 7.5 to calculate the distribution of the internal energy in the $x - y$ plane, shown in fig. 7.40(a). We can readily see that our estimate of a few times $10^9 Jm^{-3}$ is valid nearly everywhere.

To calculate the ionization energy we need to know the ion density, charge state and the ionization potentials for the various ionic states of Al. For this calculation we assume that all Al ions are in the ground state. The ionization potentials are given in table. 7.1. In order to evaluate the sum in eqn. 7.8 precisely we must know the charge state distribution and sum over all species weighted by their individual densities. However, we do not have access to the charge state distribution calculated by SCRAM. A good approximation is to round the average ionization, Z, to the nearest integer and evaluate the sum up to this new value, Z'.

In order to appropriately estimate the ionization energy of the plasma we must also include continuum lowering, which is caused by the fact that the ions do not exist in isolation[18]. The presence of the surrounding ions and, especially, the electrons lowers the energy of the free (continuum) states of the ions. This effectively eliminates highly excited levels in the ion and results in less energy being required to remove additional electrons. At the densities of interest in our experiment this effect can be substantial. A useful approximation is given in ref. [43]

$$\Delta E_{CL} = 3.5 \times 10^{-7}(1 + Z)\left(\frac{n_e}{Z}\right)^{1/3} \tag{7.10}$$

which gives the change in energy of the continuum in eV when n_e is expressed in cm^{-3}. This effect results in a $10eV$ change in the ionization potential at densities

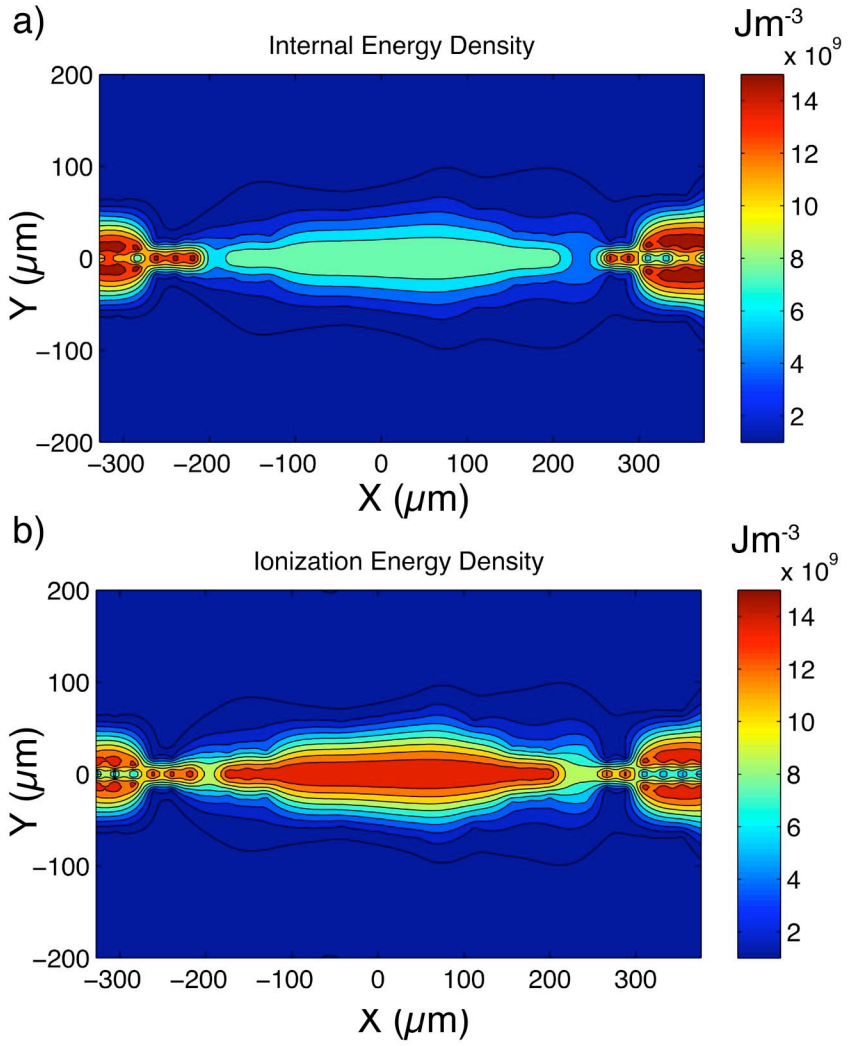

Figure 7.40: (Color) (a) Internal energy density in Jm^{-3} calculated from the experimental data for COBRA shot 2034. (b) Ionization energy density in Jm^{-3} calculated for the same shot.

of order $10^{21} cm^{-3}$. Consulting table 7.1 we can see that this is a $\sim 10\%$ correction. We have all of the information we need to account for this effect from the data. Thus, the expression for the ionization energy becomes

$$\epsilon_Z = n_i \left[\left(\sum_{k=1}^{Z'} \chi_k \right) - \Delta E_{CL} \right] \tag{7.11}$$

The ionization energy calculated in this way is shown in fig. 7.40(b). Comparing the internal and ionization energy we can see that in the plasma collect-

Table 7.1: Ionization potential for various Al ions[19]. χ corresponds to the energy required to remove one electron from an existing ion. Therefore, the potential corresponding to Al-like Al in the table is the energy required to ionize neutral Al, resulting in a Mg-like Al ion.

Z	χ $(eV/particle)$
Al-like	5.98
Mg-like	18.82
Na-like	28.44
Ne-like	119.96
F-like	153.77
O-like	190.42

ing between the wires the ionization energy is almost twice as large as the internal energy. This suggests that a significant amount of the energy that would have otherwise gone into increasing the pressure and the temperature in this region has instead been input into ionization. Much of this energy has likely come from the directed kinetic energy in the ablation streams. As a result of the reduced temperature there is less of a tendency for this plasma to explode which may explain why the plasma seems to remain confined in the experiment. Additionally, energy that is input into the explosion of material at the center line will be dissipated by ionization. Therefore, while it may occur initially in the experiment, it will be damped significantly by ionization.

Knowing that the peak ionization energy is approximately twice the internal energy, we can use this information to estimate what the effective adiabatic index, γ_{eff}, is in the experiment. To do this we equate the approximate internal

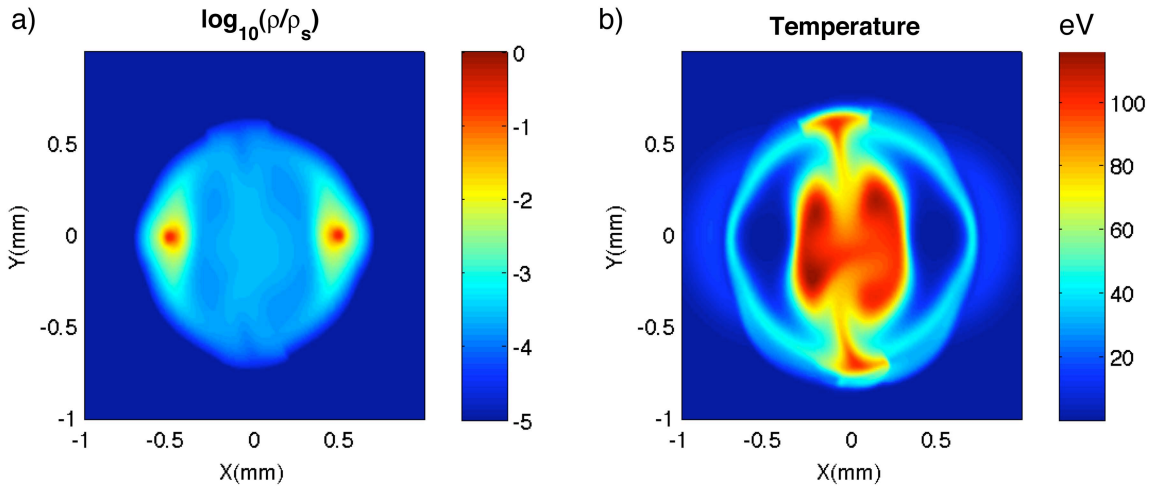

Figure 7.41: (Color) (a) Density predicted by PERSEUS at $t = 112ns$ with $\gamma = 1.15$. (b) Temperature predicted by PERSEUS at the corresponding time.

energy using the effective adiabatic index to the total measured internal energy

$$\frac{p}{\gamma_{eff} - 1} = \frac{p}{\frac{5}{3} - 1} + \epsilon_Z \tag{7.12}$$

where we have assumed $\gamma = 5/3$ to calculate the internal energy on the right hand side. This is valid because the ionization term is present and therefore no correction is needed when calculating the energy. Substituting $\epsilon_Z = 2\left(\frac{p}{5/3-1}\right)$ we find $\gamma_{eff} = 1.22$ which should approximately account for ionization in the internal energy, however it ignores the substantial losses due to radiation during ionization.

Figure 7.41 shows the density and temperature predicted by PERSEUS in a new simulation with $\gamma = 1.22$ at $t = 112ns$ corresponding to the time when the image from COBRA shot 2034 was taken. There is still obvious disagreement in the structure of the plasma. The density, fig. 7.41(a), is lower than that predicted by the GA, and shown in fig. 7.27(b), except in the vicinity of the wire cores. Additionally, the plasma is much wider in the y-direction, however the

lower areal density could potentially account for this. The peak temperature, fig. 7.41(b), is about 4 times higher and the spatial distribution is very different than that inferred by the GA. The plasma expanding from the center line along the x-direction into the colder core material is significantly heated which is not seen in the experiment. This heating is likely produced by the collision between the cold core material and the hot material exploding from the central region which is driven by thermal expansion. Since we expect that ionization and radiation will "eat up" a large portion of the internal energy budget, it makes sense that the model would over estimate the expansion of material in the center.

Additionally, the cold material near the wire core occupies a much larger region than the experimental data indicates. This feature, in particular, is likely to be sensitive to the inclusion of losses. The ablation of material and subsequent heating in the coronal plasma will depend predominantly on the transfer of ohmic energy by processes like radiation and conduction, the relative importance of which depend on temperature and ionization state[76]. We also know that the cold core material is very weakly ionized, so a lot of ionization must occur as plasma is ablated, which requires a significant amount of energy and will likely affect the dynamics.

Acknowledging that the dynamics are different between the experiment and simulation, we can use these simulation results, with the empirically determined adiabatic index, to compare the internal energy. Figure 7.42(a) shows the total internal energy, calculated experimentally as the sum of the internal and ionization energies. The simulated internal energy is shown in fig. 7.42(b). We can readily see that the internal energy in the simulation is approximately a factor of $2-3$ *less* than the measured energy. At first thought this is surprising, since the temperature is approximately 4 times higher in the simulation than

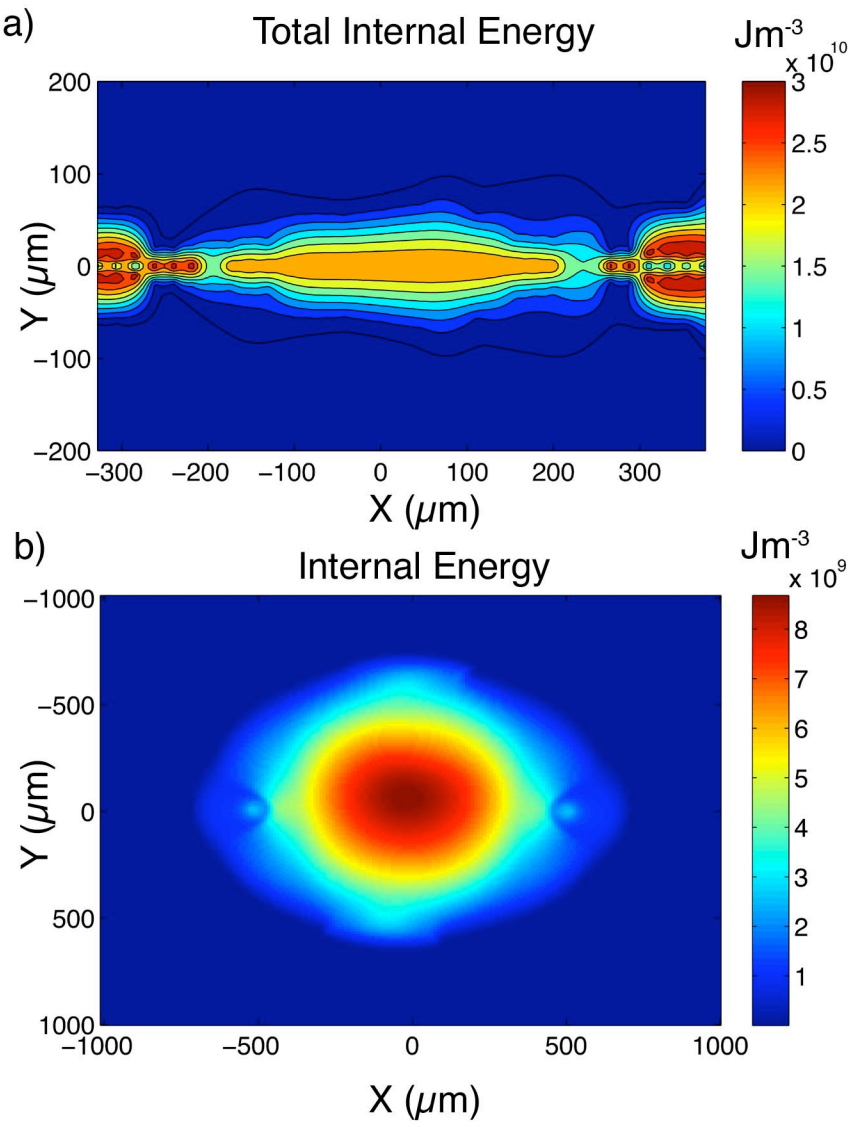

Figure 7.42: (Color) Total internal energy, including ionization, measured from the experimental data.

the experiment. However, the density is more than an order of magnitude less at the same position. Clearly, the expansion of the plasma is playing a more important role in determining the energy density than the temperature.

It is obvious from the above results that the physics missing in PERSEUS is important in our experiment. Ionization is a leading candidate for resolving the discrepancies. However, as we just saw, this will not completely reconcile the data. The addition of radiation, especially excitation radiation that goes hand-in-hand with ionization, and thermal conductivity in the model would certainly lower the peak temperatures and therefore reduce the pressure. There are also issues related to the entropy formulation employed by PERSEUS that could be affecting the dynamics, particularly if shocks are present. However, there are no signs of shocks in the experimental results.

We must admit that there is one way that the lack of an experimental measurement could be partially responsible for the experimental-computational disagreement: the current through the object was not measured on each shot and the current density profile is not measured at all. Since the current waveform is an input to the code, and is the only energy generation mechanism, the simulated dynamics will be very sensitive to it. In order to compare simulation results to experimental data in a meaningful way the experimental current density should be well characterized.

CHAPTER 8

CONCLUSIONS

8.1 Summary & Discussion

This work has focused on the development of a new diagnostic technique, point-projection x-ray absorption spectroscopy, in pulsed power HED science and application of this technique to the study of exploding wire plasmas. The development of this technique involved significant changes to the experiment and diagnostic design compared with previous x-ray absorption spectroscopy studies. The diagnostic was first fielded on the XP generator, which allowed us to optimize the setup for imaging the wire plasmas, scan a broad range of wavelengths and probe different loads. Once we felt we had learned enough about the operation of the diagnostic it was moved to COBRA. The COBRA experiments included a separate measurement of the backlighter spectrum and a calibration step wedge. These additional steps allowed us to determine the absolute transmission through the object plasma with approximately ±17% average error, including both detector (film) noise and calibration error.

Prior to this work, x-ray absorption spectroscopy had never been implemented using an x-pinch as the backlighter source. The x-pinch produces an extremely bright, short duration ($\sim 100ps$) burst of x-rays[68, 69]. The $1.45 - 2.0keV$ free-bound continuum from a Mo-wire X-pinch is emitted by a very small source region, typically $< 5\mu m$, allowing extremely high spatial resolution when used as a source for point-projection x-ray radiography[62, 64]. We found in Sec. 4.1 that the spectrum of x-rays emitted by the x-pinch in the range $7Å - 8.4Å$ ($1.45keV - 1.75keV$) is dominated by continuum radiation and shows no

identifiable spectral features. This, combined with the brightness, duration and source size, makes the x-pinch an ideal radiation source for point-projection x-ray absorption spectroscopy. The smooth backlighter spectrum avoids errors in the transmission measurement introduced by unresolved backlighter features, which were shown by Iglesias *et al.* to significantly degrade the quality of opacity measurements using a short pulse laser to produce the backlighter x-ray source [31].

We are also the first, to our knowledge, to use a spherically bent crystal as the dispersive element in an absorption spectroscopy scheme. The spherically bent crystal is able to focus x-rays in both the spatial and spectral directions, allowing for improved spatial and spectral resolution over flat or singly curved crystal x-ray spectrometers[54]. We measured our spectral resolution to be $\lambda/\Delta\lambda \sim 5000$, which is the highest reported in this type of experiment. This resolution has enabled us to see details in the K-shell absorption satellite lines of Al that have not been observed previously.

The spatial resolution of our diagnostic was measured to be about $20\mu m$. Although better resolution than this might be expected considering the small source size of the x-pinch, this is more than adequate for imaging the plasmas of interest in this study. We believe that the degradation in resolution is due primarily to crystal imperfections and film noise. This could be improved in a number of ways, such as increasing the magnification or using a less sensitive film with a smaller grain size.

Using this diagnostic we were able to observe a correlation between the structure of the wire core as seen in radiographs and the spectral profile in the vicinity of the Al K-edge as a function of radius. We first noticed that this spectral profile was distinctly different when Al alloy 5056 was used and compared

with pure Al in single wire tests on XP. The corresponding radiographs showed that Al 5056 wires develop a tube-like structure in the residual wire core, while pure Al wires develop a density profile that is peaked on axis. In the pure Al absorption spectrum, a region was visible, approximately the diameter of the densest part of the wire core, where a very broad (about 0.06Å wide) transition from strong to weak absorption was observed rather than a sharp K-edge. Outside of this small radius core, the absorption quickly became dominated by line absorption. First Mg- and Na-like Al, then giving way to Ne-like Al at larger radius. The Al 5056 absorption spectrum showed a larger radius wire core where the K-edge was still sharp, indicating the temperature was less than $2eV$. This region had a diameter approximately equal to that of the tube-like wire core in the radiograph. As the radius increased, the absorption transitioned over a distance of about $30\mu m$ to absorption by Ne- and F-like Al lines. This suggest that the state of the material changes over a very short distance from dense and cold (possibly still with a substantial fraction of neutral Al) to much more tenuous plasma with a temperature of $10eV$ or greater.

The spectra presented in this study constitute the first time the individual lines of the Al satellite groups have been observed. This is made possible through the use of the spherically bent crystal and the small source size of the x-pinch backlighter. The agreement in the $1s - 3p$ satellite lines observed between the SCRAM calculations and the experimental spectra is remarkable considering the lack of previous work.

The width of the Ne-like line at 7.886Å was shown to vary with distance from the wire core. It is proposed that this is due primarily to Stark broadening, and therefore is potentially useful as a density diagnostic. By assuming that the FWHM of the line is due entirely to Stark and employing an approximate Stark

broadening formula we have estimated the electron density in the vicinity of the wire core. The variation of n_e with position is seen to agree qualitatively with the density as a function of distance from a wire core in previous studies of W wire array z-pinches using x-ray radiography.

We developed a genetic algorithm to interpret the spectra in terms of plasma conditions and size. This optimization routine allowed us to account for variation in the plasma conditions along the line of sight of the spectrometer by using multiple plasma regions, each of which is represented by an electron temperature, mass density and path length. We have shown convergence tests which lead us to believe the algorithm is reliable. Though the solution determined by the GA is not unique, it is constrained by several conditions that ensure it is physically reasonable. We have determined the error in temperature is approximately ±25%, in density is approximately −50%/+100% and in path length is ±40%.

Using the GA we observed peak temperatures of $29 \pm 7eV$ in the plasma collecting at the center line between two wires. We did not observe an increase in density at this location. This may be because there is none in this configuration or that there is not enough sensitivity to density to observe the compression. We did observe an increase in the thickness of the hotter plasma at the center line compared with the ablation streams moving away from the wires. this suggests that the thermal pressure in the plasma collecting at the center line is greater than the magnetic pressure, allowing it to expand, instead of piling up and compressing as is known to happen in cylindrical wire-array z-pinches. This may be due to the low current in the experiment, $150kA$ peak. An alternative explanation is the lack of cylindrical symmetry in the two-wire configuration. In a cylindrical wire array, streams from each of the wires provide momentum

from all directions to contribute to the confinement of the precursor column. In the two-wire case, opposing streams exist in only one plane, allowing plasma to move perpendicular to the ablation streams as it collects on the center line.

Near the wire core we observed the highest densities, $\sim 10^{20} ions/cm^3$, along with lower temperatures, $5 \pm 1.5 eV$. The Ne- and Na-like $1s-3p$ absorption lines proved to be indispensable in interpreting the spectra in this range of plasma condtions due to their sensitivity to density and temperature. We were also able to infer the existence of the hotter coronal plasma surrounding the wire core with temperatures of $12eV$ to $20eV$.

Finally, comparison with PERSEUS calculations revealed strong disagreement. We showed that the energy invested in ionization is greater than the internal energy and comparable to the kinetic energy in our experiment. Simulations with different values of γ showed qualitatively different dynamics. This suggests that ionization must be included in the model in order to approximate the evolution of the experiment appropriately. Inclusion of radiation and thermal conduction is also likely to be important for obtaining good agreement between experiments and simulations. Additionally, experimental improvements need to be made to better characterize the structure of the plasma and the driving conditions in order to compare the experiment with simulation results in a meaningful way.

8.2 Future Possibilities

Absorption spectroscopy opens many opportunities for new avenues of study at the Laboratory of Plasma Studies. Further work is needed to map the time-

dependent behavior of the coronal and precursor plasmas. We believe we have laid the groundwork for such studies to be conducted. Because the charge state distribution is directly accessible, absorption spectroscopy is ideal for studying non-LTE atomic physics such as photoionization and beam-driven processes. In addition, the study of shocks shows promise for discovery. In particular, LPS has the ability to create high Mach number, magnetized flows of tenuous plasma, which makes the study of collisionless shocks particularly interesting. It may also be possible to produce shocks in plasmas in which Hall effects are significant. This opens the possibility of exploiting the advantages of PERSEUS to study two-fluid effects. All such areas of study require the development of diagnostics to field in tandem with the spectrometer, especially independent measurements of the electron and/or ion density. These would constrain the parameter range that could be used to fit the spectra, allowing for higher accuracy in the spectroscopically determined plasma temperature to be achieved.

Another potential use of this diagnostic is for velocity measurements. Because of the high spectral resolution of our spectrometer we should be able to measure relatively small doppler shifts in plasmas that do not emit x-rays, such as ablation streams and jets. The ability to identify different charge states opens the possibility to discriminate if each ion has a different velocity.

Finally, the high spectral resolution means that line shape measurements may be very useful with this diagnostic. The crude approximation to stark broadening employed in this work is one obvious area where detailed line shape calculations can be applied. This will give an electron density measurement independent of that determined by the fitting algorithm, which can help constrain the fit. Additionally, if the object can be adequately characterized by independent diagnostics, line shape approximations can be tested and mech-

anisms other than stark broadening can be investigated.

The discovery of the change in structure of the Al K-edge with the state of the wire core warrants specific mention. Quantitative study of the material properties of the wire core has eluded us to date. Because x-rays are able to penetrate the coronal plasma, absorption spectroscopy shows promise for finally uncovering some of the secrets hidden within. A properly designed experiment should be able to measure the structure of the K-edge as long as the areal density can be kept small enough for the absorption to remain unsaturated above the K-edge, a necessity for quantitative study. It is known that the wire core remains in a multi-phase state for much of the duration of the current pulse, which will certainly complicate interpreting the spectra.

With the introduction of the MagLIF concept at Sandia National Labs, this study may be of particular relevance. With wire array z-pinches, the residual wire core is thought of as a mass source, the details of which are not considered to be particularly important to the physics of x-ray generation at stagnation. In the MagLIF design, an ohmically heated dense metal liner compresses the fuel directly. Understanding, and potentially manipulating, the state of this liner material will be crucial to the success of this concept. Quantitative study of the wire core material may prove useful in pursuit of this goal.

APPENDIX A

COMPLETE LIST OF XP EXPERIMENTS AND DATA

Table A.1: List of experiments performed on XP. In the image column a "Y" indicates that an image was obtained and a "N" indicates that none was obtained. In addition "SE" indicates that self-emission was significant, "UE" indicates that the image was underexposed and "defect" indicates that there was an unknown defect in the image. In the object column "(F)" indicates the sample was placed in the far position as described in sec: 5.1. For all other shots the sample was in the close position. The "DBL" column indicates whether a direct backlighting radiograph was obtained on the shot.

Shot#	**XP**	**Object**	**Bandwidth**	**Image**	**DBL**
5735	4x40μm Mo	2x25μm Al (F)	7.6 – 8.28Å	Y	N
5736	4x40μm Mo	2x40μm Al (F)	7.6 – 8.28Å	Y	N
5739	4x66μm Al	None	7.6 – 8.28Å	Y	N
5744	4x40μm Mo	2x25μm Al (F)	7.6 – 8.28Å	N	N
5745	4x40μm Mo	2x25μm Al (F)	7.6 – 8.28Å	Y	N
5746	4x40μm Mo	2x12μm Al (F)	7.6 – 8.28Å	Y	N
5747	4x40μm Mo	2x40μm Al (F)	7.6 – 8.28Å	Y	N
5748	4x40μm Mo	2x40μm Al (F)	7.6 – 8.28Å	N	N
5750	4x40μm Mo	2x40μm Al (F)	7.6 – 8.28Å	Y	N
5751	4x40μm Mo	1x17μm Al (F)	7.6 – 8.28Å	Y	N
5753	4x40μm Mo	2x40μm Al	7.6 – 8.28Å	Y	N
5754	4x40μm Mo	2x40μm Al	7.6 – 8.28Å	Y	N

Continued on next page

Shot#	XP	Object	Bandwidth	Image	DBL
5755	4x40μm Mo	1x40μm Al	7.6 – 8.28Å	Y	N
5756	4x40μm Mo	1x40μm Al	7.6 – 8.28Å	Y	Y
5783	4x40μm Mo	1x38μm Al 1199	7.57 – 8.23Å	Y/SE	Y
5784	4x40μm Mo	4x40μm Al	7.57 – 8.23Å	Y	Y
5785	4x40μm Mo	1x38μm Al 1199	7.57 – 8.23Å	Y/SE	Y
5786	4x40μm Mo	1x40μm Al	7.57 – 8.23Å	Y/SE	Y
5789	4x40μm Mo	2x25μm Al	7.57 – 8.23Å	Y	Y
5790	4x40μm Mo	2x25μm Al	7.57 – 8.23Å	Y	Y
5791	4x40μm Mo	2x25μm Al	7.57 – 8.23Å	Y	Y
5792	4x40μm Mo	2x25μm Al	7.57 – 8.23Å	Y/UE	N
5802	4x40μm Mo	2x25μm Al	7.55 – 8.19Å	Y	Y
5803	4x40μm Mo	2x25μm Al	7.4 – 8Å	Y/defect	Y
5804	4x40μm Mo	2x25μm Al	7.4 – 8Å	Y	Y
5844	4x40μm Mo	2x25μm Al, 1mm	7.9 – 8.37Å	Y	Y
5845	4x40μm Mo	2x25μm Al, 1mm	7.95 – 8.5Å	Y	Y
5846	4x40μm Mo	2x25μm Al, 1mm	7.85 – 8.35Å	Y	Y
5850	4x40μm Mo	2x17μm Al, 1mm	7.55 – 8.2Å	Y	Y

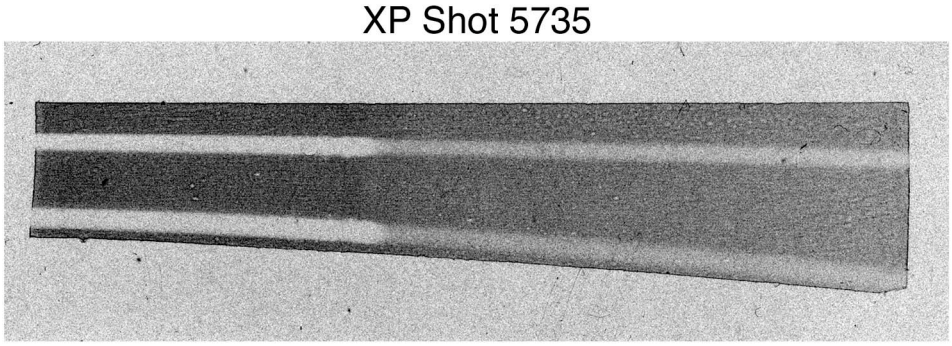

Figure A.1: Absorption spectrum obtained on XP shot 5735.

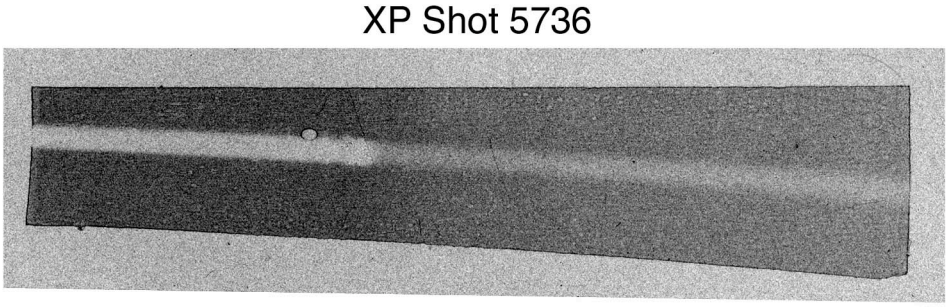

Figure A.2: Absorption spectrum obtained on XP shot 5736.

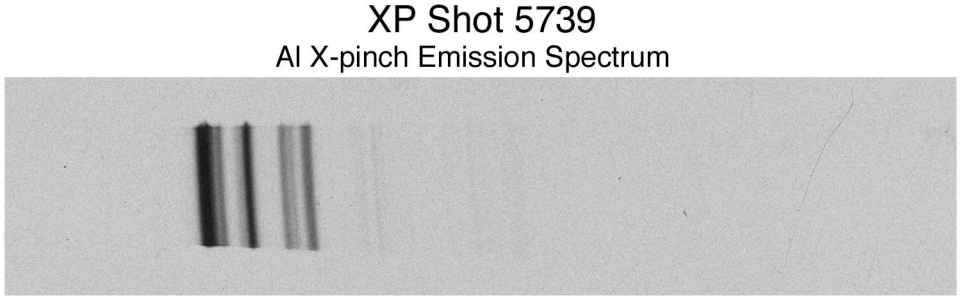

Figure A.3: Emission spectrum from an Al x-pinch obtained on XP shot 5739.

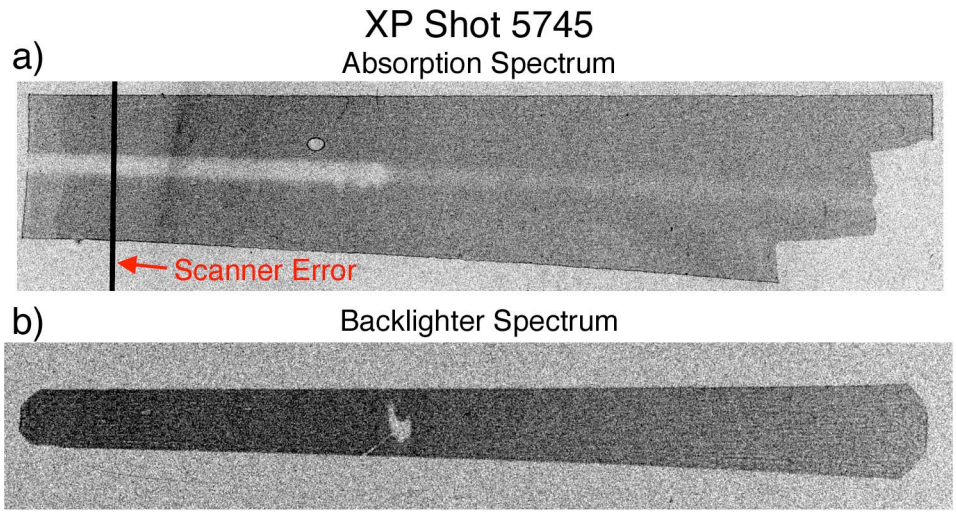

Figure A.4: (a) Absorption spectrum obtained on XP shot 5745. The vertical black line is a defect that occurred during scanning. (b) Unattenuated backlighter spectrum obtained using a second spectrometer on the same shot.

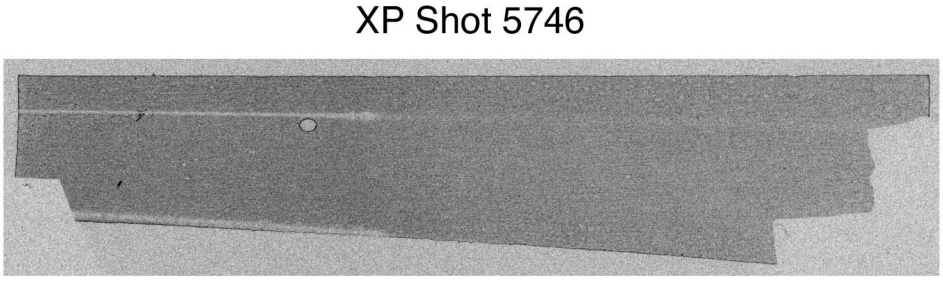

Figure A.5: Absorption spectrum obtained on XP shot 5746.

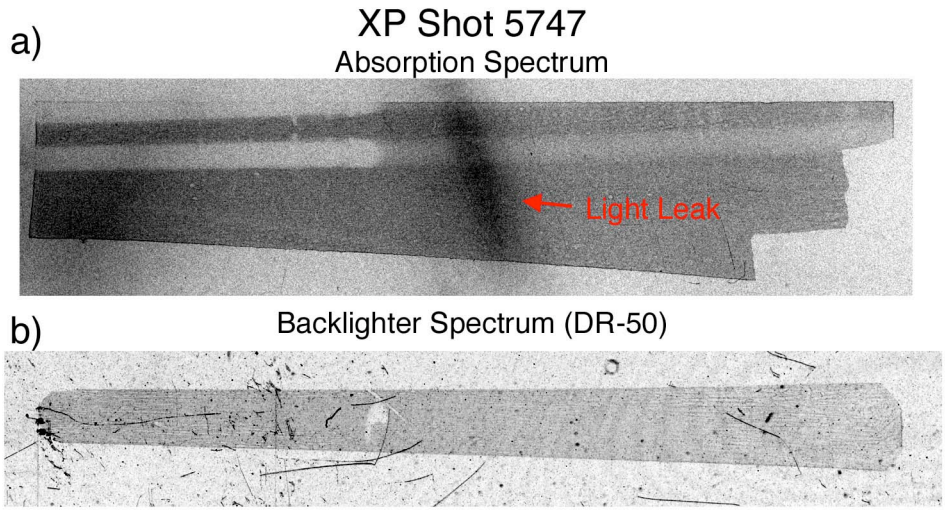

Figure A.6: (a) Absorption spectrum obtained on XP shot 5747. The black region in the center of the image is due to a light leak in the filter. (b) Unattenuated backlighter spectrum obtained using a second spectrometer with Kodak DR-50 film as the detector on the same shot.

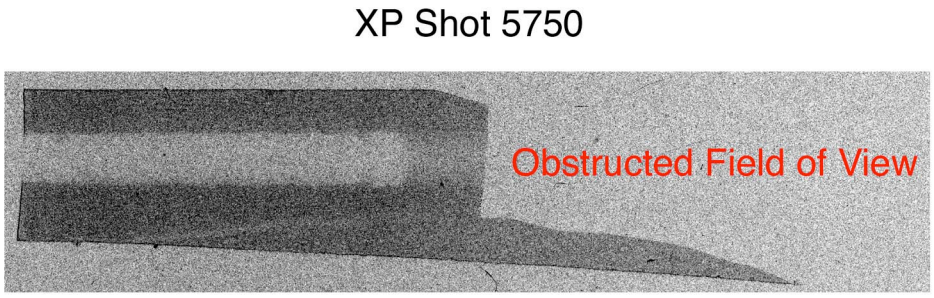

Figure A.7: Absorption spectrum obtained on XP shot 5750.

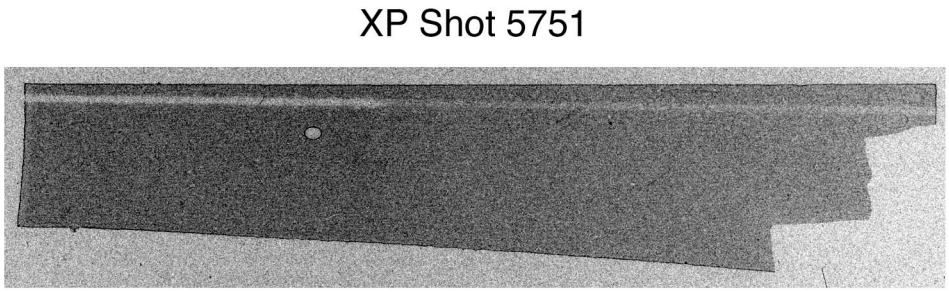

Figure A.8: Absorption spectrum obtained on XP shot 5751.

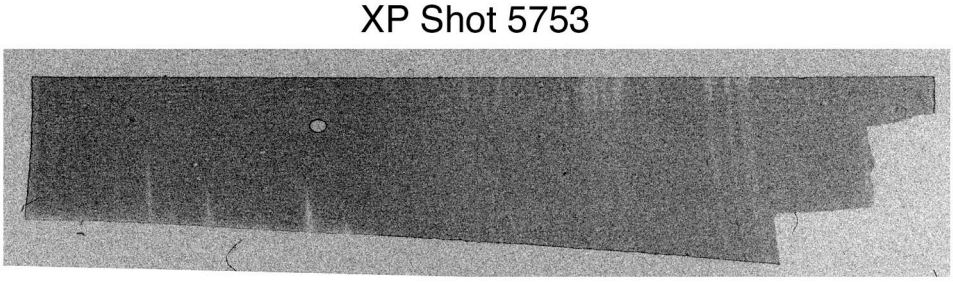

Figure A.9: Absorption spectrum obtained on XP shot 5753.

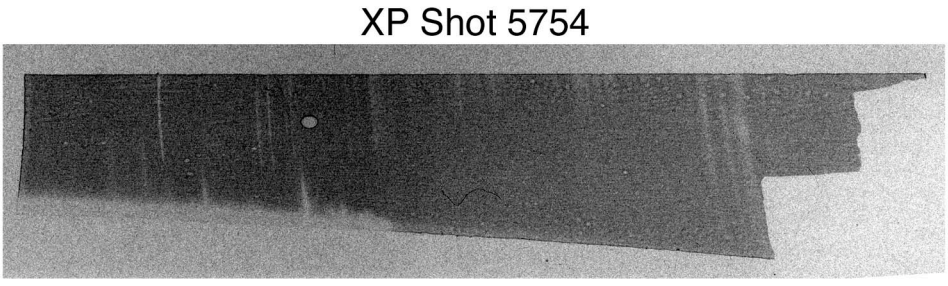

Figure A.10: Absorption spectrum obtained on XP shot 5754.

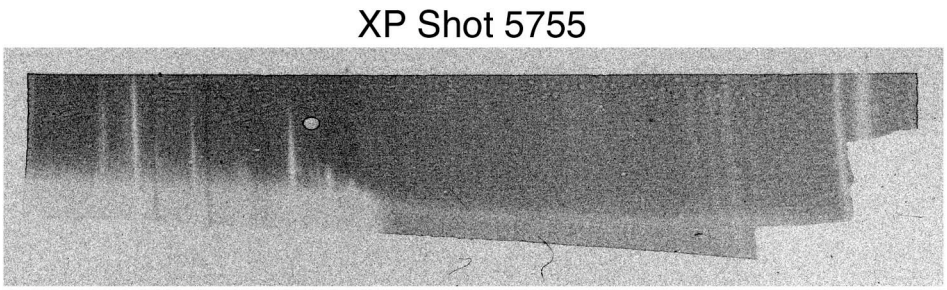

Figure A.11: Absorption spectrum obtained on XP shot 5755.

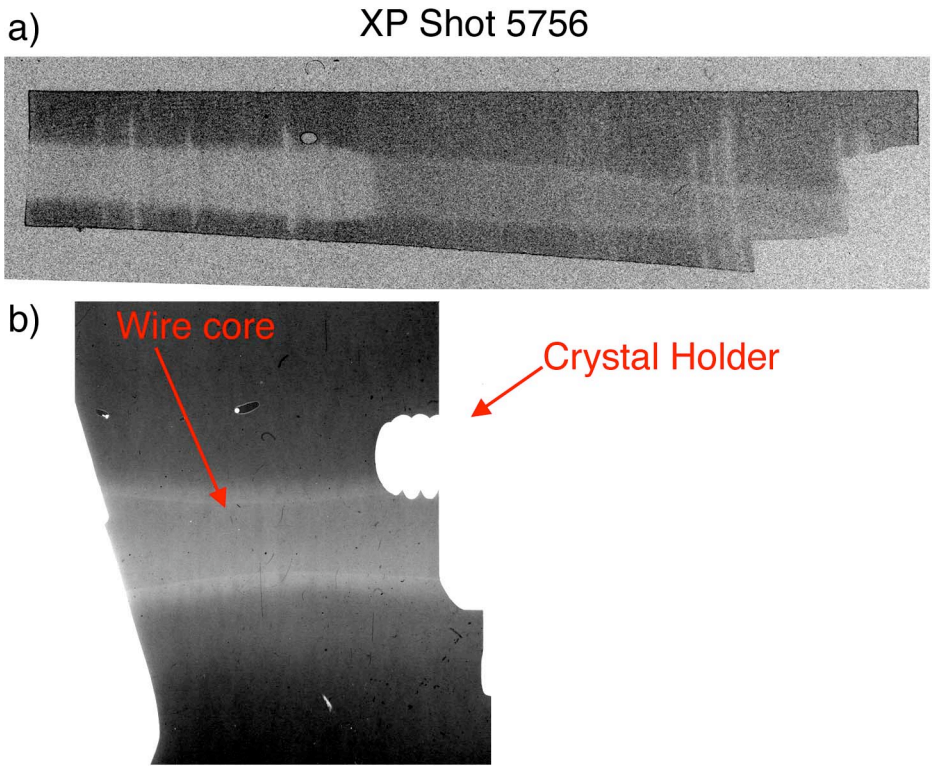

Figure A.12: (a) Absorption spectrum obtained on XP shot 5756. (b) Direct backlighting radiograph obtained on the same shot. The images of the crystal holder and wire core are marked.

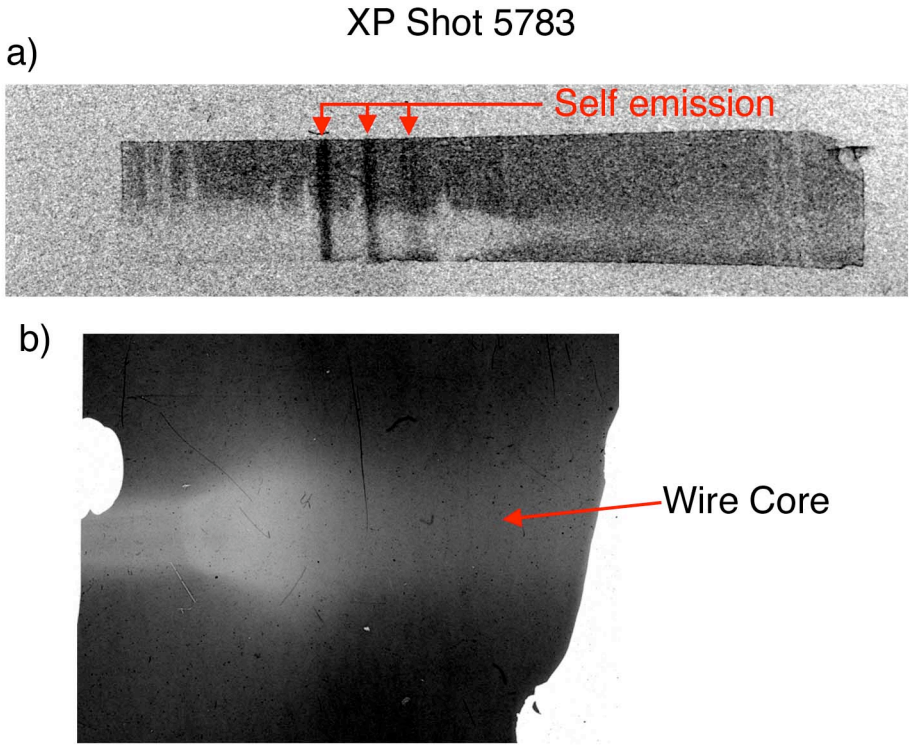

Figure A.13: (a) Absorption spectrum obtained on XP shot 5783. Self emission from the exploding wire is visible. (b) Direct backlighting radiograph obtained on the same shot. The image of the wire core is marked.

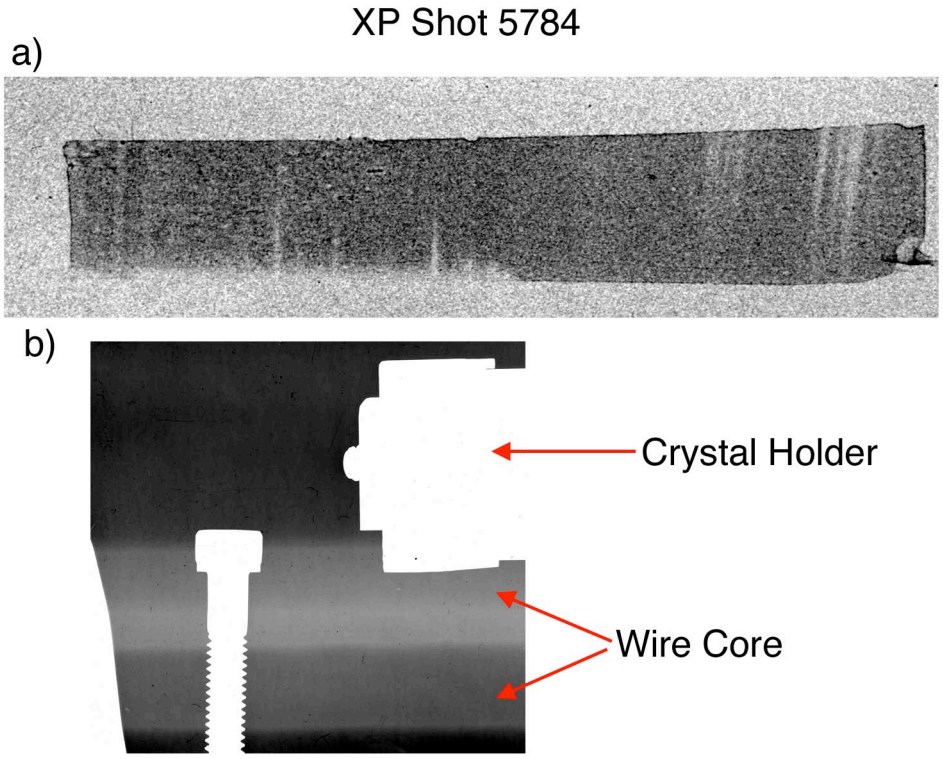

Figure A.14: (a) Absorption spectrum obtained on XP shot 5784. (b) Direct backlighting radiograph obtained on the same shot. The images of two visible wire cores and the crystal holder are marked.

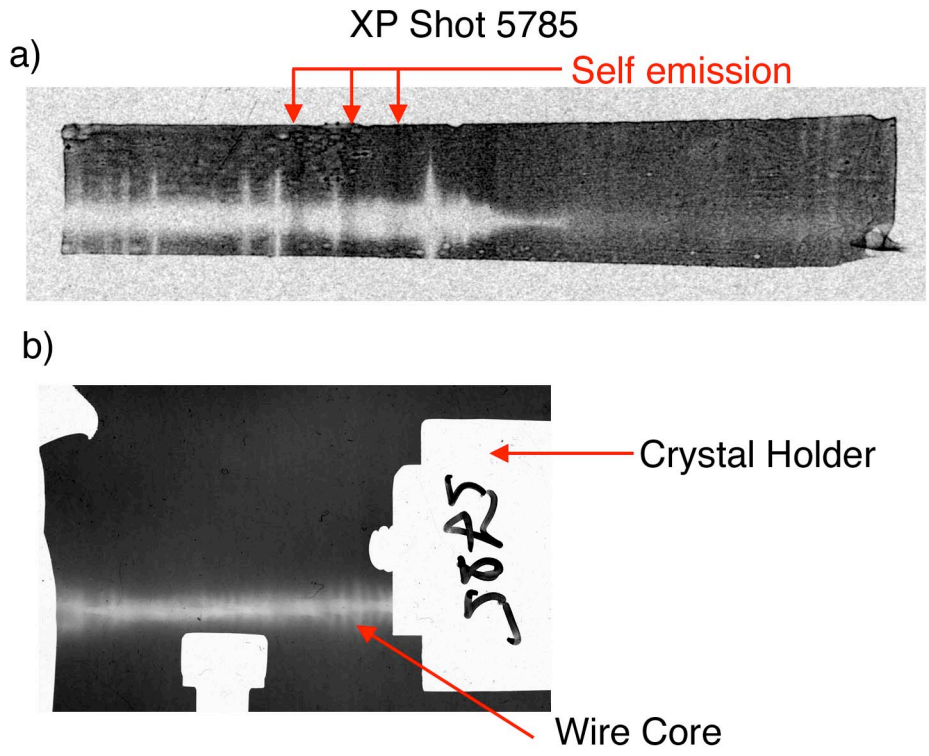

Figure A.15: (a) Absorption spectrum obtained on XP shot 5785. Self emission from the exploding wire is visible. (b) Direct backlighting radiograph obtained on the same shot. The images of the wire core and crystal holder are marked.

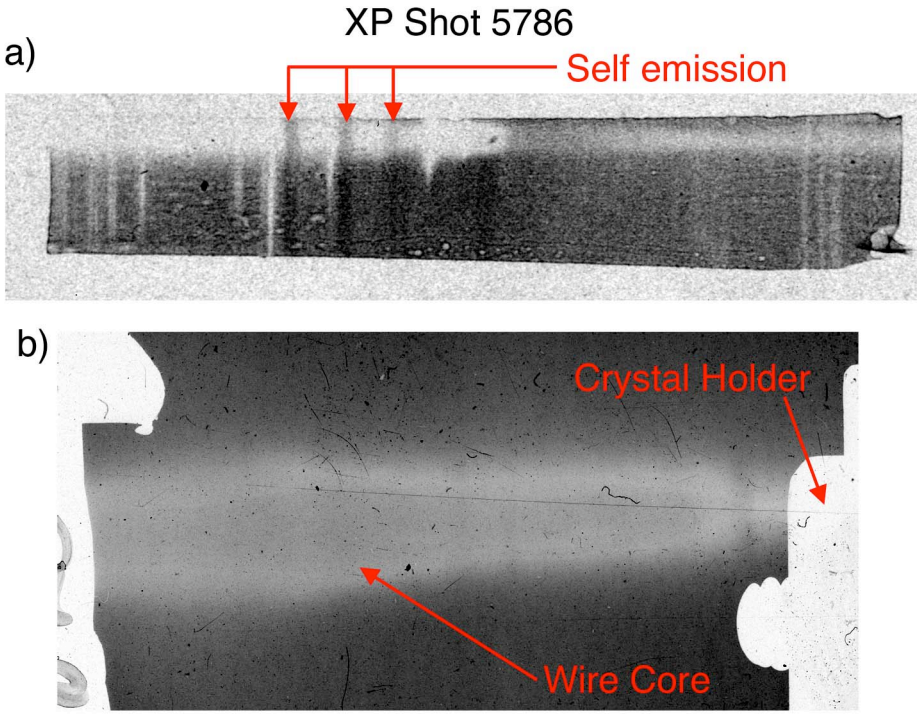

Figure A.16: (a) Absorption spectrum obtained on XP shot 5786. Self emission from the exploding wire is visible. (b) Direct backlighting radiograph obtained on the same shot. The images of the wire core and crystal holder are marked.

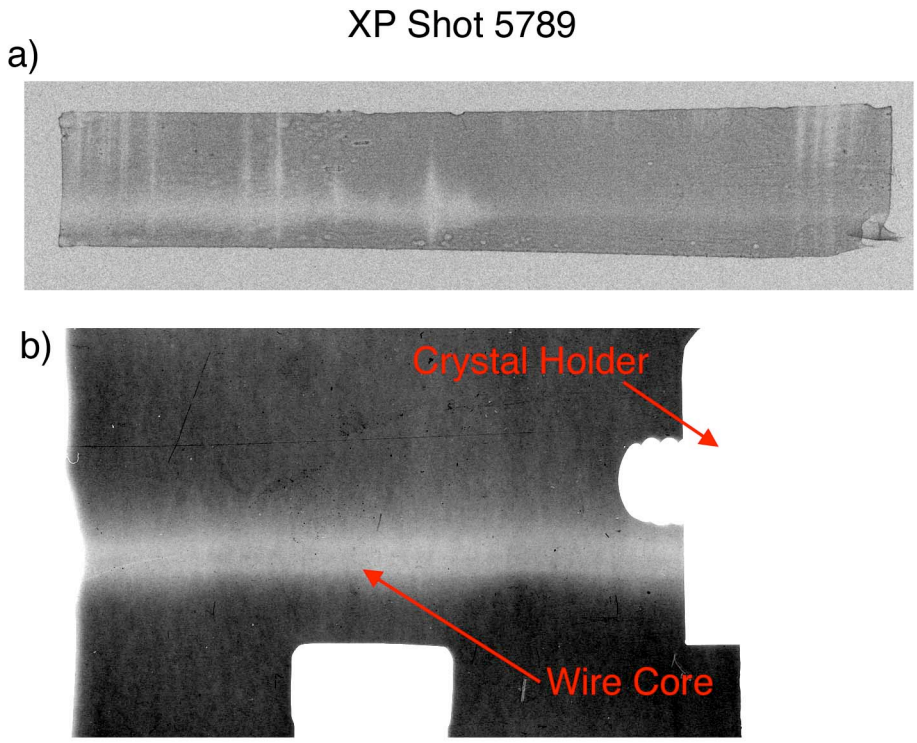

Figure A.17: (a) Absorption spectrum obtained on XP shot 5789. (b) Direct backlighting radiograph obtained on the same shot. The images of one of the wire cores and crystal holder are marked.

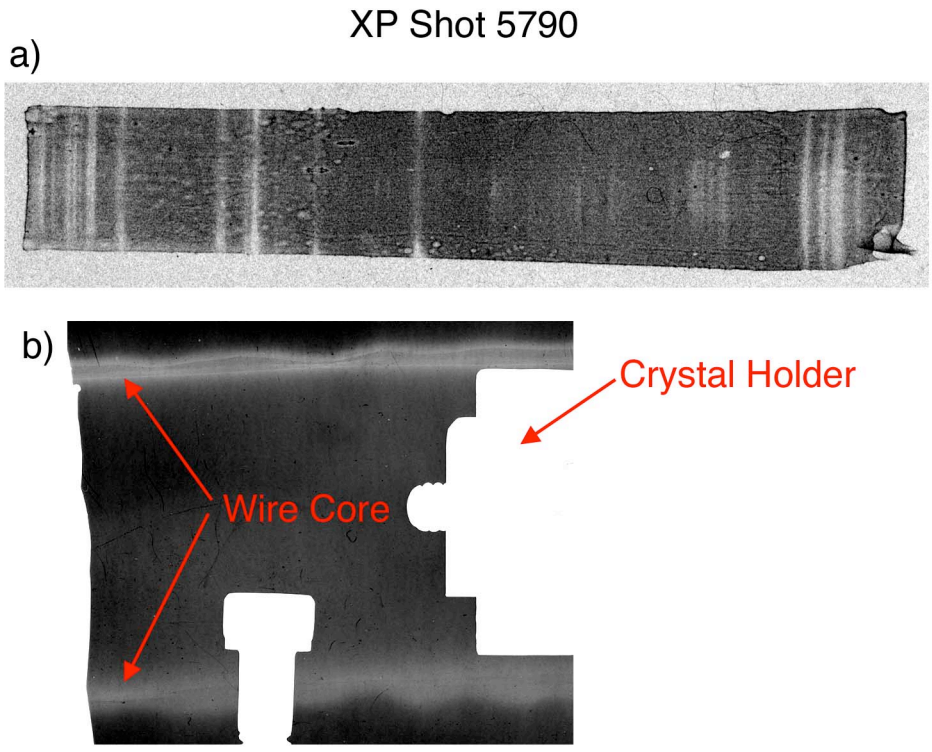

Figure A.18: (a) Absorption spectrum obtained on XP shot 5790. (b) Direct backlighting radiograph obtained on the same shot. The images of both of the wire cores and crystal holder are marked.

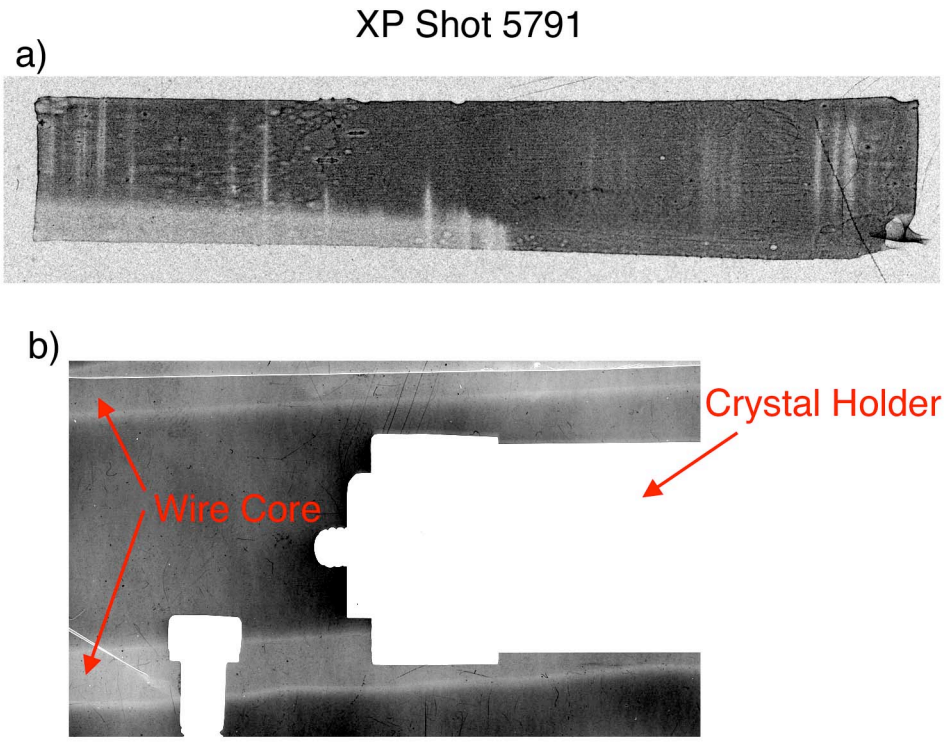

Figure A.19: (a) Absorption spectrum obtained on XP shot 5791. (b) Direct backlighting radiograph obtained on the same shot. The images of both of the wire cores and crystal holder are marked.

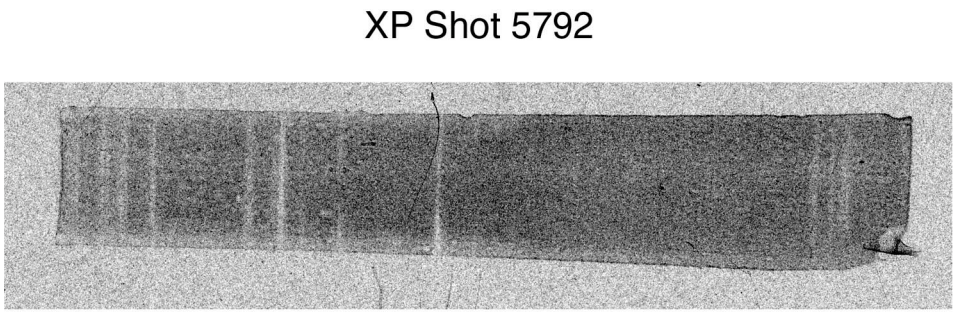

Figure A.20: Absorption spectrum obtained on XP shot 5792.

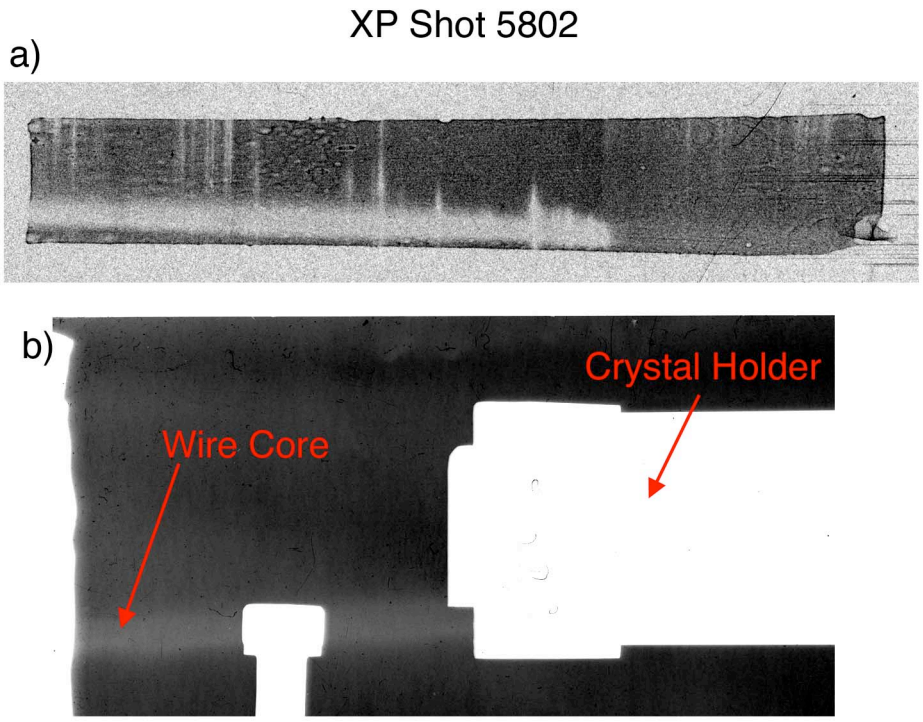

Figure A.21: (a) Absorption spectrum obtained on XP shot 5802. (b) Direct backlighting radiograph obtained on the same shot. The images of one of the wire cores and crystal holder are marked.

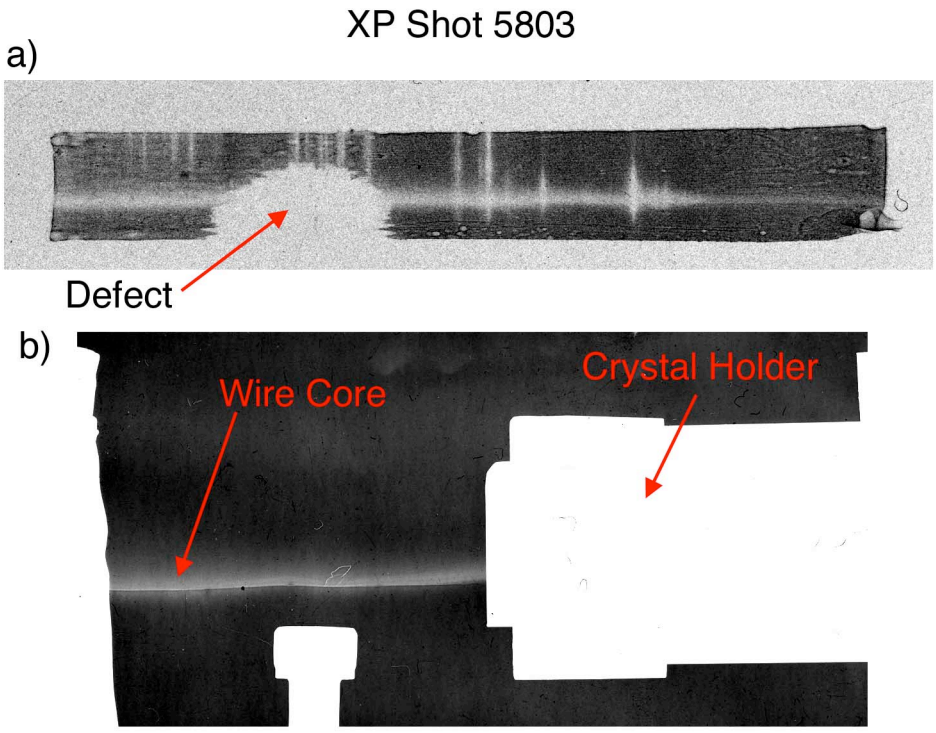

Figure A.22: (a) Absorption spectrum obtained on XP shot 5803. (b) Direct backlighting radiograph obtained on the same shot. The images of one of the wire cores and crystal holder are marked.

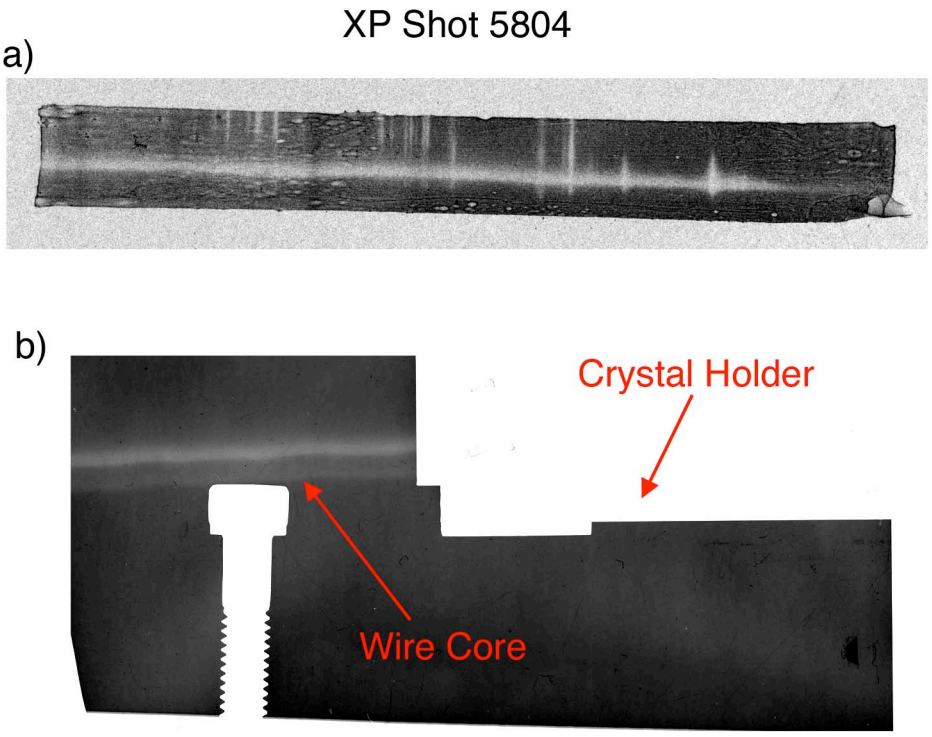

Figure A.23: (a) Absorption spectrum obtained on XP shot 5804. (b) Direct backlighting radiograph obtained on the same shot. The images of one of the wire cores and crystal holder are marked.

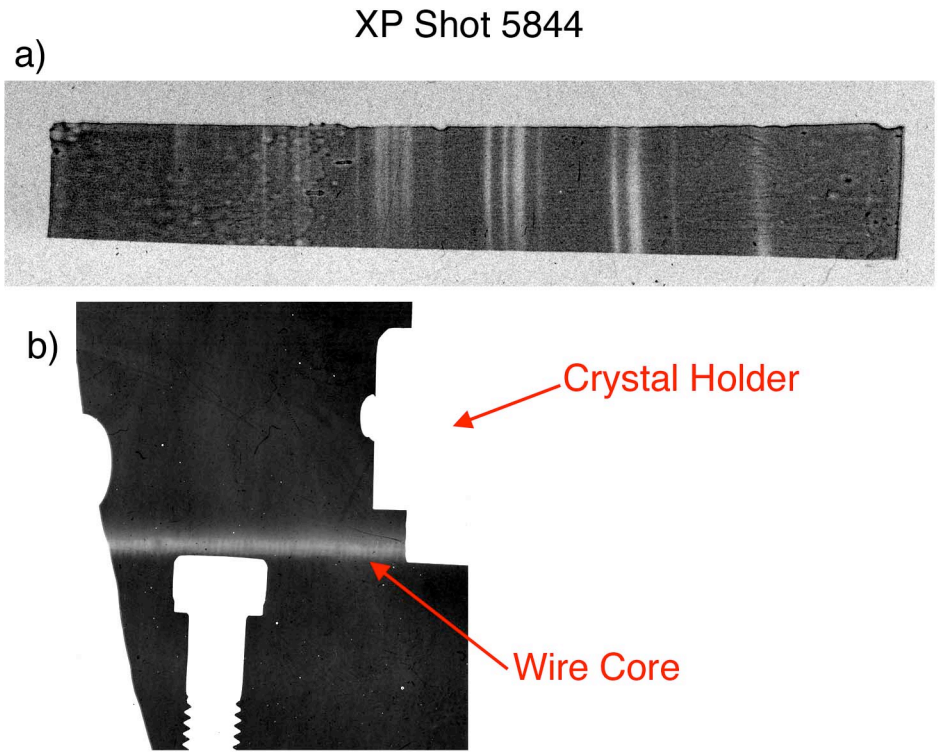

Figure A.24: (a) Absorption spectrum obtained on XP shot 5844. (b) Direct backlighting radiograph obtained on the same shot. The images of one of the wire cores and crystal holder are marked.

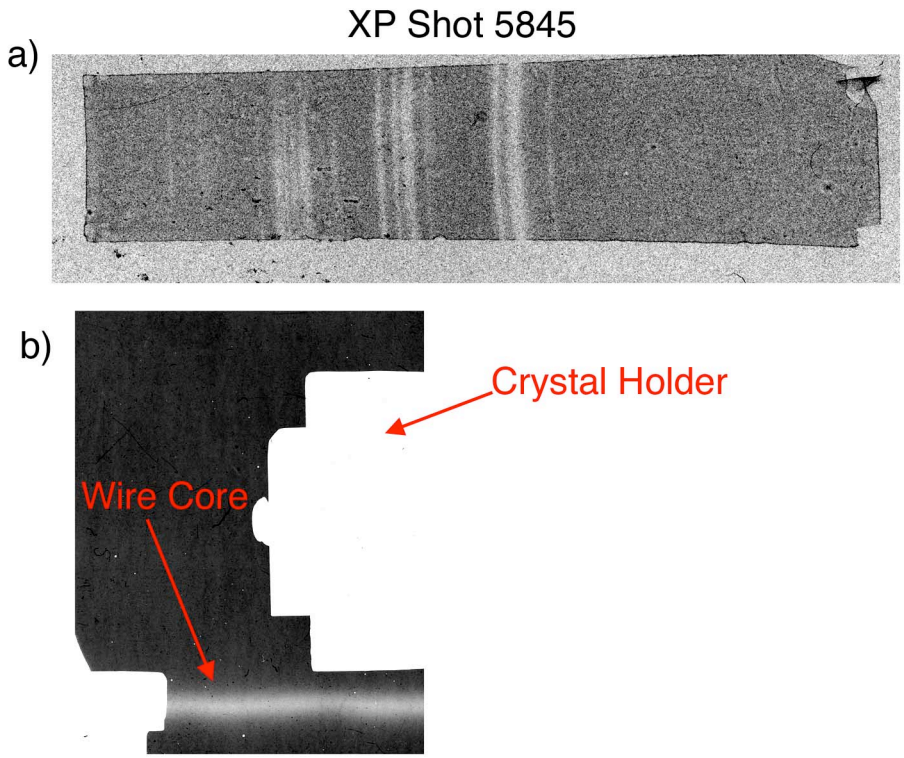

Figure A.25: (a) Absorption spectrum obtained on XP shot 5845. (b) Direct backlighting radiograph obtained on the same shot. The images of one of the wire cores and crystal holder are marked.

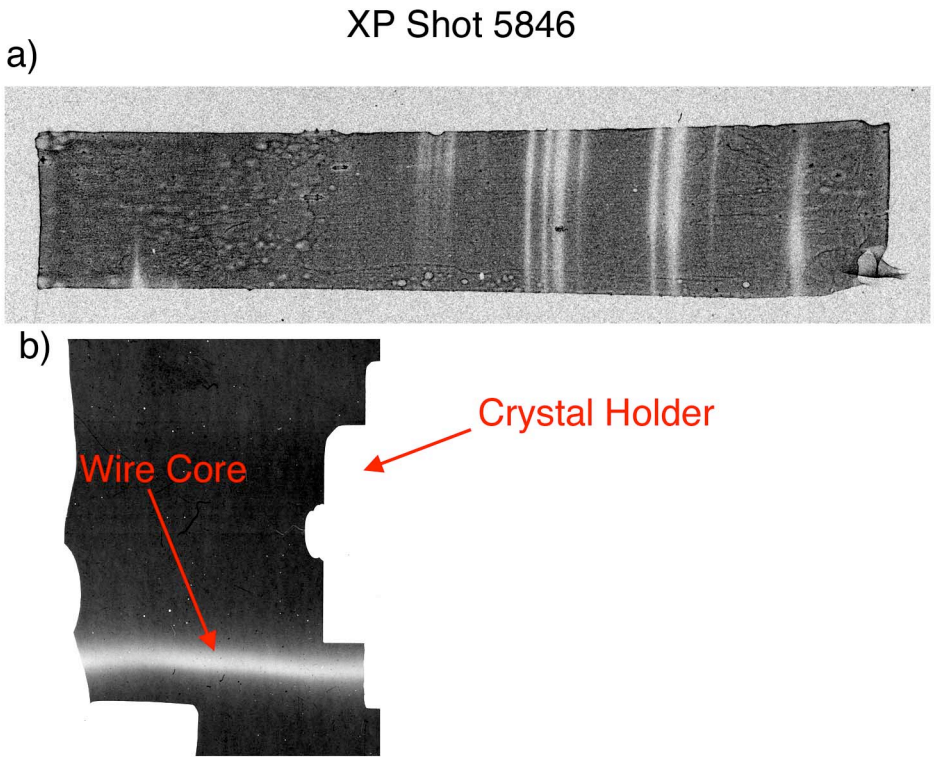

Figure A.26: (a) Absorption spectrum obtained on XP shot 5846. (b) Direct backlighting radiograph obtained on the same shot. The images of one of the wire cores and crystal holder are marked.

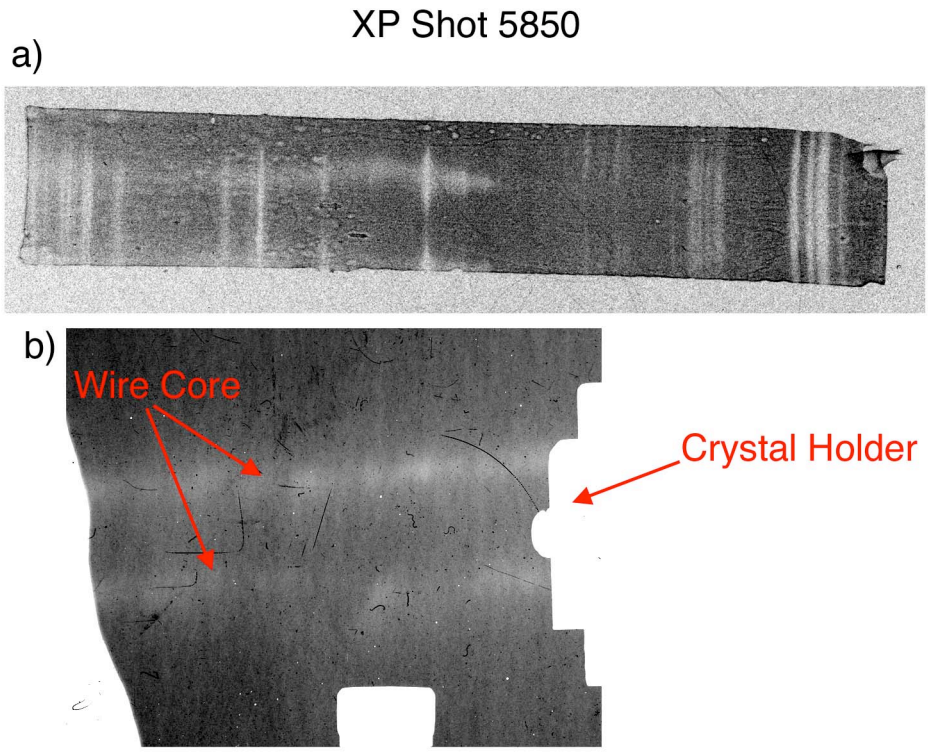

Figure A.27: (a) Absorption spectrum obtained on XP shot 5850. (b) Direct backlighting radiograph obtained on the same shot. The original locations of both of the wire cores and the image of the crystal holder are marked.

APPENDIX B

COMPLETE LIST OF COBRA EXPERIMENTS AND DATA

Table B.1: List of experiments performed on COBRA. A "†" next to the shot number indicates the absorbing sample was in the primary load and the x-pinch was in the return current. All others, the x-pinch was the primary load and the sample was in a return current rod gap. In the image column a "Y" indicates that an image was obtained, "SE" indicates that self-emission was significant, "UE" indicates that the image was underexposed and the "*" indicates that an image was obtained but the Be filter was broken so it was unusable. On most shots a Slit Step Wedge (SSW) camera, Open Pin Hole (OPH) camera and Direct BackLighting (DBL) images were obtained. This column indicates which were obtained for each shot.

Shot#	**XP**	**Object**	**Bandwidth**	**Image**	**SSW/OPH/DBL**
2018†	1x67μm Al	8mm short	N/A	Y	N/Y/Y
2019†	1x40μm Al	8mm short	N/A	Y/UE	N/Y/N
2020†	1x40μm Mo	$8 \times 33 \mu m$ Al	N/A	Y/SE	N/Y/Y
2021†	1x40μm Mo	$8 \times 33 \mu m$ Al	N/A	Y/SE	N/Y/N
2022†	1x40μm Mo	$8 \times 33 \mu m$ Al	N/A	Y/SE	N/Y/Y
2023†	1x35μm Mo	6mm short	N/A	Y	N/Y/Y
2024†	1x35μm Mo	6mm short w/mesh	N/A	Y	Y/Y/Y
2025†	1x35μm Mo	$8 \times 40 \mu m$ Al	N/A	Y/SE	Y/Y/Y
2026	1x152μm Mo	$1 \times 40 \mu m$ Al	N/A	Y/UE	Y/Y/Y
2027	1x152μm Mo	$1 \times 40 \mu m$ Al	N/A	N	Y/Y/Y
2028	1x152μm Mo	$1 \times 40 \mu m$ Al	N/A	Y*	Y/Y/Y
2029	1x152μm Mo	$2 \times 40 \mu m$ Al	N/A	N	Y/Y/Y
2030	1x152μm Mo	$2 \times 40 \mu m$ Al	7.5 – 8.2Å	Y	Y/Y/Y

Continued on next page

Shot#	XP	Object	Bandwidth	Image	SSW/OPH/DBL
2031	$1x152\mu m$ Mo	$2 \times 40\mu m$ Al	7.52 – 8.25Å	Y	N/Y/Y
2032	$1x152\mu m$ Mo	$2 \times 40\mu m$ Al	N/A	N	Y/Y/Y
2033	$1x152\mu m$ Mo	$2 \times 40\mu m$ Al	7.6 – 8.28Å	Y/UE	N/Y/Y
2034	$1x152\mu m$ Mo	$2 \times 40\mu m$ Al	7.6 – 8.28Å	Y	N/Y/Y
2035	$1x254\mu m$ Al	None	7.6 – 8.28Å	Y	N/N/N
2036	$1x152\mu m$ Mo	Mesh	7.6 – 8.28Å	Y	N/Y/Y
2110	$1x152\mu m$ Mo	Mesh	7.6 – 8.28Å	Y	N/N/N

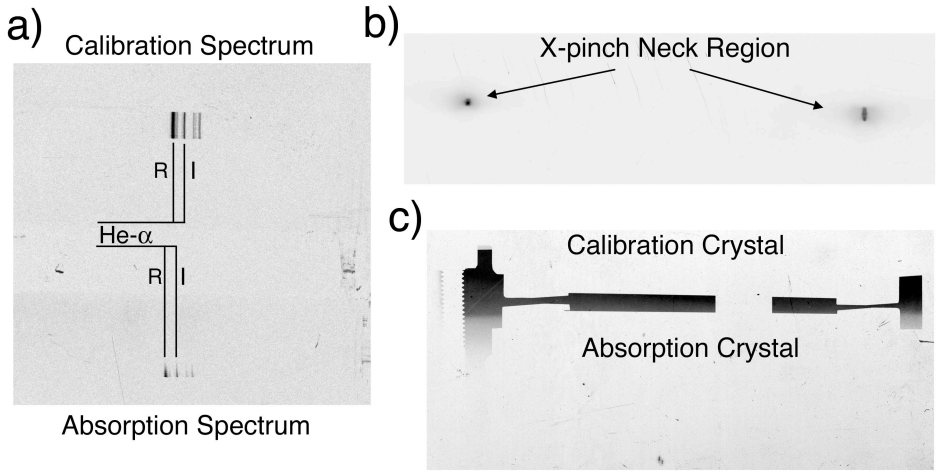

Figure B.1: (a) Emission spectra from an Al x-pinch obtained on COBRA shot 2018 from both crystals. (b) Open pin hole image showing the emission region of two of the three x-pinches. (c) Direct backlighting radiograph obtained on the same shot. The two crystal holders are marked.

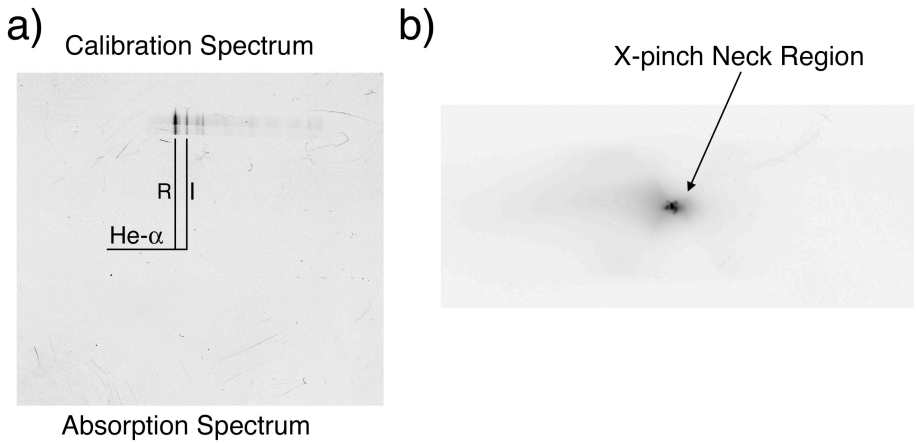

Figure B.2: (a) Emission spectrum from an Al x-pinch obtained on COBRA shot 2019 with the calibration crystal. The line of sight with the other crystal is blocked by the load. (b) Open pin hole image showing the emission region of one of the three x-pinches.

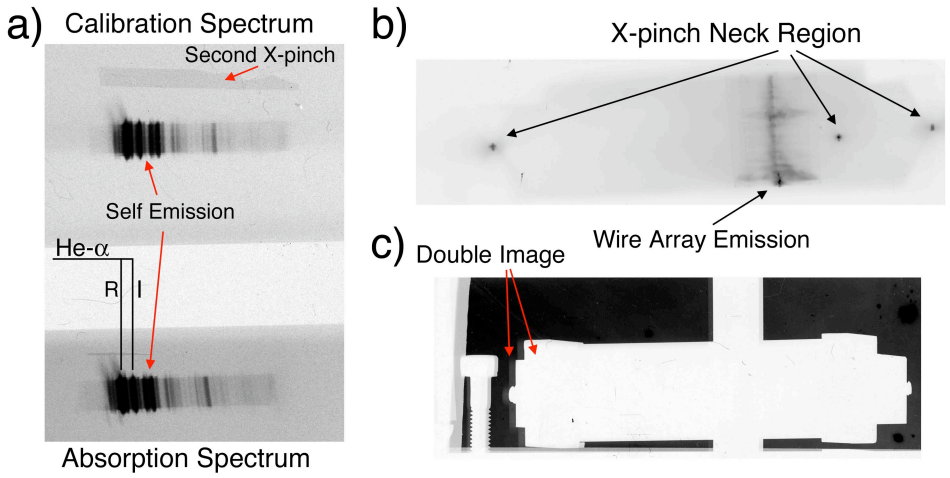

Figure B.3: (a) Spectra obtained on COBRA shot 2020 from both crystals. Self emission from the wire array is visible along with continuum from the x-pinch. Continuum emission from a second x-pinch is visible at the top of the film. (b) Open pin hole image showing the emission region of the three x-pinches as well as the wire array. (c) Direct backlighting radiograph obtained on the same shot. A double image is visible on this film.

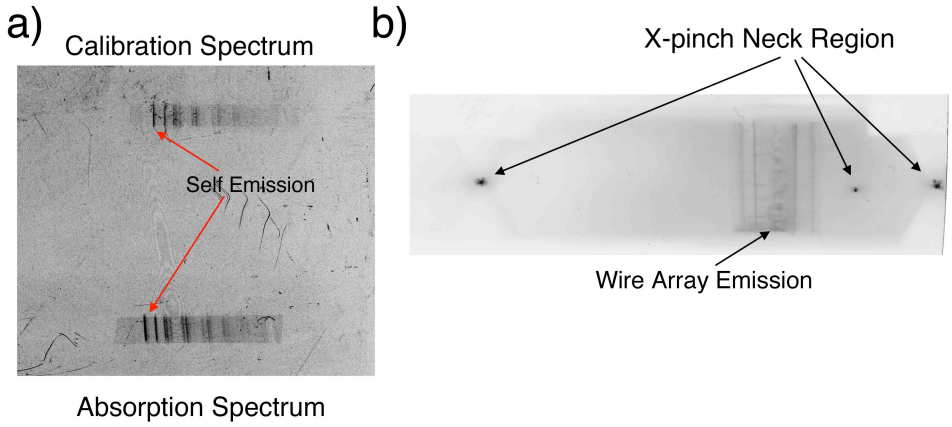

Figure B.4: (a) Spectra obtained on COBRA shot 2021 from both crystals. Self emission from the wire array is visible along with continuum from the x-pinch. (b) Open pin hole image showing the emission region of the three x-pinches as well as the wire array.

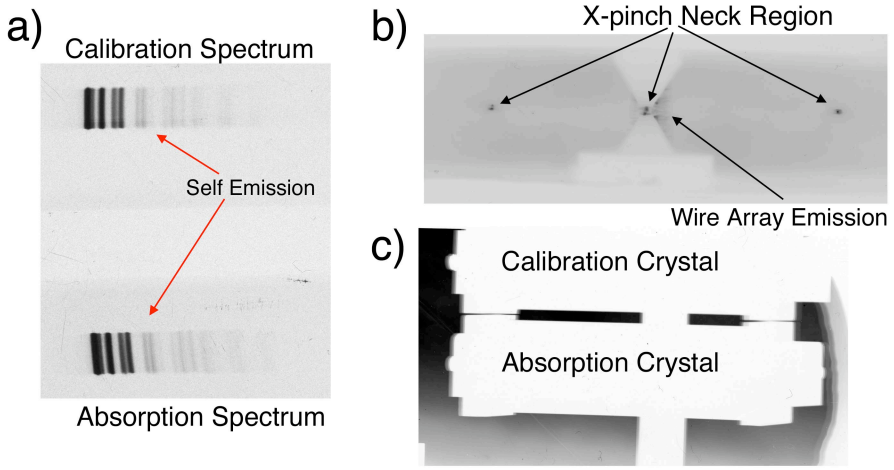

Figure B.5: (a) Spectra obtained on COBRA shot 2022 from both crystals. No continuum emission from the x-pinch is visible, only self emission from the wire array. (b) Open pin hole image showing the emission region of the three x-pinches as well as the wire array. (c) Direct backlighting radiograph obtained on the same shot. The calibration and absorption crystals are labeled.

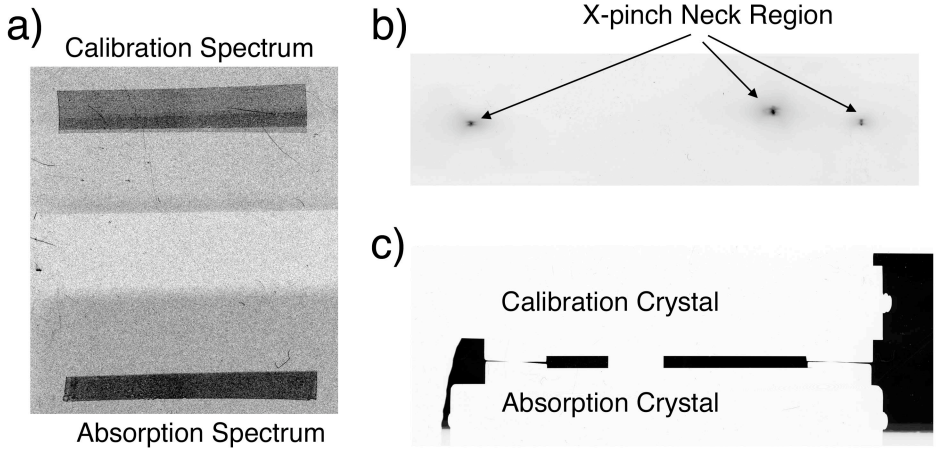

Figure B.6: (a) Continuum Spectra obtained on COBRA shot 2023 from both crystals. (b) Open pin hole image showing the emission region of the three x-pinches.s (c) Direct backlighting radiograph obtained on the same shot. The calibration and absorption crystals are labeled.

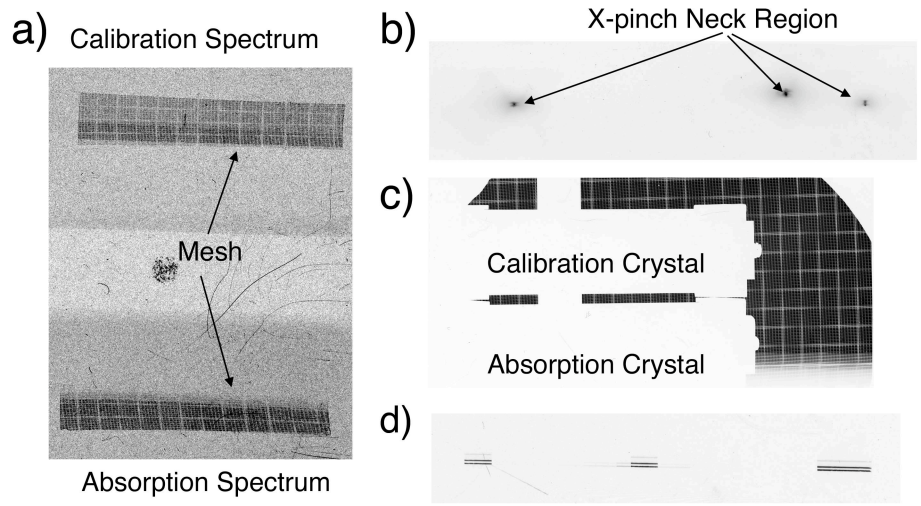

Figure B.7: (a) Continuum Spectra obtained on COBRA shot 2024 from both crystals. A mesh was used to estimate the spatial resolution. (b) Open pin hole image showing the emission region of the three x-pinches.s (c) Direct backlighting radiograph obtained on the same shot. The calibration and absorption crystals are labeled. (d) Slit step wedge camera image showing the three x-pinch x-ray bursts.

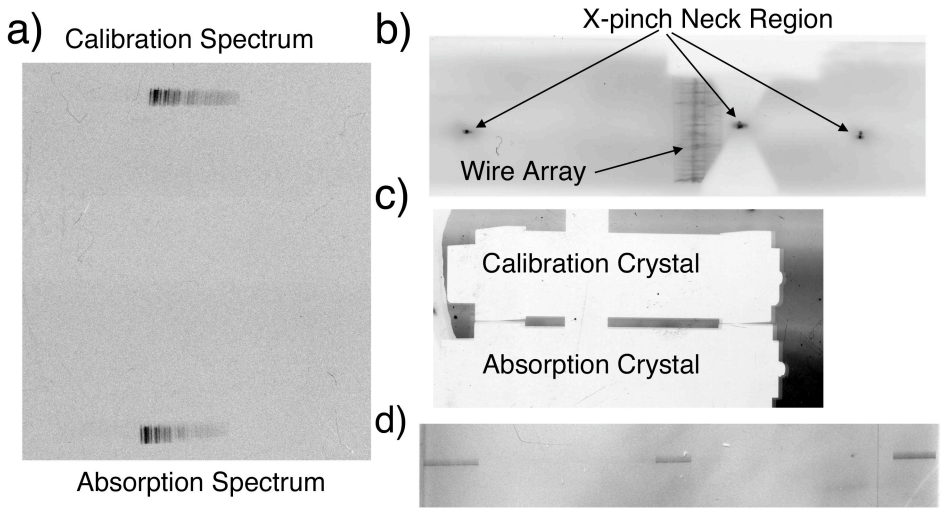

Figure B.8: (a) Spectra obtained on COBRA shot 2025 from both crystals. No continuum radiation from the x-pinch is visible, only self-emission from the array. (b) Open pin hole image showing the emission region of the three x-pinches and the wire array. (c) Direct backlighting radiograph obtained on the same shot. The calibration and absorption crystals are labeled. (d) Slit step wedge camera image showing that the three x-pinch x-ray bursts were relatively weak.

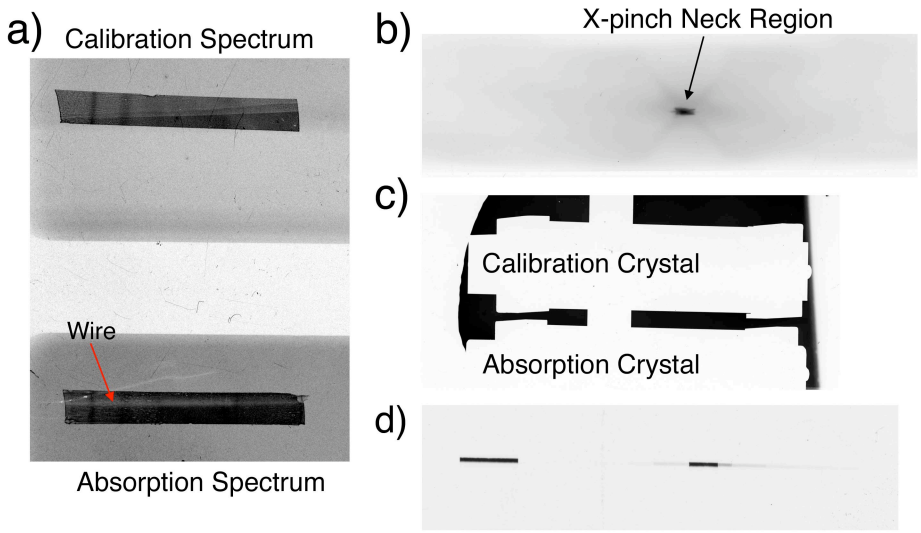

Figure B.9: (a) Absorption and calibration spectra obtained on COBRA shot 2026. (b) Open pin hole image showing the emission region of the x-pinch in the main load. (c) Direct backlighting radiograph obtained on the same shot. The calibration and absorption crystals are labeled. (d) Slit step wedge camera image showing a single x-pinch x-ray burst.

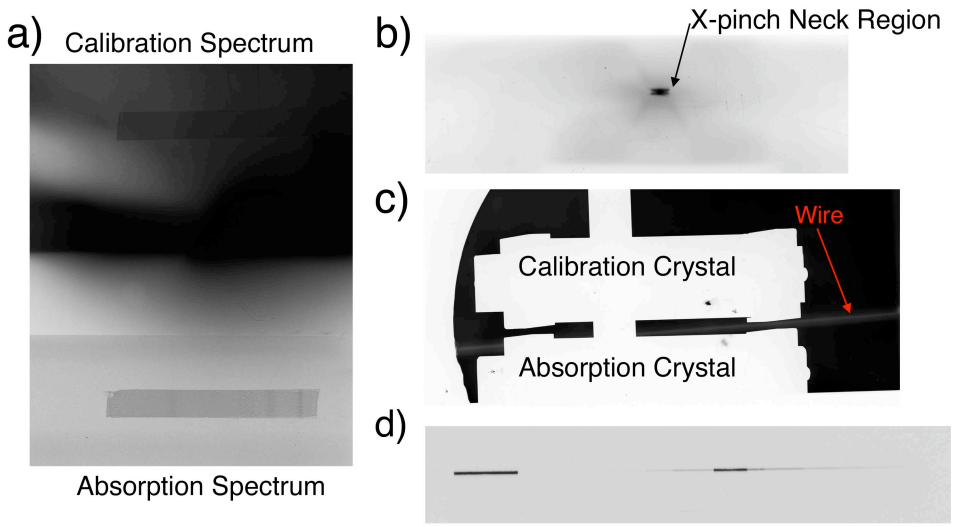

Figure B.10: (a) Absorption and calibration spectra obtained on COBRA shot 2028. The filter broke after the shot, exposing the film. (b) Open pin hole image showing the emission region of the x-pinch in the main load. (c) Direct backlighting radiograph obtained on the same shot. The calibration and absorption crystals are labeled. The wire core is also labeled. (d) Slit step wedge camera image showing a single x-pinch x-ray burst.

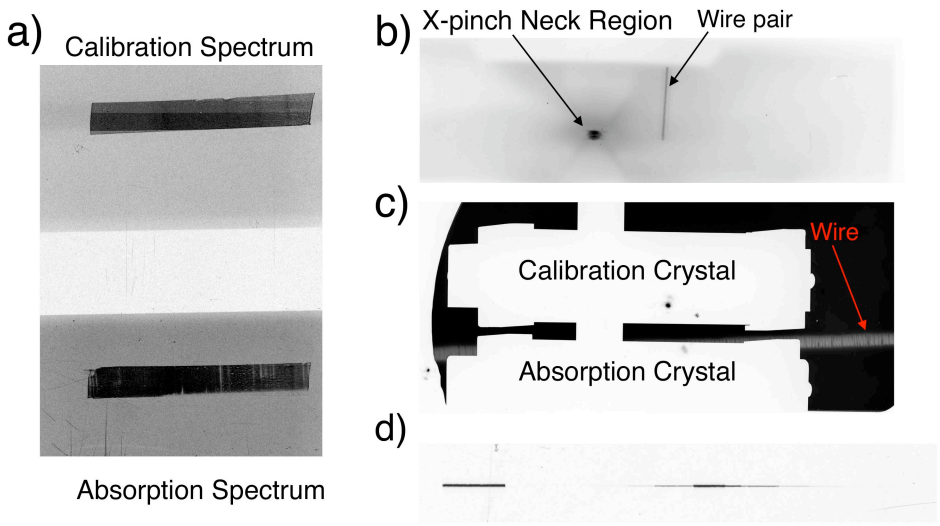

Figure B.11: (a) Absorption and calibration spectra obtained on COBRA shot 2030. (b) Open pin hole image showing the emission region of the x-pinch in the main load and the wire pair in the return current. (c) Direct backlighting radiograph obtained on the same shot. The calibration and absorption crystals are labeled. The wire core is also labeled. (d) Slit step wedge camera image showing a single x-pinch x-ray burst.

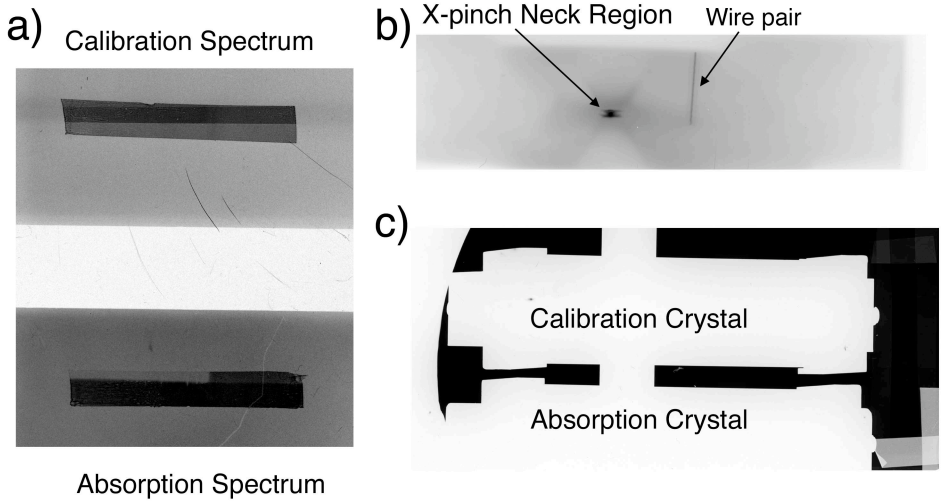

Figure B.12: (a) Absorption and calibration spectra obtained on COBRA shot 2031. (b) Open pin hole image showing the emission region of the x-pinch in the main load and the wire pair in the return current. (c) Direct backlighting radiograph obtained on the same shot. The calibration and absorption crystals are labeled.

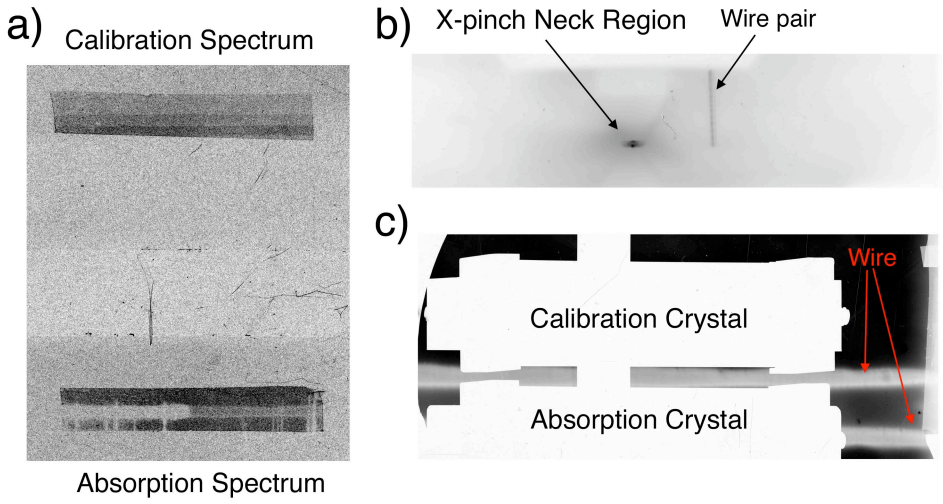

Figure B.13: (a) Absorption and calibration spectra obtained on COBRA shot 2033. (b) Open pin hole image showing the emission region of the x-pinch in the main load and the wire pair in the return current. (c) Direct backlighting radiograph obtained on the same shot. The calibration and absorption crystals are labeled. The wire cores are also labeled.

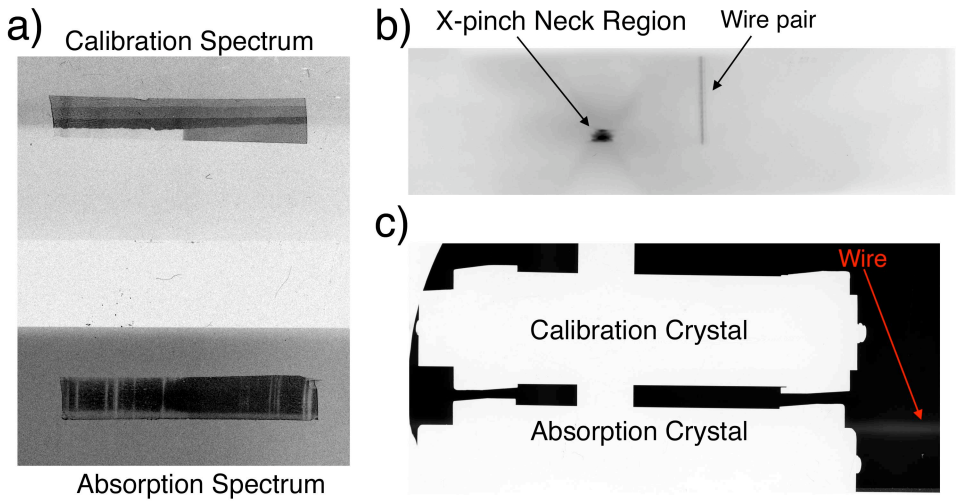

Figure B.14: (a) Absorption and calibration spectra obtained on COBRA shot 2034. (b) Open pin hole image showing the emission region of the x-pinch in the main load and the wire pair in the return current. (c) Direct backlighting radiograph obtained on the same shot. The calibration and absorption crystals are labeled. The wire core is also labeled.

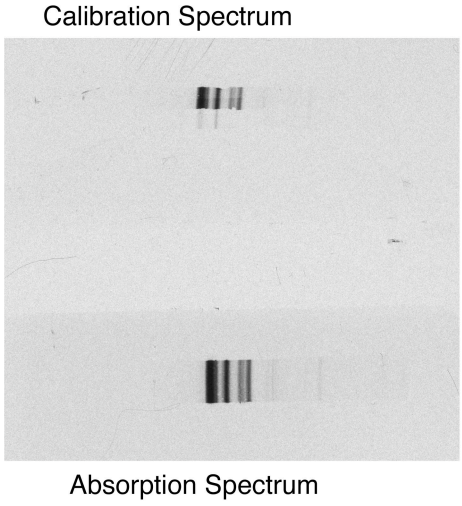

Figure B.15: Emission spectra obtained from both crystals using an Al x-pinch on COBRA shot 2035.

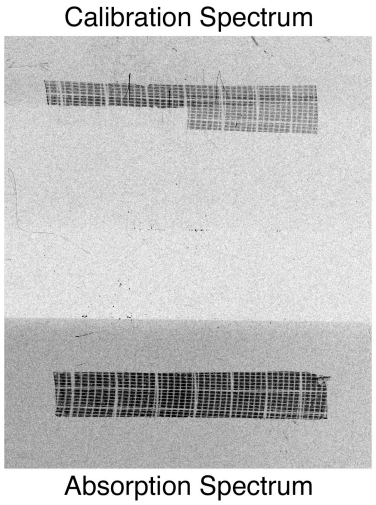

Figure B.16: Backlit image of a fine wire mesh obtained from both crystals using an Mo x-pinch on COBRA shot 2036.

APPENDIX C

RAY TRACING METHODOLOGY AND PROGRAM

C.1 Methodology

Ray tracing is a numerical method used to compute the path of a ray of light through possibly many reflections on its way to a detector. Typically many such rays are traced through the system and an image is compiled. The characteristics of the reflecting surfaces determine the intensity and spectral characteristics of the reflected ray. In general, rays can be traced from the source to the detector, or backwards from the detector to the source. For complicated systems with many objects it is more efficient to perform backwards ray tracing. In the program discussed here the forward method is employed.

The system is initialized by defining a source volume, a reflecting surface, which in our case is a spherically bent crystal, and a detector. The source can be any simple geometric shape. The most useful types are a sphere, representing an isotropic emitter and a cylinder, approximating a z-pinch. A point is randomly chosen within the source volume and on the surface of the crystal. These two points define the incident ray , **I**. The reflected ray, **R**, is simply computed using the following relationship

$$\mathbf{R} = \mathbf{I} - 2(\hat{\mathbf{n}} \cdot \mathbf{I})\mathbf{I} \tag{C.1}$$

where $\hat{\mathbf{n}}$ is the unit normal vector inward from the surface of the crystal. We note that this relationship is independent of dimension or crystal geometry. Since it does not exploit any specific properties of the crystal this program can be used with virtually any type of spectrometer and any number of elements. The normal vector is computed by taking the cross product of two vectors on the

surface of the crystal, again preserving generality.

We use the Bragg condition to determine which wavelengths are reflected in the current ray. Rewriting the Bragg condition in terms of the angle made between the incident ray and the surface normal, ϕ_i, and setting the order of reflection equal to one we obtain for the reflected wavelength

$$\lambda_B = 2d\cos(\phi_i) = 2d\hat{\mathbf{n}} \cdot \mathbf{I}/\mathrm{I} \tag{C.2}$$

where I is the magnitude of the incident ray.

To first order we can assume that only the wavelength satisfying the Bragg condition is reflected. Therefore given an incident spectrum, $I_{\lambda,i}$, we can write the reflected spectrum as

$$I_{\lambda,r} = \int_0^\infty I_{\lambda,i}\delta(\lambda - \lambda_B)d\lambda \tag{C.3}$$

This equation evaluates the intensity of the input spectrum only at the Bragg wavelength, λ_B, and transmits it along the relfected ray. In reality the reflection is not perfect due to distortions and imperfections in the crystal lattice. This degree of imperfection is characteristic to a given crystal material and is called the rocking curve. The effect of the rocking curve can be seen by examining what happens when a divergent source impinges the crystal. Each ray leaving the source has a solid angle $d\Omega$ associated with it and therefore strikes the crystal surface with a finite distribution of incidence angles. Due to imperfections in the lattice the Bragg condition can be satisfied for multiple angles in a small window about θ_B, and all of these rays are transmitted into the reflected ray. The rocking curve determines how these reflections are weighted by angle and is typically approximated as a gaussian centered at θ_B with FWHM $\epsilon \sim 0.1^\circ$. A prototype rocking curve function is shown below.

$$W(\theta - \theta_B) = \sqrt{2}Ge^{-2\pi G^2(\theta-\theta_B)^2} \tag{C.4}$$

where G is a constant normalizing the integral of W over all angles to be unity and contains the FWHM of the gaussian.

$$G = \frac{2}{\epsilon}\sqrt{\frac{\ln 2}{2\pi}} \tag{C.5}$$

In the present situation we are dealing with perfect rays, i.e. divergence free. However, every ray transmitted from the source contains the entire incident spectrum, so we can transform $W(\theta - \theta_B)$ into a function of λ by substituting the Bragg condition for θ and replacing θ_B with the incidence angle.

$$W(\lambda) = \sqrt{2}Ge^{-2\pi G^2(\sin^{-1}(\lambda/2d)-\theta_i)^2} \tag{C.6}$$

Now, we can replace the Dirac-delta function in eqn. C.3 with the new rocking curve in terms of lambda and obtain a new expression for the reflected intensity which incorporates the imperfect crystal

$$I_{\lambda,r} = \int_0^\infty I_{\lambda,i}W(\lambda)d\lambda = \int_0^\infty I_{\lambda,i}\sqrt{2}Ge^{-2\pi G^2(\sin^{-1}(\lambda/2d)-\theta_i)^2}d\lambda \tag{C.7}$$

By keeping θ_i fixed and evaluating this integral explicitly for each reflection we can accurately determine the spectrum at the detector. After a great many computed reflections we have effectively computed a convolution of the incident spectrum with the rocking curve. We can see this by retaining θ_B in the rocking curve equation and transforming the incident intensity to a function of θ_B. Then if we perform the integral over all possible θ_B instead of λ we get

$$I_{\theta,r} = \int_0^{\pi/2} I_{\theta_B,i}\sqrt{2}Ge^{-2\pi G^2(\theta-\theta_B)^2}d\theta_B \tag{C.8}$$

$$= I_{\theta_B,i} * W(\theta - \theta_B) \tag{C.9}$$

C.2 2D Ray Tracer

```
function Data_out = TwodRayTracer(Spectrometer_params,Detector_params,sourcePt,plot_geometry)
%% Data_out = TwodRayTracer(Spectrometer_params,Detector_params,sourcePt,plot_geometry)
% Inputs:
%   Spectrometer_params.L -- source to center of curvature
%   Spectrometer_params.Rc -- mirror radius of curvature
%   Spectrometer_params.w -- mirror width
%   Spectrometer_params.offset -- complement of bragg angle at mirror center
%   Spectrometer_params.two_d -- quartz 1010
%
%   Detector_params.ld -- detector length
%   Detector_params.xo -- x corner locations
%   Detector_params.yo -- y corner locations
%
%   sourcePt -- location of source
%
%   plot_geometry -- 'y' -> plot the setup schematically
%                 -- 'n' -> do not plot
% Output:
%   Data_out -- Nx3 array -> [X lambda Magnification]
%       X -- intersection of reflected ray with detector
%       lambda -- Bragg wavelength as a function of position on detector
%       Magnification -- Spatial magnification as a function of position
%% x and y unit vectors
% xhat = [1 0];
% yhat = [0 1];
%% Unpack mirror and detector parameters
L = Spectrometer_params.L; %700;    % source to center of curvature
Rc = Spectrometer_params.Rc; %180;   %mirror radius of curvature
w = Spectrometer_params.w; %55;     % mirror width
offset = Spectrometer_params.offset; %(pi/180)*20;
two_d = Spectrometer_params.two_d; %8.5;        % quartz 1010


ld = Detector_params.ld; %80;
detectorX = Detector_params.xo; %5;
detectorY = Detector_params.yo; %-20;


%% Define spectrometer
Rrwd = Rc/2;    % rowland circle radius
arc = w/Rc;
mirrorCtr = [L 0];
theta = -arc/2+offset:0.0001:arc/2+offset;
```

```
x = Rc*cos(theta)+mirrorCtr(1);
y = Rc*sin(theta)+mirrorCtr(2);

%% create rowland circle
theta = 0:0.01:2*pi;
xr = Rrwd*cos(theta);
yr = Rrwd*sin(theta);

%% locate center of mirror
centralPt = [x(round(size(x,2)/2)) y(round(size(x,2)/2))];

%% Matrix elements for determining intersection of R with detector
A2 = detectorY(2) - detectorY(1);
B2 = detectorX(1) - detectorX(2);
C2 = A2*detectorX(1)+B2*detectorY(1);

%% creat figure for spectrometer geometry
PlotFlag = 0;
if strcmp(plot_geometry,'y')
    x0 = (centralPt(1)-L)/2+L;
    y0 = centralPt(2)/2;

    figure('Units','inches','Position',[7,6,6.5,5.5]);
    ax2 = gca;
    set(ax2,'Position',[.125  .15  .7  .75],'XAxisLocation','bottom',...
        'YAxisLocation','left','Color','w','XColor','k','YColor','k',...
        'FontSize',20,'Parent',gcf);
    axis equal
    hold on
    %     xlim([0 400])
    %     ylim([-50 150])
    line([mirrorCtr(1) centralPt(1)],[mirrorCtr(2) centralPt(2)],...
        'Color','r','LineStyle','--','LineWidth',2,'Parent',ax2);
    line(xr+x0,yr+y0,'Color','c','LineWidth',2,'Parent',ax2);
    line(detectorX,detectorY,'Color','k','LineWidth',2,'Parent',ax2);
    line([0 L], [0 0],'Color', 'r','Marker','+','MarkerSize',10,...
        'LineWidth',2,'LineStyle','none','Parent',ax2);
    line(x,y,'LineWidth',2,'Parent',ax2);
    PlotFlag = 1;
end
%% initialize loop arrays
xint = zeros(size(x,2)-2,1);
yint = zeros(size(x,2)-2,1);
Kspat = zeros(size(x,2)-2,1);
Kspect = zeros(size(x,2)-2,1);
```

```
lambda_B = zeros(size(x,2)-2,1);
Xfilm = zeros(size(x,2)-2,1);
%% loop through mirror points and source points to determine reflection
for n = 1:size(x,2)-2
    i = n+1;

    dy = y(i+1) - y(i-1);
    dx = x(i+1) - x(i-1);

    % unit tangent and normal vector
    that = [dx dy]/norm([dx dy]);
    nhat = that*[0 -1;1 0];

    % compute angle between tangent and x-axis
    mirrorPt_vec = [x(i)-sourcePt(1,1) y(i)-sourcePt(1,2)]...
        /norm([x(i)-sourcePt(1,1) y(i)-sourcePt(1,2)]);
    %Bragg angle
    theta_B = acos(that(1)*mirrorPt_vec(1) + that(2)*mirrorPt_vec(2));
    lambda_B(n,1) = two_d*sin(theta_B);

    % compute intersection of reflected ray and detector
    reflection_vec1 = mirrorPt_vec - 2*((nhat(1)*mirrorPt_vec(1)...
        +nhat(2)*mirrorPt_vec(2)))*nhat;
    reflection_vec = reflection_vec1/norm(reflection_vec1) + [x(i) y(i)];

    A1 = reflection_vec(2) - y(i);
    B1 = x(i) - reflection_vec(1);
    C1 = A1*x(i)+B1*y(i);

    determinant = A1*B2 - A2*B1;

    xint(n,1) = (B2*C1 - B1*C2)/determinant;
    yint(n,1) = (A1*C2 - A2*C1)/determinant;

    % compute magnification
    a = norm([x(i)-sourcePt(1,1) y(i)-sourcePt(1,2)]);
    b = norm([x(i)-xint(n,1) y(i)-yint(n,1)]);
    Kspat(n,1) = b/a;
    q = b - Rc*sin(theta_B);
    p = a - Rc*sin(theta_B);
    Kspect(n,1) = q/p;
    if PlotFlag == 1
        if  mod(n,1000) == 0
            line([xint(n,1) x(i)],[yint(n,1) y(i)],'Color','k',...
                'LineStyle','-','LineWidth',2,'Parent',ax2);
```

```
            line([0 x(i)],[0 y(i)],'Color','k','LineStyle','-',...
                'LineWidth',2,'Parent',ax2);
            line([x(i) x(i)+nhat(1)],[y(i) y(i)+nhat(2)],...
                'Color','m','Parent',ax2);
        end
    end
end
for i = 1:size(x,2)-2
    Xfilm(i,1) = norm([xint(i,1) yint(i,1)]) -...
        norm([detectorX(1) detectorY(1)]);
end
Data_out = [Xfilm lambda_B Kspect Kspat];
```

APPENDIX D

FILM CALIBRATION PROGRAMS

D.1 Background Correction

```
function background(shot_number)
%% Background Correction
%   This function selects the region of the image containing the background
%   and interpolates it over the whole image so that it can be subtracted.
%% Load image file and create array of double values from image intensity
shot = int2str(shot_number);
Iorig = imread(strcat('/scans/',shot,'-fssrB-distort.tif'));


I = imcomplement(Iorig);
Jdouble = im2double(I);
[nrows,ncols] = size(I);


I = imadjust(I);
imshow(I);
hold on


%% draw region of interest (ROI) around spectrum
BW = roipoly;
% invert ROI so that region outside spectrum ==1
BW = (~BW);
%% Randomly choose points in ROI excluding all edges
M = 100;
m = 1;
values = zeros(M,3);
while m <=M
    xim = round((ncols-1)*rand(1)+1);
    yim = round((nrows-1)*rand(1)+1);
    if BW(yim,xim) == 1
        if yim > 2 && yim < nrows-1 && xim > 2 && xim < ncols-1
            values(m,1) = xim;
            values(m,2) = yim;
            values(m,3) = mean(mean(Jdouble(yim-2:yim+2,...
                xim-2:xim+2)));
            m = m+1;
        end
    end
end
```

```
plot(values(:,1),values(:,2),'Color','r','Marker','o',...
    'LineWidth',2,'LineStyle','None','MarkerSize',10)



%% Interpolate background over entire image using RBF
x = values(:,1);
y = values(:,2);
z = values(:,3);
[XI YI] = meshgrid(1:1:ncols,1:1:nrows);
ZI = rbfinterp([XI(:)'; YI(:)'], rbfcreate([x'; y'], z',...
    'RBFFunction','gaussian', 'RBFConstant', 2));
ZI = reshape(ZI, size(XI));

figure
set(gca,'FontSize',20)
mesh(XI,YI,ZI)
xlabel('pixels')
ylabel('pixels')
zlabel('Background Level')
colorbar
%% subtract interpolated background from image
Icorrected = Jdouble - ZI;
%% Plot corrected image and write to file
figure
imagesc(Icorrected)
colorbar

imwrite(Icorrected,strcat(shot,...
    '-fssrB-distort-invert_bgsub.tif'),'tif')
```

D.2 Intensity Calibration Using Step Wedge

```
function CalibrateFilm(shot)
%% Create Film Intensity Calibration
%  This function takes a shot number string as input and generates the
%  calibration fucntion coefficients based on the model in Knauer et al.
%  using the step wedge filter responses from the CXRO website
%% load filter transmission data
PP16 = dlmread('PP16um.txt');
Al5 = dlmread('Al5um.txt');
Al04 = dlmread('Al04um.txt');
Mylar6 = dlmread('Mylar6um.txt');
```

```
Be10 = dlmread('Be10um.txt');
%% Create step wedge transmission curves
lambda = 12398./PP16(:,1);  %create wavelength array
step0 = ones(size(Be10(:,2)));
step1 = step0.*PP16(:,2).^0.25;
step2 = step0.*PP16(:,2);
step3 = step0.*Mylar6(:,2);

FilterTx = [lambda step0 step1 step2];

%%  Load wavelength calibration data
Data_out = dlmread(strcat(shot,'wavelength.txt'));
%%  Load image
Iorig = imread(strcat('/scans/',shot,'-FSSR-cropLower-invert_bgsub.tif'));
[nrows,ncols] = size(Iorig);

%% Plot image
Iadj = imadjust(Iorig); %auto-contrast
fig1 = figure;
imshow(Iadj)
%% create array of x position values
% image resolution
xres_inch = 3200;
% convert to pixels per millimeter
xres_mm = xres_inch/25.4;
x_film = (1:ncols)';

%% locate K-edge and translate wavelength calibration
Lambda_Kedge = 8.208; %for 2030 use 'red' edge of film to align
[Kx,Ky] = ginput(1);

%% Using K-edge create lambda(x)
x_cal = interp1(Data_out(:,1),Data_out(:,2),Lambda_Kedge);
x_translate = Kx;
x_film_mm = (1/xres_mm)*(x_film - x_translate);
lambda_film = interp1(Data_out(:,2) - x_cal,Data_out(:,1),x_film_mm);
film_data = [x_film, lambda_film];

%%  Determine film calibration at N positions
N = 6;
G = 0:1:60;
coeffs = zeros(N,2);
Is = zeros(N,3);    %preallocate array for measured intensity values
Gs = zeros(N,3);    %preallocate array for grayscale values
I = zeros(N,length(G)); %preallocate array for approx. intensity values
```

```
for i = 1:N
    [coeffs(i,:) Is(i,:) Gs(i,:)] = CreateCalibrationCurve(FilterTx,film_data,Iorig);
    I(i,:) = coeffs(i,1)*(exp(coeffs(i,2)*G) - 1);
end
close(fig1)

%% Plot calibration Intensity vs. grayscale values
figure
hold on
plot(Gs(1,:),Is(1,:),'o')
plot(G,I(1,:),'b')
plot(Gs(2,:),Is(2,:),'ro')
plot(G,I(2,:),'r')
plot(Gs(3,:),Is(3,:),'ko')
plot(G,I(3,:),'k')

%% assume calibration is constant over lambda and create one cal. curve
Gstotal = reshape(Gs,1,numel(Gs));
Istotal = reshape(Is,1,numel(Is));

%% Calculate fit using nonlinear least squares method
a0 = [0.1 0.1]; %starting guess
[coeffs_total,resnorm] = lsqnonlin(@myfun,a0);
% calculate approx Intensity vs. grayscale
Itotal(1,:) = coeffs_total(1,1)*(exp(coeffs_total(1,2)*G) - 1);

%% Plot Measured and approx. intensity curves
figure
plot(Gstotal,Istotal,'o')
hold on
plot(G,Itotal)
%% Model film calibration function
    function F = myfun(a)
        F = a(1)*(exp(a(2)*Gstotal) - 1) - Istotal;
    end
%% Pull lineout of backlighter
figure
imshow(Iadj)

[cx,cy] = ginput(1);
row = round(cy);
lineout = mean(Iorig(row-20:row+20,:));
% Apply correction
lineout_cal = coeffs_total(1,1)*(exp(coeffs_total(1,2)*lineout) - 1);
% Apply smoothing filter
```

```
slineout_cal = sgolayfilt(lineout_cal,3,81);

%% write calibrated backlighter intensity to file
dlmwrite(strcat(shot,'-BacklighterCal.txt'),[lambda_film,slineout_cal']);
%% write calibration coefficients to file
dlmwrite(strcat(shot,'-CalibrationCoefficients.txt'),coeffs_total);

end
```

D.2.1 Calibration Curve

```
function [coeffs Istep Gstep] = CreateCalibrationCurve(FilterTx,film_data,Iorig)
%  [coeffs Istep Gstep] = CreateCalibrationCurve(FilterTx,film_data,Iorig)
%   This function grabs grayscale values from the image of a stepwedge and
%   calculates the corresponding calibration curve for the film according
%   to the function I(g) = a*(exp(b*g)-1), where g is grayscale value
%   Inputs: FilterTx - [nx4] array with transmission curves for the three
%                      steps of the stepwedge in columns 2-4.  Column 1
%                      has the wavelength
%           film_data - [nx2] array:    Column 1: x coordinates of film
%                                       Column 2: lambda at film
%           Iorig - Image
%
%   Outputs:    coeffs - coefficients for fitting function
%               Istep - intensity values at each step according to FilterTx
%               Gstep - measured Grayscale values at each step
%
%   Created By: PFK
%           on: 12/30/10
%% Average over an area in each step to get grayscale
% get x interval first, use same interval for all steps
[x,y] = ginput(2);
x1 = round(x(1));  x2 = round(x(2));
xInterval = round(mean(x));
Linterval = film_data(x1:x2,2);
% choose each y interval
[x,y] = ginput(2);
y1 = round(y(1));  y2 = round(y(2));
Gstep(1) = mean(mean(Iorig(y1:y2,x1:x2)));
Ifilt = interp1(FilterTx(:,1),FilterTx(:,2),Linterval);
Istep(1) = mean(Ifilt);
```

```
[x,y] = ginput(2);
y1 = round(y(1));  y2 = round(y(2));
Gstep(2) = mean(mean(Iorig(y1:y2,x1:x2)));
Ifilt = interp1(FilterTx(:,1),FilterTx(:,3),Linterval);
Istep(2) = mean(Ifilt);

[x,y] = ginput(2);
y1 = round(y(1));  y2 = round(y(2));
Gstep(3) = mean(mean(Iorig(y1:y2,x1:x2)));
Ifilt = interp1(FilterTx(:,1),FilterTx(:,4),Linterval);
Istep(3) = mean(Ifilt);

%% Calculate fit using nonlinear least squares method
a0 = [0.1 0.1];
[coeffs,resnorm] = lsqnonlin(@myfun,a0);

    function F = myfun(a)
        F = a(1)*(exp(a(2)*Gstep) - 1) - Istep;
    end
end
```

D.2.2 Determination of Film Noise

```
function [coeffs] = FilmNoise(shot,N)
%% Determine film noise vs. intensity
%  This function samples N regions of the film and determines the variance
%  of the noise as a function of intensity.  Output is the coefficients for
%  the fitting function
%%  Load, autocontrast and display image
Iorig = imread(strcat('/scans/',shot,'-FSSR-cropLower-invert_bgsub.tif'));
[nrows,ncols] = size(Iorig);

Iadj = imadjust(Iorig);
fig1 = figure;
imshow(Iadj)
hold on
%% Load Film calibration coefficients
coeffs = dlmread(strcat(shot,'-CalibrationCoefficients.txt'));

%% Select N regions to sample for mean and variance of intensity
ExposureStats = zeros(N,3);
for n = 1:N
```

```
    rect = getrect;
    Xindeces = [round(rect(1)) round(rect(1))+round(rect(3))];
    Yindeces = [round(rect(2)) round(rect(2))+round(rect(4))];

    box = Iorig(Yindeces(1):Yindeces(2),Xindeces(1):Xindeces(2));
    box = reshape(double(box),1,numel(box));
    box = coeffs(1,1)*(exp(coeffs(1,2)*box) - 1);

    ExposureStats(n,1) = mean(box); %mean intensity
    ExposureStats(n,2) = sqrt(var(box));    %std. deviation
    ExposureStats(n,3) = ExposureStats(n,2)/ExposureStats(n,1);  %Error
    clear box
end
%% Calculate exponential fit
P = polyfit(ExposureStats(:,1),ExposureStats(:,3),2);
E = 0:0.01:1.4;
a0 = [0.1 0.1];
[coeffs,resnorm] = lsqnonlin(@myfun,a0)

%% Plot Error vs. Intensity and exponential fit
figure
plot(ExposureStats(:,1),ExposureStats(:,3),'o')
hold on
plot(E,polyval(P,E))
plot(E,coeffs(1)*exp(-coeffs(2)*E),'r')
%% Exponential fitting function
    function F = myfun(a)
        F = a(1)*exp(-a(2)*ExposureStats(:,1)) - ExposureStats(:,3);
    end

end
```

D.3 Wavelength Calibration

```
function OptimizeLambda_thesis(shot,Lmeas)
%% Load image file
shot_number = int2str(shot);
Ipath = strcat('scans/',shot_number,'-FSSR-cropUpperRotate.tif');

I = imread(Ipath); Iadj = imadjust(I);
[nrows,ncols] = size(I);
figure; hold on; imshow(Iadj);
```

```
% determine image resolution in dpi
info = imfinfo(Ipath); xres_inch = info.XResolution;
% convert to pixels per millimeter
xres_mm = xres_inch/25.4; x_film = (1:ncols)';

%% Find location of wavelength fiducials
N = length(Lmeas);
x_fiducial = zeros(1,N);
y_fiducial = zeros(1,N);
for n = 1:N
    h_box = msgbox(strcat('Choose calibration line #',int2str(n)));
    uiwait(h_box)
    [cx,cy,c] = improfile;
    peak_loc = CenterFind(c,0.7);
    x_fiducial(n) = cx(peak_loc);
    y_fiducial(n) = cy(peak_loc);
    line(x_fiducial(n),y_fiducial(n),...
        'LineStyle','none','Marker','o','Color','r');
    clear cx cy c
end
%% Starting Guess for Spectrometer parameters (mm)
L = [1038 1056];
a = [151 108];
b = [141 142];
S = 55;
Rc = 180;

%% Determine x1 and x2
gamma = acos((L(1)*L(1) + L(2)*L(2) - S*S)/(2*L(1)*L(2)));
X1 = [L(1)*cos(gamma);L(1)*sin(gamma)];
X2 = [L(2);0];

%% determine center of curvature(Xc) and detector ends(Xd1,Xd2)
x_guess = [0;0];
Xc = FindCenterofCurv(x_guess,X1,X2,Rc);
[Xd1 Xd2] = LocateDetector(X1,X2,a,b);

%% Transform to coordinate system so source & mirror center lie on x-axis
angle = acos(dot([1 0],Xc)/norm(Xc));
L = norm(Xc);
Rot = [cos(angle) -sin(angle);sin(angle) cos(angle)];
Xcprime = Rot*Xc;
X1prime = Rot*X1;
X2prime = Rot*X2;
```

```
Xd1prime = Rot*Xd1;
Xd2prime = Rot*Xd2;

%% Map derived quantities to those required for ray tracer routine
alpha1 = acos(dot([1; 0],(X2prime-Xcprime)/norm(X2prime-Xcprime)));
alpha2 = acos(dot((X2prime-Xcprime)/norm(X2prime-Xcprime),...
    (X1prime-Xcprime)/norm(X1prime-Xcprime)));

offset = alpha1 + 1*alpha2/2;
x0 = [L offset Xd1prime(1) Xd1prime(2) Xd2prime(1) Xd2prime(2)];
options = optimset('LargeScale','off','MaxFunEvals',5000);

%% find best fit parameters using least squares
X = lsqnonlin(@objfun,x0,[],[],options);

%%
spectrometer.L = X(1);
spectrometer.Rc = Rc;
spectrometer.w = S;
spectrometer.offset = X(2);
spectrometer.two_d = 8.5;
sourcePt = [0 0];

Detector.ld = norm([X(3) X(4)] - [X(5) X(6)]);
Detector.xo = [X(3) X(5)];
Detector.yo = [X(4) X(6)];

Data_out = TwodRayTracer(spectrometer,Detector,sourcePt,'n');

%% Calculate dispersion curve on film
x_film_mm = (1/xres_mm)*(x_film);
x_meas = (1/xres_mm)*(x_fiducial);
lambda_film = interp1(Data_out(:,1),Data_out(:,2),x_film_mm);
quad_coeffs = polyfit(x_meas,Lmeas,2);
quad = polyval(quad_coeffs,x_film_mm);

%% Plot
figure('Units','inches','Position',[7,6,6.5,5.5]);
ax1 = gca;
set(ax1,'Position',[.15  .15  .75  .75],'XAxisLocation','bottom',...
    'YAxisLocation','left','Color','w','XColor','k','YColor','k',...
    'FontSize',20,'Parent',gcf);
plot(Data_out(:,1),Data_out(:,2),'LineWidth',2)
hold on
plot(x_meas,Lmeas,'ro','LineWidth',2)
```

```
plot(x_film_mm,quad,'r')

%% write results to file
dlmwrite(strcat(shot_number,'wavelength_quadratic.txt')...
    ,[quad x_film_mm]);
dlmwrite(strcat(shot_number,'wavelength_optimize.txt')...
    ,[lambda_film x_film_mm]);

%% Objective function
    function f = objfun(X)
        %% Populate structures to pass to ray tracer routine

        spectrometer.L = X(1);
        spectrometer.Rc = Rc;
        spectrometer.w = S;
        spectrometer.offset = X(2);
        spectrometer.two_d = 8.5;
        sourcePt = [0 0];

        Detector.ld = norm([X(3) X(4)] - [X(5) X(6)]);
        Detector.xo = [X(3) X(5)];
        Detector.yo = [X(4) X(6)];

        %% Run ray tracing
        Data_out = TwodRayTracer(spectrometer,Detector,sourcePt,'n');

        %% Shift dispersion curve to line up with
        x_cal = interp1(Data_out(:,2),Data_out(:,1),Lmeas(1));
        x_cal_index = round(x_cal*xres_mm);
        x_translate = x_fiducial(1) - x_cal_index;
        x_film_mm = (1/xres_mm)*(x_film - x_translate);
        x_meas = (1/xres_mm)*(x_fiducial- x_translate);

        %%
        lambda_film = interp1(Data_out(:,1),Data_out(:,2),x_film_mm);
        Lcalc = interp1(x_film_mm,lambda_film,x_meas);
        f = norm(Lmeas - Lcalc)^2;
    end
end
```

D.4 Calculating Transmission

```
function SelectTxRegion(shot_number)
%%
path = '/Users/pfknapp/Documents/LPS/Absorption Spectroscopy/ScramData/';
shot = int2str(shot_number); % shot number
%%  Load wavelength calibration data
Data = dlmread(strcat(shot,'wavelength.txt'));
lambda_film = Data(:,1);

%% load film response calibration
coeffs = dlmread(strcat(shot,'-CalibrationCoefficients_Ldep10.txt'));
backlighter_import = dlmread(strcat(shot,'-BacklighterCal_Ldep10.txt'));
backlighter = interp1(backlighter_import(:,1),...
    backlighter_import(:,2),lambda_film);

%%  Load image
Iorig = imread(strcat('/scans/',shot,'-FSSR-cropUpper-invert_bgsub.tif'));
Iadj = imadjust(Iorig);
figure;
imshow(Iadj)

%% Choose Region From Image
rect = getrect(1);
Xindeces = [round(rect(1)) round(rect(1))+round(rect(3))];
Yindeces = [round(rect(2)) round(rect(2))+round(rect(4))];

lambdaRegion = lambda_film(Xindeces(1):Xindeces(2));
BLRegion = backlighter(Xindeces(1):Xindeces(2));

%% Calculate calibrated transmission
box = double(Iorig(Yindeces(1):Yindeces(2),Xindeces(1):Xindeces(2)));
P1 = coeffs(1,:);
P2 = coeffs(2,:);
coeff1 = polyval(P1,lambdaRegion)';
coeff2 = polyval(P2,lambdaRegion)';
ImRegion = zeros(size(box));
for i = 1:size(box,1)
    ImRegion(i,:) = coeff1.*(exp(coeff2.*box(i,:)) - 1);
end
%% Average over 11 pixels (~20m)
offset = 5;
i = 1;
row = offset+1;
```

```
while row < size(ImRegion,1)-offset
    TxRegion(i,:) = mean(ImRegion(row-offset:row+offset,:))./BLRegion';
    xVal(i,1) = row*1.9;
    i = i+1;
    row = row + 2*offset +1;
end

imagesc(TxRegion,[0 1])
colormap('jet')
colorbar

dlmwrite(strcat(path,shot,'-WholeTx.dat'),[lambdaRegion';TxRegion]);
```

APPENDIX E

GENETIC ALGORITHM FOR FITTING SPECTRA

The building blocks and basic code structure for the genetic algorithm were written by the Evolutionary Computation Research Team at the University of Sheffield, UK[12]. They have made available a free, open source toolbox for use with Matlab®. The toolbox comes with documentation which fully explains all of the functions and cites relevant works.

The toolbox can be found at:

http://www.shef.ac.uk/acse/research/ecrg/gat.html

E.1 Genetic Algorithm Script

```
clear all; clc;
%% Values to initialize GA
random = 1; %Flag to randomly initialize population
shot_No_str = '5844';
objStr = 'ChiSq';
NIND = 100; % Number of individuals
MAXGEN = 100; % Maximum no. of generations
Nreg = 3;   %Num. of regions to approx. plasma
rho_prec = 3; %Num bits representing density
Te_prec = 4; %Num bits representing temperature
dL_prec = 5; %Num bits representing path length
shift_prec = 4; %Num bits representing wavelength shift
Lreg = rho_prec + Te_prec + dL_prec; %length encoding for one region
MaxIter = 5;

%% Wavelength Intervals corresponding to each Satellite group
Ne_B = [7.76; 7.95]; F_B = [7.582;7.77]; O_B = [7.52; 7.65]; O_B5790 = [7.524; 7.582];
F_A = [8.3;8.35]; O_A = [8.245;8.28]; N_A = [8.16;8.205]; C_A = [8.08;8.135]; B_A = [7.98;8.07];

if strcmp(shot_No_str,'2034')
    LambdaWindows = [F_B Ne_B C_A N_A O_A];
elseif strcmp(shot_No_str,'2030')
```

```
    LambdaWindows = [O_B F_B Ne_B C_A N_A];
elseif strcmp(shot_No_str,'5846')
    LambdaWindows = [Ne_B F_A O_A N_A C_A];
elseif strcmp(shot_No_str,'5844')
    LambdaWindows = [Ne_B F_A O_A N_A C_A B_A];
elseif strcmp(shot_No_str,'5790')
    LambdaWindows = [O_B5790 F_B Ne_B N_A C_A B_A];
end

Nlambda = size(LambdaWindows,2);   %Num. of wavelength windows to use
%% Create array of init. conditions to pass to GA
initVals = [Nreg rho_prec Te_prec dL_prec NIND MAXGEN Nlambda shift_prec];

%% Import SCRAM Data
scram_data_path = '/Users/pfknapp/Documents/LPS/Absorption Spectroscopy/ScramData/';
header_data = dlmread(strcat(scram_data_path,'Header3.txt'),'\t');
rho_in = header_data(3,1:9); %create array of T_e
Te_in = header_data(4,1:9:end); %create array of rho
opacity_data = dlmread(strcat(scram_data_path,'opacity_data3.txt'),'\t');
lambda = opacity_data(:,1);
opacity_in = opacity_data(:,2:end);
clear opacity_data header_data

%% Import measured transmission
TXfile = dlmread(strcat(scram_data_path,shot_No_str,'-WholeTx.dat'));
opacity = interp1(lambda,opacity_in,TXfile(1,:)');
NumLines = size(TXfile,1);

%% Convert lambda windows to indeces
Llims = zeros(2,Nlambda);
for i = 1:Nlambda
    if strcmp(shot_No_str,'5846')||strcmp(shot_No_str,'5844')
        lmax_index = find((TXfile(1,:) - LambdaWindows(1,i)) >= 0,1);
        lmin_index = find((TXfile(1,:) - LambdaWindows(2,i)) >= 0,1);
        Llims(:,i) = [lmax_index;lmin_index];
    else
        lmax_index = find((TXfile(1,:) - LambdaWindows(1,i)) <= 0,1);
        lmin_index = find((TXfile(1,:) - LambdaWindows(2,i)) <= 0,1);
        Llims(:,i) = [lmin_index;lmax_index];
    end
end
%% Plot Tx image
%%{
figure
subplot(2,1,1)
```

```
imagesc(TXfile(2:end,:),[0 1])
colormap('jet')
colorbar
%}
%% Create Instrument Function
sig = 7.75/5000; % spectral resolution
dl = abs(TXfile(end,1)-TXfile(1,1))/length(TXfile(:,1));
x = -10*sig:dl:10*sig;
halfx = ceil(length(x)/2);
G = (1/sqrt(2*pi))*exp(-x.^2/(2*sig^2)); %gaussian instrument fcn

%%
KappaNu = [TXfile(1,:)' opacity];

%% Initialize arrays for loop
TxOut = zeros(NumLines-1,size(TXfile,2));
rho_out = zeros(NumLines-1,Nreg);
Te_out = zeros(NumLines-1,Nreg);
dL_out = zeros(NumLines-1,Nreg);
ChiSqr = zeros(NumLines-1,1);
ChiSqr_total = zeros(MaxIter,1);
TxExp = zeros(MaxIter,(NumLines-1)*size(TXfile,2));

%% initialize injected population
if random
    inj = [];
end

%% Outer Loop over X-positions
for i = 2:NumLines
    data = [(TXfile(1,:)') TXfile(i,:)'];
    n = 0;

    % initialize inner loop arrays
    rho_temp = ones(MaxIter,Nreg);
    Te_temp = ones(MaxIter,Nreg);
    dL_temp = ones(MaxIter,Nreg);
    ChiSqr_temp = ones(MaxIter,1);
    shift_temp = ones(MaxIter,Nlambda);
    ChrTemp = ones(MaxIter,Nreg*Lreg+Nlambda*shift_prec);

    while n < MaxIter
        %% Genetic Algorithm
        [ChrFinal ObjV cumObjV] = FitSpectrum_8x12(initVals,...
            inj,data,KappaNu,rho_in,objStr,Llims);
```

```
        [rho, Te, dL, shift] = DecodeCrAll_8x12(ChrFinal,Nreg,rho_prec,...
            Te_prec,dL_prec,Nlambda,shift_prec);
        [minVal index] = min(ObjV);

        n = n+1;
        rho_temp(n,1:Nreg) = rho(index,1:Nreg);
        Te_temp(n,1:Nreg) = Te(index,1:Nreg);
        dL_temp(n,1:Nreg) = dL(index,1:Nreg);
        shift_temp(n,1:Nlambda) = shift(index,1:Nlambda);
        ChrTemp(n,:) = ChrFinal(index,:);
        ChiSqr_temp(n,1) = minVal;

        %% Create population to inject to next iteration
        dL_i = zeros(size(dL));
        for j = 1:Nreg
            dL_i(1,j) = b2d(ChrFinal(index,...
                (j-1)*Lreg+rho_prec+Te_prec+1:(j-1)*Lreg+Lreg));
        end
        inj = perturbSolution(round(NIND/2),Nreg,rho(index,:),Te(index,:),...
            dL_i,shift(index,:),rho_prec,Te_prec,dL_prec,Nlambda,shift_prec);
    end
    %% Find optimum solution from above iterations
    [minVal index] = min(ChiSqr_temp);

    %% Create Tx spectrum from solution
    Txf = ones(size(size(data,1),1));
    for k = 1:Nreg
        Txf = Txf.*exp(-opacity(:,9*(Te_temp(index,k)-1)+rho_temp(index,k))...
            *rho_in(rho_temp(index,k))*dL_temp(index,k));
    end
    %% Convolve with instrument function
    X = [G zeros(1,length(Txf)-1)];
    Y = [Txf;zeros(length(G)-1,1)];
    temp = (1/(2*pi))*conv(X',Y);
    Txf = temp(halfx:size(Txf,1)+halfx-1,1);

    %% Write solution to outer loop arrays
    rho_out(i-1,1:Nreg) = rho_temp(index,1:Nreg);
    Te_out(i-1,1:Nreg) = Te_temp(index,1:Nreg);
    dL_out(i-1,1:Nreg) = dL_temp(index,1:Nreg);
    ChiSqr(i-1,1) = minVal;
    TxOut(i-1,:) = Txf';
    disp(int2str(i-1));
end
%% Wrute output to file
```

```
output = [rho_out Te_out dL_out ChiSqr];
dlmwrite(strcat('/Users/pfknapp/Documents/LPS/Absorption Spectroscopy/',shot_No_str,'/',shot_No_str,'-GA-Out_8x16_3reg.txt'),...
    output,'delimiter','\t')

%% Plot synthetic spectrum
subplot(2,1,2)
imagesc(TxOut(1:end,:),[0 1])
colormap('jet')
colorbar
```

E.2 Genetic Algorithm

```
function [ChrFinal ObjV cumObjV] = FitSpectrum_8x12(initVals,inj,data,KappaNu,rho_in,objStr,Llims)
%% [rho_out Te_out dL_out ObjV] = FitTxGA(objStr)
% FitTxGA uses the genetic algorithm toolbox provided for free from the
% evolutionary computation research tem at the univ. of Sheffield, UK to
% fit a plasma parameters to experimental transmission spectra.
% The algorithm approximates the plasma as a discrete number of regions
% each with uniform density and temperature and variable path length.  The
% GA optimizes the fit of the composite spectrum to the experimental
% spectrum using an opacity table at a discrete set of (rho,Te) combinations
% and returns the parameters of each region for the fittest solution.
%   Inputs: initVals:1x6 array of values used to initialize the GA
%                   [Nregions rho_precision Te_precision dL_precision NIND MAXGEN]
%           data: Nptsx2 array [lambda TxExp]
%           KappaNu: Opacity Table, 1st column is lambda, remainder are
%                       opacity values
%           rho_in: rho values associated with Opacity table
%           objstr: string to choose which objective function to use
%   Outputs: rho_out: a 2xNregions matrix [density1 density2 ... densityN;
%                                          index1   index2  ...  indexN]
%                   where densityn is the value of the density and indexn
%                   is the index to the density in the opacity table
%            Te_out: same as rho_out but with Temperature values
%            dL_out: 1xNregions matrix with path length of each region in cm
%            ObjV: the fitness value of the fittest solution
%   Written By:  Patrick Knapp
%   Written On:  1/4/2011
%% Initialize GA parameters
NIND = initVals(5); % Number of individuals
MAXGEN = initVals(6); % Maximum no. of generations
```

```
Nregions = initVals(1);   %Num. of regions to approx. plasma
rho_precision = initVals(2); %Num bits representing density
Te_precision = initVals(3); %Num bits representing temperature
dL_precision = initVals(4); %Num bits representing path length
shift_precision = initVals(8);
Nlambda = initVals(7);
LEN_Lambda_fit = sum(diff(Llims));
diffL = diff(Llims);
Llims_indeces = zeros(1,length(diffL)+1);
Llims_indeces(2:end) = cumsum(diffL);

LEN_region = rho_precision + Te_precision + dL_precision; %bit length representing each region
LEN = Nregions*LEN_region + Nlambda*shift_precision;  %length of entire chromosome
GGAP = 0.9; % Generation gap

% Initialise population
Chrom = crtbp(NIND, LEN); %creates random binary population
% inject former poulation if exists
if (isempty(inj) == 0)
   num_inj = size(inj,1);
   Chrom(1:num_inj,:) = inj;
end
%% Decode the initial population
[rho, Te, dL, shift] = DecodeCrAll_8x12(Chrom,Nregions,rho_precision,Te_precision,dL_precision,Nlambda,shift_precision);
%% Create Instrument Function
sig = 7.75/5000; % spectral resolution
dl = abs(data(end,1)-data(1,1))/length(data(:,1));
x = -10*sig:dl:10*sig;
halfx = ceil(length(x)/2);
G = (1/sqrt(2*pi))*exp(-x.^2/(2*sig^2));
%% Compute weights
reduce = 1/(LEN_Lambda_fit-3-1);
sigma = (-0.12*data(:,2).^3+ 0.55*data(:,2).^2-0.85*data(:,2) +0.59);
%% load opacity table
opacity = KappaNu(:,2:end);
%% Choose Objective Function
if strcmp(objStr,'ChiSqr'); objfun = @objfunChiSqr;
elseif strcmp(objStr,'ChiSq'); objfun = @objfunChiSq;
elseif strcmp(objStr,'RMS'); objfun = @objfunRMS;
end
%% Evaluate initial population
ObjV = objfun(rho,Te,dL,shift);

%% Generational loop
gen = 0; % Counter
```

```
cumObjV = zeros(MAXGEN,1);
while gen < MAXGEN,
    FitnV = ranking(ObjV);  % Assign fitness values to entire population
    SelCh = select('sus', Chrom, FitnV, GGAP);  % Select individuals for breeding
    SelCh = recombin('xovmp',SelCh,0.7); % Recombine individuals (crossover)
    SelCh = mut(SelCh);     % Apply mutation
    [rhoSel, TeSel, dLSel shiftSel] = DecodeCrAll_8x12(SelCh,Nregions,...
        rho_precision,Te_precision,dL_precision,Nlambda,shift_precision);% Evaluate offspring
    ObjVSel = objfun(rhoSel,TeSel,dLSel,shiftSel);  % Call objective function
    [Chrom ObjV]=reins(Chrom,SelCh,1,1,ObjV,ObjVSel); % Reinsert offspring into population
    cumObjV(gen+1,1) = min(ObjV);
    gen = gen+1;    % Increment counter
end

%% readout final best fit chromosome
ChrFinal = Chrom;

%% Objective Function
    function f = objfunChiSq(rho,Te,dL,shift)  % Chi-squared vectorized programming
        popSize = size(rho,1);
        ftemp = zeros(popSize,LEN_Lambda_fit);
        f = zeros(popSize,1);
            for m = 1:Nlambda
                Tx = ones(diffL(m)+1,popSize);
                for k = 1:Nregions
                    rhoL = rho_in(rho(:,k)).*dL(:,k)';
                    Tx = Tx.*exp(opacity(Llims(1,m)+shift(:,m):Llims(2,m)+shift(:,m),...
                        9*(Te(:,k)-1)+rho(:,k)).*rhoL(ones(diffL(m)+1,1),:));
                end
                %%{
                X = [G zeros(1,size(Tx,1)-1)];
                Y = [Tx;zeros(size(G,2)-1,popSize)];
                for j = 1:popSize
                    temp = (1/(2*pi))*conv(X',Y(:,j));
                    Tx(:,j) = temp(halfx:size(Tx,1)+halfx-1,1);
                end
                %}
                TxExp_temp = data(Llims(1,m):Llims(2,m),2);
                sigma_temp = sigma(Llims(1,m):Llims(2,m),1);
                ftemp(:,Llims_indeces(m)+1:Llims_indeces(m+1)+1) =...
                    ((TxExp_temp(:,ones(popSize,1)) - Tx)./sigma_temp(:,ones(popSize,1)))';
            end
            if Nregions == 1
                f(:,1) = abs(reduce*sum(ftemp.^2,2)-1);
            elseif Nregions == 3
```

```
            f(:,1) = abs(reduce*sum(ftemp.^2,2)-1)+(rho(:,2)<rho(:,1))+(rho(:,3)<rho(:,2));
        end
    end
end
```

E.2.1 Decoding the Chromosome

```
function [rho, Te, dL, shift] = Decode(Chrom,Nreg,rho_prec,Te_prec,dL_prec,Nlambda,shift_prec)
rho = zeros(size(Chrom,1),Nreg);
Te = zeros(size(Chrom,1),Nreg);
dL = zeros(size(Chrom,1),Nreg);
shift = zeros(size(Chrom,1),Nlambda);
Lreg = rho_prec + Te_prec + dL_prec; %length encoding for one region

if Nreg==1
    L = linspace(5,100,2^dL_prec);
elseif Nreg == 3
    L1 = linspace(1,100,2^dL_prec);
    L2 = linspace(20,200,2^dL_prec);
    L3 = linspace(60,500,2^dL_prec);
    L = [L1; L2; L3];
end
for i = 1:Nreg
    rho(:,i) = b2d(Chrom(:,(i-1)*Lreg+1:(i-1)*Lreg+rho_prec))+2;
    Te(:,i) = b2d(Chrom(:,(i-1)*Lreg+rho_prec+1:(i-1)*Lreg+rho_prec+Te_prec))+1;
    dL(:,i) = 10^-4*L(i,b2d(Chrom(:,(i-1)*Lreg+rho_prec+Te_prec+1:(i-1)...
        *Lreg+rho_prec+Te_prec+dL_prec))+1);
end
for i = 1:Nlambda
    shift(:,i) = b2d(Chrom(:,Nreg*Lreg+(i-1)*shift_prec+1:Nreg*Lreg+i...
        *shift_prec))-2^(shift_prec-1);
end
```

E.2.2 Encoding the Chromosome

```
function Chrom = Encode(rho,Te,dL,shift,Nreg,rho_prec,Te_prec,dL_prec,Nlambda,shift_prec,N)
Lreg = rho_prec + Te_prec + dL_prec; %length encoding for one region
Chrom = zeros(N,Nreg*Lreg+Nlambda*shift_prec);
for i = 1:Nreg
```

```
    Chrom(:,Lreg*(i-1)+1:Lreg*i) = ...
        [d2b(rho(:,i)-2,rho_prec) d2b(Te(:,i)-2,Te_prec) d2b(dL(:,i),dL_prec)];
end
for i = 1:Nlambda
    for n = 1:N
        Chrom(n,Nreg*Lreg+(i-1)*shift_prec+1:Nreg*Lreg+i*shift_prec)...
            = d2b(2^(shift_prec-1)+shift(i),shift_prec);
    end
end
```

BIBLIOGRAPHY

[1] P. Audebert, P. Renaudin, S. Bastiani-Ceccotti, J.-P. Geindre, C. Chenais-Popovics, S. Tzortzakis, V. Nagels-Silvert, R. Shepherd, I. Matsushima, S. Gary, F. Girard, O. Peyrusse, and J.-C. Gauthier. Picosecond time-resolved x-ray absorption spectroscopy of ultrafast aluminum plasmas. *Phys. Rev. Lett.*, 94(2):025004, Jan 2005.

[2] J. E. Bailey, G. A. Chandler, D. Cohen, M. E. Cuneo, M. E. Foord, R. F. Heeter, D. Jobe, P. W. Lake, J. J. MacFarlane, T. J. Nash, D. S. Nielson, R. Smelser, and J. Torres. Radiation science using z-pinch x rays. *Phys. Plasmas*, 9(5):2186–2194, 2002.

[3] J. Balmer, C. L. S. Lewis, R. E. Corbett, E. Robertson, S. Saadat, D. O'Neill, J. D. Kilkenny, C. A. Back, and R. W. Lee. X-ray absorption spectroscopy of laser-produced plasmas: A study of the experiment and data analysis. *Phys. Rev. A*, 40(1):330–340, Jul 1989.

[4] C. Bauche-Arnoult and J. Bauche. The temperature law for superconfigurations in non-lte plasmas. *Journal of Quantitative Spectroscopy and Radiative Transfer*, 71(2-6):189 – 199, 2001.

[5] F. N. Beg, K. Krushelnick, P. Lichtsteiner, A. Meakins, A. Kennedy, N. Kajumba, G. Burt, and A. E. Dangor. Table-top x-pinch for x-ray radiography. *Applied Physics Letters*, 82(25):4602–4604, 2003.

[6] I. C. Blesener, J. B. Greenly, S. A. Pikuz, T. A. Shelkovenko, S. Vishniakou, D. A. Hammer, and B. R. Kusse. Axial x-ray backlighting of wire-array z-pinches using x pinches. *Review of Scientific Instruments*, 80(12):123505, 2009.

[7] S. C. Bott, D. M. Haas, Y. Eshaq, U. Ueda, F. N. Beg, D. A. Hammer, B. Kusse, J. Greenly, T. A. Shelkovenko, S. A. Pikuz, I. C. Blesener, R. D. McBride, J. D. Douglass, K. Bell, P. Knapp, J. P. Chittenden, S. V. Lebedev, S. N. Bland, G. N. Hall, F. A. Suzuki Vidal, A. Marocchino, A. Harvey-Thomson, M. G. Haines, J. B. A. Palmer, A. Esaulov, and D. J. Ampleford. Study of the effect of current rise time on the formation of the precursor column in cylindrical wire array z pinches at 1 ma. *Phys. Plasmas*, 16(7):072701, 2009.

[8] S. C. Bott, S. V. Lebedev, D. J. Ampleford, S. N. Bland, J. P. Chittenden, A. Ciardi, M. G. Haines, C. Jennings, M. Sherlock, G. Hall, J. Rapley, F. N.

Beg, and J. Palmer. Dynamics of cylindrically converging precursor plasma flow in wire-array z -pinch experiments. *Phys. Rev. E*, 74(4):046403, Oct 2006.

[9] S. C. Bott, J. B. A. Palmer, D. J. Ampleford, S. N. Bland, J. P. Chittenden, and S. V. Lebedev. Use of x-pinches of diagnose behavior of low density ch foams on axis of wire array z-pinches. *Review of Scientific Instruments*, 75(10):3944–3946, 2004.

[10] K. M. Chandler, S. A. Pikuz, T. A. Shelkovenko, M. D. Mitchell, D. A. Hammer, and J. P. Knauer. Cross calibration of new x-ray films against direct exposure film from 1 to 8 kev using the x-pinch x-ray source. *Review of Scientific Instruments*, 76(11):113111, 2005.

[11] C. Chenais-Popovics, C. Fievet, J. P. Geindre, J. C. Gauthier, E. Luc-Koenig, J. F. Wyart, H. Pépin, and M. Chaker. K alpha absorption spectroscopy: Diagnostic of the radiative preheating of a laser-irradiated layered target. *Phys. Rev. A*, 40(6):3194–3208, Sep 1989.

[12] AJ Chipperfield, PJ Fleming, and H Pohlheim. genetic algorithm toolbox for matlab. In *Proc Int Conf on Systems Engineering, Coventry, UK*, pages 200–207, 1994.

[13] C. A. Coverdale, A. S. Safronova, V. L. Kantsyrev, N. D. Ouart, A. A. Esaulov, C. Deeney, K. M. Williamson, G. C. Osborne, I. Shrestha, D. J. Ampleford, and B. Jones. Observation of $\>400 - ev$ precursor plasmas from low-wire-number copper arrays at the 1-ma zebra facility. *Phys. Rev. Lett.*, 102(15):155006, Apr 2009.

[14] M. E. Cuneo, E. M. Waisman, S. V. Lebedev, J. P. Chittenden, W. A. Stygar, G. A. Chandler, R. A. Vesey, E. P. Yu, T. J. Nash, D. E. Bliss, G. S. Sarkisov, T. C. Wagoner, G. R. Bennett, D. B. Sinars, J. L. Porter, W. W. Simpson, L. E. Ruggles, D. F. Wenger, C. J. Garasi, B. V. Oliver, R A. Aragon, W. E. Fowler, M. C. Hettrick, G. C. Idzorek, D. Johnson, K. Keller, and S. E. Lazier. Characteristics and scaling of tungsten-wire-array z -pinch implosion dynamics at 20 ma. *Phys. Rev. E*, 71(4):046406, Apr 2005.

[15] M. P. Desjarlais. Practical improvements to the lee-more conductivity near the metal-insulator transition. *Contributions to Plasma Physics*, 41(2-3):267–270, 2001.

[16] J. D. Douglass, S. A. Pikuz, T. A. Shelkovenko, D. A. Hammer, S. N. Bland, S. C. Bott, and R. D. McBride. Structure of the dense cores and ablation

plasmas in the initiation phase of tungsten wire-array z pinches. *Phys. Plasmas*, 14(1):012704, 2007.

[17] J.D. Douglass. *AN EXPERIMENTAL STUDY OF TUNGSTEN WIRE-ARRAY Z-PINCH PLASMAS USING TIME-GATED POINT-PROJECTION X-RAY IMAGING*. PhD thesis, Cornell University, 2007.

[18] R. Paul Drake. *High Energy Density Physics*. Spinger, 2006.

[19] H. Drawin and P. Felenbok. *Data For Plasmas in Local Thermodynamic Equilibrium*. Gauthier-Villars, 1965.

[20] M. E. Foord, R. F. Heeter, H. K. Chung, P. A. M. van Hoof, J. E. Bailey, M. E. Cuneo, D. A. Liedahl, K. B. Fournier, V. Jonauskas, R. Kisielius, C. Ramsbottom, P. T. Springer, F. P. Keenan, S. J. Rose, and W. H. Goldstein. Study of x-ray photoionized fe plasma and comparisons with astrophysical modeling codes. *Journal of Quantitative Spectroscopy and Radiative Transfer*, 99(1-3):712 – 729, 2006.

[21] Alan P. Lightman George B. Rybicki. *Radiative Processes in Astrophysics*. Wiley-VCH, 2004.

[22] E. Grabovskii, K. Mitrofanov, G. Oleinik, and I. Porofeev. X-ray backlighting of the periphery of an imploding multiwire array in the angara-5-1 facility. *Plasma Physics Reports*, 30:121–127, 2004. 10.1134/1.1648936.

[23] J. B. Greenly, J. D. Douglass, D. A. Hammer, B. R. Kusse, S. C. Glidden, and H. D. Sanders. A 1 ma, variable risetime pulse generator for high energy density plasma research. *Rev. Sci. Instrum.*, 79(7):073501, 2008.

[24] Hans R. Griem. *Principles of Plasma Spectroscopy*. Cambridge University Press, 2005.

[25] T. A. Hall, J. Al-Kuzee, A. Benuzzi, M. Koenig, J. Krishnan, N. Grandjouan, D. Batani, S. Bossi, and S. Nicolella. Experimental observation of the shift and width of the aluminium k absorption edge in laser shock-compressed plasmas. *EPL (Europhysics Letters)*, 41(5):495, 1998.

[26] S. B. Hansen. Private Communication.

[27] S. B. Hansen, J. Bauche, C. Bauche-Arnoult, and M. F. Gu. Hybrid atomic

models for spectroscopic plasma diagnostics. *High Energy Density Physics*, 3(1-2):109 – 114, 2007. Radiative Properties of Hot Dense Matter.

[28] B. L. Henke, E. M. Gullikson, and J. C. Davis. X-ray interactions: photoabsorption, scattering, transmission, and reflection at e=50-30000 ev, z=1-92,. *Atomic Data and Nuclear Data Tables*, 54:181–342, 1993.

[29] B. L. Henke, J. Y. Uejio, G. F. Stone, C. H. Dittmore, and F. G. Fujiwara. High-energy x-ray response of photographic films: models and measurement. *J. Opt. Soc. Am. B*, 3(11):1540–1550, Nov 1986.

[30] J.D. Huba. Nrl plasma formulary. Naval Research Laboratory, Washington D.C., 2009.

[31] Carlos A. Iglesias. Effects of backlight structure on absorption experiments. *Journal of Quantitative Spectroscopy and Radiative Transfer*, 99(1-3):295 – 304, 2006. Radiative Properties of Hot Dense Matter.

[32] Prism Computational Sciences Inc. Madison. WI 53711.

[33] Fengtao Jin, Jiaolong Zeng, and Jianmin Yuan. Detailed diagnostics of a laser produced aluminum plasma by the k[alpha] satellites. *Journal of Quantitative Spectroscopy and Radiative Transfer*, 109(16):2707 – 2714, 2008.

[34] D.H. Kalantar. *An experimental study of the dynamics of x-pinch and z-pinch plasmas*. PhD thesis, Cornell University, 1993.

[35] Jun Kawai. *Absorption Techniques in X-Ray Spectrometry*. John Wiley & Sons, Ltd, 2006.

[36] P. F. Knapp, J. B. Greenly, P.-A. Gourdain, C. L. Hoyt, M. R. Martin, S. A. Pikuz, C. E. Seyler, T. A. Shelkovenko, and D. A. Hammer. Growth and saturation of the axial instability in low wire number wire array z pinches. *Physics of Plasmas*, 17(1):012704, 2010.

[37] J. P. Knauer, F. J. Marshall, B. Yaakobi, D. Anderson, B. A. Schmitt, K. M. Chandler, S. A. Pikuz, T. A. Shelkovenko, M. D. Mitchell, and D. A. Hammer. Response model for kodak biomax-ms film to x rays. *Review of Scientific Instruments*, 77(10):10F331, 2006.

[38] S. V. Lebedev, R. Aliaga-Rossel, S. N. Bland, J. P. Chittenden, A. E. Dan-

gor, M. G. Haines, and I. H. Mitchell. The dynamics of wire array z-pinch implosions. *Physics of Plasmas*, 6(5):2016–2022, 1999.

[39] S. V. Lebedev, F. N. Beg, S. N. Bland, J. P. Chittenden, A. E. Dangor, M. G. Haines, K. H. Kwek, S. A. Pikuz, and T. A. Shelkovenko. Effect of discrete wires on the implosion dynamics of wire array z pinches. *Phys. Plasmas*, 8(8):3734–3747, 2001.

[40] S. V. Lebedev, F. N. Beg, S. N. Bland, J. P. Chittenden, A. E. Dangor, M. G. Haines, M. Zakaullah, S. A. Pikuz, T. A. Shelkovenko, and D. A. Hammer. X-ray backlighting of wire array z-pinch implosions using x pinch. *Review of Scientific Instruments*, 72(1):671–673, 2001.

[41] L. Lecherbourg, P. Renaudin, S. Bastiani-Ceccotti, J.-P. Geindre, C. Blancard, P. Coss, G. Faussurier, R. Shepherd, and P. Audebert. X-ray absorption of a warm dense aluminum plasma created by an ultra-short laser pulse. *High Energy Density Physics*, 3(1-2):175 – 180, 2007.

[42] A Levy, F Dorchies, M Harmand, C Fourment, S Hulin, O Peyrusse, J J Santos, P Antici, P Audebert, J Fuchs, L Lancia, A Mancic, M Nakatsutsumi, S Mazevet, V Recoules, P Renaudin, and S Fourmaux. X-ray absorption for the study of warm dense matter. *Plasma Phys. Control. Fusion*, Volume 51, Number 12, 2009.

[43] D. Liberman and J. Albritton. Dense plasma equation of state model. *Journal of Quantitative Spectroscopy and Radiative Transfer*, 51(1-2):197 – 200, 1994. Special Issue Radiative Properties of Hot Dense Matter.

[44] J. J. MacFarlane, J. E. Bailey, G. A. Chandler, C. Deeney, M. R. Douglas, D. Jobe, P. Lake, T. J. Nash, D. S. Nielsen, R. B. Spielman, P. Wang, and P. Woodruff. X-ray absorption spectroscopy measurements of thin foil heating by z-pinch radiation. *Phys. Rev. E*, 66(4):046416, Oct 2002.

[45] R. Marchand, S. Caill, and Y. T. Lee. Improved screening coefficients for the hydrogenic ion model. *Journal of Quantitative Spectroscopy and Radiative Transfer*, 43(2):149 – 154, 1990.

[46] M. R. Martin, C. E. Seyler, and J. B. Greenly. The role of magnetic field in the transition to streaming ablation in wire arrays. *Physics of Plasmas*, 17(5):052706, 2010.

[47] Matthew R. Martin. *Generalized Ohm's Law at the plasma vacuum interface*. PhD thesis, Cornell Univesity, 2010.

[48] R. D. McBride. *Implosion dynamics, radiation characteristics, and spectroscopic measurements of wire-array z-pinches on the cornell beam research accelerator (COBRA)*. PhD thesis, Cornell University, 2009.

[49] B. S. Morse, T. S. Yoo, P. Rheingans, D. T. Chen, and K. R. Subramanian. Interpolating implicit surfaces from scattered surface data using compactly supported radial basis functions. In *Shape Modeling and Applications, SMI 2001 International Conference on.*, pages 89 –98, may 2001.

[50] The National Academy of Sciences. *Frontiers in Highe Energy Density Physics: The X-Games of Contemporary Science*. The National Acadamies Press, 2003.

[51] D. M. O'Neill, C. L. S. Lewis, D. Neely, S. J. Davidson, S. J. Rose, and R. W. Lee. Characterization of a laser-produced plasma using the technique of point-projection absorption spectroscopy. *Phys. Rev. A*, 44(4):2641–2648, Aug 1991.

[52] T. S. Perry, S. J. Davidson, F. J. D. Serduke, D. R. Bach, C. C. Smith, J. M. Foster, R. J. Doyas, R. A. Ward, C. A. Iglesias, F. J. Rogers, J. Abdallah, R. E. Stewart, J. D. Kilkenny, and R. W. Lee. Opacity measurements in a hot dense medium. *Phys. Rev. Lett.*, 67(27):3784–3787, Dec 1991.

[53] S. A. Pikuz. Cavitation and foam-like hollow structure formation in the dense core of exploded wire. *To be published in Proceedings of the 8th International Conference on Dense Z Pinches*, 2011.

[54] S. A. Pikuz, J. D. Douglass, T. A. Shelkovenko, D. B. Sinars, and D. A. Hammer. Wide band focusing x-ray spectrograph with spatial resolution. *Review of Scientific Instruments*, 79(1):013106, 2008.

[55] S. A. Pikuz, T. A. Shelkovenko, D. B. Sinars, J. B. Greenly, Y. S. Dimant, and D. A. Hammer. Multiphase foamlike structure of exploding wire cores. *Phys. Rev. Lett.*, 83(21):4313–4316, Nov 1999.

[56] David Salzmann. *Atomic Physics In Hot Plasmas*. Oxford University Press, 1998.

[57] H. Sawada, S. P. Regan, P. B. Radha, R. Epstein, D. Li, V. N. Goncharov, S. X. Hu, D. D. Meyerhofer, J. A. Delettrez, P. A. Jaanimagi, V. A. Smalyuk, T. R. Boehly, T. C. Sangster, B. Yaakobi, and R. C. Mancini. Al 1s-2p absorption spectroscopy of shock-wave heating and compression in laser-driven planar foil. *Physics of Plasmas*, 16(5):052702, 2009.

[58] Lothar M. Schmitt. Theory of genetic algorithms. *Theoretical Computer Science*, 259(1-2):1 – 61, 2001.

[59] C. E. Seyler and M. R. Martin. Relaxation model for extended magnetohydrodynamics: Comparison to magnetohydrodynamics for dense z-pinches. *Physics of Plasmas*, 18(1):012703, 2011.

[60] T. A. Shelkovenko, S. A. Pikuz, A. D. Cahill, P. F. Knapp, D. A. Hammer, D. B. Sinars, I. N. Tilikin, and S. N. Mishin. Hybrid x-pinch with conical electrodes. *Physics of Plasmas*, 17(11):112707, 2010.

[61] T. A. Shelkovenko, S. A. Pikuz, J. D. Douglass, I. C. Blesener, J. B. Greenly, R. D. McBride, D. A. Hammer, and B. R. Kusse. Wire core and coronal plasma expansion in wire-array z pinches with small numbers of wires. *Physics of Plasmas*, 14(10):102702, 2007.

[62] T. A. Shelkovenko, S. A. Pikuz, R. D. McBride, P. F. Knapp, H. Wilhelm, D. A. Hammer, and D. B. Sinars. Nested multilayered x pinches for generators with mega-ampere current level. *Physics of Plasmas*, 16(5):050702, 2009.

[63] T. A. Shelkovenko, D. B. Sinars, S. A. Pikuz, K. M. Chandler, and D. A. Hammer. Point-projection x-ray radiography using an x pinch as the radiation source. *Review of Scientific Instruments*, 72(1):667 –670, jan 2001.

[64] T. A. Shelkovenko, D. B. Sinars, S. A. Pikuz, and D. A. Hammer. Radiographic and spectroscopic studies of x-pinch plasma implosion dynamics and x-ray burst emission characteristics. *Phy. Plasmas*, 8(4):1305–1318, 2001.

[65] D. B. Sinars, M. E. Cuneo, B. Jones, C. A. Coverdale, T. J. Nash, M. G. Mazarakis, J. L. Porter, C. Deeney, D. F. Wenger, R. G. Adams, E. P. Yu, D. E. Bliss, and G. S. Sarkisov. Measurements of the mass distribution and instability growth for wire-array z-pinch implosions driven by 14–20 ma. *Phys. Plasmas*, 12(5):056303, 2005.

[66] D. B. Sinars, Min Hu, K. M. Chandler, T. A. Shelkovenko, S. A. Pikuz, J. B. Greenly, D. A. Hammer, and B. R. Kusse. Experiments measuring the initial energy deposition, expansion rates and morphology of exploding wires with about 1 ka/wire. *Phys. Plasmas*, 8(1):216–230, 2001.

[67] D. B. Sinars, S. A. Pikuz, J. D. Douglass, R. D. McBride, D. J. Ampleford, P. Knapp, K. Bell, D. Chalenksi, M. E. Cuneo, J. B. Greenly, D. A. Hammer,

B. R. Kusse, A. Mingaleev, T. A. Shelkovenko, and D. F. Wenger. Bright spots in 1 ma x pinches as a function of wire number and material. *Physics of Plasmas*, 15(9):092703, 2008.

[68] D. B. Sinars, S. A. Pikuz, T. A. Shelkovenko, K. M. Chandler, and D. A. Hammer. Temporal parameters of the x-pinch x-ray source. *Rev. Sci. Instrum.*, 72(7):2948–2956, 2001.

[69] D. B. Sinars, S. A. Pikuz, T. A. Shelkovenko, K. M. Chandler, D. A. Hammer, and J. P. Apruzese. Time-resolved spectroscopy of al, ti, and mo x pinch radiation using an x-ray streak camera. *Journal of Quantitative Spectroscopy and Radiative Transfer*, 78(1):61 – 83, 2003.

[70] S. N. Sivanandam and S. N. Deepa. *Introduction to Genetic Algorithms*. Springer-Verlag Berlin Heidelberg, 2008.

[71] S. A. Slutz, M. C. Herrmann, R. A. Vesey, A. B. Sefkow, D. B. Sinars, D. C. Rovang, K. J. Peterson, and M. E. Cuneo. Pulsed-power-driven cylindrical liner implosions of laser preheated fuel magnetized with an axial field. *Physics of Plasmas*, 17(5):056303, 2010.

[72] Igor I. Sobelman. *Atomic Spectra and Radiative Transitions*. Springer-Verlag Berlin Heidelberg New York, 1979.

[73] Byung Moo Song, Sergei A. Pikuz, Tatiania A. Shelkovenko, and David A. Hammer. Determination of the size and structure of an x-pinch x-ray source from the diffraction pattern produced by microfabricated slits. *Appl. Opt.*, 44(12):2349–2358, Apr 2005.

[74] R. B. Spielman, C. Deeney, G. A. Chandler, M. R. Douglas, D. L. Fehl, M. K. Matzen, D. H. McDaniel, T. J. Nash, J. L. Porter, T. W. L. Sanford, J. F. Seamen, W. A. Stygar, K. W. Struve, S. P. Breeze, J. S. McGurn, J. A. Torres, D. M. Zagar, T. L. Gilliland, D. O. Jobe, J. L. McKenney, R. C. Mock, M. Vargas, T. Wagoner, and D. L. Peterson. Tungsten wire-array z-pinch experiments at 200 tw and 2 mj. *Phys. Plasmas*, 5(5):2105–2111, 1998.

[75] S. Tzortzakis, P. Audebert, P. Renaudin, S. Bastiani-Ceccotti, J.P. Geindre, C. Chenais-Popovics, V. Nagels, S. Gary, R. Shepherd, F. Girard, I. Matsushima, O. Peyrusse, and J.-C. Gauthier. Time- and space-resolved x-ray absorption spectroscopy of aluminum irradiated by a subpicosecond high-power laser. *Journal of Quantitative Spectroscopy and Radiative Transfer*, 99(1-3):614 – 626, 2006.

[76] Edmund P. Yu, B. V. Oliver, D. B. Sinars, T. A. Mehlhorn, M. E. Cuneo, P. V. Sasorov, M. G. Haines, and S. V. Lebedev. Steady-state radiation ablation in the wire-array z pinch. *Physics of Plasmas*, 14(2):022705, 2007.